

Influence of temperature on concrete beams strengthened in flexure with CFRP

Citation for published version (APA):

Klamer, E. L. (2009). *Influence of temperature on concrete beams strengthened in flexure with CFRP*. [Phd Thesis 1 (Research TU/e / Graduation TU/e), Built Environment]. Technische Universiteit Eindhoven.
<https://doi.org/10.6100/IR656177>

DOI:

[10.6100/IR656177](https://doi.org/10.6100/IR656177)

Document status and date:

Published: 01/01/2009

Document Version:

Publisher's PDF, also known as Version of Record (includes final page, issue and volume numbers)

Please check the document version of this publication:

- A submitted manuscript is the version of the article upon submission and before peer-review. There can be important differences between the submitted version and the official published version of record. People interested in the research are advised to contact the author for the final version of the publication, or visit the DOI to the publisher's website.
- The final author version and the galley proof are versions of the publication after peer review.
- The final published version features the final layout of the paper including the volume, issue and page numbers.

[Link to publication](#)

General rights

Copyright and moral rights for the publications made accessible in the public portal are retained by the authors and/or other copyright owners and it is a condition of accessing publications that users recognise and abide by the legal requirements associated with these rights.

- Users may download and print one copy of any publication from the public portal for the purpose of private study or research.
- You may not further distribute the material or use it for any profit-making activity or commercial gain
- You may freely distribute the URL identifying the publication in the public portal.

If the publication is distributed under the terms of Article 25fa of the Dutch Copyright Act, indicated by the "Taverne" license above, please follow below link for the End User Agreement:

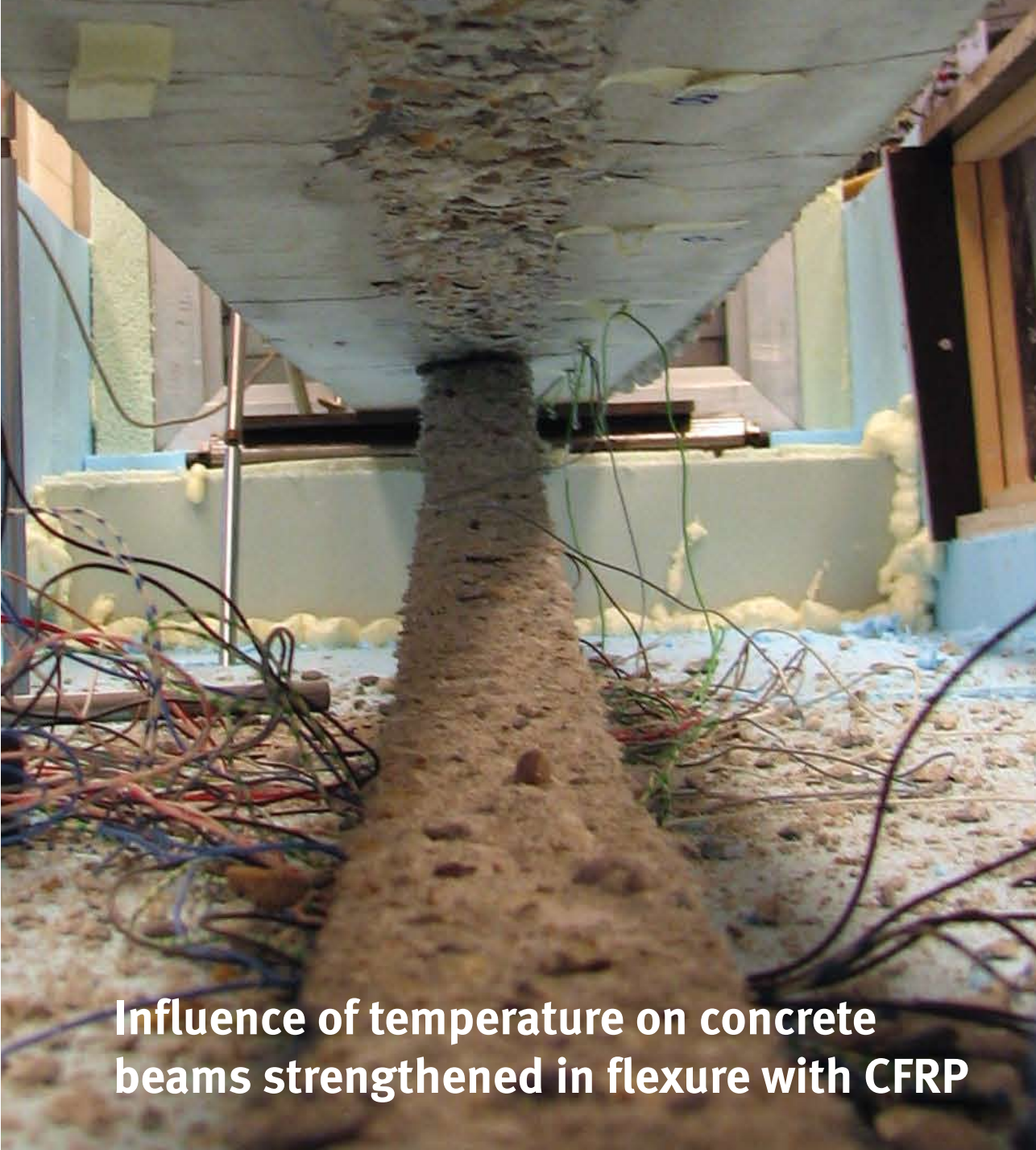
www.tue.nl/taverne

Take down policy

If you believe that this document breaches copyright please contact us at:

openaccess@tue.nl

providing details and we will investigate your claim.



Influence of temperature on concrete beams strengthened in flexure with CFRP

Ernst-Lucas Klamer

/ faculty of architecture building and planning tu eindhoven

bouwstenen

136

**INFLUENCE OF TEMPERATURE
ON CONCRETE BEAMS
STRENGTHENED IN FLEXURE WITH CFRP**

Ernst-Lucas Klamer

Technische Universiteit Eindhoven

Bouwstenen 136

Cover by A.W.M. Van Gennip / E.L. Klamer
Printed by Eindhoven University Press Facilities

ISBN 978-90-6814-619-6

Copyright © 2009 E.L. Klamer

All rights reserved. No part of this publication may be reproduced, stored in a retrieval system or transmitted in any form by any means without prior written consent of the author.

**INFLUENCE OF TEMPERATURE
ON CONCRETE BEAMS
STRENGTHENED IN FLEXURE WITH CFRP**

PROEFSCHRIFT

ter verkrijging van de graad van doctor aan de
Technische Universiteit Eindhoven, op gezag van de
rector magnificus, prof.dr.ir. C.J. van Duijn, voor een
commissie aangewezen door het College voor
Promoties in het openbaar te verdedigen
op maandag 23 november 2009 om 16.00 uur

door

Ernst-Lucas Klamer

geboren te Utrecht

Dit proefschrift is goedgekeurd door de promotoren:

prof.dr.ir. D.A. Hordijk

en

prof.ir. C.S. Kleinman

Constitution of the Doctoral Committee:

prof.ir. J. Westra (chair)

Department of Architecture, Building and Planning,
Eindhoven University of Technology, the Netherlands

prof.dr.ir. D.A. Hordijk

Department of Architecture, Building and Planning,
Eindhoven University of Technology, the Netherlands

prof.ir. C.S. Kleinman

Department of Architecture, Building and Planning,
Eindhoven University of Technology, the Netherlands

prof.dr.ir. S. Matthys

Laboratorium Magnel voor betononderzoek
Ghent University, Belgium

prof. T.C. Triantafillou MSc. PhD

Department of Civil Engineering
University of Patras, Greece

prof.ir. H.H. Snijder

Department of Architecture, Building and Planning,
Eindhoven University of Technology, the Netherlands

prof.dr.ir. J.C. Walraven

Department of Civil Engineering and Geosciences
Delft University of Technology, the Netherlands

ir. A. de Boer

Centre for Public Works
Ministry of Transport, Public Works and Water Management, the Netherlands

Acknowledgements

First of all, I would like to express my sincere gratitude to Prof. Dick Hordijk for his supervision and support during my PhD research at Eindhoven University of Technology. His enthusiasm and valuable remarks were of great help and highly improved the quality of my thesis. The remarks of Prof. Cees Kleinman were also highly appreciated, as he forced me to have a different look at the results of the experiments and analyses.

I owe many thanks to Ane de Boer from the Centre of Public Works (Rijkswaterstaat), who helped me during my Master and PhD research projects with learning and using DIANA and helped me improving and solving my DIANA analyses of the experiments, especially when DIANA was having a will on her own.

The time and effort in reading and reviewing this thesis by all members of the doctoral committee is also highly appreciated. I especially wish to express my gratitude to Prof. Stijn Matthys of Ghent University for the discussions during the mutual visits throughout the research project and for the introduction in the *fib*-Task Group meetings, which showed me the relevance of the research that is carried out into FRP.

The support of the Centre of Public Works (Rijkswaterstaat) to this PhD project is also highly appreciated. Rijkswaterstaat supported the project both financially as well as with the guidance of Ane de Boer, as mentioned before. I also owe many thanks to Sika Nederland B.V.. Sika supported the research project by providing all the required materials for the CFRP strengthening of all specimens in this thesis free of charge.

I also wish to say thanks to all my former colleagues of the unit Structural Design and Construction Technology of Eindhoven University of Technology for the great time I had during my PhD. I especially wish to thank my roommates Sander Zegers and Paul Teeuwen for the great time we have had and for the many squash games we have played, Mirek Rosmanit for letting me win at least one time with playing squash and Vincent Tabak of the Design and Decision Support Systems group for the company during fitness and for organizing the 'social events' of the PhD network. I also enjoyed the company of my fellow PhD researchers, Steffen Zimmerman, Bright N'Gandu, Dagowin La Poutré, Johan Maljaars, Natalia Kutanova, Edwin Huveners, Dennis Schoenmakers and Roel Sporenburg. I also wish to express my gratitude to Harrie Janssen, for his advice and support during my PhD.

Furthermore, I wish to acknowledge the great help from the people from the Pieter van Musschenbroek Laboratory of Eindhoven University of Technology, who helped me with setting up the experiments and building the test set-ups. Especially the help of Eric Wijen, Theo van de Loo, Johan van den Oever and Rien Canters was highly appreciated. Besides my former colleagues at Eindhoven University of Technology, I also wish to express my gratitude for the mental support of my current colleagues at Corsmit Raadgevend Ingenieurs and Royal Haskoning during the last bits of finishing my thesis.

The help of several students of both Eindhoven and Delft University of Technology was of great importance for the results in this thesis. I especially wish to thank Michael Hermes, who prepared and carried out the full scale experiments. Also the help of Reinier Ringers, Linda Schetters, Dennis Schoenmakers, Mariëlle Rutten and Rob Graat was highly appreciated.

Last, but by no means the least, I want to thank my parents and parents-in-law for their encouraging moral support during my PhD and, most important, I would like to thank my partner Lauretta for her understanding and patience during all the evenings and weekends I had to work on my thesis. She supported and encouraged me during all those years, for which I'm very, very grateful.

Ernst Klamer
Eindhoven, October 2009

Summary

The increasingly faster changing demands to existing buildings and ongoing deterioration of buildings and infrastructure have increased the need to strengthen existing structures. One of developments during the last two decades is the use of externally bonded Carbon Fiber Reinforced Polymer (CFRP) reinforcement to strengthen existing concrete structures. Failure of CFRP strengthened concrete structures is generally initiated by debonding of the CFRP reinforcement from the concrete surface. It can be expected that the debonding is affected by temperature, due to the significant difference in the coefficient of thermal expansion between concrete ($\alpha_c \approx 10 \times 10^{-6} / ^\circ\text{C}$) and CFRP ($\alpha_f \approx -1 \times 10^{-6} / ^\circ\text{C}$ in the fiber direction) and due to the change in material properties at elevated temperatures, especially those of the adhesive.

So far, only a limited amount of research has been carried out into the effect of temperature on the debonding behavior of externally bonded CFRP. Moreover, the available research has mainly been carried out with small scale test setups, while full scale CFRP strengthened structures could be affected by temperature in a different way. In this research project, the effect of temperature on the CFRP strengthening of concrete structures has been investigated both with small scale bond tests and with full scale beams, strengthened in flexure. Experimental results have been verified by numerical simulations of the tests by means of finite element analyses.

First the effect of temperature was investigated with small scale bond tests, for which two different types of test setups were used; the double-lap shear test and the three-point bending test. With both test setups, the capacity of the joint initially increased with increasing temperatures up to the glass transition temperature of the adhesive ($T_g = 62^\circ\text{C}$). Above this temperature, the type of failure changed from cracking in the concrete adjacent to the concrete-adhesive interface, leaving a small layer of concrete remaining attached to the adhesive, to failure exactly in between the concrete and the adhesive. This was accompanied by a significantly reduced, but also scattering bond strength.

The results of the numerical simulations confirmed the experimental results and showed that the increasing failure load with increasing temperature, up to the glass transition temperature, was mainly related to the difference in coefficient of thermal expansion between concrete and CFRP. This can be explained with the development of thermal shear stresses that are mainly concentrated at the plate-ends. These shear stresses acted at elevated temperature in the opposite direction as the shear stresses due to loading. Other observed effects of temperature were a reduced Young's modulus and creep of the adhesive, especially close to and above the glass transition temperature of the adhesive. Both effects caused a decrease in the peak in thermal shear stresses close to the plate-end, but did not have a significant effect on the failure load.

Additionally to the small scale bond tests, an experimental test program was set up to investigate the influence of temperature on full scale beams that were strengthened in flexure with externally bonded CFRP reinforcement. Four different beam configurations were investigated, each at three different temperatures, 20°C, 50°C and 70°C. Test results showed that the type of bond failure and the capacity of the beams that were tested at 50°C were not significantly affected by the temperature increase. At 70°C, the type of failure did not change or changed only partly, from failure in the concrete to failure exactly in the concrete-adhesive interface. This can be explained by the temperature cycle that was applied during heating of the beam to 70°C. A temperature cycle increases the glass transition temperature of the adhesive. Hence, the load capacity was not significantly affected at 70°C, except for the beam with a relatively short laminate length. This beam was designed to fail after debonding in the end anchorage zone. It turned out that the beams where failure initiated after cracking exactly at the plate-end or debonding close to the plate-end were more sensitive to the effects of temperature compared to the beams that failed after debonding further away from the plate-end. This can be explained by the fact that most effects of temperature, like the development of thermal stresses and the lower Young's modulus and creep of the adhesive at elevated temperatures, mainly affect the (shear) stress distributions close to the plate-end, and not significantly further away from the plate-end.

Finite element analyses of the full scale tests confirmed the findings of the experiments and were able to simulate the experiments both qualitatively and quantitatively. The performed full scale experiments and nonlinear numerical analyses, that can be regarded to be unique, provided a good insight in the effects of temperature on the strengthening of concrete structures with externally bonded CFRP, but also provided insight in the debonding behavior in general. The most important conclusion of the research is that the influence of temperature can safely be neglected up to about 10°C below the glass transition temperature of the adhesive. CFRP strengthened concrete structures should not be exposed to higher temperatures, as the capacity can suddenly drop above the glass transition temperature. Higher temperatures can be allowed by applying an adhesive with a higher glass transition temperature.

Samenvatting

De vraag om constructies te versterken is de afgelopen decennia sterkt toegenomen door de steeds sneller veranderende eisen aan bestaande gebouwen en de achteruitgang van bestaande bouwkundige en civiele constructies. Een van de meest recente ontwikkelingen op dit gebied is het gebruik van uitwendig opgelijmde koolstofvezelwapening ter versterking van bestaande betonnen constructies. Het bezwijken van met koolstofvezelwapening versterkte betonnen constructies wordt over het algemeen voorafgegaan door het onthechten van de koolstofvezelwapening van het betonoppervlak. Het valt te verwachten dat het (ont)hechtgedrag wordt beïnvloed door temperatuur, gezien het significante verschil in uitzettingscoëfficiënt tussen beton ($\alpha_c \approx 10 \times 10^{-6} / ^\circ\text{C}$) en koolstofvezelwapening ($\alpha_f \approx -1 \times 10^{-6} / ^\circ\text{C}$ in vezelrichting) en de verandering van verschillende materiaaleigenschappen bij verhoogde temperatuur, voornamelijk die van de lijm.

Tot nog toe is er slechts een beperkte hoeveelheid onderzoek uitgevoerd naar de invloed van temperatuur op het onthechten van uitwendig opgelijmde koolstofvezelwapening. Bovendien zijn de onderzoeken die zijn uitgevoerd hoofdzakelijk onderzoeken met kleine verschaalde proefstukken, terwijl koolstofvezelversterkte betonconstructies van normale grootte mogelijk op een andere manier door temperatuur worden beïnvloed. Het effect van temperatuur op de versterking van betonconstructies met uitwendig opgelijmde koolstofvezelversterkte is in dit onderzoeksproject zowel met kleine proefstukken als met grote, op buiging versterkte, balken onderzocht. De resultaten van de experimenten zijn geverifieerd met numerieke simulaties op basis van de eindige elementen methode.

Als eerste is de invloed van temperatuur met kleine hechtproeven in twee verschillende testopstellingen onderzocht, de 'double-lap shear test' en de drie-punts-buigproef. In beide testopstellingen bleek dat de capaciteit toenam met toenemende temperatuur, tot aan de glas-rubberovergangstemperatuur van de lijm ($T_g = 62^\circ\text{C}$). Boven deze temperatuur veranderde het onthechtingsgedrag, van onthechten door het scheuren van het beton evenwijdig aan de beton-lijm interface, waarbij een dunne laag beton op de lijmlaag achterbleef, naar het onthechten precies tussen het beton en de lijmlaag in. Deze verandering ging gepaard met een significante afname, maar ook grotere spreiding van de hechtsterkte.

De resultaten van de numerieke simulaties bevestigden de experimentele resultaten en lieten zien dat de toenemende bezwijklast met toenemende temperaturen, tot aan de glas-rubberovergangstemperatuur, voornamelijk veroorzaakt werd door het verschil in uitzettingscoëfficiënt tussen beton en koolstofvezelwapening. Dit verschil resulteerde in thermische schuifspanningen in het beton, evenwijdig aan de lijmlaag, die zich voornamelijk aan het einde van de koolstofvezelwapening concentreerden. Deze schuifspanningen werken in de tegenovergestelde richting als de schuifspanningen door het belasten van de proefstukken, wat de toenemende bezwijklast met toenemende temperatuur (tot T_g) verklaart.

Andere effecten van temperatuur die werden waargenomen tijdens de proeven waren een afnemende stijfheid en kruip van de lijm bij verhoogde temperaturen, vooral vlak voor en boven de glas-rubberovergangstemperatuur. Beide effecten veroorzaakten een afname van de (thermische) schuifspanningspieken aan het einde van de koolstofvezelwapening, maar hadden geen significant effect op de bezwijkbelastingen.

Na de hechtproeven werd een testprogramma opgezet om de invloed van temperatuur op, met uitwendig opgelijmde koolstofvezelwapening versterkte, betonnen balken van normale grootte te onderzoeken. Vier verschillende balkconfiguraties zijn onderzocht, elk bij drie verschillende temperaturen, te weten 20°C, 50°C en 70°C. De resultaten lieten zien dat bij 50°C de wijze van onthechten en de capaciteit van de balken niet significant beïnvloed werden door de temperatuur. Bij 70°C veranderde het type onthechten niet of slechts gedeeltelijk, van onthechten in het beton naar onthechten precies tussen de lijm en het beton in. Dit kan waarschijnlijk verklaard worden door de temperatuurscyclus die was toegepast gedurende het verwarmen van de balk naar 70°C. Een temperatuurscyclus verhoogt namelijk de glas-rubberovergangstemperatuur van de lijm. De bezwijkbelasting was daardoor ook niet significant beïnvloed op 70°C, met uitzondering van de balk met een relatief korte koolstofvezelwapeningsstrip. Deze balk was ontworpen om te bezwijken na onthechten in de eindverankeringszone. Het bleek dat de balken waarbij het bezwijken geïnitieerd werd door een scheur precies aan het einde of onthechten vlak bij het einde van de koolstofvezelwapening gevoeliger waren voor de invloed van temperatuur dan de balken waarbij het onthechten op een plaats verder weg van het einde begon. Dit kan worden verklaard door het feit dat de meeste temperatuurseffecten, zoals het ontstaan van thermische spanningen en een lagere stijfheid en kruip van de lijm bij verhoogde temperaturen, voornamelijk de spanningsverdeling vlak bij de einden van de koolstofvezelwapening beïnvloeden, en niet verder weg van de einden.

De eindige elementen analyses van de balken bevestigden de bevindingen van de experimenten en waren in staat om het onthechten zowel kwalitatief als kwantitatief te simuleren. De uitgevoerde proeven en niet-lineaire analyses, welke als uniek kunnen worden beschouwd, gaven een goed inzicht in de effecten van verhoogde temperatuur op de versterking van betonconstructies op buiging met uitwendig opgelijmde koolstofvezelwapening, maar gaven ook inzicht in het onthechtingsgedrag in het algemeen. De belangrijkste conclusie van het onderzoek is dat, tot ongeveer 10°C onder de glas-rubberovergangstemperatuur, de invloed van temperatuur kan worden verwaarloosd. Het blootstellen van een met koolstofvezelwapening versterkte betonconstructies aan hogere temperaturen moet worden voorkomen, omdat de capaciteit plotseling sterk terug kan lopen. Door het toepassen van een lijm met een hogere glas-rubberovergangstemperatuur kunnen hogere temperaturen toegelaten worden.

Contents

Acknowledgements	vii
Summary	ix
Samenvatting	xi
Notations	xxi
Indices	xxi
Symbols	xxi
1 Introduction	1
1.1 General	1
1.2 Scope of the research	2
1.3 Research objective	3
1.4 Outline	4
2 Strengthening of structures with externally bonded FRP	5
2.1 Introduction	5
2.2 FRP reinforcement	5
2.2.1 General	5
2.2.2 Internal FRP reinforcement	7
2.2.3 Externally bonded FRP reinforcement	8
2.3 Adhesive	12
2.4 Failure of flexural FRP strengthened concrete structures	13
2.4.1 Flexural failure of a beam	14
2.4.2 Shear failure of a beam	14
2.4.3 Debonding of the externally bonded FRP	15

3	Effect of temperature on FRP strengthened structures – state of the art.....	28
3.1	Introduction	28
3.2	Double-lap shear tests	28
3.2.1	Externally bonded steel strips	28
3.2.2	Externally bonded FRP.....	29
3.3	Small scale flexural tests	33
3.3.1	Externally bonded FRP.....	33
3.4	Full scale FRP strengthened concrete structures.....	35
3.4.1	General	35
3.4.2	Externally bonded CFRP.....	36
3.4.3	CFRP strengthened bridge deck at elevated temperature	37
3.4.4	Externally bonded prestressed CFRP.....	39
3.5	Theoretical stress development due to thermal mismatch.....	39
3.6	Summary.....	41
4	Effect of temperature on the material properties.....	42
4.1	Introduction	42
4.2	Concrete.....	42
4.2.1	General	42
4.2.2	Compressive strength.....	43
4.2.3	Tensile strength	44
4.2.4	Fracture energy	45
4.2.5	Creep and shrinkage.....	46
4.2.6	Young’s modulus	47
4.2.7	Coefficient of thermal expansion	48
4.3	Steel reinforcement	49
4.3.1	Tensile strength.....	49
4.3.2	Young’s modulus	49
4.3.3	Coefficient of thermal expansion	50
4.4	Fiber Reinforced Polymers.....	50
4.4.1	General	50
4.4.2	Tensile strength and Young’s modulus.....	51

4.4.3	Coefficient of thermal expansion	56
4.5	Adhesive	59
4.5.1	General	59
4.5.2	Flexural strength	60
4.5.3	Young's modulus	61
4.5.4	Glass transition temperature	62
4.5.5	Coefficient of thermal expansion	63
4.6	Summary	64
5	Effect of temperature on the bond behavior	65
5.1	Introduction	65
5.2	Mode I bond fracture	66
5.2.1	General	66
5.2.2	Concrete-adhesive joint	66
5.2.3	Adhesive-CFRP joint	67
5.3	Mode II bond fracture – Double-lap shear test	69
5.3.1	Test setup	69
5.3.2	Failure load as function of temperature	71
5.3.3	Type of failure	72
5.3.4	Thermal strain development	73
5.3.5	Strain development during loading	75
5.4	Mode II bond fracture – Three-point bending test	77
5.4.1	Test setup	77
5.4.2	Failure load as function of temperature	79
5.4.3	Type of failure	80
5.4.4	Thermal strain development	81
5.4.5	Strain development during loading	84
5.5	Effect of the angle of loading on the debonding of externally bonded CFRP	85
5.5.1	Test setup	85
5.5.2	Failure load as function of the angle of loading	87
5.5.3	Type of failure	88
5.6	Summary	89

6	Finite element analyses of bond shear tests	90
6.1	Introduction	90
6.2	Finite element method	90
6.3	Modeling approach	91
6.4	Double-lap shear tests	91
6.4.1	Finite element model	91
6.4.2	Applied material properties	93
6.4.3	Load-displacement curves.....	96
6.4.4	Heating and cooling of the specimens	98
6.4.5	Loading of the specimens.....	102
6.4.6	Effects of temperature on the failure load.....	104
6.4.7	Summary	105
6.5	Three-point bending tests.....	106
6.5.1	Finite element model	106
6.5.2	Applied material properties	107
6.5.3	Load-displacement curves.....	107
6.5.4	Heating and cooling of the specimens	109
6.5.5	Loading of the specimens.....	110
6.5.6	Temperature effects on the failure load	112
6.6	Bond behavior in the perpendicular shear direction	112
6.6.1	General	112
6.6.2	Finite element model	113
6.6.3	Material properties	114
6.6.4	Thermal strains and stresses	114
6.7	Summary.....	115

7	Effect of temperature on full scale CFRP strengthened beams.....	116
7.1	Test program.....	116
7.2	Test setup	117
7.3	Material properties.....	120
7.4	Heating of the beams	121
7.5	Loading of the beams	124
7.5.1	Beam A	124
7.5.2	Beam B	128
7.5.3	Beam C	131
7.5.4	Beam D.....	135
7.6	Conclusions.....	138
8	Finite element analyses of the full scale experiments	139
8.1	Introduction	139
8.2	Finite element model.....	139
8.3	Material properties.....	141
8.3.1	Concrete and bond layer	141
8.3.2	Steel reinforcement, adhesive and CFRP	144
8.3.3	Coefficient of thermal expansion	145
8.4	Results of the finite element analyses.....	146
8.4.1	General.....	146
8.4.2	Beam A	147
8.4.3	Beam B	157
8.4.4	Beam C	163
8.4.5	Beam D.....	169
8.5	Summary.....	174

9	Discussion	176
9.1	Introduction	176
9.2	The development of thermal stresses	178
9.2.1	General	178
9.2.2	Zone A: The end anchorage zone	179
9.2.3	Point B: At the plate-end	180
9.2.4	Zone C: Outside the anchorage zone.....	181
9.3	The reduced Young's modulus of the adhesive at elevated temperatures	183
9.3.1	General	183
9.3.2	Zone A: The end anchorage zone	184
9.3.3	Point B: At the plate-end	185
9.3.4	Zone C: Outside the anchorage zone.....	186
9.4	The increased creep of the adhesive at elevated temperatures	186
9.5	The reduced bond strength at elevated temperatures	187
9.5.1	General	187
9.5.2	Zone A: The end anchorage zone	188
9.5.3	Point B: At the plate-end	189
9.5.4	Zone C: Outside the anchorage zone.....	189
9.6	The reduced tensile strength and fracture energy of concrete at elevated temperatures	190
9.6.1	General	190
9.6.2	Point B: At the plate-end	190
9.7	Summary	191
10	Conclusions and recommendations	193
10.1	Conclusions	193
10.1.1	General	193
10.1.2	Small scale bond tests	193
10.1.3	Full scale experiments	194
10.2	Recommendations	195
10.2.1	General recommendations.....	195
10.2.2	Recommendations for future research	196

References	199
Appendix A. Development of thermal stresses.....	210
Appendix B. Double-lap shear tests	214
B.1 Material properties.....	214
B.2 Strain gauge properties	214
B.3 Load-displacement curves	215
B.4 Thermal strains	217
B.4.1 Thermal strains after heating to 50°C, cooling to 20°C and heating to 50°C 217	
B.4.2 Thermal strains after heating to 40°C, 50°C and 70°C	218
Appendix C. Three-point bending tests.....	219
C.1 Load-displacement curves	219
C.2 Thermal strains	221
C.2.1 Thermal strains after heating to 50°C, cooling to 20°C and heating to 50°C 221	
C.2.2 Thermal strains after heating to 40°C, 50°C and 70°C	222
Appendix D. Loading angle tests	223
D.1 Material properties.....	223
Appendix E. Finite element analyses	224
E.1 Double-lap shear tests.....	224
E.1.1 Lower strength concrete specimens	224
E.1.2 Higher strength concrete specimens	225
E.2 Three-point bending tests	226
E.2.1 Lower strength concrete specimens	226
E.2.2 Higher strength concrete specimens	227
Appendix F. Material properties full scale experiments	228
F.1 Concrete material properties	228

Appendix G. Full scale experiments	230
G.1 Thermal strains CFRP	230
G.2 Thermal shear stresses in the concrete-adhesive interface	232
Appendix H. Analytical calculations full scale beams.....	233
H.1 Introduction	233
H.2 Cracking of the concrete	234
H.3 Yielding of the tensile steel reinforcement.....	236
H.4 Failure of the beam.....	237
Appendix I. Analytical calculation debonding mechanisms.....	239
I.1 Debonding due to high shear stresses	239
I.2 Debonding at shear cracks	240
I.3 Debonding at the end anchorage	241
I.4 Concrete cover rip-off/plate-end shear failure.....	243
I.5 Overview	244
Appendix J. Modified model of Yuan et al.....	245
J.1 Young’s modulus of the adhesive - anchorage length relation.....	245
Curriculum Vitae	249

Notations

Indices

The “_x” in the symbols list can be replaced by one of the following material indices.

a	Adhesive
c	Concrete
f	FRP
fib	Fibers
matrix	Matrix material
s	Steel reinforcement

Symbols

Roman upper case symbols

A_x	Area [mm ²]
E_x	Young's modulus [N/mm ²]
F	Load [kN]
G_F^I	Mode I fracture energy of concrete [J/m ²]
G_F^{II}	Mode II fracture energy of concrete [J/m ²]
I	Moment of inertia [mm ⁴]
M_d	Design moment [kNm]
$N_{fa,max}$	Maximum anchorage capacity [kN]
N_{fd}	Design value of axial force in FRP [kN]
N_{rd}	Design value of axial force in FRP and steel reinforcement together [kN]
N_{sd}	Design value of axial force in steel reinforcement [kN]
T	Temperature [°C]
T_g	Glass transition temperature [°C]
V_{sd}	Design value of acting shear force [kN]
V_{Rd}	Design shear resistance for debonding at shear cracks [kN] / concrete cover rip-off [N]
V_x	Volume fraction

Roman lower case symbols

a	Shear span [mm]
b_x	Width [mm]
C_1, C_2, C_F	Calibration factor
d	Effective depth of the member [mm]
$f_{cm,cube}$	Mean cube compressive strength of concrete [N/mm ²]
f_k	Characteristic compressive strength [N/mm ²]
f_{xbm}	Mean bond strength [N/mm ²]
f_{xm}	Mean compressive strength [N/mm ²]
f_{xsm}	Mean shear strength [N/mm ²]
f_{xt}	Tensile strength [N/mm ²]
f_{xtk}	Characteristic tensile strength [N/mm ²]

$f_{x\text{tm}}$	Mean tensile strength [N/mm ²]
$f_{x\text{tm,fl}}$	Mean flexural strength [N/mm ²]
$f_{x\text{tm,sp}}$	Mean tensile splitting strength [N/mm ²]
$f_{y\text{m}}$	Mean yield strength of steel [N/mm ²]
h	Crack band width [mm]
$h_{c,\text{ef}}$	Effective height of concrete [mm]
k_b	Geometry factor
k_c	Factor accounting for the state of compaction of concrete
k_G	Factor accounting for the shear stiffness [N/mm ³]
L	Distance between the support and the end of the FRP [mm]
ℓ	Bonded length [mm]
ℓ_{fa}	Available anchorage length of FRP [mm]
$\ell_{\text{fa,max}}$	Maximum anchorage length of FRP [mm]
q	Distributed load [kN/m]
s	Relative displacement between FRP and concrete (slip) [mm]
t_x	Thickness [mm]
t_n	Normal traction [N/mm ²]
t_t	Shear traction [N/mm ²]
u	Displacement [mm]
x	Distance [mm]
z_x	Lever arm [mm]

Greek lower case symbols

α	Reduction factor accounting for the influence of inclined cracks on the bond strength
α_x	Coefficient of thermal expansion [1/°C]
γ_x	Material safety factor
$\varepsilon_{\Delta T}$	Thermal strain
ε_x	Strain
$\varepsilon_{\text{cu}2}$	Strain in the concrete at compressive failure
ε_{s1}	Tensile steel strain
ε_{s2}	Compressive steel strain
$\varepsilon_{f,\text{lim}}$	FRP strain limit
ν_x	Poisson ratio
ρ_{eq}	Equivalent reinforcement ratio [-]
ρ_x	Reinforcement ratio [-]
ρ_x	Density [kg/m ³]
σ_x	Stress [N/mm ²]
τ_x	Shear stress [N/mm ²]
τ_{cbd}	Design bond strength in shear [N/mm ²]
τ_{Rd}	Design shear strength [N/mm ²]
τ_{Rpd}	Design shear strength for debonding at shear cracks [N/mm ²]
τ_{Rpk}	Characteristic shear strength for debonding at shear cracks [N/mm ²]

1 Introduction

1.1 General

Strengthening of existing structures has become increasingly important in the construction industry nowadays and is being applied more and more often due to several reasons. First of all, ongoing deterioration of structures and a rise in the number of faults in design and execution has increased the need for structural upgrading of existing structures. Furthermore, our demands to buildings are changing faster and faster, resulting in an increased need to adjust existing structures far before the end of their initially intended life span. Moreover, many civil structures are in the need of upgrading due to a traffic load increase. These developments have led to a significant growth in the number of repair and strengthening applications worldwide.

From an environmental and economical point of view, it is generally preferred to strengthen an existing structure instead of demolishing it and subsequently rebuilding it. Strengthening of a structure is in most cases less expensive and less interfering compared to rebuilding. Moreover, it is generally faster than rebuilding, which reduces closure of bridges and buildings to a minimum.

One of the recent developments in the strengthening industry is the use of externally bonded Fiber Reinforced Polymer (FRP) reinforcement for strengthening of existing structures, such as reinforced concrete, steel, timber and masonry structures. Last decade FRP has become increasingly popular as a strengthening material given the increasing number of FRP strengthening applications worldwide.

Design guidelines for the application and use of externally bonded FRP for strengthening of concrete structures, like *fib*-Bulletin 14 (*fib* 2001) in Europe and ACI 440.2R-02 (ACI 2002) in the USA, have been published in the beginning of this century. In these guidelines, available knowledge at the time of publishing was gathered and design rules for a safe application are given. The availability of these design guidelines has contributed to the rapid increase in the number of applications. These guidelines are, however, still conservative and restricted in their field of application, as they mainly deal with the subjects that were sufficiently investigated at the time of publishing. Most guidelines will be updated in the future, as various topics related to the FRP strengthening technique are subject of ongoing research and development.

The main property governing the design of a FRP strengthening application is the debonding of the externally bonded FRP, which is generally initiated well before the tensile strength of the FRP reinforcement is reached. An extensive amount of research into this debonding behavior has led to the development of various analytical models of which some are incorporated in the current design guidelines. Although these guidelines provide reliable models taking into account the debonding of the FRP, there is still no complete agreement amongst international experts on the debonding mechanisms that represent the actual behavior the best.

Despite the amount of research that has been carried out so far, there are still some research needs in the field of externally bonded FRP. One of these research needs, which so far has received only little attention, is the effect of temperature on the FRP strengthening of concrete structures.

1.2 Scope of the research

The acceptance of the FRP strengthening technique in the construction industry is closely related to the level of confidence of structural engineers, building authorities and owners in this technique. A sufficient level of confidence can be reached by good experience with and understanding of the behavior of FRP strengthened structures in various circumstances. A good understanding of the behavior at normal, but also at low and elevated temperatures is therefore essential for the acceptance of the technique.

Harries et al. (2003) conducted a survey into the research needs in the field of FRP materials in concrete applications amongst the members of ACI subcommittee 440-D (FRP research). It turned out that 'durability' and 'fire resistance' were perceived as the most important research needs. One of the durability aspects in this survey, which is also closely related to fire resistance, was the effect of temperature on the behavior of a FRP strengthened structure. Karbhari et al. (2003) carried out a study in which critical gaps in the available data on the durability of both externally bonded and internal FRP reinforcement were identified and prioritized. It was concluded that, amongst others, there is a lack of available data about the behavior of FRP strengthened structures in the case of fire and when subjected to thermal effects, like elevated temperatures and freeze-thaw cycling.

In the current design guidelines, the effect of fire on a FRP strengthened concrete structure is taken into account as an accidental load case, in which the contribution of the FRP is neglected. This means that after loss of the FRP, the structure should be able to resist the loads with safety factors (load and material factors) equal to 1.0. In this way, sudden collapse of the FRP strengthened structure after accidental loss of the bond between FRP and concrete, for example due to fire or vandalism, is prevented. This restriction limits the maximum possible strengthening ratio to the difference in the safety factors between the accidental load case and the ultimate load case.

Deuring (1994), Meier (1995), Blontrock (2003), Bisby et al. (2005), Williams et al. (2006), Gamage et al. (2006), Kodur et al. (2006) and others have investigated the response to fire of concrete structures that are strengthened with externally bonded FRP. The bond between concrete and FRP was found to be lost at temperatures close to or above the glass transition temperature of the adhesive (T_g). It was concluded that fire protection has to be designed such that the adhesive temperature stays below the glass transition temperature of the adhesive (with a certain tolerance) for a sufficient long period, to allow for the evacuation of people from the building.

The effect of changes in the ambient temperature on the behavior of the FRP strengthening of a concrete structure is currently assumed to be negligible within a certain temperature range. This temperature range is given in the design guidelines and/or by the manufacturer of the FRP/adhesive system. *fib*-Bulletin 14 (*fib* 2001) , for example, defines an upper limit for the maximum shade air temperature in service, which is equal to the glass transition temperature of the adhesive according to EN 12614 (CEN 2004a) minus 20°C. Below this temperature, the effect of temperature can be neglected. This assumption has however never been investigated thoroughly.

The behavior of the FRP strengthening could possibly be affected by an ambient temperature change, given the significant difference in the coefficient of thermal expansion between concrete ($\alpha_c \approx 10 \times 10^{-6} / ^\circ\text{C}$) and for example Carbon Fiber Reinforced Polymer reinforcement (CFRP) ($\alpha_f \approx -1 \times 10^{-6} / ^\circ\text{C}$ in the longitudinal direction). This thermal mismatch will induce thermal stresses in the concrete-adhesive-FRP joint, which may affect the structural behavior. Moreover, the material properties of concrete, adhesive and FRP and the bond between these materials are likely to be affected by changes in temperature. Increasing the temperature especially has a negative effect on the adhesive properties, even below the glass transition temperature (Plechnik et al. 1980). For this research project, it was decided to focus on the effect of ambient temperature (changes) on the behavior of the FRP strengthening of (reinforced) concrete structures.

1.3 Research objective

Many FRP strengthening applications are being applied in outdoor situations and are being exposed to various temperature conditions during their life span (Figure 1-1). The ambient temperature in Western Europe for example ranges from about -20°C up to about 40°C in extreme conditions. In specific applications, temperatures could even reach higher temperatures, due to direct or indirect (for example under a layer of asphalt) exposure of the FRP to the sun (Figure 1-2).



Figure 1-1: Application of CFRP laminates in cold weather conditions (Busel and White 2003)



Figure 1-2: CFRP laminates that are, after applying asphalt, indirectly exposed to the sun (Busel and White 2003)

Even in the moderate climate of the Netherlands, asphalt can reach temperatures up to 65°C in the summer. For a safe application of externally bonded FRP reinforcement, the behavior of the FRP strengthening in these extreme temperature conditions should be known. It was decided to adopt an ambient temperature range between -20°C and +80°C in this research project, which will cover the outdoor temperature conditions for a large part of the world.

So far, only a limited amount of research into the effect of ambient temperature has been carried out (Tadeu and Branco 2000; Di Tommaso et al. 2001; Blontrock 2003; Wu et al. 2005; Gamage, Al-Mahaidi, and Wong 2006; Leone, Aiello, and Matthys 2006). These investigations have shown that the failure load and the type of failure are affected by temperature changes, although contradictory results have been reported (Chapter 3). Moreover, these investigations only have been carried out with small scale bond tests, while debonding in full scale structures is much more complex and cannot fully be understood by the bond behavior in these small scale tests. It was therefore decided to investigate the effect of temperature on both small scale specimens and full scale beams that are strengthened in flexure with externally bonded CFRP. Only CFRP reinforcement (based on carbon fibers) is investigated, as this is the most common type of FRP reinforcement in the construction industry at the moment.

The objective of this research project is to investigate the influence of ambient temperature on the strengthening of concrete structures in flexure with externally bonded CFRP.

1.4 Outline

In this first chapter, a brief overview of the scope and objective of the research project is given. In Chapter 2, the basics of the FRP strengthening technique and the different types of debonding that can be distinguished in literature for FRP strengthened concrete structures are discussed. Chapter 3 deals with the state of the art with respect to the effect of ambient temperature on FRP strengthened concrete structures.

In Chapter 4, the effects of temperature on the material properties of concrete, internal steel reinforcement, adhesive and FRP are discussed, while in Chapter 5 the effects of temperature on the bond behavior of the concrete-adhesive-CFRP joint are described, including the results of the bond tests that have been carried out. In order to get a better insight in the bond behavior of the joint at low and elevated temperatures, finite element analyses with the FE-code DIANA were performed. The results of these analyses are presented in Chapter 6.

The behavior of flexural CFRP strengthened concrete beams, which were designed to fail by different types of debonding, was studied at various temperatures by full scale experiments as well as by FE-analyses. The results are presented in, respectively, Chapters 7 and 8. In Chapter 9, the gathered knowledge is summarized and discussed. In Chapter 10, finally, the conclusions and recommendations are given.

2 Strengthening of structures with externally bonded FRP

2.1 Introduction

In this chapter a brief overview of the FRP strengthening technique for concrete structures is given. The properties of the involved materials, like the adhesive and the FRP are discussed, as well as the available strengthening techniques. In Section 2.4, an overview of the different failure modes that can be distinguished in literature for FRP strengthened structures is given. The focus will be on the debonding of externally bonded FRP, as the design of a FRP strengthened structure is generally governed by this type of failure.

2.2 FRP reinforcement

2.2.1 General

Fiber Reinforced Polymer (FRP) materials are widely used in many industries nowadays, like the airline industry, the car industry and the construction industry. Important application fields in the construction industry are the strengthening of existing structures with externally bonded FRP reinforcement and the reinforcement of concrete structures with internal FRP bars (fib 2001). Another upcoming application field is the application of FRP composite bridge decks (Zureick, Shih, and Muley 1995).

FRP reinforcement is a composite that is composed of small fibers (\varnothing 5-20 μm) embedded in a polymer matrix (fib 2001). The most commonly used high performance fibers for FRP reinforcement are carbon, aramid and glass fibers. The main differences between these types of fibers are the resistance against (aggressive) environmental influences and the mechanical properties (Feldman 1989; Kim 1995; fib 2001). Carbon fibers are in most cases preferred in the construction industry, as they have excellent resistance against UV-light, moisture and chemical influences and they have good mechanical properties, like a high strength and high Young's modulus (Table 2-1). Glass fibers are generally cheaper compared to carbon fibers, while aramid fibers have a better impact resistance and a lower density (NetComposites 2006).

Table 2-1: Mechanical properties of fibers (fib 2001)

	Young's modulus [N/mm ²]	Tensile strength [N/mm ²]	Ultimate tensile strain [%]
Aramid	70,000 – 130,000	3500 – 4100	2.5 – 5.0
Carbon	215,000 – 700,000	2100 – 6000	0.2 – 2.3
Glass	70,000 – 90,000	1900 – 4800	3.0 – 5.5

The fibers in FRP reinforcement are generally embedded in a polymer matrix. The main function of the polymer matrix is to spread the load between the individual fibers and to protect the fibers against environmental influences, like moisture, corrosion and wear (NetComposites 2006). Polymers are formed from a non-reversible chemical reaction by mixing a resin with a hardener or catalyst. The polymer matrix is usually a polyester, vinylester or epoxy, which are all thermosetting polymers, also referred to as thermosets (Table 2-2) (Morgan 2005). The major property of thermosetting polymers is that they, once cured, will not become liquid anymore when heated, although the mechanical properties will change from a glass-like material to a more rubber-like material at a certain temperature. This temperature is generally referred to as the glass transition temperature (T_g). Around this temperature, the mechanical properties, like the Young's modulus and strength, will drop significantly. Cooling down from a temperature above T_g to a temperature below T_g will reverse the change in mechanical properties back to the original properties. The glass transition temperature can vary significantly amongst the various available polymer matrix materials (Table 2-2).

Table 2-2: Mechanical properties of polymer matrix materials (Morgan 2005)

	Young's modulus [N/mm ²]	Tensile strength [N/mm ²]	Ultimate tensile strain [%]	Glass transition temperature [°C]
Polyester	3200 – 3500	60 – 85	2 – 5	100 – 140
Vinylester	3300	70 – 80	5 – 6	210 – 340
Epoxy	2000 – 4000	80 – 150	1 – 8	50 – 260

FRP reinforcement, both as internal reinforcement bar and as externally bonded laminate, is fabricated in a pultrusion process, by pulling fibers from a creel through a polymer matrix (NetComposites 2006) (Figure 2-1). The polymer matrix and fibers are then pulled through a heated die, where the fibers are impregnated and the material is cured and shaped. At the end of the process the reinforcement is cut to length.

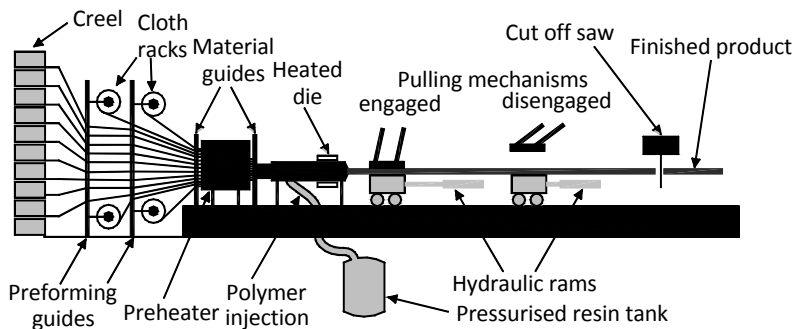


Figure 2-1: Pultrusion process for FRP laminates (NetComposites 2006)

The stress-strain relation of FRP reinforcement is linear elastic up to failure, which implies that it fails brittle. Figure 2-2 shows the variation in the stress-strain relations for different types of FRP reinforcement that are produced with carbon, aramid and glass fibers, as well as for steel.

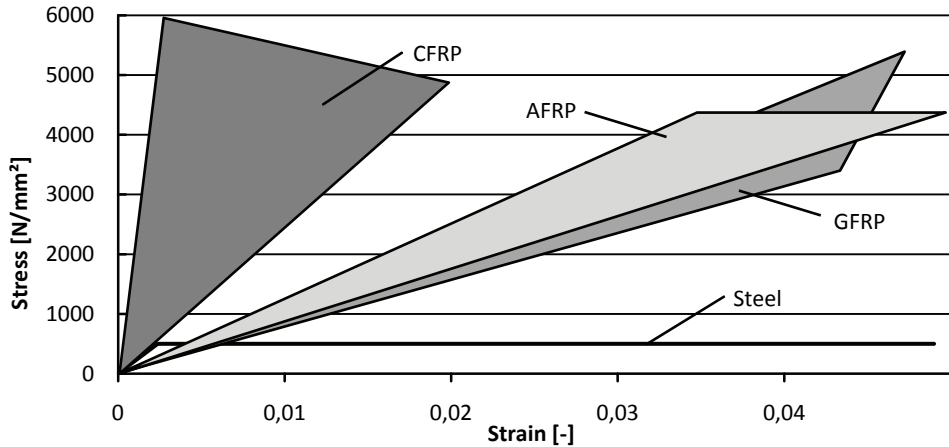


Figure 2-2: Uni-axial stress-strain relations in tension for uni-directional FRPs and steel (fib 2001)

2.2.2 Internal FRP reinforcement

Internal FRP reinforcement is produced as a bar (Figure 2-3), also referred to as a rod, which can be used as replacement for traditional steel reinforcement (Figure 2-4). Due to the relative high costs of FRP reinforcement, applications are still limited to specific situations, e.g. to avoid corrosion in highly aggressive environments, like in marine environments and in the chemical industry, and in situations where electromagnetic neutrality is required, like for magnetic railway systems and scanning facilities in hospitals (Pilakoutas 2000).

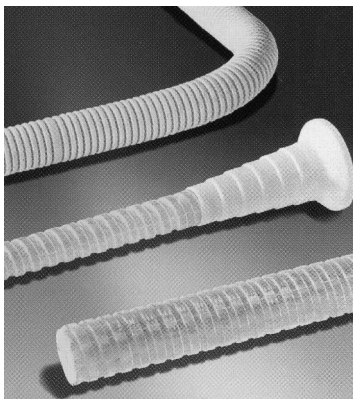


Figure 2-3: GFRP reinforcement bars (Schöck 2004)



Figure 2-4: Application of GFRP reinforcement bars in a bridge deck in Canada (Hughes Brothers 2007)

2.2.3 Externally bonded FRP reinforcement

The focus in this thesis is on externally bonded FRP reinforcement for strengthening of (concrete) structures. Extensive information about externally bonded FRP reinforcement can be found in *fib-Bulletin 14* (fib 2001). Strengthening of concrete structures was traditionally being carried out with externally bonded steel strips. Applying steel strips has however several disadvantages, like the need for protection against corrosion, the heavy weight, resulting in the need for scaffolding during the curing process, and the limitation in the plate length. Applying FRP reinforcement instead of steel strips eliminates these disadvantages, due to its non-corrosiveness, low weight, high strength and the possibility to produce the FRP reinforcement in basically any length. FRP reinforcement is, however, more expensive than steel. For every strengthening application, it should be evaluated which material is the best for that specific situation. The two most important types of externally bonded FRP reinforcement are the prefabricated FRP laminates and the FRP fabrics, which are used for the so called wet lay-up system (Matthys 2000).

2.2.3.1 Externally bonded FRP laminates

The majority of FRP strengthening applications is carried out by bonding prefabricated FRP laminates to a concrete structure. Most prefabricated laminates are produced with carbon fibers that are oriented in one direction and are therefore referred to as uni-directional CFRP laminates (fib 2001). The mechanical properties of these laminates in the fiber direction are different from those in the direction perpendicular to the fiber direction. Table 2-3 shows the typical properties of uni-directional CFRP laminates in the fiber direction. It is also possible to produce multi-directional FRP laminates, with fibers in more than one direction, by using fabrics in the pultrusion process.

Table 2-3: Typical mechanical properties of CFRP laminates in the fiber direction (fib 2001)

	Young's modulus [N/mm ²]	Tensile strength [N/mm ²]	Ultimate tensile strain [%]	Glass transition temperature [°C]
Low Young's modulus	170,000	2800	1.6	100 – 140
High Young's modulus	300,000	1300	0.5	210 – 340

FRP laminates can be used for strengthening of a concrete structure in flexure but also in shear. Before applying a FRP laminate, one has to make sure that large unevenness of the concrete surface is removed. The concrete surface also has to be roughened, for example by sandblasting, and cleaned, to provide a good bond surface. After applying the adhesive (Section 2.3) (Figure 2-5), the laminate can be applied to the concrete surface by hand (Figure 2-6). Air in between the concrete and FRP laminate has to be removed, e.g. by applying pressure to the FRP laminate by hand or a roller. Most polymer adhesives, like epoxy, are cold curing. It is however possible to accelerate the curing process by applying heat.

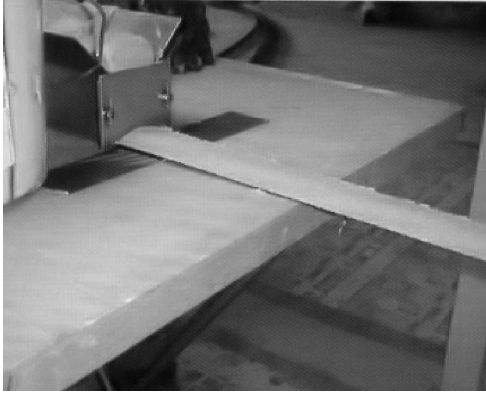


Figure 2-5: Applying the adhesive with a special device (Sika 2004)



Figure 2-6: Externally bonded CFRP laminates under a bridge (Sika 2004)

2.2.3.2 Externally bonded FRP fabrics

The second type of FRP strengthening system is the so called wet or hand lay-up system (fib 2001) (Figure 2-7). For this system, the FRP reinforcement is produced as woven, knitted, stitched or bonded fabrics (fib 2001; NetComposites 2006) (Figure 2-8). A fabric is generally composed of several layers of fibers. Fabrics can be uni-axial, woven (0° and 90° fiber direction) or multi-axial (multiple fiber directions). In uni-axial fabrics the majority of the fibers are oriented in one direction, while a small amount of fibers is applied in the perpendicular direction to keep the fibers in place. It is also possible to use different types of fibers in one fabric, like carbon/aramid fabrics, which combines the high impact resistance and tensile strength of aramid fibers with the high compressive and tensile strength of carbon, or carbon/glass fabrics, where the glass fibers reduce the costs of the fabric (NetComposites 2006).



Figure 2-7: Applying the wet lay-up fabrics (Mapei 2001)

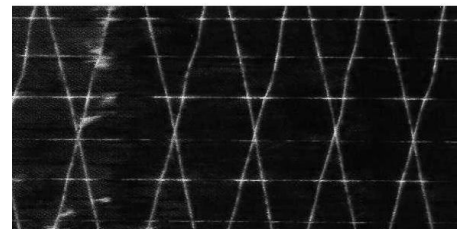
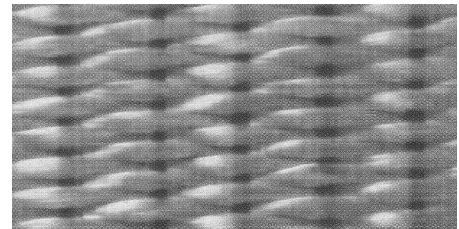


Figure 2-8: Different types of wet lay-up fabrics (Sika 2006)

The flexible fabrics are bonded to the concrete surface with a polymer adhesive that takes care of both the impregnation and the bonding. A roller or a brush can be used to apply the adhesive. Generally more than one layer of fabric has to be applied to obtain the required capacity. An advantage of the wet lay-up system is that it can be applied in different shapes and that the surface does not need to be straight, but can, for example, also be curved. Strengthening over sharp corners should however be avoided in order to prevent damage to the fibers. A disadvantage of the wet lay-up system is the fact that the quality of the end product highly depends on the skills of the laborer (fib 2001). The fiber volume fraction (volume of fibers divided by the total volume of fibers and matrix material) is also significant lower ($\pm 30\%$) compared to prefabricated laminates ($\pm 70\%$), which results in a larger cross-sectional area in order to obtain the same strength, and therefore in higher costs.

2.2.3.3 Special systems

The FRP strengthening technique by bonding prefabricated laminates or fabrics to a concrete structure has become more and more accepted nowadays and new developments are continuously going on. One of the more recent developments is the mechanical anchorage and prestressing of FRP laminates, which makes it possible to take more advantage of the FRP strength (Garden and Hollaway 1998; Štěpánek, Švaricková, and Adámek 2004).

The most important advantage of anchorage is the fact that most types of debonding (Section 2.4.3) can be prevented. A mechanical anchorage can be obtained by applying specially designed anchors that are fixed to the structure (Figure 2-10) or by steel bolts that are drilled through a FRP laminate into the concrete (Figure 2-9a), where in the latter case a multi-directional FRP laminate has to be used to avoid splitting of the FRP laminate. It is also possible to use externally bonded U- or L-shaped profiles (Figure 2-9b and c) or fabrics (Figure 2-9d) to anchor the ends of a laminate (Ritchie et al. 1991).

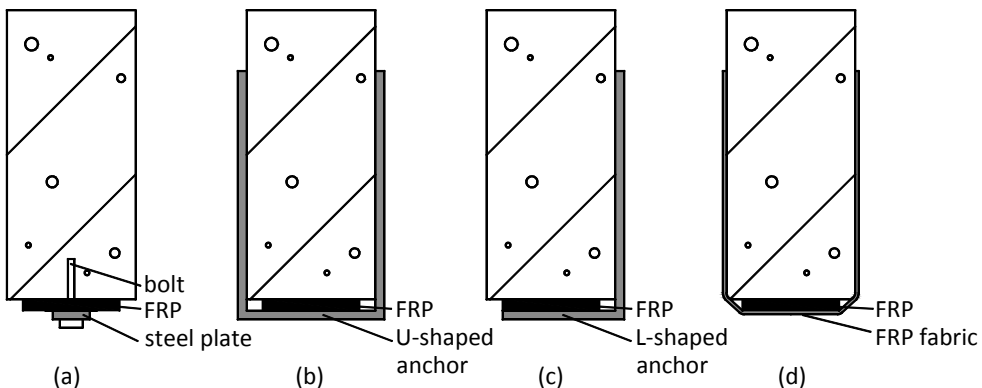


Figure 2-9: Mechanical anchorage with (a) bolt, (b) U-shaped profile, (c) L-shaped profile and (d) FRP fabric

Prestressed FRP systems (Figure 2-10) have several advantages over non-prestressed systems (El-Hacha, Wight, and Green 2001), like the reduction of the crack width and the delay in onset of cracking. Moreover, the tensile strains in the steel reinforcement and the deflection of the beam are reduced, while the load capacity can be increased. A disadvantage of anchored and pre-stressed FRP systems is the fact that these systems are more expensive compared to externally bonded FRP systems, due to the need of anchorage and extra labor.



Figure 2-10: Fixed (a) and movable (b) end anchor with hydraulic jack to apply the prestress to the FRP (SIKA Stress-Head system)

Another recent development is the application of Near Surface Mounted (NSM) FRP reinforcement that can be used as an alternative to externally bonded FRP laminates (Figure 2-11) (De Lorenzis and Nanni 2002; El-Hacha and Rizkalla 2004). In the NSM strengthening technique, FRP laminates (Figure 2-12a) or rods (Figure 2-12b) are embedded in a slit in the concrete that is filled with an adhesive.



Figure 2-11: Application of NSM FRP laminates into the slit (Hughes Brothers 2002)

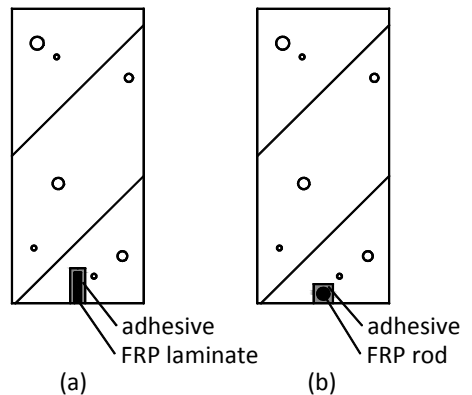


Figure 2-12: NSM FRP application with a (a) FRP laminate and (b) FRP rod

Like for externally bonded FRP reinforcement, this technique was originally being developed for steel reinforcement bars, but has been replaced by FRP reinforcement, due to its non-corrosiveness, low weight and high strength. The high strength of FRP makes it possible to use a smaller cross-sectional area compared to steel for the same capacity, which reduces the size of the slit. NSM applications have the advantage that the FRP is better protected against environmental influences and vandalism. Moreover, it has a larger bond area compared to the externally bonded FRP and thus the potential for a higher capacity. Because of the need to make a slit, this technique requires more preparation work and is therefore more expensive compared to externally bonded FRP application. Moreover, the existing structure should have sufficient cover, to be able to make the slit in the concrete.

The last special strengthening technique worth mentioning is the confinement of columns by wrapping FRP fabrics around a column (fib 2001) (Figure 2-13). This technique was first developed in the early 90's in Japan and increases the axial load and impact capacity of columns. The process of wrapping can be automated by means of a robot (Figure 2-14).

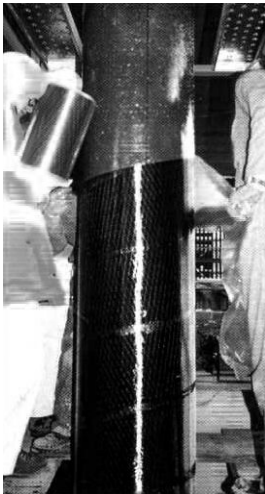


Figure 2-13: Wrapping of a column (Fortius 2004)



Figure 2-14: Automated FRP wrapping (fib 2001)

2.3 Adhesive

The aim of the adhesive is to transfer the stresses from the FRP reinforcement to the concrete and vice versa. Just as for matrix materials, most commonly used adhesives are polymers, like epoxy, vinylester and polyester (fib 2001). Polymer adhesives are composed of a resin and a hardener, which are mixed together just before the application, and are therefore referred to as two-component adhesives. Especially epoxy adhesives have good mechanical properties and a high resistance against environmental degradation (Morgan 2005) and are therefore preferred in the construction industry, despite the relatively high costs. One of the other major advantages of epoxy is the low shrinkage during cure.

Table 2-4 shows the material properties of commercially available epoxy adhesives that are used for externally bonded FRP reinforcement. Most adhesives are, just like the matrix materials, thermosetting materials. It can however be seen that the glass transition temperature of commercially available epoxy adhesives is relatively low compared to the glass transition temperature of matrix materials (Table 2-2).

Table 2-4: Typical material properties of epoxy adhesives (fib 2001)

	Properties
Density	1100 – 1700 kg/m ³
Young's modulus	500 – 20,000 N/mm ²
Shear modulus	200 – 8000 N/mm ²
Poisson ratio	0.3 – 0.4
Tensile strength	9 – 30 N/mm ²
Shear strength	10 – 30 N/mm ²
Compressive strength	55 – 110 N/mm ²
Strain at failure	0.5 – 5 %
Fracture energy	200 – 1000 J/m ²
Coefficient of thermal expansion	25 – 100 × 10 ⁻⁶ /°C
Water absorption	0.1 – 3 %
Glass transition temperature	45 – 80 °C

2.4 Failure of flexural FRP strengthened concrete structures

To be able to investigate the effect of temperature on the FRP strengthening of concrete structures, one first must have a good understanding of the possible failure modes of a FRP strengthened structure at room temperature. The failure modes described in this section are for externally bonded FRP reinforcement in general. It has however to be kept in mind that externally bonded FRP reinforcement is mainly produced as CFRP laminates. The main focus of this research project is therefore on the strengthening of reinforced concrete structures with externally bonded CFRP reinforcement.

Three major categories of failure modes can be distinguished that are governing the design of a FRP strengthened structure; flexural failure, shear failure and debonding of the externally bonded FRP reinforcement. Flexural and shear failure of a beam are common failure modes similar to those for Reinforced Concrete (RC) structures. The design of a FRP strengthened structure is, however, in most cases governed by debonding of the FRP reinforcement (Triantafillou and Plevris 1992; Matthys 2000; Teng et al. 2002). Nevertheless, flexural and shear failure of a FRP strengthened beam are also briefly discussed to provide a complete overview of all possible failure modes.

2.4.1 Flexural failure of a beam

Three types of flexural failure of a FRP strengthened structure can be distinguished in literature (Matthys 2000; fib 2001), yielding of the internal steel reinforcement followed by FRP rupture (Figure 2-15a), yielding of the internal steel reinforcement followed by concrete crushing, or concrete crushing without yielding of the steel reinforcement (Figure 2-15b). FRP rupture is generally governing the design when anchorage or relatively low steel and FRP reinforcement ratios are applied. Concrete crushing without steel yielding could be governing for relatively high reinforcement ratios. This last type of flexural failure is undesirable, due to the brittle behavior.

In the design of a FRP strengthened beam, it should be verified that flexural failure will not occur. This can be done by performing a cross-sectional analysis, taken the FRP reinforcement as additional reinforcement into account. Initial strains in the structure as a result of loads that are present at the time of strengthening should be taken into account.

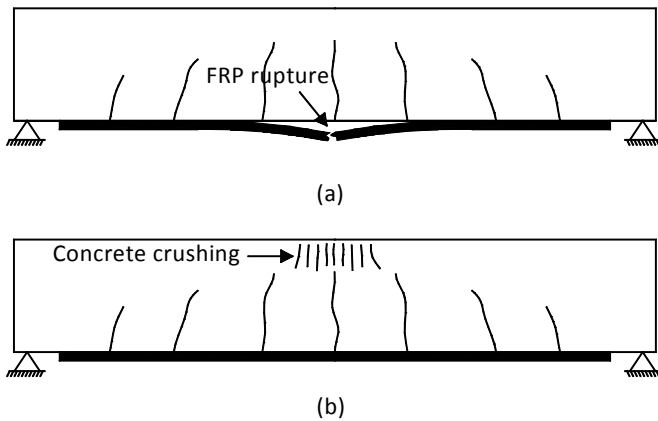


Figure 2-15: Flexural failure due to (a) FRP rupture and (b) concrete crushing

2.4.2 Shear failure of a beam

The shear capacity of a structure that is strengthened by FRP in flexure is not significantly increased by the FRP reinforcement, opposite to the flexural capacity. In the design of a FRP strengthened beam it should be verified that shear capacity is sufficient, as shear failure could be governing over flexural failure. If the shear capacity turns out to be insufficient, it is possible to strengthen the beam in shear with externally bonded FRP.

2.4.3 Debonding of the externally bonded FRP

As mentioned before, the design of the FRP strengthening of a concrete structure is in most cases governed by the debonding of the externally bonded FRP. Debonding can, in theory, be caused by interfacial failure in the concrete-adhesive interface or in the adhesive-FRP interface, or by cohesive failure in one of the materials of the joint (concrete, adhesive or FRP) (Figure 2-16). When applied correctly, debonding is governed by the failure of the concrete (at room temperature), as concrete is the weakest component in the joint.

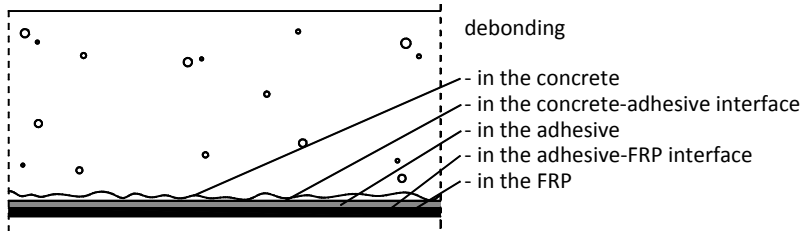


Figure 2-16: Different interfaces for bond failure (fib 2001)

Debonding can initiate at several places along the length of a beam (Figure 2-17 (1, 2, 3, 4 and 7)) (fib 2001). The FRP reinforcement is generally ended at some distance from the support, which results in stress concentrations in the concrete at the end of the FRP reinforcement. These stress concentrations could result in a vertical crack that propagates further as a shear crack or along the level of the internal steel reinforcement, ripping of the concrete cover (Figure 2-17 (5 and 6)). These types of failure are not related to debonding failure of the concrete-adhesive-FRP joint, as the bond between the materials stays intact. They can however also lead to premature failure of the beam. The failure modes that can be distinguished in literature (Matthys 2000; fib 2001) are;

1. Debonding at flexural cracks
2. Debonding due to high shear stresses
3. Debonding at shear cracks
4. Debonding at the end anchorage
5. Plate-end shear failure
6. Concrete cover rip-off
7. Debonding due to the unevenness of the concrete surface

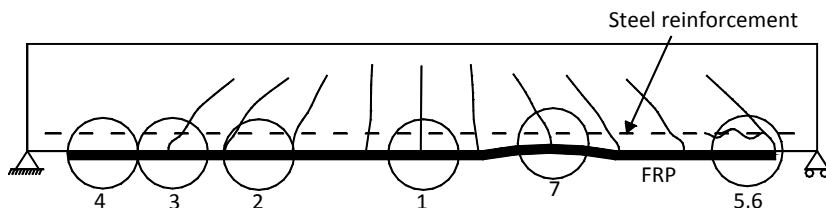


Figure 2-17: Failure modes of a RC beam with externally bonded FRP (partial from (fib 2001))

2.4.3.1 Debonding at flexural cracks

This debonding mechanism is described by Matthyss (2000) as flexural crack bridging. When concrete cracks, tensile stresses in the concrete have to be taken over by the FRP and steel reinforcement and will result in a peak in the tensile stress in the steel and FRP reinforcement at the intersection with the crack (Figure 2-18). The peak in the tensile stress in the FRP will be transferred to the concrete at both sides of the crack tip (end of the crack at the FRP reinforcement) by interfacial shear stresses. Most researchers believe that these stresses will only lead to local debonding close to the crack tips (microcracking), as the peak in tensile stress in the FRP reinforcement, and consequently the shear stresses in the concrete, will drop after debonding over a small distance (Figure 2-18). It is therefore unlikely that this type of debonding will lead to progressive debonding, and thus failure of the beam.

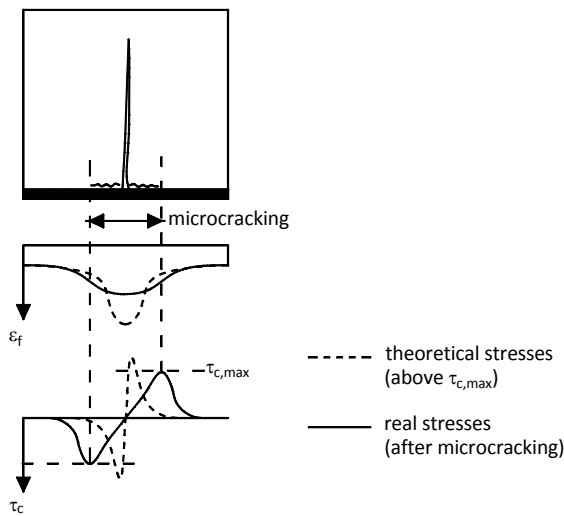


Figure 2-18. Local debonding near flexural cracks (Matthyss 2000)

2.4.3.2 Debonding due to high shear stresses

A change in bending moment along the length of the beam will result in a change in the FRP force along the length of the laminate (Figure 2-19). The difference in FRP force over a small length Δx has to be transferred to the concrete by means of shear stresses. These shear stresses could lead to the initiation of debonding, when the bond capacity over the length Δx is insufficient (Matthyss 2000; Niedermeier and Zilch 2001; Teng et al. 2003). One has to keep in mind that these shear stresses are accompanied by local stress peaks at the tips of the cracks in the concrete, as described in the previous section.

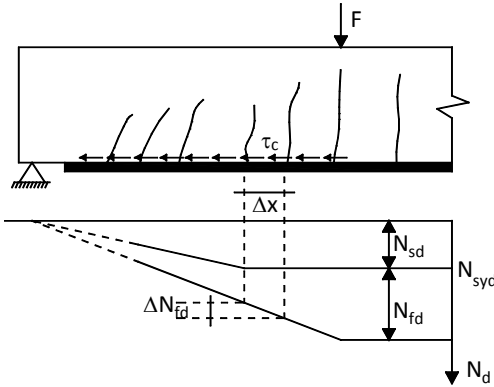


Figure 2-19: Shear stresses in the concrete due to the FRP force distribution

fib-Bulletin 14 (2001) offers three approaches to deal with debonding due to high shear stresses. One simple way to ensure that bond failure due to high shear stresses is prevented, is limiting the FRP strain to a certain value ($\epsilon_{f,lim}$) in the Ultimate Limit State (ULS). Although this is a very crude simplification of the actual behavior, the method is used in quite a number of design guidelines because of its simplicity (Concrete Society 2004). The limitation of ϵ_f is generally ranging from 6.5‰ to 8.5‰ (fib 2001). The actual bond failure will depend on a series of parameters, like the moment-shear relation, the strain in the tensile steel reinforcement and the crack spacing. This strain limitation procedure could lead to a non-economical use of FRP reinforcement, especially in structures with a large span (fib 2001).

Another way to deal with debonding due to high shear stresses is limiting the shear stress (τ_c) in the concrete at the interface with the FRP. The model proposed by Matthyss (2000) is considering two cross-sections at a distance Δx , subjected to a moment M_d and $M_d + \Delta M_d$ (Figure 2-20).

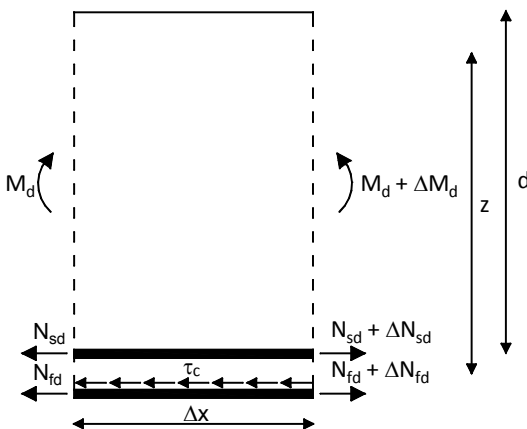


Figure 2-20: Shear stresses in the concrete at the interface with the FRP (Matthyss 2000)

The shear stress that has to be transferred over Δx is;

$$\tau_c = \frac{\Delta N_{fd}}{b_f \cdot \Delta x} \leq \tau_{cbd} \quad (2.1)$$

where

ΔN_{fd} is the difference in FRP axial force over the length Δx

τ_{cbd} is the bond strength in shear

$$\approx 1.8 \cdot \frac{f_{ctk}}{\gamma_c}$$

f_{ctk} is the characteristic concrete tensile strength, preferably determined by pull-off tensile tests

γ_c is the material safety factor for the concrete

Equation (2.1) can be simplified by using $N_{rd} = N_{fd} + N_{sd}$. Depending on whether the steel reinforcement is yielding or not, the total capacity of steel and FRP reinforcement (N_{rd}) can be approximated with;

$$\varepsilon_s < \varepsilon_{yd} : N_{rd} = N_{fd} \cdot \left(1 + \frac{A_s \cdot E_s \cdot \varepsilon_s}{A_f \cdot E_f \cdot \varepsilon_f} \right) \approx N_{fd} \cdot \left(1 + \frac{A_s \cdot E_s}{A_f \cdot E_f} \right) \quad (\text{assuming } \varepsilon_s / \varepsilon_f \approx 1) \quad (2.2)$$

$$\varepsilon_s \geq \varepsilon_{yd} : N_{rd} = N_{fd} + A_s \cdot f_{yd} \quad (2.3)$$

Based on $\Delta N_{rd} = \Delta M_d / z$, the increase in FRP force (ΔN_{fd}) can be expressed with;

$$\varepsilon_s < \varepsilon_{yd} : \Delta N_{fd} \approx \frac{\Delta M_d}{z \cdot \left(1 + \frac{A_s \cdot E_s}{A_f \cdot E_f} \right)} \quad (2.4)$$

$$\varepsilon_s \geq \varepsilon_{yd} : \Delta N_{fd} = \frac{\Delta M_d}{z} \quad (2.5)$$

With $\Delta M_d / \Delta x \approx V_d$ and $z = (z_s + z_f) / 2 \approx 0.95d$, the following design equations can be given;

$$\varepsilon_s < \varepsilon_{yd} : \frac{V_d}{b_f \cdot (0.95 \cdot d) \cdot \left(1 + \frac{A_s \cdot E_s}{A_f \cdot E_f} \right)} \leq \frac{\Delta N_{fd}}{\Delta x \cdot b_f} = \tau_{cbd} \quad (2.6)$$

$$\varepsilon_s \geq \varepsilon_{yd} : \frac{V_d}{b_f \cdot (0.95 \cdot d)} \leq \frac{\Delta N_{fd}}{\Delta x \cdot b_f} = \tau_{cbd} \quad (2.7)$$

A third way to deal with debonding due to high shear stresses, but also with debonding at the end anchorage (Section 2.4.3.4), is proposed by Niedermeier (2001). In his approach, the maximum possible increase in tensile stress of the FRP reinforcement that can be transferred by shear stresses to the concrete in between two cracks is determined. Crack spacing has an important influence on the stresses that can be transferred, so first of all, a prediction of the most unfavorable crack spacing has to be made. Then the change in tensile force in the FRP reinforcement between two subsequent cracks has to be determined. This should be smaller than the maximum possible increase in tensile stress in the FRP reinforcement. The advantage of this model is that it deals with two debonding mechanisms at once. The main disadvantage of this model is however its complexity.

2.4.3.3 Debonding at shear cracks

Debonding can also initiate at the crack tip of a shear crack (Triantafillou and Plevris 1992; Matthys 2000). Because of the slanting shape of shear cracks, both a difference in horizontal (w) and in vertical (v) displacement will occur between the two sides of the crack (Figure 2-21). The difference in vertical displacement will induce tensile stresses perpendicular to the concrete surface at one side of the crack, which could, in combination with the shear stresses in the concrete as described in the previous sections, lead to the initiation of debonding of the FRP reinforcement. This generally occurs in the areas with a combination of a high shear force and a high bending moment, as the shear cracks in this region are less inclined. This implies that the shear crack is crossed by no or only a small number of stirrups, which results in a larger vertical displacement (v).

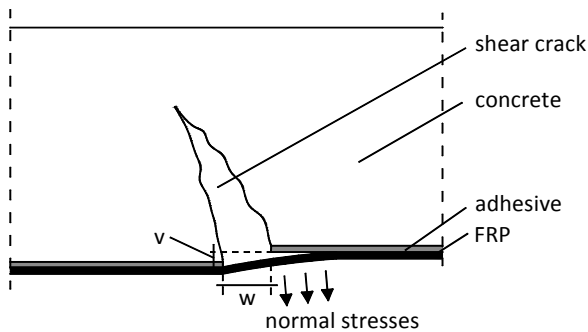


Figure 2-21: Debonding at shear cracks (fib 2001)

There are several models available in literature, but most of them are not directly related to the stress concentrations at the crack tip or the geometry of the shear crack. Most models relate debonding at shear cracks to the shear capacity of a cracked beam cross-section.

Deuring (1993) proposed a shear capacity based model in which the horizontal and vertical crack displacements were taken into account. It turned out that this model was too complex for use in guidelines.

A simpler model is proposed by Blaschko (1997) and has about the same approach as Eurocode 2 part 1-1 (CEN 1997a) for computing the shear resistance. An even simpler model is proposed by Matthys (2000), which is based on experimental data fitting of test results of FRP strengthened RC beams (C25/30 and C30/37). This model resulted in the following simple design guide rule;

$$V_{Sd} \leq V_{Rpd} \quad (2.8)$$

where

V_{Sd} is the acting shear force

V_{Rpd} is the design shear capacity for debonding at shear cracks

$$= \tau_{Rpd} \cdot d \cdot b_c$$

τ_{Rpd} is the design shear strength

$$\tau_{Rpd} = \tau_{Rpk} / \gamma_c$$

τ_{Rpk} is the characteristic shear strength

$$= 0.38 + 151 \cdot \rho_{eq}$$

$$\rho_{eq} = \frac{A_s + A_f \cdot \frac{E_f}{E_s}}{b_c \cdot d}$$

2.4.3.4 Debonding at the end anchorage

FRP reinforcement is generally ended at some distance from the support. At the end of the FRP reinforcement, the FRP force has to be reduced to zero, which can only be done by transferring the force from the FRP to the concrete (and subsequently to the tensile reinforcement) by means of shear stresses (Figure 2-22) (Holzenkämpfer 1997; Neubauer and Rostásy 1999; Matthys 2000; Maalej and Bian 2001; Niedermeier and Zilch 2001). In this case, the shear stresses are not only a result of the difference in bending moment, as was seen in the second debonding mechanism, but also a result of the sudden ending of the FRP reinforcement. It should be ensured that sufficient anchorage length (ℓ_{fa}) is available to be able to transfer the tensile force in the FRP to the concrete.

The difficulty is to indicate where the anchorage length can start. The common approach (Matthys 2000; CUR 2007) is to start with a check at the location where the internal steel reinforcement starts yielding, taking the shifted moment line into account (Figure 2-22). From this cross-section, towards the end of the FRP reinforcement, the internal steel reinforcement is capable of carrying the load by itself, which allows the FRP to transfer its tensile force to the concrete. If the FRP tensile force in this cross-section is smaller than the maximum anchorage force ($N_{fa,max}$), and the distance till the plate-end (anchorage length) is longer than the required anchorage length, the design can be assumed to be safe. If the FRP force in this cross-section is larger, then the anchorage length should be verified at the cross-section where the FRP tensile force is equal to the maximum anchorage force.

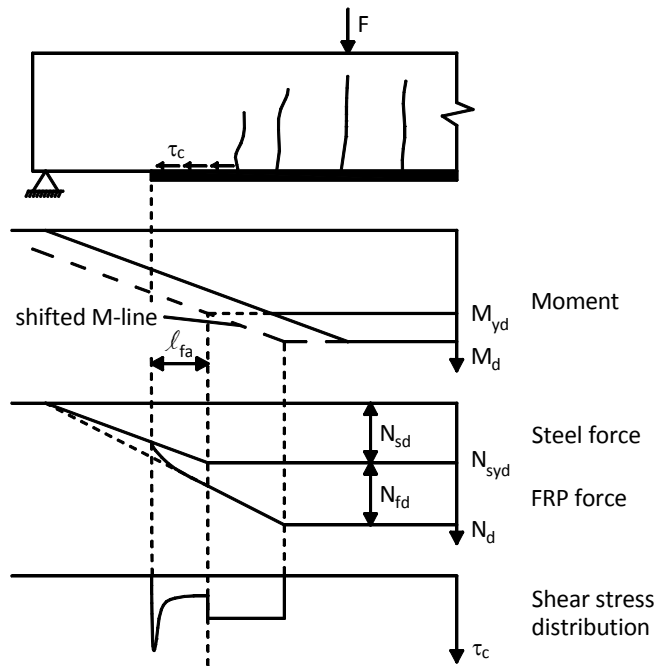


Figure 2-22: Moment, force and shear stress distributions in a FRP strengthened beam

Note that, besides shear stresses, also normal stresses perpendicular to the bonded area will develop, due to the distance between the FRP and the concrete surface. The effect of these stresses is generally indirectly incorporated in the models, e.g. in the calibration factors.

Several models have been developed to describe the debonding behavior in the end anchorage zone (Holzenkämpfer 1997; Neubauer and Rostásy 1999; Nakaba et al. 2001; Savoia, Ferracuti, and Mazzotti 2003; Neto et al. 2004; Lu et al. 2005). Some of these models are based on the calculation of a mean (bond) shear stress in between the concrete and the FRP, others on a linear elastic bond–slip (τ -s) relation. It turned out that both models underestimate the actual capacity of the anchorage zone, as the bond-slip behavior in reality is non-linear (Matthys 2000).

Fracture mechanics based models turn out to describe the actual bond behavior in the end anchorage zone better, as they also take the cracking of concrete, adjacent to the adhesive layer, into account. The most widely used fracture mechanics based model is the model of Holzenkämpfer (1997), modified by Neubauer and Rostásy (1999), because of its relative simplicity. This model is based on a bilinear bond-slip (τ -s) relation (Figure 2-23) and relates the maximum FRP anchorage force ($N_{fa,max}$) to the mode II fracture energy of concrete (G_F^{II}), which corresponds to the area enclosed by the τ -s diagram.

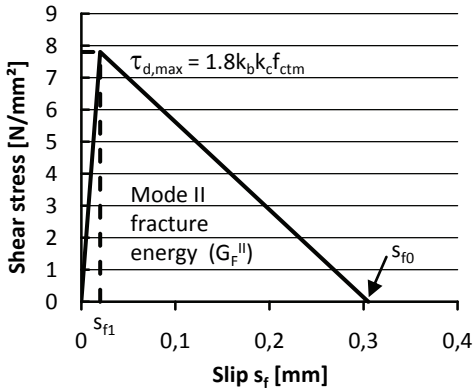


Figure 2-23: Bond-slip relation according to Holzenkämpfer (1997)

The maximum anchorage force ($N_{fa,max}$) and corresponding maximum anchorage length ($l_{fa,max}$) are;

$$N_{fa,max} = \alpha \cdot c_1 \cdot k_c \cdot k_b \cdot b_f \cdot \sqrt{E_f \cdot t_f \cdot f_{ctm}} \quad (2.9)$$

$$l_{fa,max} = \sqrt{\frac{E_f \cdot t_f}{c_2 \cdot f_{ctm}}} \quad (2.10)$$

where

α is the reduction factor accounting for the influence of inclined cracks on the bond strength

≈ 0.9

$c_1 = 0.64 \text{ mm}^{-1/2}$ (for CFRP)

$c_2 = 2 \text{ mm}^{-1}$ (for CFRP)

k_c is the factor accounting for the state of compaction of concrete

≈ 1.0

k_b is the geometry factor

$$= 1.06 \sqrt{\frac{2 \frac{b_f}{b_c}}{1 + \frac{b_f}{400 \text{ mm}}}} \geq 1$$

b_f is the width of the FRP [in mm]

t_f is the thickness of the FRP [in mm]

E_f is the Young's modulus of the FRP [in N/mm²]

f_{ctm} is the mean tensile strength of concrete [in N/mm²]

For anchorage lengths (ℓ_{fa}) smaller than the maximum anchorage length ($\ell_{fa,max}$), a smaller FRP anchorage force will be found (Figure 2-24), which can be calculated with equation (2.11). Increasing the anchorage length above $\ell_{fa,max}$ will however not result in a higher anchorage force, due to the limitation of the maximum anchorage force ($N_{fa,max}$) as a result of the mode II fracture energy of concrete (G_F^{II}).

$$N_{fa} = N_{fa,max} \cdot \frac{\ell_{fa}}{\ell_{fa,max}} \cdot \left(2 - \frac{\ell_{fa}}{\ell_{fa,max}} \right) \quad (2.11)$$

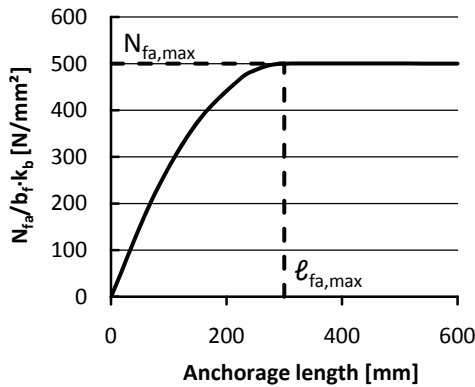


Figure 2-24: Anchorage force related to the anchorage length (Holzenkämpfer 1997)

2.4.3.5 Plate-end shear failure and concrete cover rip-off

Stress concentrations in the concrete at the end of the laminate could lead to the initiation of a vertical crack from the end of the laminate to the internal steel reinforcement. This crack could propagate further along the level of the internal steel reinforcement towards midspan, ripping-off the concrete cover (Figure 2-25a), or as a shear crack (Figure 2-25b).

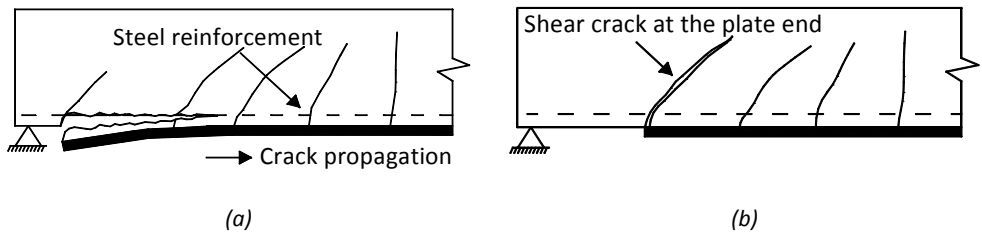


Figure 2-25: Concrete cover rip-off (a) and plate-end shear failure (b)

Whether concrete cover rip-off or plate-end shear failure occurs mainly depends on the amount of shear reinforcement. Large amounts of shear reinforcement generally lead to concrete cover rip-off, while low amounts lead to plate-end shear failure. These types of failure have been investigated by many researchers (Jones, Swamy, and Charif 1988; Roberts 1989; Oehlers 1992; Jansze 1997; Raof and Zhang 1997; Täljsten 1997; Malek, Saadatmanesh, and Ehsani 1998; Smith and Teng 2001; Teng and Yao 2007).

Three different approaches are proposed in literature to evaluate plate-end shear failure. These are the concrete tooth models, the interfacial stress based models and the shear capacity based models (Smith and Teng 2002). Concrete tooth models (Raof and Zhang 1997) assume that there is a “concrete tooth” between two subsequent cracks (Figure 2-26). This tooth tends to bend under the influence of shear stresses at the concrete-FRP interface at the end of the tooth. Concrete cover rip-off or plate-end shear failure is assumed to initiate when the tensile strength in point A is exceeded.

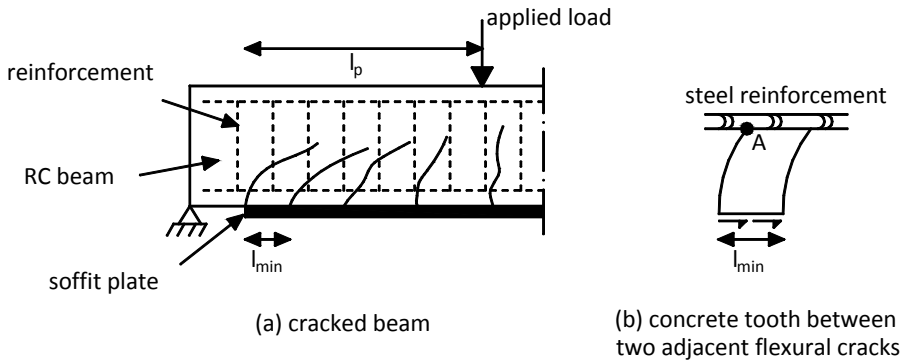


Figure 2-26: Concrete tooth model (Zhang, Raof, and Wood 1995)

Another way to deal with concrete cover rip-off and plate-end shear failure is to determine the normal stress concentrations perpendicular to the bonded area and the shear stress concentrations parallel to the bonded area at the plate-end (Figure 2-27) (Roberts 1989; Täljsten 1997; Malek, Saadatmanesh, and Ehsani 1998). Exceeding the normal and/or shear strength (combination) could lead to the initiation of concrete cover-rip-off or plate-end shear failure, but also to debonding. These models can therefore also be used for debonding in the end anchorage. These models are, however, generally too complex for the use in design guidelines (fib 2001).

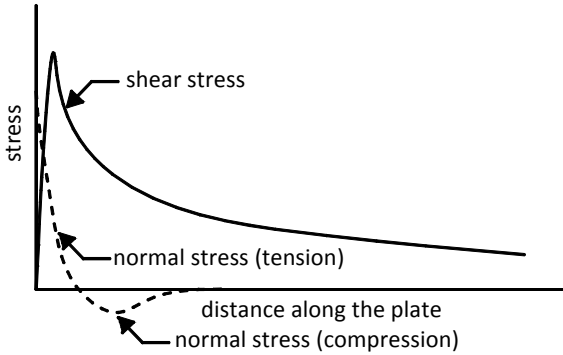


Figure 2-27: Shear and normal stresses in the concrete close to the FRP end (Roberts 1989)

The third way to deal with concrete cover rip-off and plate-end shear failure are the shear capacity based models, which are relatively easy to use compared to the concrete tooth models and interfacial stress models, and are therefore preferred in the design guidelines. Shear capacity based models (Oehlers 1992; Jansze 1997) relate the debonding load to the load when shear cracks are expected to initiate at the plate-end. Because concrete cover rip-off is initiated at the same location and in the same way as plate-end shear failure, Jansze (1997) suggested that both types of failure can be dealt with in the same way. Jansze proposed a model that is based on the analogy between a non-strengthened and a strengthened beam (Figure 2-28). The model for the non-strengthened beam has been developed by Kim and White (1991).

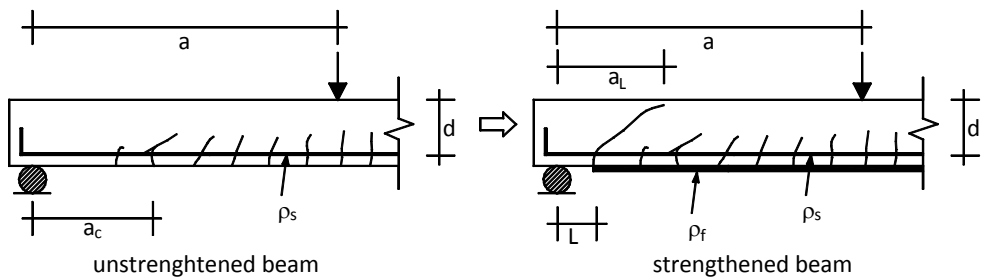


Figure 2-28: Modeling analogy of end-shear failure (fib 2001)

The shear resistance at the plate-end can be calculated using a fictitious shear span and the Model Code 1990 (CEB 1993) expression for the shear force (V_{Rd1}) causing shear cracking (all units in N and mm);

$$V_{sd} \leq V_{Rd} = \tau_{Rd} \cdot b_c \cdot d \quad (2.12)$$

where

τ_{Rd} the design value of the nominal maximum shear stress at debonding

$$= 0.15 \cdot \sqrt[3]{3 \cdot \frac{d}{a_L}} \cdot \left(1 + \sqrt{\frac{200}{d}} \right) \cdot \sqrt[3]{100 \cdot \rho_s \cdot f_{ck}} \quad (2.13)$$

$$a_L = \sqrt[4]{\frac{(1 - \sqrt{\rho_s})^2}{\rho_s}} \cdot L^3 \cdot d \quad (2.14)$$

f_{ck} is the characteristic concrete compressive strength

L is the distance between the support and the end of the FRP reinforcement

The model is only applicable within certain limits, for $a > L + d$ and $a_L < a$ (Figure 2-28). The first restriction is a limitation where the original model was derived for. The second restriction is proposed by Jansze, because the model is only developed for situations in which a shear crack develops at the plate-end between the support and the load introduction. The model has been evaluated by Jansze for both externally bonded steel and CFRP reinforcement. It was concluded that the model is an accurate lower bound model for the prediction of plate-end shear failure and concrete cover rip-off.

2.4.3.6 Debonding due to the unevenness of the concrete surface

Unevenness of the concrete surface may also result in (local) debonding of the FRP reinforcement (Figure 2-29), although it is unlikely that it causes complete FRP debonding. Most guidelines provide values for the maximum permissible unevenness of the concrete surface over a certain length (Table 2-5). Larger unevenness of the concrete surface has to be removed, for example by applying a primer before applying the FRP reinforcement (fib 2001).

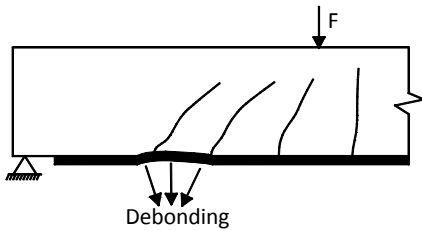


Figure 2-29: Debonding due to the unevenness of the concrete surface

Table 2-5: Permissible unevenness of the concrete surface (fib 2001)

Type of FRP-EBR	Permissible unevenness on a 2.0 m base [mm]	Permissible unevenness on a 0.3 m base [mm]
"Prefab", thickness > 1 mm	10	4
"Prefab", thickness < 1 mm	6	2
"Cured in situ"	4	2



3 Effect of temperature on FRP strengthened structures – state of the art

3.1 Introduction

The amount of research into the effect of temperature on the FRP strengthening of concrete structures turns out to be limited. Furthermore, research in this field has mainly been carried out with small scale specimens, like double-lap shear tests and flexural tests, which can only be used to investigate the local bond behavior of the concrete-adhesive-FRP joint. Most debonding mechanisms, as described in the previous chapter, are however related to this bond behavior.

This chapter provides a brief overview of previous research projects by other researchers in which the effect of temperature (changes) on FRP strengthened concrete structures has been investigated. Comparison of the results between the different investigations is however difficult, as different types of adhesive with different temperature characteristics have been used amongst the different investigations. Note that this chapter only focuses on ambient temperature changes, and not on the effect of fire, which is outside the scope of this research project.

3.2 Double-lap shear tests

3.2.1 Externally bonded steel strips

The most widely used bond test setup to investigate the bond behavior of a concrete-adhesive-FRP joint subjected to loading in shear is the double-lap shear test (Figure 3-1). This test has been used by Tadeu and Branco (2000) to investigate the influence of temperature on concrete specimens strengthened with externally bonded steel strips. The bond behavior of three different concrete grades was investigated at 20°C, 30°C, 60°C, 90°C and 120°C. Steel and concrete have approximately the same coefficient of thermal expansion, which implies that the development of thermal stresses when heating the specimens was not an issue for these tests.

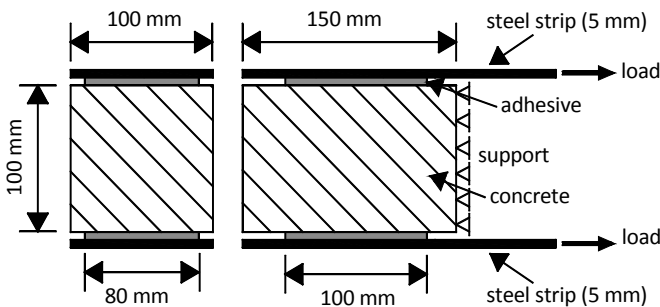


Figure 3-1: Double-lap shear test (Tadeu and Branco 2000)

The experimental results obtained in this study showed a reduction of the failure load with an increase in temperature (Figure 3-2), which was, at low temperatures, more pronounced for the high strength concrete. It was expected by Tadeu and Branco that the decreasing failure load with increasing temperatures was a result of a change in the type of failure at elevated temperatures.

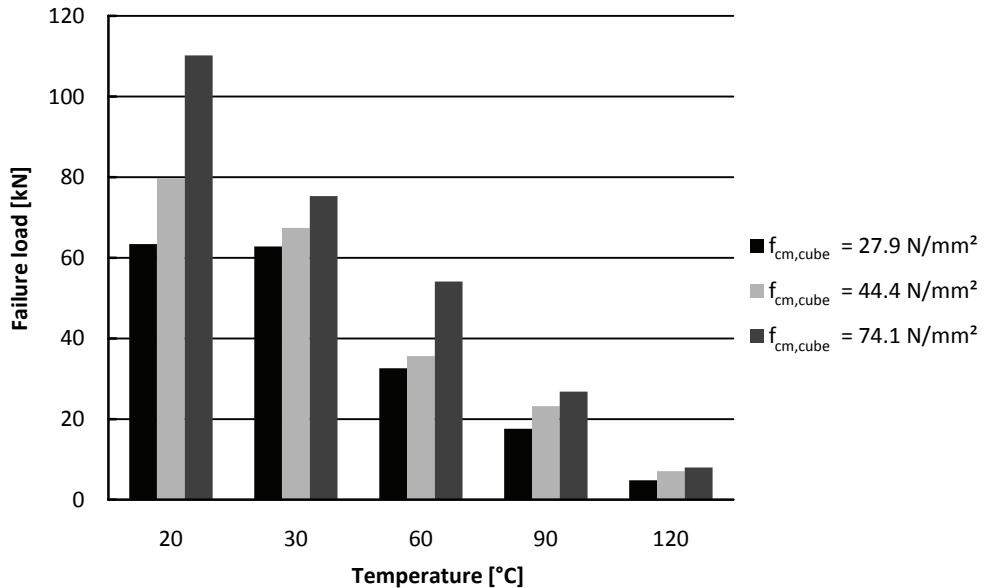


Figure 3-2: Temperature-failure load relation (Tadeu and Branco 2000)

At 20°C and 30°C, failure initiated in the concrete at about 30 mm from the bonded surface, while for higher temperatures, cohesive failure of the adhesive was found. Based on this difference in type of failure, it is likely that the glass transition temperature of the adhesive was somewhere in between 30°C and 60°C. For the specimens tested at 120°C, an additional phenomenon was observed. Besides deterioration of the adhesive, also a film of water was observed on the surface of the concrete, due to the evaporation of free water above 100°C.

3.2.2 Externally bonded FRP

Double-lap shear tests have also been carried out with concrete specimens strengthened with externally bonded CFRP laminates (Blontrock 2003), although in a slightly different test setup (Figure 3-3). The concrete specimens (f_{cm,cube} = 40 N/mm²) were tested at 20°C, 40°C, 55°C and 70°C (Figure 3-4). Steel clamps were applied at one side to make sure that debonding occurred at the other side, where the strain distribution was recorded by means of strain gauges. The glass transition temperature of the adhesive was 62°C.

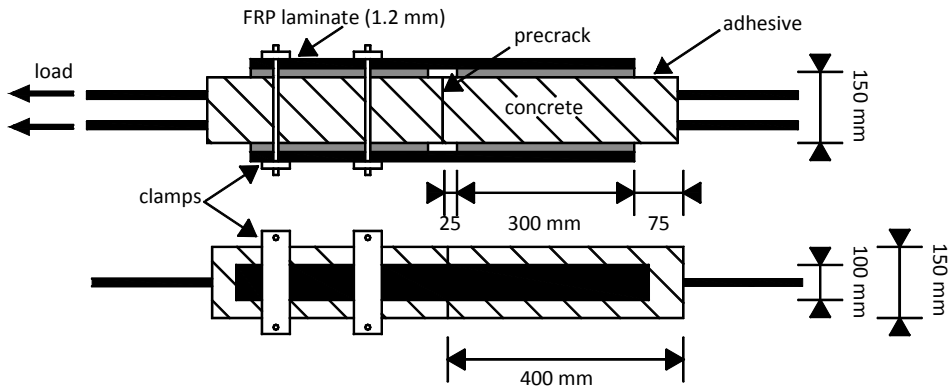


Figure 3-3: Double-lap shear test (Blontrock 2003)

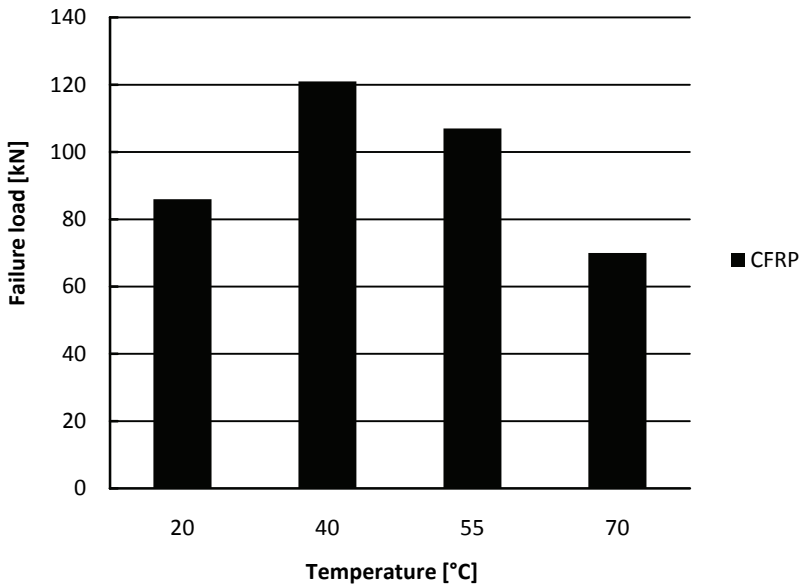


Figure 3-4: Temperature-failure load relation (Blontrock 2003)

The experimental results were different from the results of Tadeu and Branco for steel plates. Increasing the temperature from 20°C to 40°C resulted in a significant higher failure load (41%) instead of a lower failure load. Further increasing the temperature to 55°C and 70°C resulted in a decreasing failure load, although at 55°C, still higher than the initial failure load at 20°C. Blontrock mentioned two possible causes for the different results compared to those of Tadeu and Branco:

1. The dimensions of the specimens: A significant larger bonded surface ($300 \times 100 \text{ mm}^2$ (CFRP) vs. $100 \times 80 \text{ mm}^2$ (steel)) resulted in a different failure mode. Failure occurred in the concrete adjacent to the bonded surface at a depth of approximately 0-1 mm, whereas Tadeu and Branco found failure of the concrete at a depth of 30 mm from the bonded surface.
2. The difference in coefficient of thermal expansion. For steel and concrete, the coefficient of thermal expansion is about the same, whereas it is significantly different in case of CFRP and concrete. This difference induced thermal stresses in the CFRP and concrete, which could have affected the load capacity.

The experiments of Blontrock were continued by Leone et al. (2006) for CFRP- and GFRP fabrics (wet lay-up) and prefabricated CFRP laminates. The same test setup was used as for the experiments by Blontrock, with slightly longer FRP fabrics/laminates (700 mm). Two different adhesives were applied, one for the fabrics and one for the laminate, both with a lower glass transition temperature (55°C) compared to the one used by Blontrock (62°C).

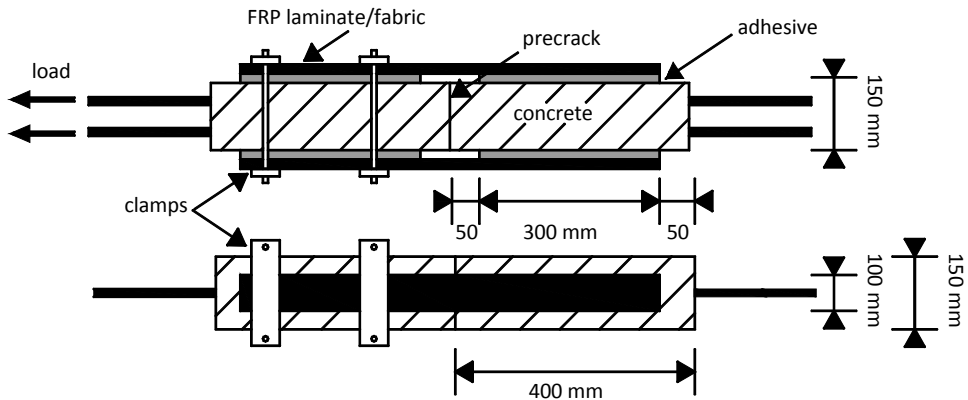


Figure 3-5: Double-lap shear test (Leone, Aiello, and Matthys 2006)

For the CFRP fabrics ($t_f = 0.117 \text{ mm}$), increasing the temperature resulted first in an increasing failure load, which was followed by a decreasing failure load at higher temperatures (Figure 3-6). The GFRP fabrics ($t_f = 0.300 \text{ mm}$) were only tested at 20°C and 80°C , with the lowest failure load at 80°C . For the CFRP laminates ($t_f = 1.0 \text{ mm}$), an opposite tendency was observed. At 50°C , a lower failure load was found compared to room temperature, while at 80°C a higher failure load was found. It was expected by Leone et al. that this different behavior of the CFRP laminates, compared to the CFRP fabrics, could possibly be explained by the lower concrete quality of these specimens and the eccentricities that were observed in the tests. Failure changed for all types of FRP reinforcement from failure in the concrete, adjacent to the concrete-adhesive interface at 20°C and 50°C to failure of the adhesive-FRP interface at 80°C . At 65°C , both types of failure were found for the CFRP fabrics.

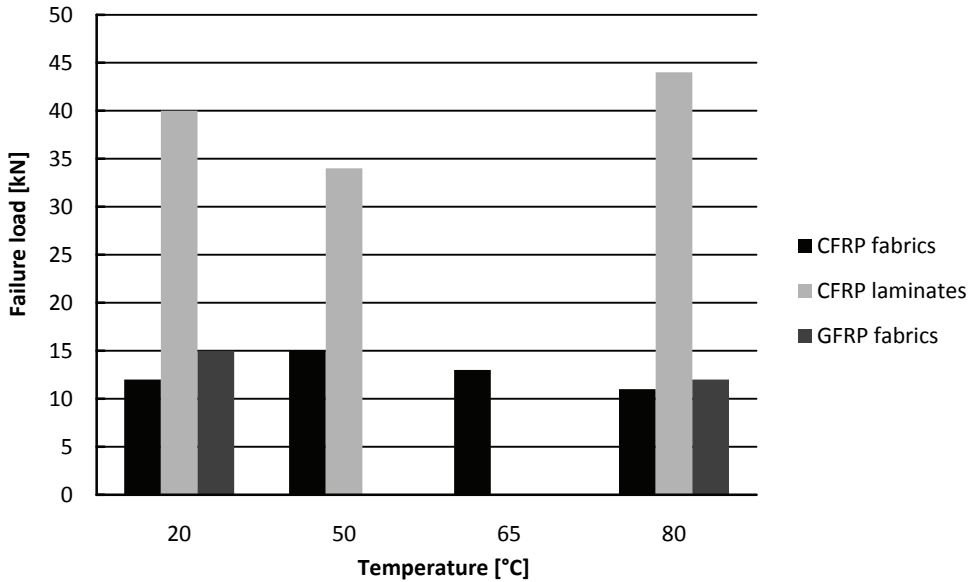


Figure 3-6: Temperature-failure load relation (Leone, Aiello, and Matthys 2006)

Double-lap shear tests with externally bonded CFRP fabrics have also been carried out by Wu et al. (2005). The CFRP fabrics were applied in two steps. First an epoxy primer was applied to the concrete surface, followed by an epoxy adhesive for bonding the CFRP to the primer. Both the primer and adhesive were applied in an ordinary and a thermo-resistant variant (primer: $T_g = 34^\circ\text{C}$ and 55°C respectively, adhesive: $T_g = 34^\circ\text{C}$ and 40°C respectively) (Figure 3-7). The specimens were tested with the ordinary primer and adhesive at 26°C , 30°C , 40°C and 50°C and with the thermo-resistant primer and adhesive at 26°C , 40°C , 50°C and 60°C .

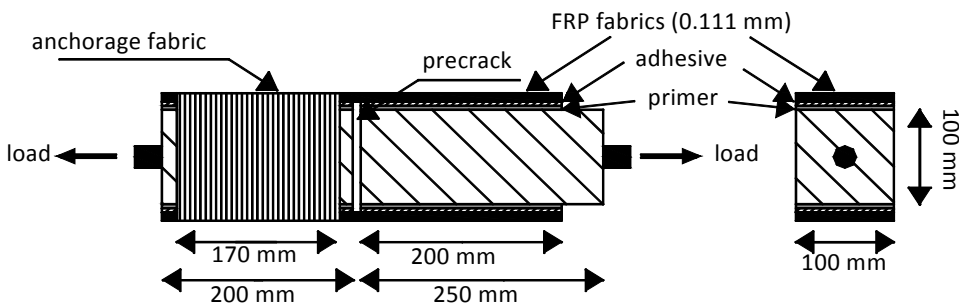


Figure 3-7: Double-lap shear test (Wu et al. 2005)

Test results showed a decreasing failure load with increasing temperatures for both types of primer/adhesive (Figure 3-8). The decrease in failure load turned out to be more significant at a certain temperature for the ordinary epoxy adhesive, as expected. It also turned out that the failure mode changed from a mixed type of failure in the concrete and in the primer-adhesive interface at 26°C to failure in the primer-adhesive interface alone at 30°C and above. The reduction in the failure load with increasing temperature is therefore mainly related to a reduced bond capacity of the primer-adhesive interface at elevated temperatures. From the test results, it was concluded that the specially developed thermo-resistant primer/adhesive was more resistant to temperature influences than the normal primer/adhesive.

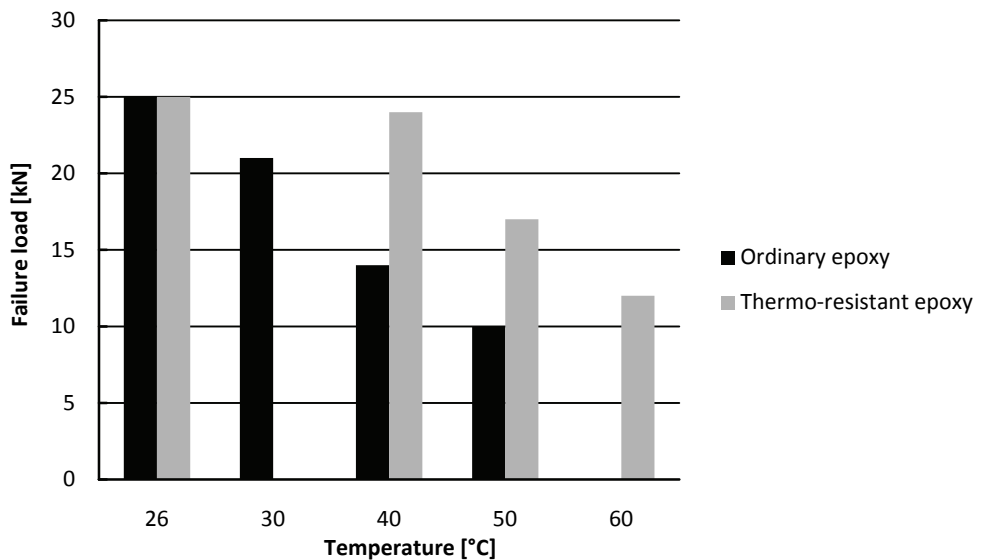


Figure 3-8: Temperature-failure load relation (Wu et al. 2005)

3.3 Small scale flexural tests

3.3.1 Externally bonded FRP

In the double-lap shear test setup, the concrete-adhesive-FRP joint is loaded in almost pure shear. In a flexural test, the joint is still mainly loaded in shear, but curvature of the specimen will also cause normal stresses perpendicular to the bonded surface. Curvature of a structure will also occur in most strengthened structures in practice, like beams and slabs. Three-point bending tests have been carried out by Di Tommaso et al. (2001) on small scale concrete specimens ($100 \times 100 \times 800 \text{ mm}^3$) without internal steel reinforcement (Figure 3-9). The specimens were strengthened at room temperature with two different types of CFRP laminates (normal and high Young's modulus laminates) of $20 \times 590 \text{ mm}^2$. The laminates had a thickness of 1.24 mm and 1.4 mm respectively and were tested at four different temperatures, -100°C, -30°C, 20°C and 40°C. The applied adhesive had a glass transition temperature of about 60°C.

In the experiments, three different types of failure (Figure 3-9 and Table 3-1) were observed. For low temperatures CFRP delamination was found after the initiation of a crack in the concrete. For moderate temperatures, concrete failure adjacent to the concrete-adhesive interface was found, while at 40°C cohesive failure in the adhesive layer was found due to the softening of the adhesive.

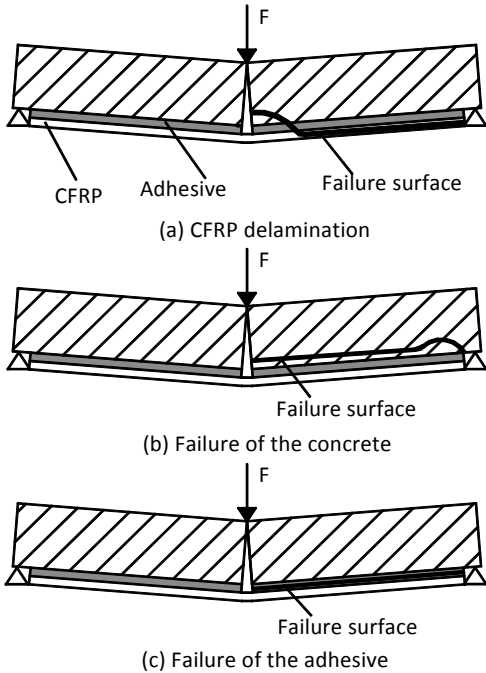


Figure 3-9: Test setup and types of failure in the CFRP strengthened beams (Di Tommaso et al. 2001)

Table 3-1: Type of failure at different temperatures (Di Tommaso et al. 2001)

Temperature	Young's modulus CFRP laminate	
	170,000 N/mm ²	300,000 N/mm ²
-100°C	CFRP delamination	CFRP delamination
-30°C	Concrete failure	CFRP delamination
20°C	Concrete failure	Concrete failure
40°C	Concrete and Adhesive failure	Adhesive failure

The results showed that the load capacity decreased when increasing the temperature from 20°C to 40°C (Figure 3-10). This effect was explained by the reduced bond strength due to the changed type of failure. Decreasing the temperature to -30°C and -100°C also resulted in a decreasing failure load, except for the specimen with the normal modulus CFRP ($E_f = 170,000 \text{ N/mm}^2$) that was tested at -100°C. No sound explanation was given for this behavior at low temperatures. It appeared that the behavior was less ductile at low temperatures.

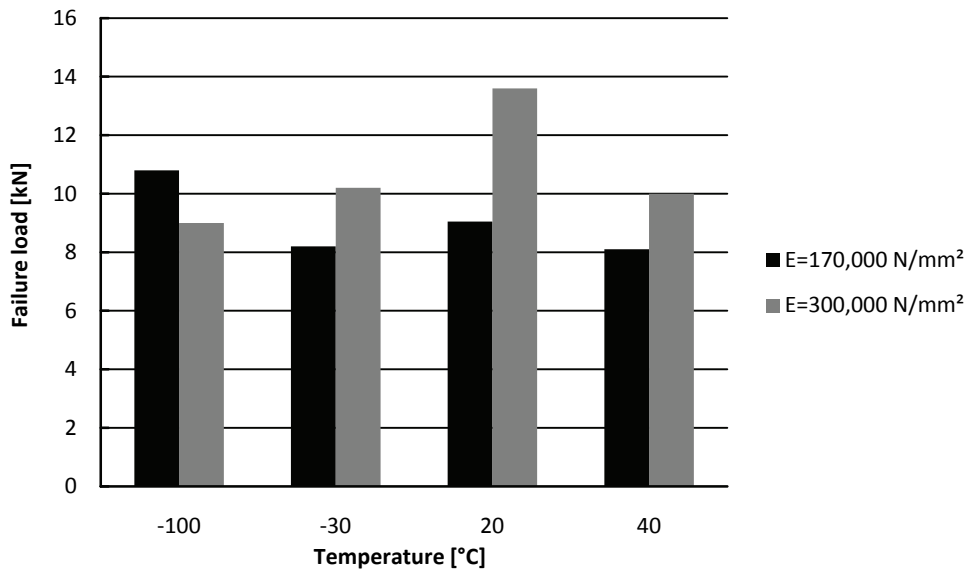


Figure 3-10: Failure load of the specimens for two different Young's moduli of CFRP at different temperatures (Di Tommaso et al. 2001)

3.4 Full scale FRP strengthened concrete structures

3.4.1 General

Research into the effect of temperature on full scale FRP strengthened concrete structures is rather limited. Only three research projects are known to the author. These are an (experimental) investigation into concrete beams with externally bonded CFRP fabrics at room and low temperature (Section 3.4.2), a (numerical) investigation into the behavior of a CFRP strengthened bridge deck at elevated temperatures (Section 3.4.2) and an (experimental) investigation into the behavior of reinforced concrete beams with externally bonded prestressed CFRP fabrics at low and room temperatures (Section 3.4.4).

3.4.2 Externally bonded CFRP

Baumert et al. (1996) tested both small and large scale concrete beams that were strengthened with three layers of externally bonded CFRP fabrics. Twelve non-reinforced concrete beams ($150 \times 150 \times 1000 \text{ mm}^3$) and six reinforced concrete beams ($150 \times 300 \times 2000 \text{ mm}^3$) were investigated (Figure 3-11) at room (21°C) and low temperature (-27°C) in four point bending.

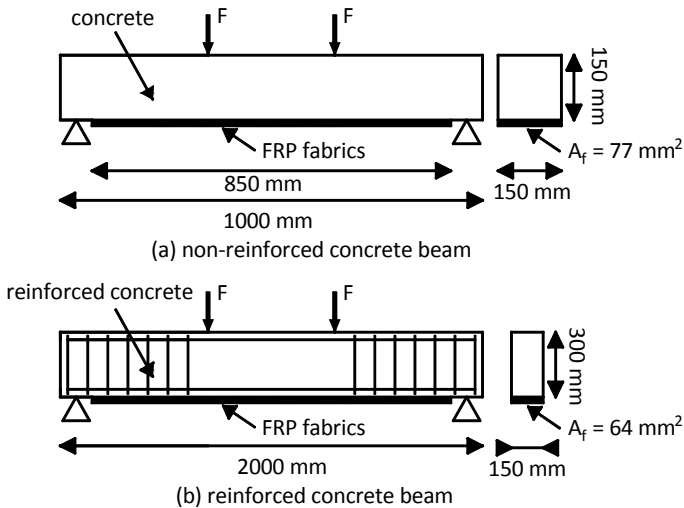


Figure 3-11: Test setup of non-reinforced (a) and reinforced (b) concrete specimens (Baumert, Green, and Erki 1996)

In the non-reinforced concrete beams shear failure of the beam was followed by debonding of the CFRP fabrics, while in the reinforced concrete beams debonding initiated first, just outside the constant moment region. After debonding outside the constant moment region, debonding extended in the constant moment region along the level of the internal steel reinforcement. No difference in type of failure was found between the specimens tested at low and room temperature. Also the failure load was not significantly affected by the low temperature, as can be seen in Figure 3-12.

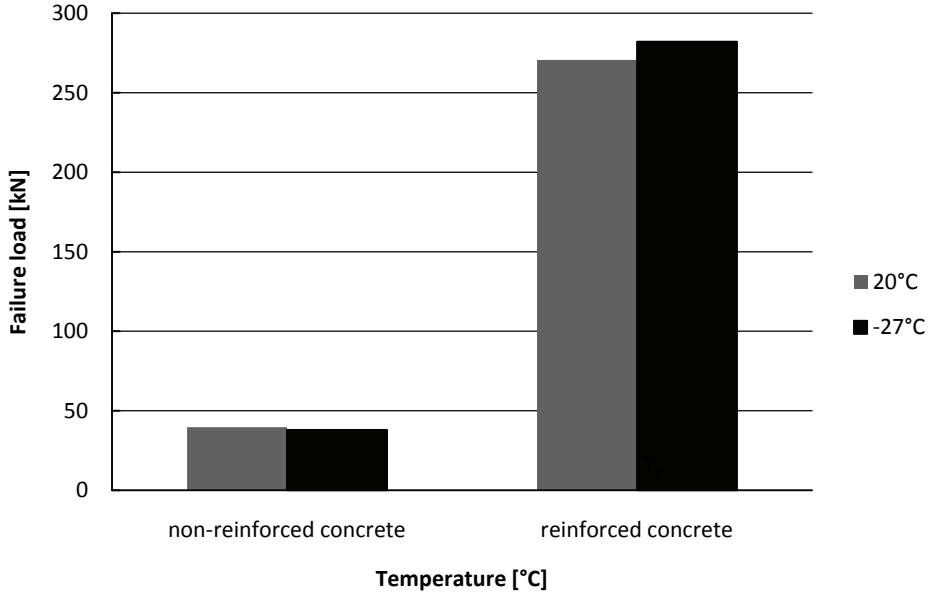


Figure 3-12: Failure load of non-reinforced and reinforced concrete specimens at low and room temperature

3.4.3 CFRP strengthened bridge deck at elevated temperature

Nigro et al. (2006) have investigated the performance of a CFRP strengthened reinforced concrete bridge at elevated temperature. In this research project, the elevated temperature was a result of the maintenance of the bituminous paving, which was cast in place on a bridge deck. The bituminous paving had a temperature of 180°C (Nigro et al. 2006). Two situation were evaluated, CFRP applied at the soffit of the bridge deck (Figure 3-13a) and CFRP applied at the top of the bridge deck (Figure 3-13b). Nigro et al. also investigated the effect of fire, but this is outside the scope of this thesis.

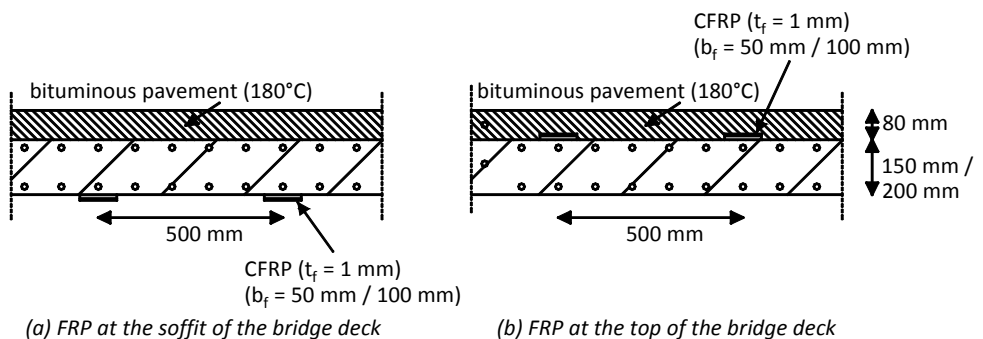


Figure 3-13: Bituminous paving of a bridge deck with FRP at the soffit (a) and at the top (b) of the deck (Nigro et al. 2006)

The structural safety of the bridge deck was only verified by thermal finite element analyses, in which the temperature distribution in the structure was determined over time. The structure was assumed to be safe when the strains in the different materials did not exceed the ultimate limit strains of these materials within a certain amount of time. These ultimate limit strains for the different materials were assumed to be temperature dependent. The ultimate limit strain of the internal steel reinforcement and concrete were taken according to Eurocode 2 (part 1-2) (CEN 2004b). The ultimate limit strain of the CFRP was taken according to the Italian code for FRP strengthening, CNR-DT 200/2004 (Italian National Research Council 2004), in which a FRP strain limit is given for “debonding due to high shear stresses” (at room temperature) (Section 2.4.3.2). The strain limit was modified for elevated temperature according to a specific fracture energy reduction as was found by Wu et al. (2005). Note however that using a FRP strain limit is a very crude simplification of the actual debonding behavior and does not cover all types of debonding as discussed in Chapter 2.

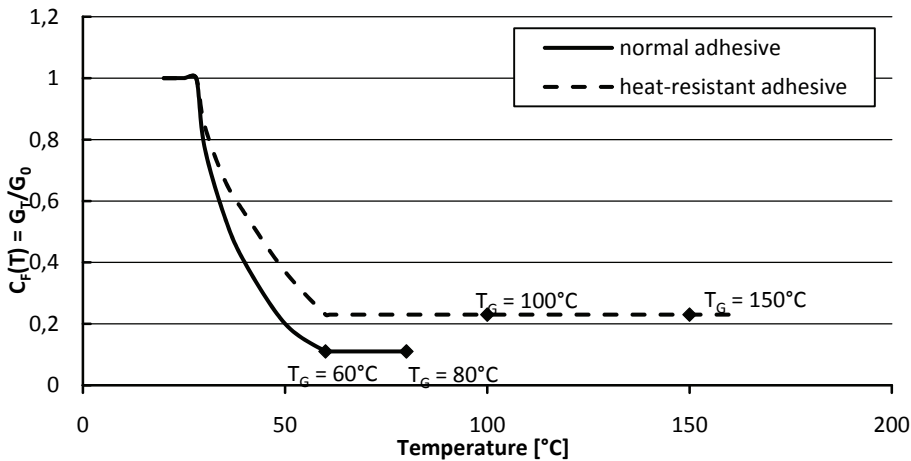


Figure 3-14: Temperature dependent specific fracture energy of normal and heat resistant adhesives (Nigro et al. 2006)

The results of the safety analyses unfortunately haven't been verified with experimental results, which make the results of limited value. Main conclusions were that in the case where the CFRP reinforcement was applied to the soffit of the bridge deck (Figure 3-13a), the ultimate limit strains were not exceeded and the level of safety was sufficient during the application of the bituminous pavement. When the CFRP was applied on top of the bridge deck with a normal adhesive (Figure 3-13b), a concrete protective layer of at least 4 cm had to be applied on top of the CFRP to keep the temperature of the adhesive below the glass transition temperature. Moreover, the safety of the structure became insufficient during the application of the bituminous pavement. The thermal analyses of the structure with the heat resistant adhesive however showed that the safety of the structure could be guaranteed during the application of the pavement with a heat resistant adhesive.

3.4.4 Externally bonded prestressed CFRP

El-Hacha et al. (2004) investigated the flexural behavior of RC beams strengthened with prestressed CFRP fabrics at room temperature (+22°C) and at low temperature (-28°C). The CFRP fabrics were anchored with a specially designed fixed anchor at one side and a movable anchor at the other side, where the prestress was applied to the fabrics. The T-beams spanned 4 m. Failure in the prestressed FRP strengthened beams occurred due to failure of the FRP fabrics, as debonding was prevented by the anchorage. It turned out that the behavior of the beam was not adversely affected by the low temperature, although some loss in prestress was found at low temperatures. These tests unfortunately do not provide insight into the effect on temperature on the debonding of externally bonded CFRP, as no debonding occurred during the tests.

3.5 Theoretical stress development due to thermal mismatch

The difference in the coefficient of thermal expansion between concrete ($\alpha_c \approx 10 \times 10^{-6} / ^\circ\text{C}$) and e.g. CFRP ($\alpha_f \approx 0 \text{ à } -1 \times 10^{-6} / ^\circ\text{C}$ in the fiber direction) will result in the development of thermal stresses in concrete and FRP when changing the temperature. A kinematic model (theoretical beam model) was introduced by Di Tommaso et al. (2001) to compute the shear stresses in the concrete and the normal stresses in the FRP (Appendix A). The model is used throughout this research project and is therefore explained in this section. The model only takes linear elastic material behavior of the concrete and the FRP into account, as thermal stresses can be expected to be small. It also neglects the adhesive layer in between the concrete and FRP, which implies that the concrete is assumed to be directly connected to the FRP (Figure 3-15).

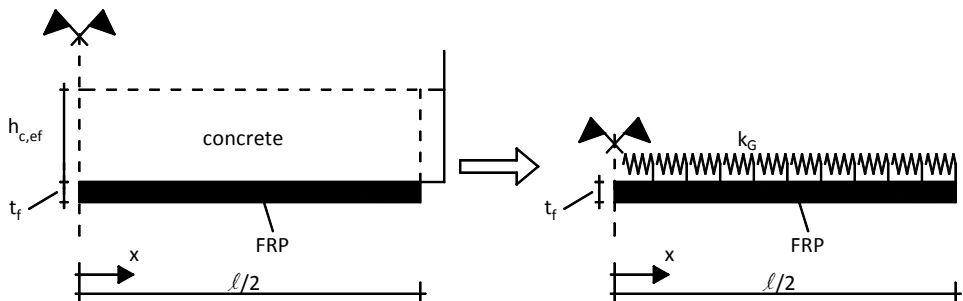


Figure 3-15: Theoretical beam model (Di Tommaso et al. 2001)

The normal stresses in the FRP and shear stresses in the concrete along the length of the laminate can be determined with;

$$\sigma_{f\Delta T}(x) = -E_f \cdot \left[\frac{\varepsilon_{\Delta T}}{\cosh(\omega \cdot \ell / 2)} \cdot \cosh(\omega \cdot x) - \varepsilon_{\Delta T} \right] \quad (3.1)$$

$$\tau_{c\Delta T}(x) = -E_f \cdot t_f \cdot \omega \cdot \frac{\varepsilon_{\Delta T}}{\cosh(\omega \cdot \ell / 2)} \sinh(\omega \cdot x) \quad (3.2)$$

where

E_f is the Young's modulus of the FRP reinforcement

$\varepsilon_{\Delta T} = \alpha_c \Delta T$

α_c is the coefficient of thermal expansion of concrete

ΔT is the change in temperature

$\omega^2 = \frac{k_{GC}}{E_f \cdot t_f}$

$k_{GC} = \frac{E_c}{2 \cdot (1 + \nu_c) \cdot h_{c,ef}}$

E_c is the Young's modulus of concrete

ν_c is the Poisson ratio of concrete

$h_{c,ef} \approx 50$ mm or two times the maximum aggregate size (both definitions are used in literature)

t_f is the thickness of the FRP

ℓ is the bonded length

x is the distance from the middle of the bonded length

Figure 3-16 shows the normal (a) and shear (b) stress distributions for a low and high Young's modulus CFRP laminate of 300 mm ($E_f = 170,000$ N/mm² and $E_f = 300,000$ N/mm² respectively) after an increase in temperature from 20°C to 50°C. A positive value of $\sigma_{f\Delta T}$ in Equation 3.1 and Figure 3-16a corresponds to tension. For the computation, the Young's modulus of concrete was taken equal to $E_c = 30,000$ N/mm² and the coefficients of thermal expansion equal to $\alpha_f = 0 \times 10^{-6}$ /°C, $\alpha_c = 10 \times 10^{-6}$ /°C. It can be seen that a higher Young's modulus of the CFRP results in higher normal stresses in the CFRP and shear stresses in the concrete-CFRP interface. In Section 6.4.4, this model is modified in such way that the properties of the adhesive layer are included in the model.

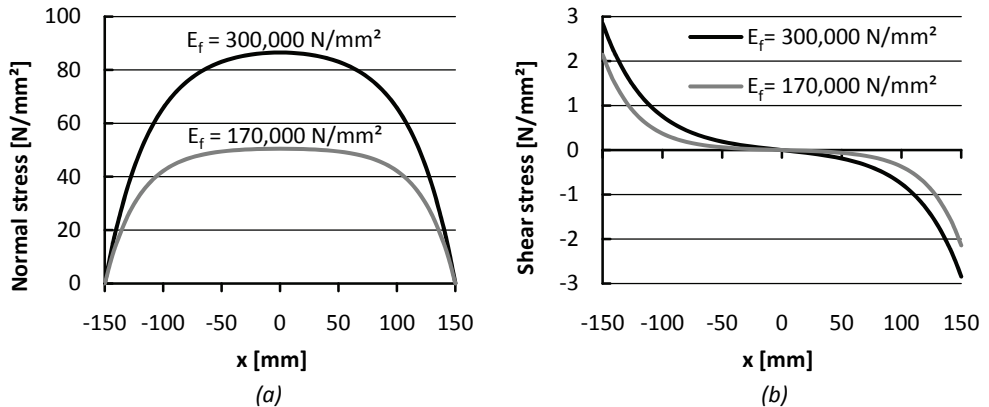


Figure 3-16: Normal (a) and shear (b) stresses at 50°C for two typical CFRP laminates

3.6 Summary

Experimental research into the effect of ambient temperature on the FRP strengthening of concrete structures has so far mainly been carried out with small scale specimens. It turns out that contradictory results were found between the different research projects. For example, both increasing as well as decreasing failure loads were found with increasing temperatures, even for similar test setups. The different results could possibly be explained by the fact that the material and geometry properties varied between the different investigations. Especially the material properties of the adhesive, like the glass transition temperature, were different for each type of adhesive, which makes comparison of the test results rather difficult.

Some similarities can however be distinguished. In general, the type of failure changed from failure in the concrete at moderate temperatures to failure in the adhesive or failure exactly in one of the interfaces (concrete-adhesive or adhesive-FRP) at temperatures near or above the glass transition temperature of the adhesive. This change in type of failure was generally accompanied by a decrease in the bond capacity. The number of test results at temperatures below room temperature was rather limited, which makes it difficult to draw conclusions for this temperature range yet.

The effect of the difference in the coefficient of thermal expansion between concrete and FRP on the behavior of the strengthened specimens has not been investigated by most of the researchers. This could, however, possibly explain some of the differences between the various investigations. Moreover, to the knowledge of the author, no experimental research has been carried out so far in which the effect of elevated temperature is investigated for full scale FRP strengthened beams. For full scale beams, other types of debonding could occur (Section 2.4) as for small scale specimens, which could be affected by temperature in a different way. It is important to investigate the effect of temperature on all possible debonding mechanisms. Chapter 7 and 8 will therefore describe the results of the investigation into the effect of temperature on the behavior of full scale CFRP strengthened beams that were designed to fail by different types of debonding.

4 Effect of temperature on the material properties

4.1 Introduction

A FRP strengthened reinforced concrete structure is composed out of the materials concrete, steel reinforcement, FRP and adhesive. The effect of temperature on the material properties of each of these materials will be discussed in this chapter, as they are all likely to be affected by temperature. Some of them are, however, affected more than others. Especially the material properties of the adhesive change significantly around the glass transition temperature.

For concrete and steel reinforcement, reference will be made to literature, while for the adhesive and FRP also experiments have been carried out, of which the results will be presented. Main focus will be on the effect of temperature within the temperature range from -20°C to $+80^{\circ}\text{C}$, although the effects of higher temperatures are also discussed briefly.

4.2 Concrete

4.2.1 General

The effect of temperature on the material properties of concrete has been investigated extensively by many researchers in the last century. Bažant and Kaplan (1996) gathered the results of many of these investigations. They concluded that the effect of temperature on the concrete material properties is mainly related to the evaporation of water from the concrete and to changes in the chemical composition and physical structure of the concrete. These effects turned out to occur for the most part in the cement paste, while the aggregates stay more or less unaffected. The temperature effects that can be distinguished with increasing temperature are (Bažant and Kaplan 1996);

- Expulsion of evaporable water from hardened cement paste and aggregates ($\pm 100^{\circ}\text{C}$);
- Dehydration of the cement gel ($\pm 180^{\circ}\text{C}$);
- Decomposition of calcium hydroxide ($\pm 500^{\circ}\text{C}$);
- Transformation of α -quartz to β -quartz in quartzite and basalt aggregate concretes ($\pm 570^{\circ}\text{C}$);
- Decomposition of calcium silicate hydrates ($\pm 700^{\circ}\text{C}$);
- Decarbonation of calcium carbonate in limestone aggregate concretes ($\pm 800^{\circ}\text{C}$);
- Melting of the cement paste and aggregates (between 1150°C and 1200°C).

Other effects of an increase in temperature are the change in pore structure and the development of high-water vapor pressure in the concrete pores, which could result in thermal spalling of the concrete. Also localized heating could result in spalling, especially when the thermal expansion is restricted by surrounding cool concrete, which results in high compressive stresses in the heated concrete.

4.2.2 Compressive strength

Figure 4-1 shows the effect of temperature on the compressive strength of ordinary Portland cement concretes with different conventional aggregates (Bažant and Kaplan 1996). At 90°C, the compressive strength is reduced to about 65% to 90% of the initial strength. The reduction is mainly caused by evaporation of free water, microcracking of the concrete and loss of bond between the cement paste and the aggregates due to the difference in the coefficient of thermal expansion between these materials.

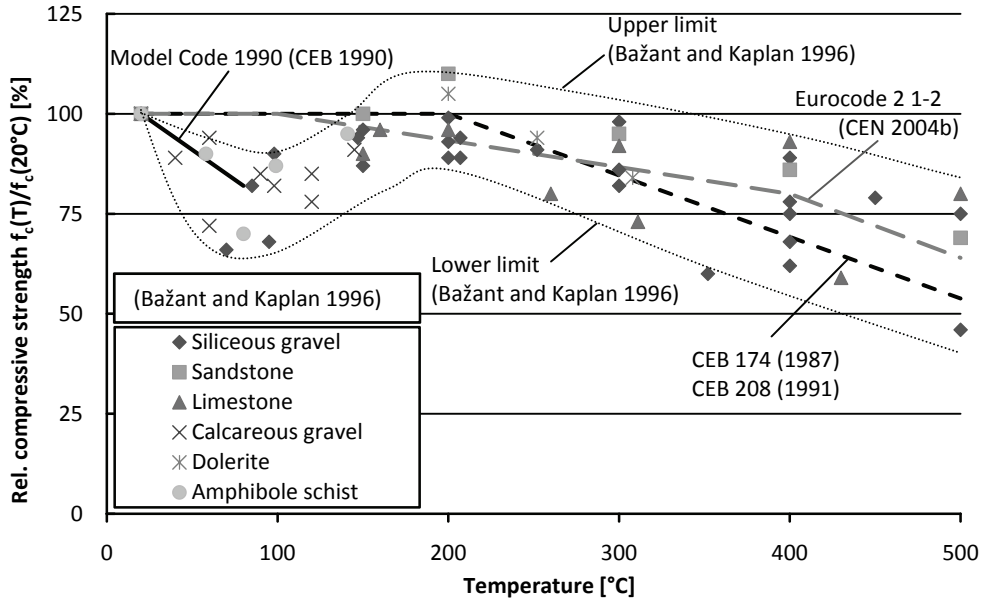


Figure 4-1: Influence of temperature on the compressive strength of concrete

Further increasing the temperature up to 200°C resulted in an increase of the compressive strength, mainly due to the rapid drying of the concrete and the change in pore structure. The residual strength at 200°C is about 85% to 110% of the initial strength at room temperature. Above this temperature, the compressive strength is almost linear decreasing with increasing temperatures.

Eurocode 2 part 1-2 (CEN 2004b), Model Code 1990 (CEB 1993) and CEB Bulletin 174/208 (CEB 1987; CEB 1991) all provide different relations between the temperature and the concrete compressive strength (Figure 4-1). Eurocode 2 part 1-2, CEB 174 and CEB 208 were originally developed for fire design of concrete structures, for which it is allowed to simplify the behavior at moderate temperatures. These guidelines neglect the effects of temperature in the temperature range in between 0°C and 100°C. Model Code 1990 only provides a relation for moderate temperatures ($\leq 80^\circ\text{C}$) and fits the experimental results in this temperature range the best;

Model Code 1990 (CEB 1993):

$$f_{cm}(T) = f_{cm} \left(1.06 - \frac{0.003 \cdot T}{T_0} \right) \quad (4.1)$$

where

- $f_{cm}(T)$ is the mean concrete compressive strength at the temperature T
- T is the temperature in ($^{\circ}\text{C}$)
- f_{cm} is the mean concrete compressive strength at 20°C
- $T_0 = 1^{\circ}\text{C}$

4.2.3 Tensile strength

The tensile strength of concrete turned out to be more sensitive to temperature than the compressive strength (Bažant and Kaplan 1996). Figure 4-2 shows the effect of temperature on the tensile splitting strength of concrete with ordinary aggregate materials. Similar results were found for the flexural strength of concrete. It can be seen that increasing the temperature resulted in a degradation of the tensile strength, but also in a large scatter in results. The loss of tensile strength turned out to be irreversible.

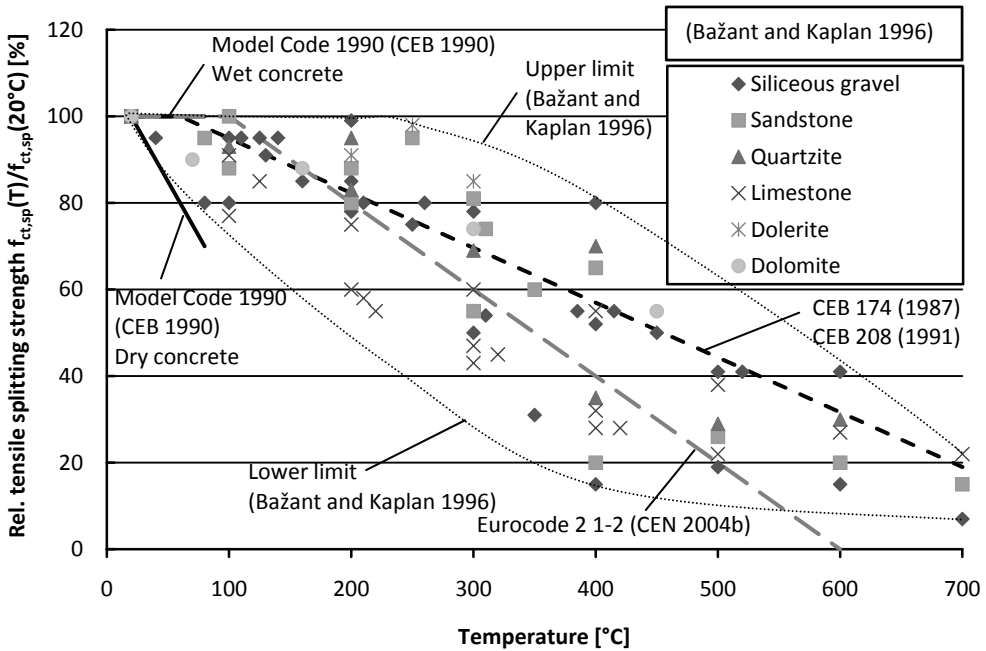


Figure 4-2: Influence of temperature on the tensile splitting strength of concrete

In the temperature range from 0°C to 80°C, no influence of temperature has to be taken into account according to Eurocode 2 part 1-2 (CEN 2004b). Model Code 1990 (CEB 1993) only takes an effect of temperature on the flexural strength into account for dry concrete (equation (4.2)), while the effect of temperature is neglected for wet concrete. For wet concrete, the decrease in tensile strength due to the temperature increase is assumed to be compensated by the increase in tensile strength due to drying of the concrete. The two relations seem to be corresponding to the lower and upper limits found by Bažant and Kaplan, as can be seen in Figure 4-2.

$$\text{Model Code 1990, dry concrete (CEB 1993): } f_{ct,fl}(T) = f_{ct,fl} \left(1.1 - \frac{0.005 \cdot T}{T_0} \right) \quad (4.2)$$

where

- $f_{ct,fl}(T)$ is the flexural strength of concrete at the temperature T
- T is the temperature in °C
- $f_{ct,fl}$ is the flexural strength of concrete at 20°C
- $T_0 = 1^\circ\text{C}$

4.2.4 Fracture energy

In tensile experiments, fracture energy is defined as the amount of energy that is required to create one unit area of crack and is expressed in J/m². In fracture tests the amount of energy required for fracturing is generally represented by the area under the load-deformation diagram. The fracture energy of concrete is also affected by temperature. Test results (Bažant and Prat 1988) have shown that the relation between temperature and fracture energy depends on the moisture content, as can be seen in Figure 4-3.

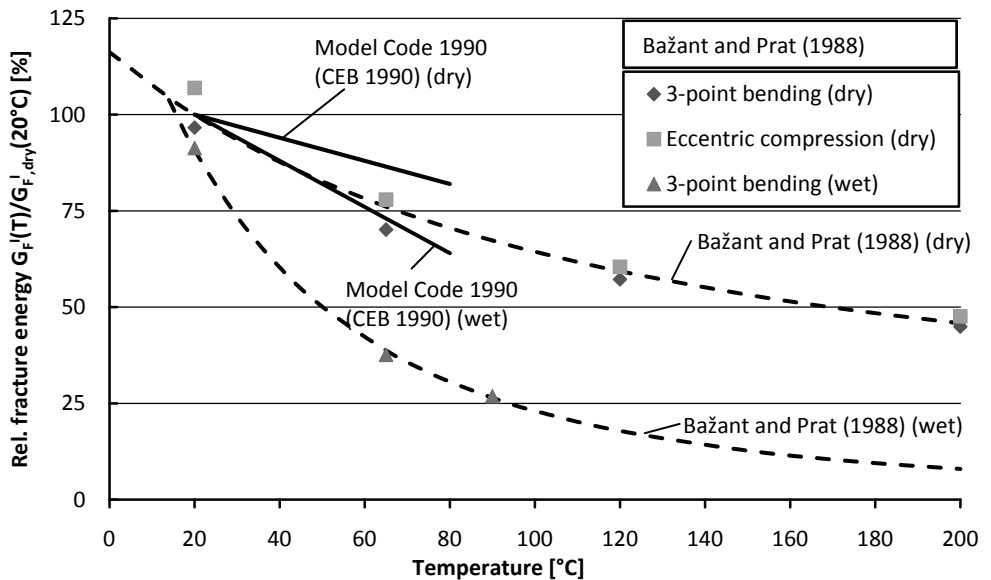


Figure 4-3: Influence of temperature on the fracture energy of concrete

For wet concrete, the effect of temperature on the fracture energy turned out to be more pronounced than for dry concrete, due to the additional water vapor pressure in the concrete pores. Only Model Code 1990 (CEB 1993) provides equations that take the effect of temperature on the fracture energy into account. Equation (4.3) and (4.4) can be used for dry concrete and wet concrete respectively. It can however be seen that this relation does not fit the results found by Bažant and Prat, possibly due to other factors that have not been taken into account in either the tests or the formulas.

$$\text{Model Code 1990, dry concrete (CEB 1993): } G_f(T) = G_f \left(1.06 - \frac{0.003 \cdot T}{T_0} \right) \quad (4.3)$$

$$\text{Model Code 1990, wet concrete (CEB 1993): } G_f(T) = G_f \left(1.12 - \frac{0.006 \cdot T}{T_0} \right) \quad (4.4)$$

where

$G_f(T)$ is the fracture energy of concrete at temperature T

T is the temperature in $^{\circ}\text{C}$

G_f is the fracture energy of concrete at 20°C

$T_0 = 1^{\circ}\text{C}$

4.2.5 Creep and shrinkage

The total strain in the concrete at a certain load and temperature can be divided in the mechanical strain (due to the load), the creep strain (due to creep effects), the thermal strain (due to the thermal expansion), and the hygral strain (due to a humidity change (shrinkage/swelling)). The creep of concrete increases with increasing temperature (Bažant and Kaplan 1996). Up to 100°C , creep is expected to be caused by the breaking and reformation of bonds in the cement gel. This process is accelerated by the moisture diffusion between micropores of cement gel and the relatively high diffusion through larger (capillary) pores, which occurs when concrete is drying (or wetting). Another effect of temperature on the creep is the acceleration of the hydration (ageing) at moderate elevated temperatures. Above 105°C , the reverse effect takes place, dehydration in a loaded concrete specimen, which probably also accelerates creep. Shrinkage of the concrete also increases with increasing temperature, due to the faster loss of the water in the concrete at elevated temperature.

4.2.6 Young's modulus

The Young's modulus of concrete decreases with increasing temperature, due to the loss of bond in the microstructure of the cement paste (Bažant and Kaplan 1996). At the same time, an apparent decrease of the Young's modulus can be observed due to the increase of creep caused by the temperature increase. Bažant and Kaplan concluded that it was difficult to make a fair comparison between the results of different investigations, due to the fact that the moisture state, the drying of concrete, the initial loading and the heating rate were all affecting the Young's modulus. Figure 4-4 shows the relation between the temperature and the Young's modulus of concrete with different types of aggregates according to Bažant and Kaplan (1996).

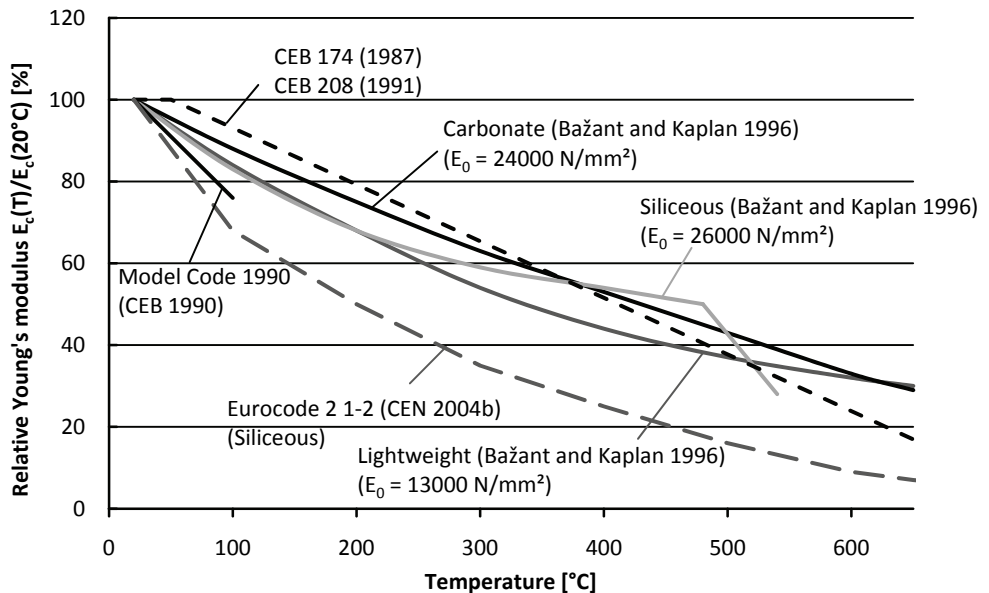


Figure 4-4: Influence of temperature on the Young's modulus of Portland cement concretes

The relations between temperature and Young's modulus according to Eurocode 2 part 1-2 (CEN 2004b), Model Code 1990 (CEB 1993) and CEB Bulletin 174/208 (CEB 1987; CEB 1991) are also shown in Figure 4-4. The Young's modulus according to Eurocode 2 part 1-2 is indirectly calculated from the relation between f_c and ϵ_{c1} (strain at f_c). Eurocode 2 part 1-2 and Model Code 1990 provide the following equations to take the effect of temperature between 20°C and 80°C into account;

Eurocode 2 part 1-2 (CEN 2004b):
$$E_c(T) = E_c \left(1.08 - \frac{0.004 \cdot T}{T_0} \right) \quad (4.5)$$

Model Code 1990 (CEB 1993):
$$E_c(T) = E_c \left(1.06 - \frac{0.003 \cdot T}{T_0} \right) \quad (4.6)$$

where

$E_c(T)$ is the Young's modulus of concrete at the temperature T
 T is the temperature in °C
 E_c is the Young's modulus of concrete at 20°C
 $T_0 = 1^\circ\text{C}$

Especially the temperature-Young's modulus relation according to Eurocode 2 part 1-2 seems to be different compared to the relations that represent the experimental results according to Bažant and Kaplan (1996). This can be explained by the fact that Eurocode 2 part 1-2 indirectly takes the higher creep of concrete at elevated temperature into account, which results in lower values for the Young's modulus (Blontrock 2003).

4.2.7 Coefficient of thermal expansion

The coefficient of thermal expansion of concrete is mainly governed by the type of aggregate that has been used (Table 4-1) (Bažant and Kaplan 1996). It can be seen that the coefficient of thermal expansion is higher for aggregates with a higher weight percentage of silica. The coefficient of thermal expansion can be assumed to be constant up to about 100°C, while at higher temperatures, it will slightly increase with increasing temperature (CEB 1987; CEB 1991).

Table 4-1: Coefficient of thermal expansion of concrete for different aggregates (Bažant and Kaplan 1996)

Aggregate	Typical silica content in the aggregate by weight [%]	Coefficient of thermal expansion [10^{-6} /°C]	
		Range	Average
Chert	94	11.4-12.2 ^[1]	13.2 ^[1]
Quartzite	94	11.7-14.6	12.1
Sandstone	84	9.2-13.3	11.4
Marble	Negligible	4.1-17.4	10.7
Siliceous limestone	45	8.1-11.0	10.7
Granite	66	8.1-10.3	9.6
Dolerite	50	-	9.6
Basalt	51	7.9-10.4	9.3
Limestone	Negligible	4.3-10.3	8.6

[1] Note that the average does not fall in this range. Probably one of the numbers is wrong

4.3 Steel reinforcement

4.3.1 Tensile strength

The tensile strength of steel reinforcement is not significantly affected up to 150°C (Figure 4-5) (FIP 1975; CEB 1978; CEB 1987; CEB 1991; CEN 2004b). At higher temperatures, the effect of temperature on the tensile strength is mainly related to the chemical composition and the mechanical treatments that have been carried out on the steel reinforcement during production (CUR 1994). Reinforcement with a high initial strength at room temperature is more subjected to degradation of the tensile strength at elevated temperature than reinforcement with a low initial strength. The reduced tensile strength is partially recovered after cooling down of the steel reinforcement.

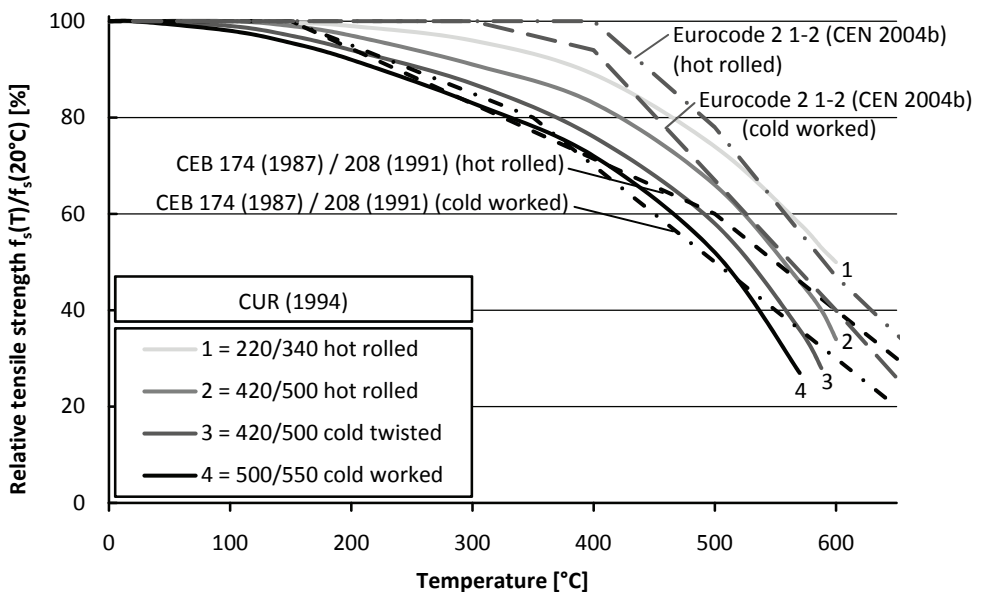


Figure 4-5: Influence of temperature on the tensile strength of steel reinforcement

4.3.2 Young's modulus

For the Young's modulus of the steel reinforcement, a similar tendency as for the tensile strength can be observed (Figure 4-6). It is more or less unaffected up to 150°C, while for higher temperatures an almost linear decreasing Young's modulus is found with increasing temperature (CEB 1978; CEB 1987; CEB 1991; CUR 1994; CEN 2004b).

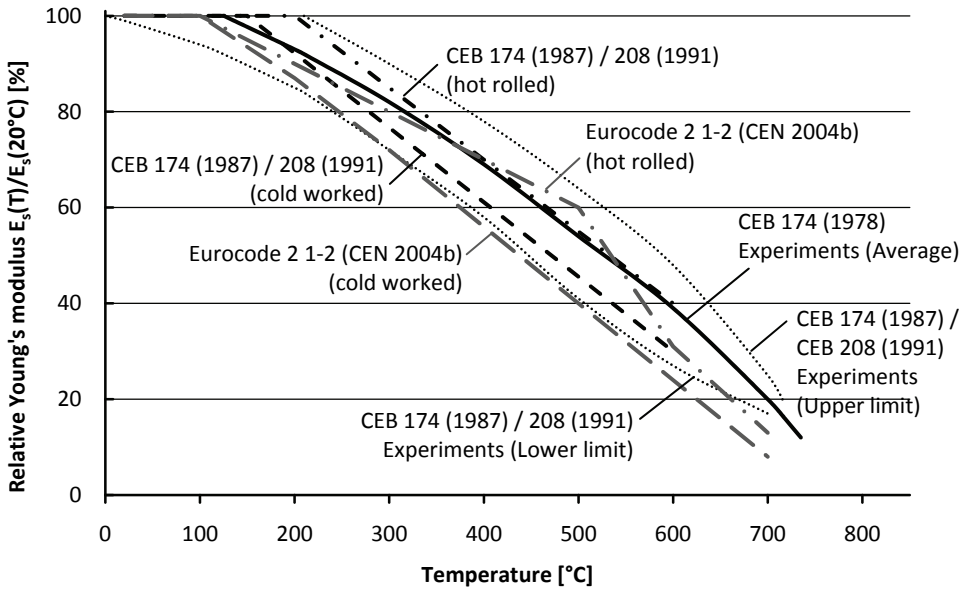


Figure 4-6: Influence of temperature on the Young's modulus of steel reinforcement

4.3.3 Coefficient of thermal expansion

The coefficient of thermal expansion of steel reinforcement ($\alpha_s \approx 8\text{-}12 \cdot 10^{-6} / ^\circ\text{C}$) can be assumed to be equal to the coefficient of thermal expansion of concrete, according to most guidelines (CEB 1978; CEB 1987; CEB 1991; CUR 1994; CEN 2004b). This assumption is valid for ordinary concrete up to about 400°C , although in some occasions a slightly higher coefficient is found for steel reinforcement (CEN 1997a). For temperatures higher than 400°C , the coefficient of thermal expansion of concrete increases faster with increasing temperature than that of steel reinforcement.

4.4 Fiber Reinforced Polymers

4.4.1 General

The available data on the material properties of FRP reinforcement at elevated temperatures is limited. Furthermore, the effect of temperature on the material properties may vary between the various products, as FRP can be composed of several types of fibers (glass, aramid and carbon) and matrix materials (polyester, vinylester, epoxy). Especially the properties of the matrix will change at elevated temperatures, which will affect the material properties of the FRP. In each of the following sections, first the effect of temperature on the material properties of the fibers and matrix materials is discussed, followed by the effect of temperature on the material properties of the composed product, FRP reinforcement.

4.4.2 Tensile strength and Young's modulus

4.4.2.1 Fibers

Blontrock (2003) gathered the available experimental data from different researchers (Figure 4-7). Rehm and Franke (1974) and Sen (1993) both investigated the effect of temperature on the tensile strength of different types of glass fibers, while Rostásy (1992) has investigated the effect of temperature on the tensile strength of glass, aramid and carbon fibers.

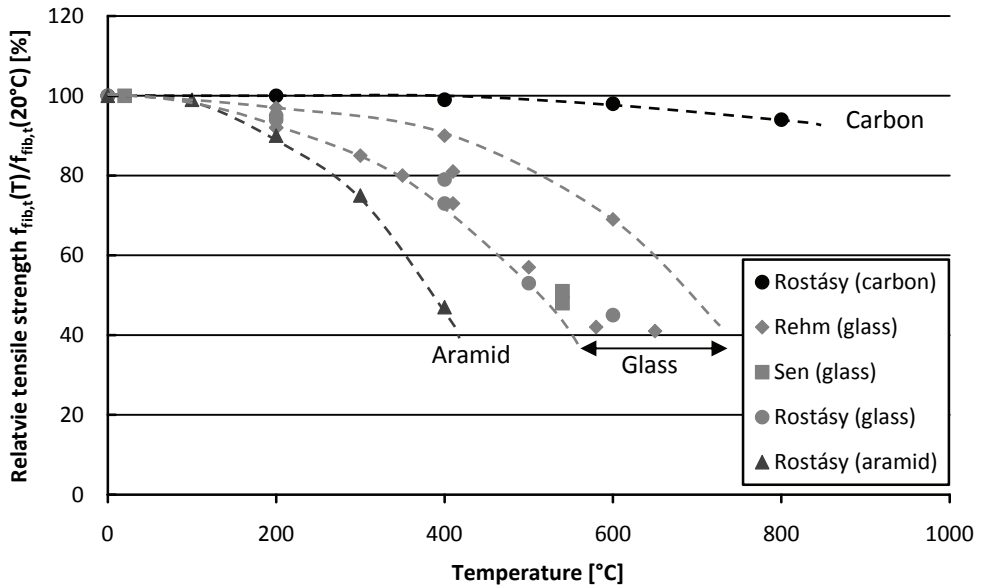


Figure 4-7: Influence of temperature on the tensile strength of different types of fibers (Blontrock 2003)

It can be seen that aramid fibers showed the largest reduction in tensile strength with increasing temperature. The different types of glass fibers showed a similar reduction in tensile strength with increasing temperature compared to each other. The tensile strength of the carbon fibers was more or less unaffected, even up to 800°C.

4.4.2.2 Matrix material

Polymer matrix materials, like epoxy, vinylester and polyester, are thermosetting polymers. The mechanical properties of thermosetting polymers will change from a glass-like material to a more rubber-like material around the glass transition temperature (T_g) (Section 2.2). This change is accompanied with a significant drop in strength and Young's modulus. The glass transition temperature and the corresponding effect of temperature on the material properties is mainly related to the specific composition and the properties of the constituents (Saafi 2002) and is therefore different for each type of matrix material. Even within the group of, for example, epoxies, significant differences can be found in the glass transition temperature (Table 4-2). It is therefore impossible to define the effect of temperature on the matrix material in a general way.

Table 4-2: Mechanical properties of polymer matrix materials (Morgan 2005)

	Young's modulus [N/mm ²]	Tensile strength [N/mm ²]	Ultimate tensile strain [%]	Glass transition temperature [°C]
Polyester	3200 – 3500	60 – 85	2 – 5	100 – 140
Vinylester	3300	70 – 80	5 – 6	210 – 340
Epoxy	2000 – 4000	80 – 150	1 – 8	50 – 260

Figure 4-8 shows the typical effects of temperature on, respectively, the tensile strength (a) and the Young's modulus (b) of (two different) epoxy matrices (Plecnik et al. 1980; Miwa et al. 1998). Both will suddenly drop around the glass transition temperature. Cooling down from a temperature above T_g to a temperature below T_g will reverse the material properties back to the original properties.

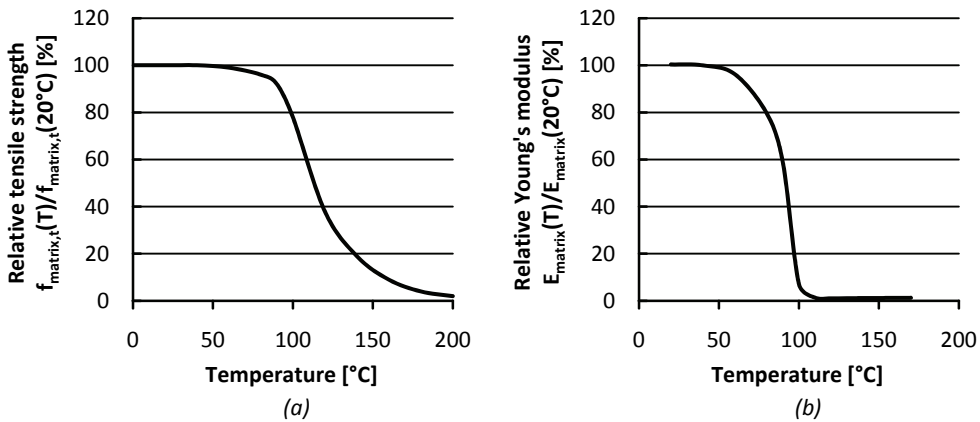


Figure 4-8: Influence of temperature on the tensile strength (Plecnik et al. 1980) (a) and the Young's modulus (Miwa et al. 1998) (b) of epoxy

4.4.2.3 Tensile strength of FRP reinforcement

The effect of temperature on the tensile strength of the composed FRP reinforcement is related to the effect of temperature on the tensile strength of both the matrix material and the fibers and has mainly been investigated for FRP reinforcement bars (rods). Test results for CFRP, GFRP and AFRP are shown in Figure 4-9 till Figure 4-11 (Blontrock 2003).

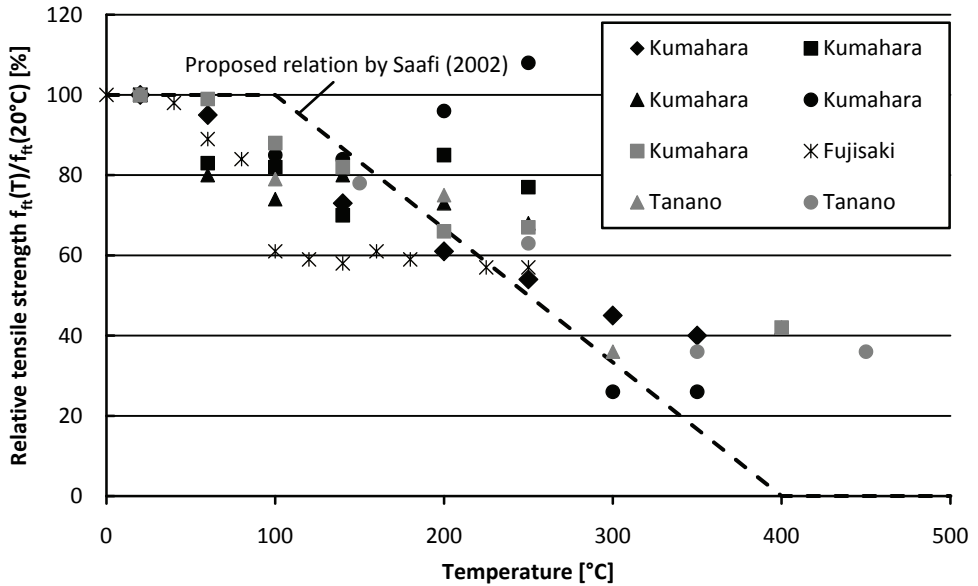


Figure 4-9: Influence of temperature on the tensile strength of Carbon FRP bars (Blontrock 2003)

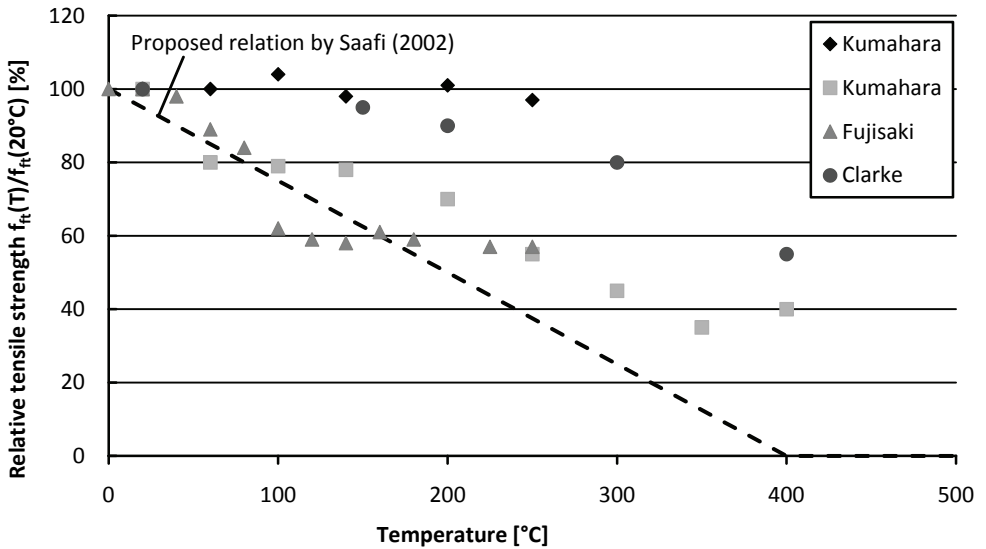


Figure 4-10: Influence of temperature on the tensile strength of Glass FRP bars (Blontrock 2003)

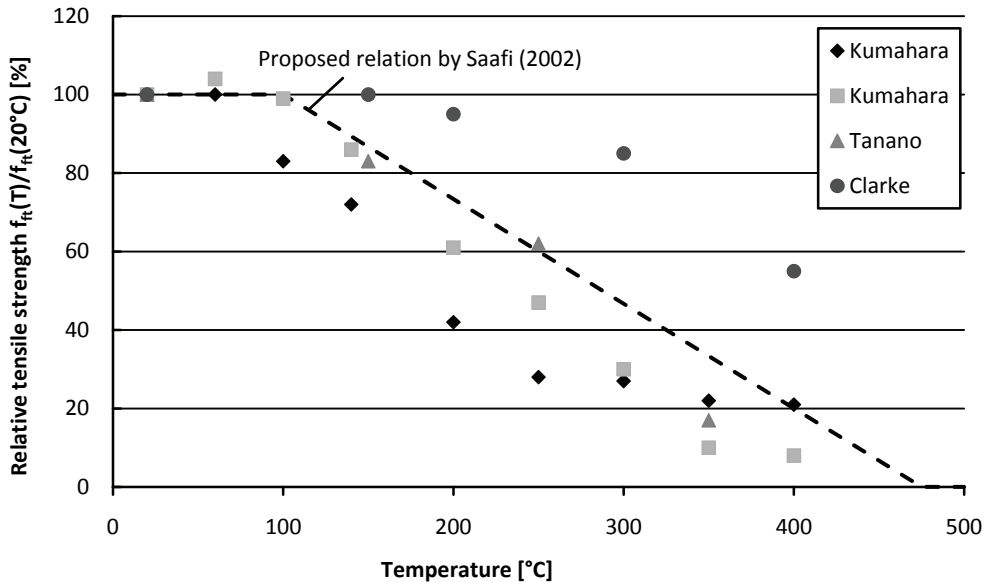


Figure 4-11: Influence of temperature on the tensile strength of Aramid FRP bars (Blontrock 2003)

All types of FRP reinforcement showed a decreasing tensile strength with increasing temperature. The reduction in tensile strength of the FRP reinforcement was more significant compared to the reduction in strength of the fibers alone (Figure 4-7), due to the matrix material that is used to embed the fibers. It can however also be seen that the FRP still has some capacity left at temperatures far beyond the glass transition temperature of the matrix material.

Saafi (2002) proposed a relation between temperature for each type of FRP, as can be seen in Figure 4-9 - Figure 4-11. According to these relations, the tensile strength of CFRP and AFRP is unaffected up to 100°C, while the tensile strength of GFRP starts to decrease immediately, starting from room temperature.

Kumahara (1993) also investigated the effect of temperature on the tensile strength of FRP reinforcement bars with different fiber configurations (straight fibers, braided fibers, bundles of fibers). The tensile strength of FRP reinforcement with straight fibers was more or less unaffected up to 400°C, while the FRPs with other fiber configurations showed a larger reduction and scatter in the tensile strength at elevated temperature.

4.4.2.4 Young's modulus of FRP reinforcement

Saafi (2002) also proposed two relationships between the temperature and the Young's modulus of FRP, one for CFRP (Figure 4-12) and one for GFRP and AFRP together (Figure 4-13). The experimental results for CFRP and AFRP showed a reduction of the Young's modulus with increasing temperatures (Blontrock 2003), although up to 100°C, the Young's modulus of these types of FRP was hardly affected. GFRP even showed an initial increase in Young's modulus, although it should be remarked that the test results are based on only one type of GFRP.

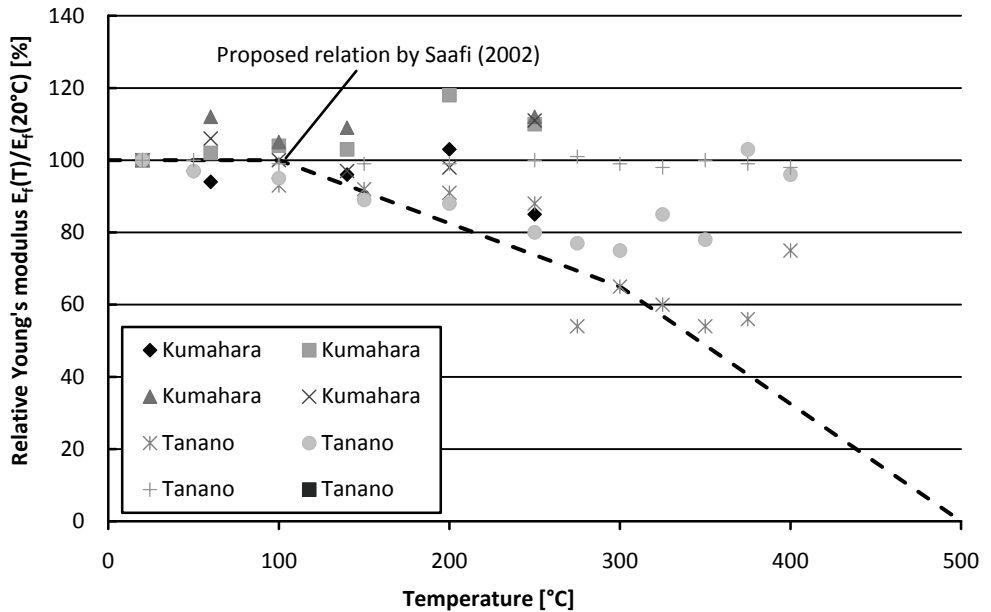


Figure 4-12: Influence of temperature on the Young's modulus of Carbon FRP bars (Blontrock 2003)

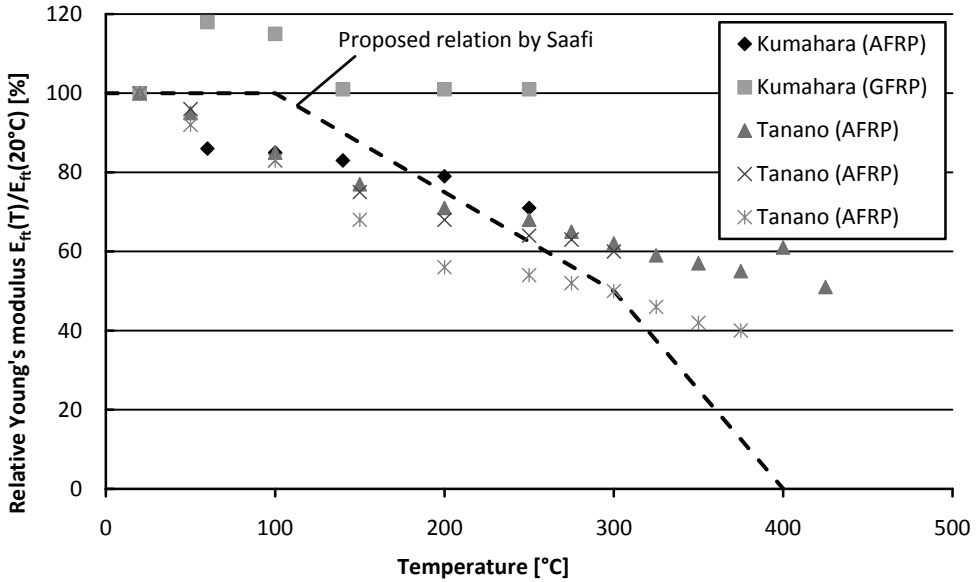


Figure 4-13: Influence of temperature on the Young's modulus of Aramid FRP and Glass FRP bars (Blonrock 2003)

4.4.3 Coefficient of thermal expansion

4.4.3.1 Fibers and matrix material

The coefficient of thermal expansion of FRP highly depends on the composition of the FRP (fibers and matrix), the orientation of the fibers and the fiber content. Table 4-3 shows the coefficient of thermal expansion of commonly used fibers and matrix materials in FRP. It can be seen that carbon and aramid fibers are orthotropic materials, while glass fibers are isotropic, like the matrix materials. Carbon and aramid fibers have a negative value for the coefficient of thermal expansion in longitudinal direction, which means that the fibers shorten with increasing temperature.

Table 4-3: Coefficient of thermal expansion of common fibers and matrix materials (Rostásy 1992; Blonrock 2003; Stormcable 2009)

	$\alpha_{\text{longitudinal}} [\cdot 10^{-6} / ^\circ\text{C}]$	$\alpha_{\text{perpendicular}} [\cdot 10^{-6} / ^\circ\text{C}]$
Carbon fiber	-0.5 - -0.6	5.5 - 10
Glass fiber	4 - 5.5	4 - 5.5
Aramid fiber	-2 - -3.5	60
Epoxy	40 - 120	40 - 120
Polyester	60 - 180	60 - 180

4.4.3.2 FRP reinforcement

The coefficient of thermal expansion of a FRP composite can be determined from the coefficients of the fibers and the matrix material with (Blontrock 2003);

$$\alpha_f = \frac{\alpha_{\text{fib}} \cdot E_{\text{fib}} \cdot V_{\text{fib}} + \alpha_{\text{matrix}} \cdot E_{\text{matrix}} \cdot V_{\text{matrix}}}{E_{\text{fib}} \cdot V_{\text{fib}} + E_{\text{matrix}} \cdot V_{\text{matrix}}} \quad (4.7)$$

where

α_{fib} , α_{matrix} is the coefficient of thermal expansion of respectively the fibers and the matrix
 E_{fib} , E_{matrix} is the Young's modulus of respectively the fibers and the matrix
 V_{fib} , V_{matrix} is the volume fraction of respectively the fibers and the matrix

Table 4-4 shows some typical values of the coefficient of thermal expansion in the longitudinal direction of different FRP materials, all composed with an epoxy adhesive and a fiber volume fraction of 60%.

Table 4-4: Typical values of the coefficient of thermal expansion of FRP materials (Stormcable 2009)

	$\alpha_{\text{longitudinal}} [\cdot 10^{-6} / ^\circ\text{C}]$	$\alpha_{\text{perpendicular}} [\cdot 10^{-6} / ^\circ\text{C}]$
CFRP	-0.5	32
GFRP	6.6	30
AFRP	-4	70

In the Pieter van Musschenbroek Laboratory of Eindhoven University of Technology, the coefficient of thermal expansion has been experimentally determined for CarboDur CFRP laminates (Sika 2005). These laminates are used in the various experiments throughout this research project. The material properties of these CFRP laminates at room temperature are given in Table 4-5, both according to the datasheet of the manufacturer (Sika 2005) and according to the test results.

Table 4-5: Material properties in the fiber direction of CarboDur CFRP laminates

	Tested at +20°C / R.H. 60%	According to datasheet (Sika 2005) at +23°C / R.H. 50%
Tensile strength at failure (f_{ft})	-	> 2,800 N/mm ²
Tensile strength (5% fraction value) ($f_{ft,5\%}$)	-	3,000 N/mm ²
Tensile strength (95% fraction value) ($f_{ft,95\%}$)	-	3,600 N/mm ²
Mean tensile strength (f_{ftm})	3,200 N/mm ² [1]	-
Young's modulus (minimum value) (E_f)	-	> 165,000 N/mm ²
Young's modulus (5% fraction value) ($E_{f,5\%}$)	-	162.000 N/mm ²
Young's modulus (95% fraction value) ($E_{f,95\%}$)	-	180.000 N/mm ²
Mean Young's modulus ($E_{f,m}$)	165,800 N/mm ²	-
Strain at failure (ε_f)	19.3 ‰	> 17 ‰
Density (ρ_f)	1670 kg/m ³	1600 kg/m ³

[1] Tested according to EN-ISO 527 (CEN 1997b)

A testing method called ESPI was used to measure the coefficient of thermal expansion of CFRP. ESPI stands for Electronic Speckle Pattern Interferometry and is a non-destructive optoelectronic technique to measure full-field surface deformations (Spagnolo and Ambrosini 2001). An advantage of this technique is that very small deformations can be measured. The measurement equipment was not affected by the elevated temperature, as it was placed outside the box (with a window) in which the specimen was heated in approximately 45 minutes from room temperature to the elevated temperature.

For measuring the deformation in one direction, two coherent lasers are needed to illuminate the (diffuse) surface of the FRP (Figure 4-14). Consequently, for measuring in two directions, four lasers are needed. A digital (CCD) camera records the scattered wave front from the illuminated area (approximately 50 x 25 mm²) simultaneously with a reference wave front, which can be transformed to a speckle pattern by the help of the interfering properties of electromagnetic waves. The speckle pattern is then converted into a corresponding video signal, which is electronically processed through a so called frame grabber, which converts texture variations of the speckle pattern into brightness variations.

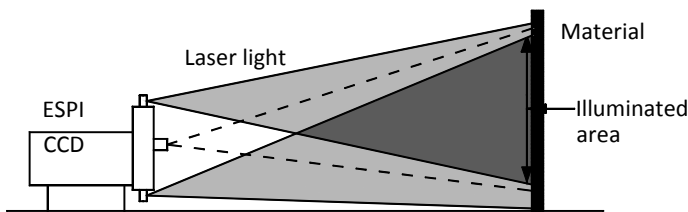


Figure 4-14: Basic principle of ESPI measurements (Spagnolo and Ambrosini 2001)

Finally, a speckle interferogram can be generated by subtracting two digitized speckle patterns. The number of lines over a certain length in an interferogram is a size for the elongation. The interference pattern clearly shows the relatively small elongation in the longitudinal direction (Figure 4-15a) (only a few lines) and the relatively large elongation in the direction perpendicular to the fiber direction (Figure 4-15b) (a large number of lines).

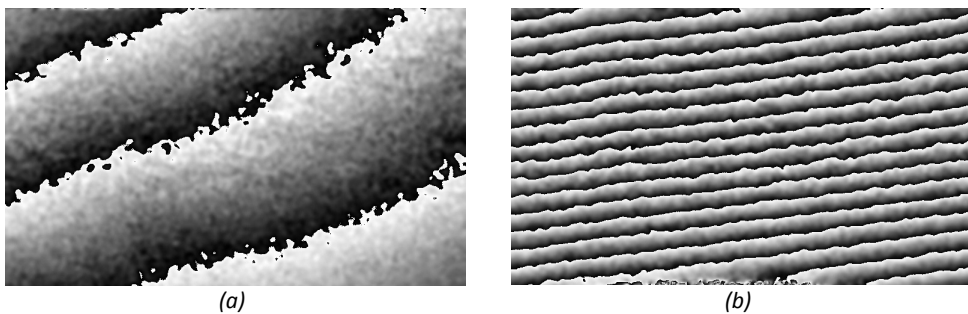


Figure 4-15: Interferogram of the CFRP deformation in fiber direction (a) and direction perpendicular to the fiber direction (b)

From the number of lines in the interferogram, the relative displacements in the CFRP laminate in the two directions can be computed by choosing an arbitrary origin on the surface as a reference (Figure 4-16). The coefficient of thermal expansion can then be determined from the calculated deformations. The coefficient of thermal expansion was determined for two temperature ranges, from 20°C to 40°C and from 20°C to 60°C. No significant differences were found between these two temperature ranges (Table 4-6) and the values correspond quite well to the values as found in literature (Table 4-4).

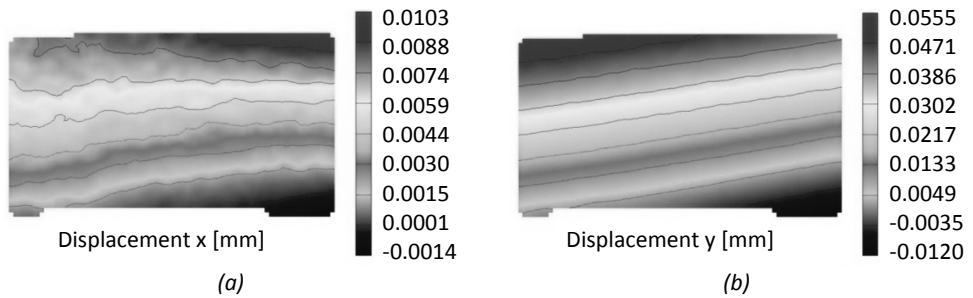


Figure 4-16: Relative displacements from an arbitrary chosen origin in fiber direction (a) and in the direction perpendicular to the fiber direction (b)

Table 4-6: Coefficient of thermal expansion of CarboDur CFRP laminates

	20°C till 40°C	20°C till 60°C
Parallel to the fiber direction ($\alpha_{f, \text{long}}$)	$-1.6 \times 10^{-6} / ^\circ\text{C}$	$-0.3 \times 10^{-6} / ^\circ\text{C}$
Perpendicular to the fiber direction ($\alpha_{f, \text{perp}}$)	$32 \times 10^{-6} / ^\circ\text{C}$	$33 \times 10^{-6} / ^\circ\text{C}$

4.5 Adhesive

4.5.1 General

For adhesives that are used to bond FRP reinforcement to the concrete, similar effects of temperature can be expected as for the matrix materials (Section 4.4.2.2), as these are basically the same materials. Again, each type of adhesive is affected differently by temperature and has a different glass transition temperature. The glass transition temperature of adhesives is however generally lower than for matrix materials (45-80°C for epoxy adhesives).

Epoxy adhesive is the most commonly used adhesive for CFRP strengthening applications. It was decided to investigate the effect of temperature on the material properties of one specific adhesive, SikaDur-30 (Sika 2009). This is a two component epoxy adhesive that is used throughout this research project. The material properties at room temperature are shown in Table 4-7, both according to the manufacturer and according to experimental results.

Table 4-7: Sikadur-30 material properties

	Tested at +20°C / R.H. 60%	According to the manufacturer (Sika 2009) at +23°C / R.H. 50%
Compressive strength (f_{am})	-	± 70 a 95 N/mm^2
Shear strength (f_{asm})	-	± 14 a 19 N/mm^2
Tensile strength (f_{atm})	-	± 24 a 31 N/mm^2
Flexural tensile strength ($f_{atm,fl}$)	48.5 N/mm^2 ^[1]	-
E-modulus (E_a)	$12,700 \text{ N/mm}^2$ ^[2]	$12,800 \text{ N/mm}^2$
Density (ρ_a)	1770 kg/m^3	1650 kg/m^3
Shrinkage	-	0.04 %
Glass transition temperature (T_g)	-	> 62°C

[1] According to EN 196-1 (CEN 1994), [2] According to EN 13412 (CEN 2002)

4.5.2 Flexural strength

The effect of temperature on the tensile strength of the adhesive was investigated with flexural tests according to EN 196-1 (CEN 1994). EN 196-1 was originally developed for the determination of the (flexural) strength of cement, but it can also be used for epoxy adhesives. Prisms ($40 \times 40 \times 160 \text{ mm}^3$) were tested in a three-point bending test with a span of 150 mm. The specimens were heated in an oven for approximately 1 hour. After heating, the specimens were packed in an insulation material and loaded in the testing machine outside the oven within 3 minutes after being taken out of the oven. Temperature was measured at the surface of the specimen and only changed with a maximum of 5°C after being taken out of the oven. The tests were performed at several temperatures in the range from -20°C up to 80°C (Figure 4-17) and took approximately 5 minutes per test. It turned out that increasing the temperature resulted in a decreasing tensile strength, as expected. At 80°C, only 20% of the initial strength was left. Decreasing the temperature to -20°C did not seem to affect the tensile strength.

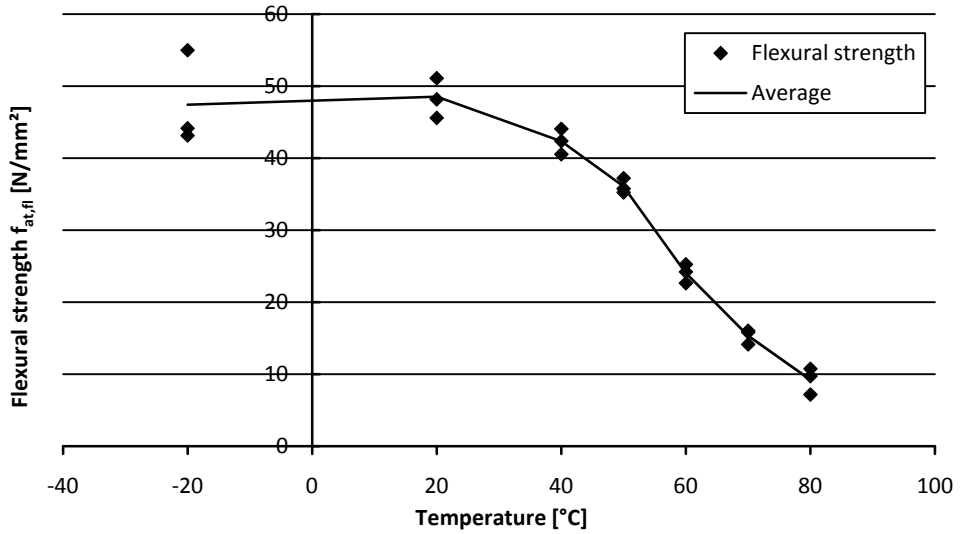


Figure 4-17: Influence of temperature on the flexural strength of SikaDur-30

4.5.3 Young's modulus

The Young's modulus of the adhesive was also expected to be temperature related and therefore determined experimentally according to EN 13412 (CEN 2002). Epoxy prisms ($40 \times 40 \times 160 \text{ mm}^3$) were loaded in compression at several temperatures in the range from 20°C to 80°C (Figure 4-18). The Young's modulus was determined between the load levels F_1 and F_2 , where F_1 is the load at a strain of $\epsilon_a = 0.002$ and F_2 is 10% of F_1 .

The effect of an initial heating cycle was also investigated. Three tests per temperature were performed on prisms that were stored at 20°C and 60% R.H. for 14 days and which were then heated up to the test temperature in 1 hour and subsequently tested. Three other prisms per temperature were stored at 20°C and 60% R.H. for 10 days, then stored at 80°C for 2 days, and subsequently stored at 20°C for another 2 days. These prisms were then heated up to the desired test temperature in 1 hour and tested at the elevated temperature. All specimens were packed with insulation material after heating in the oven and loaded in the testing machine within 3 minutes after being taken out of the oven. Figure 4-18 shows the relation between the temperature and the Young's modulus of the adhesive for both types of tests.

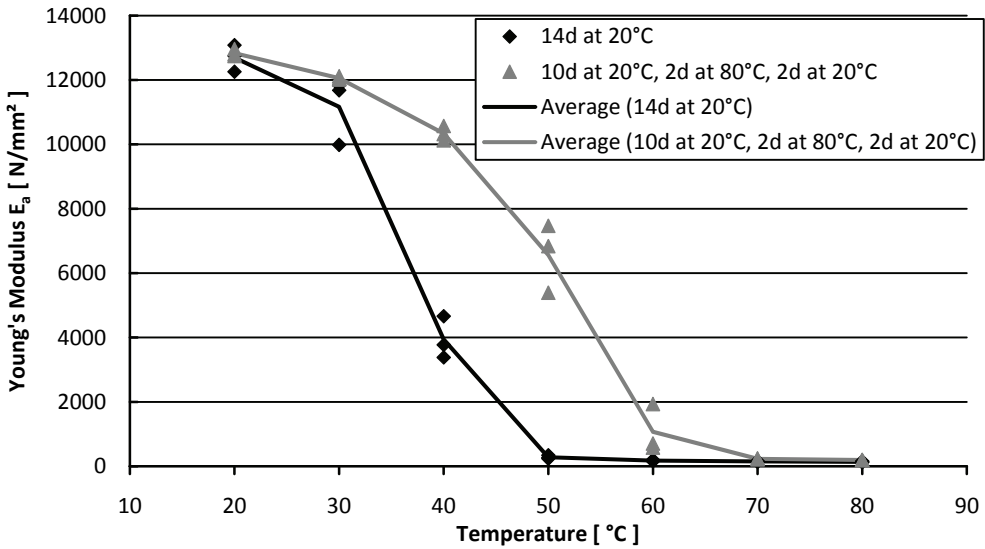


Figure 4-18: Influence of temperature on the Young's modulus of SikaDur-30

It can be seen that the Young's modulus was significantly reduced at elevated temperatures. It can also be seen that the reduction of the Young's modulus occurred at a higher temperature for the prisms that were stored at 80°C for two days prior to testing. Heating the specimens for two days at 80°C, did however not affect the Young's modulus at room temperature. This seems to suggest that the glass transition temperature (T_g) can be increased by applying a temperature cycle. This effect was also found by Leone et al. (2006), who showed that the glass transition temperature was increased from 62°C to 81°C by applying one heating cycle from -50°C to 200°C before determining the glass transition temperature.

4.5.4 Glass transition temperature

As shown in the previous two sections, the material properties of a thermosetting polymer become more rubber-like above the glass transition temperature, with a sudden drop in strength and Young's modulus. This change in material behavior is related to a change in the behavior of the atoms in the material, which get more degrees of freedom above the glass transition temperature. Cooling down from a temperature above T_g to a temperature below T_g will reverse the change in mechanical properties back to the original properties. The glass transition temperature of adhesives is generally lower than that of the matrix materials. For most commonly used epoxy adhesives for FRP strengthening applications, the glass transition temperature is ranging from 45°C till 80°C (fib 2001), although adhesives with higher glass transition temperatures are available.

The glass transition temperature of SikaDur-30 was not explicitly tested in this investigation, as it has been determined by other researchers. In Figure 4-17, it can be seen that the glass transition temperature is approximately 60°C, as the strength suddenly drops around this temperature. Values of 56°C (Ambtliche Materialprüfanstalt für das Bauwesen 1994) and 62°C (Sika 2009) (determined by Fédération Internationale de la Précontrainte) have been reported in literature for T_g . The specimens of the last investigation were cured for 7 days at 45°C, which could explain the higher T_g . Unfortunately, the curing time and temperature of the first investigation are not known to the author. Throughout this research project, the glass transition temperature of SikaDur-30 will be taken equal to 62°C, as given by the manufacturer.

4.5.5 Coefficient of thermal expansion

The coefficient of thermal expansion was experimentally determined with two different techniques. Firstly, according to EN 1770 (CEN 1998), by measuring the difference in length of $40 \times 40 \times 160 \text{ mm}^3$ prisms between -20°C and 40°C. The coefficient of thermal expansion that was determined in this way was equal to $26 \times 10^{-6} / ^\circ\text{C}$, which is almost equal to the value as given by the manufacturer ($25 \times 10^{-6} / ^\circ\text{C}$) (Sika 2009).

It was decided to determine the coefficient of thermal expansion with the same technique as has been used for CFRP laminates, Electronic Speckle Pattern Interferometry (ESPI) (Figure 4-19 and Figure 4-20).

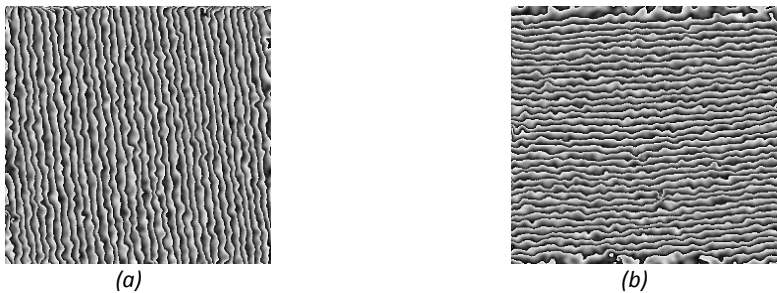


Figure 4-19: Speckle interferogram of the horizontal (a) and vertical (b) deformation of the adhesive

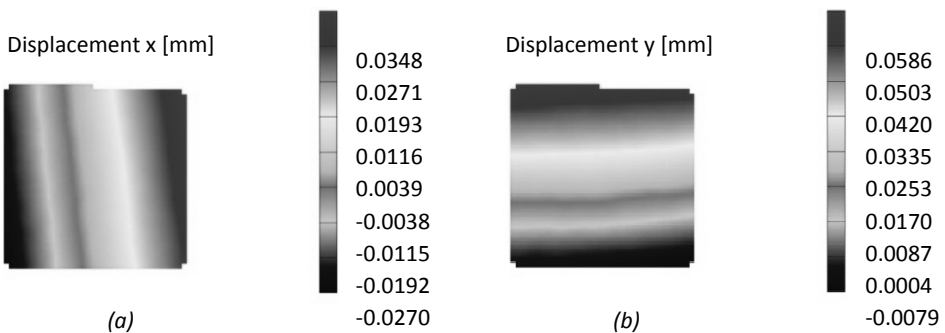


Figure 4-20: Displacements of the adhesive from an arbitrary chosen origin in the horizontal (a) and vertical (b) direction

The specimens were again placed in a box with a window, while the measurement equipment was placed outside the box. The coefficient of thermal expansion was measured on a surface of 40 x 40 mm². Temperature was increased from room temperature to elevated temperature in approximately 1.5 hours and was first measured for the range from 20°C till 40°C. It turned out that the coefficient of thermal expansion was almost similar to the coefficient of thermal expansion according to EN 1770, 29×10^{-6} /°C. The coefficient of thermal expansion was also determined for the temperature range from 20°C till 60°C. Between these two temperatures, a higher coefficient of thermal expansion was found, 45×10^{-6} /°C, probably due to the changing material properties of the adhesive at temperatures near the glass transition temperature.

4.6 Summary

In this chapter, an overview of the effect of temperature on the different material properties of concrete, internal steel reinforcement, FRP and adhesive has been given. It has been shown that, within the ambient temperature range from -20°C till 80°C, the material properties of concrete and steel reinforcement are not significantly affected. The effect of temperature on the material properties of the FRP reinforcement is also relatively small in this temperature range, as the glass transition temperature of the matrix material is generally above 100°C (Table 4-2).

More important for the behavior of a FRP strengthened structure in this temperature range is the effect of temperature on the material properties of the adhesive. Polymer adhesives show a significant reduction in tensile strength and Young's modulus around the glass transition temperature, which is likely to affect the bond behavior between FRP and concrete (Chapter 5). The glass transition temperature of most commonly used epoxy adhesives for FRP strengthening applications is somewhere in between 45°C and 80°C. Another important aspect is the significant difference in the coefficient of thermal expansion between concrete and CFRP, as has also been discussed in Section 2.2. This difference will induce thermal stresses in the concrete-adhesive-FRP joint, which could affect the behavior of the FRP strengthened structure.

5 Effect of temperature on the bond behavior

5.1 Introduction

Temperature does not only affect the individual material properties (Chapter 4), but also the bond properties between the different materials in the concrete-adhesive-FRP joint. Three different modes can be distinguished to describe bond failure (fracture) of this joint (Figure 5-1).

Mode I is the bond fracture in the direction perpendicular to the bonded area. Mode II is the shear fracture in the longitudinal direction of the joint, while mode III is the shear fracture perpendicular to the longitudinal direction. In FRP strengthened structures, the concrete-adhesive-FRP joint is mainly loaded in the longitudinal shear direction (mode II), although stresses perpendicular to the bonded area (mode I) also occur, e.g. due to the unevenness of the concrete surface (Section 2.4.3.6), at the tip of a shear crack (Section 2.4.3.3) and/or at the plate-end (Section 2.4.3.5). Mode III bond fracture is, in general, not relevant for FRP strengthened structures.

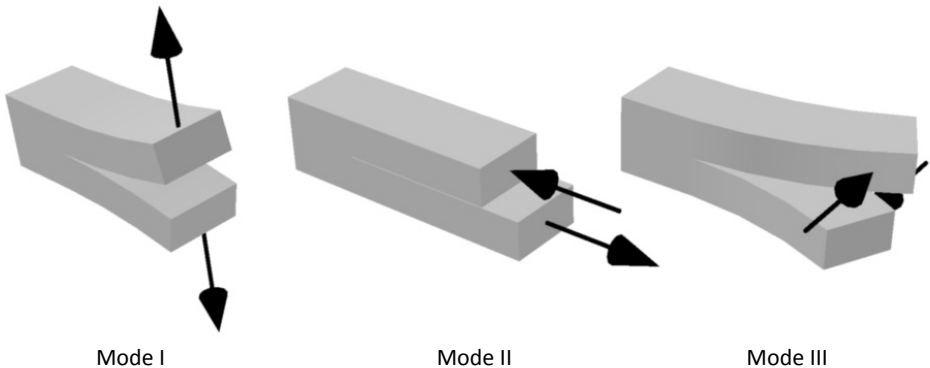


Figure 5-1: Different fracture modes that can be distinguished

Both mode I (Section 5.2) and mode II bond fracture are experimentally investigated in this research project. Mode II bond fracture was investigated with two types of test setups, the double-lap shear test (Section 5.3) and the three-point bending test (Section 5.4).

5.2 Mode I bond fracture

5.2.1 General

Mode I bond fracture of a concrete-adhesive-FRP joint can occur in one of the materials (cohesive failure) or in one of the two interfaces (interfacial failure), as described in Section 2.4. A concrete-adhesive-FRP joint is actually composed of two joints, the concrete-adhesive joint (Section 5.2.2) and the adhesive-FRP joint (Section 5.2.3). The bond behavior of each of these joints is likely to be affected by temperature, as the properties of the materials and interfaces can change with changing temperatures. Both joints will be investigated individually.

5.2.2 Concrete-adhesive joint

The mode I bond strength of the concrete-adhesive joint was determined according to CUR Recommendation 20 (CUR 1990), by gluing steel cylinders $\varnothing 50$ mm to a sand-blasted concrete surface of a concrete cube (formworked side) ($150 \times 150 \times 150 \text{ mm}^3$) and pulling them off with a hydraulic jack (Figure 5-2). The steel cylinders were glued to the concrete with a ± 1.5 mm thick epoxy adhesive (Sikadur-30) (see Section 4.5 for the material properties), after curing of the concrete for at least 28 days (at 20°C and 60% R.H.).

The tests were carried out after storing the specimens for another 14 days under the same conditions. The bond strength was determined at several temperatures in the range from -20°C up to 80°C , for two different concrete grades with a mean cubic compressive strength of 41.1 N/mm^2 and 70.8 N/mm^2 respectively. The other concrete material properties are given in Appendix B.1.

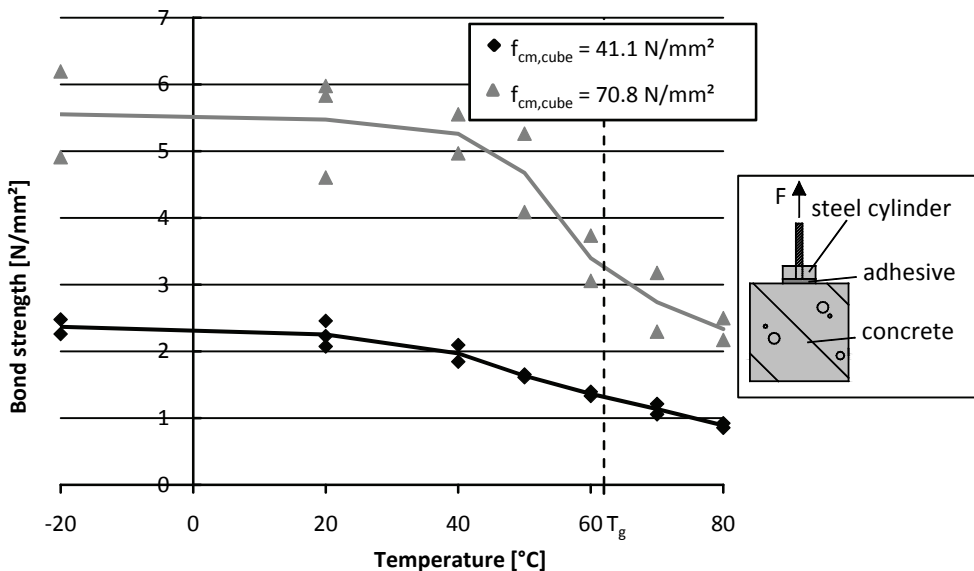


Figure 5-2: Measured bond strength of the concrete-adhesive joint as function of temperature

The specimens were heated or cooled in approximately 3 hours and tested within 3 minutes after being taken out of the oven. The bond strength of the higher strength concrete was about twice as high compared to that of the lower strength concrete. For both concrete grades, starting from room temperature, bond strength decreased with an increase in temperature, especially between 50°C and 60°C. For temperatures up to 50°C, failure occurred in the concrete, leaving a small layer of concrete attached to the adhesive (cohesive failure) (Figure 5-3a). At higher temperatures, failure occurred exactly in between the concrete and the adhesive (interfacial failure), without leaving any concrete attached to the adhesive (Figure 5-3b).

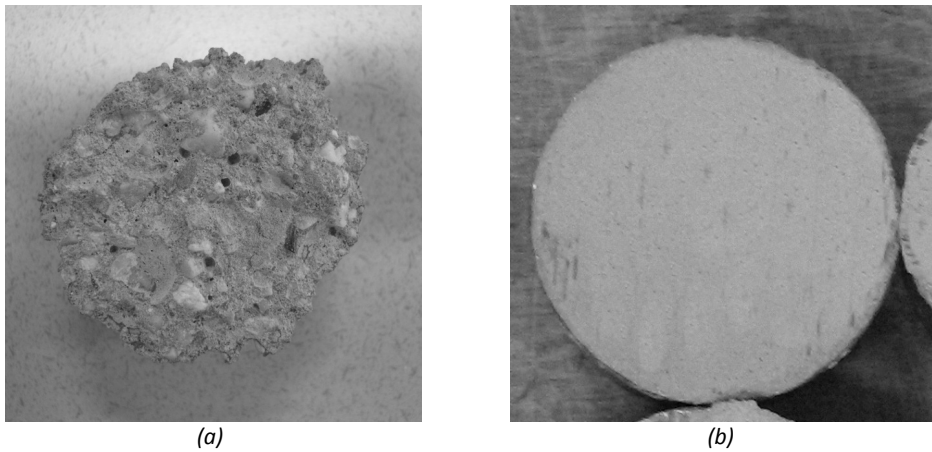


Figure 5-3: Typical failure pattern of the concrete surface for $T \leq 50^\circ\text{C}$ (a) and of the concrete-adhesive interface for $T \geq 60^\circ\text{C}$ (b)

Additional tests were carried out to investigate the effect of an initial heat cycle on the bond strength at 20°C ($f_{\text{cm,cube}} = 41.1 \text{ N/mm}^2$). Four bond tests were carried out after curing of the adhesive at 20°C and 60% R.H. for 14 days, while four other tests were carried out after curing of the adhesive under the same conditions for 13 days, subsequently at 50°C for 8 hours and finally at 20°C again for 16 hours. It turned out that the heat cycle did not affect the bond strength at room temperature. In both cases, the mean bond strength was 2.3 N/mm².

5.2.3 Adhesive-CFRP joint

The mode I bond strength of the adhesive-CFRP joint was investigated in a similar way as for the concrete-adhesive joint. A CFRP laminate (Sika CarboDur) was first bonded to a concrete surface, to avoid bending of the thin CFRP laminate during testing. Subsequently, a steel cylinder $\varnothing 50 \text{ mm}$ was glued to the CFRP laminate and cured for 14 days at 20°C and 60% R.H.. The specimens were then heated or cooled down in approximately 3 hours to the required test temperature, which was in the range from -20°C up to 80°C. The specimens were tested within 3 minutes after being taken out of the oven. The results of the bond tests are shown in Figure 5-4.

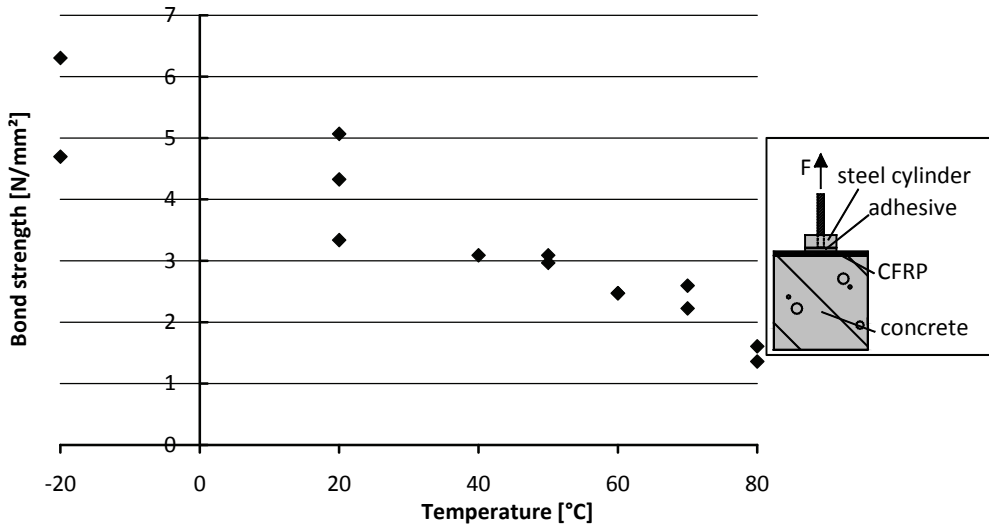
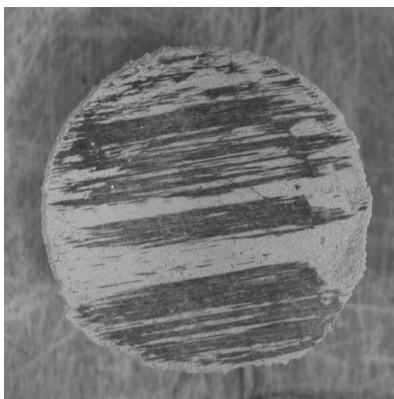
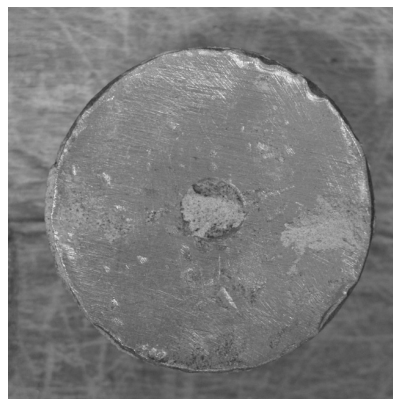


Figure 5-4: Relation between temperature and the bond strength of the adhesive-CFRP interface

The test results showed an almost linear decreasing bond strength with increasing temperature. Two types of failure were observed in the tests. At moderate temperatures, up to 50°C, failure occurred in the adhesive-CFRP interface (Figure 5-5a). A thin layer of fibers remained attached to some parts of the adhesive surface. At higher temperatures, failure occurred in the adhesive-steel interface (Figure 5-5b). The higher the temperature, the less adhesive remained attached to the steel cylinder. It may be obvious that the latter failure pattern (bond failure in the adhesive-steel interface) is not relevant for this investigation, apart from the fact that it can be stated that the bond strength of the adhesive-CFRP interface was higher than the bond strength of the adhesive-steel interface.



(a)



(b)

Figure 5-5: Typical failure pattern of the adhesive-CFRP interface for $T \leq 50^\circ\text{C}$ (a) and the steel-adhesive interface for $T \geq 60^\circ\text{C}$ (b)

Again, additional tests were carried out to investigate the effect of an initial heat cycle on the bond strength of the adhesive-CFRP interface at 20°C in the same way as for the concrete-adhesive interface. A mean bond strength (f_{cbm}) of 3.4 N/mm² was found for these specimens, which is lower than the mean bond strength of the specimens that were tested at 20°C without an initial heat cycle ($f_{cbm} = 4.2$ N/mm²).

5.3 Mode II bond fracture – Double-lap shear test

5.3.1 Test setup

The most widely used bond tests to investigate the bond behavior of a concrete-adhesive-FRP joint in the longitudinal shear direction (mode II) are the single- and double-lap shear test (Niu and Wu 2004). The double-lap shear test (Figure 5-6) is generally preferred over the single-lap shear test, due to symmetry of the specimen. The influence of temperature on the bond behavior in shear was investigated with the same lower and higher strength concrete as was used for the mode I fracture tests ($f_{cm,cube} = 41.1$ N/mm² and 70.8 N/mm²) (Appendix B.1).

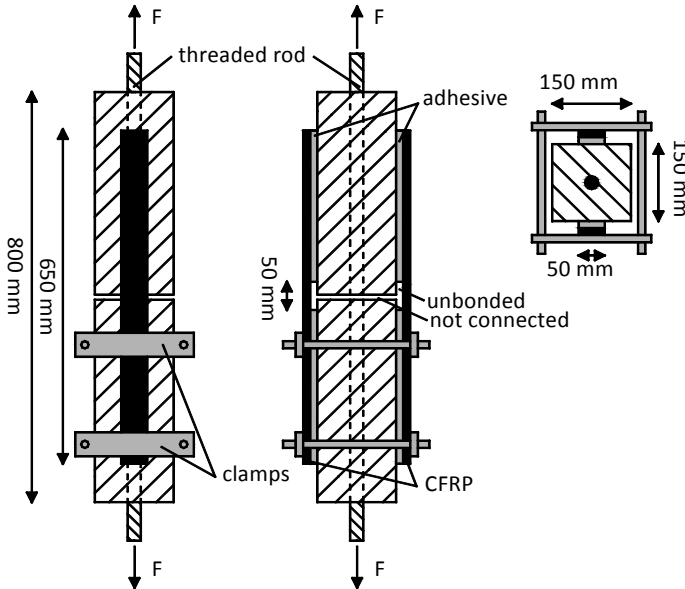


Figure 5-6: Double-lap shear test setup

Twelve specimens (150×150×800 mm³) of each concrete grade were casted with a steel threaded rod in the center (M20 for the lower and M24 for the higher strength concrete specimens) (Figure 5-6). The threaded rod of 1 meter length was applied to transfer the load from the tensile test machine to the specimen. The specimens, including the rod, were cut in two parts after curing of the concrete for at least 21 days at 60% R.H..

After sandblasting of the concrete surface, two CFRP laminates (Sika CarboDur S512) of $50 \times 1.2 \text{ mm}^2$ and a length of 650 mm were glued to two opposite (formworked) concrete surfaces with an epoxy adhesive (Sikadur-30) (thickness $t_a \approx 1.5 \text{ mm}$). The material properties of the CFRP and adhesive were given in Section 4.4 and 4.5 respectively. At each side of the saw cut, 25 mm was kept unbonded to prevent local stress concentrations near the saw cut.

Ten specimens were equipped with five strain gauges (measuring length 6 mm and 10 mm) on each CFRP laminate at 20 mm, 150 mm, 200 mm, 240 mm and 280 mm from the plate-end (Figure 5-7). Four specimens were also equipped with strain gauges on a concrete surface where no CFRP was applied and on the concrete surface right under the adhesive layer (measuring length 30 mm). The strain gauges at these three locations (on CFRP, on concrete and under the adhesive) were applied in the same cross-sections of the specimen. The strain gauges under the adhesive layer were applied after sandblasting of the concrete surface and before applying the epoxy adhesive. The properties of the strain gauges and the effect of temperature on them are given in Appendix B.2. Two LVDTs, placed symmetrically to the center of the cross-section of the specimen, were applied to measure the displacement between the two concrete parts during loading.

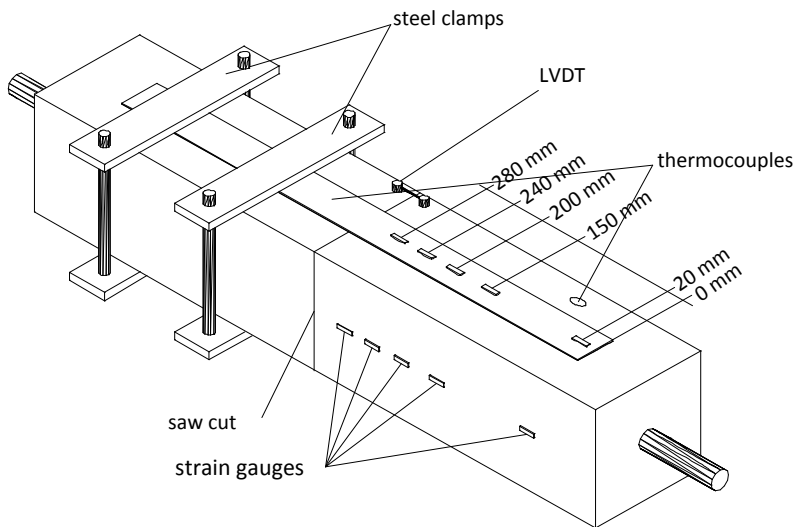


Figure 5-7: Measurement equipment on the double-lap shear test specimen

The specimens were heated in an oven or cooled down in a freezer for approximately 16 hours and subsequently tested within 15 minutes. Steel clamps were applied at one part of the specimen, to make sure that debonding failure initiated in the other part (Figure 5-8a). In this way, strain gauges only had to be applied on one part. All specimens that were tested at low or elevated temperature were packed with insulation during testing (Figure 5-8b). The temperature of the concrete surface and the adhesive was measured with thermocouples (Figure 5-7) and was, within a range of 3°C , constant during the test.

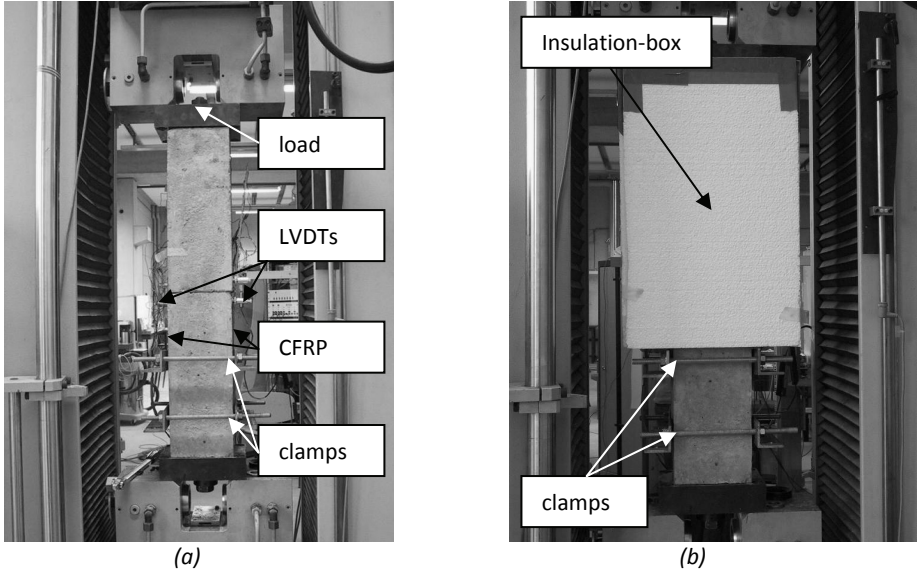


Figure 5-8: Double-lap shear test setup at room temperature (a) and at low and elevated temperature (b)

5.3.2 Failure load as function of temperature

The specimens were loaded (displacement controlled) in a 250 kN tensile testing machine. The measured failure loads as function of the applied temperature are shown in Figure 5-9 for both concrete grades. The load-displacement curves are plotted in Appendix B.3 and in Section 6.4.3, for the comparison with the results of the finite element analyses.

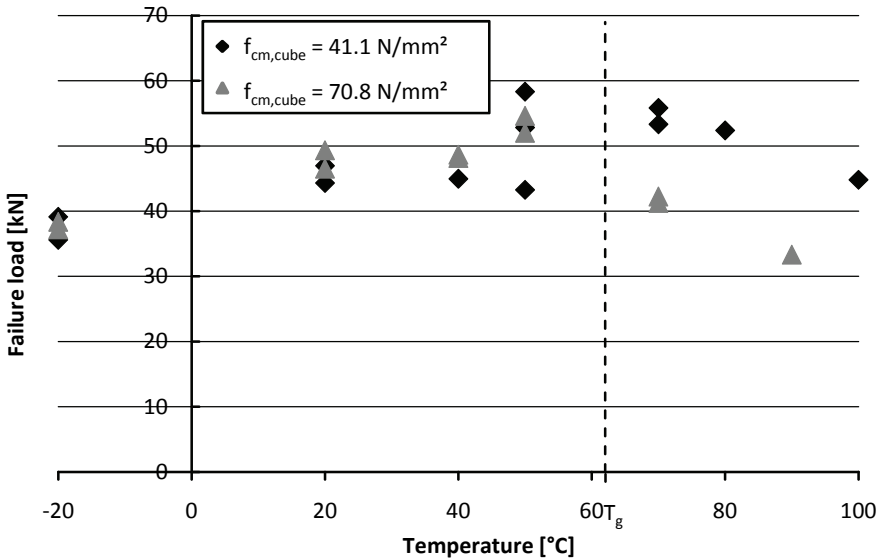


Figure 5-9: Failure load of the double-lap shear tests as function of temperature

At 20°C, there was no significant difference in failure load between the two concrete grades, which was not expected, given the difference in concrete properties. No clear explanation can be given for this behavior. For temperatures up to the glass transition temperature of the adhesive ($T_g = 62^\circ\text{C}$), the tendency turned out to be an increasing failure load with increasing temperature, while for higher temperatures, a decreasing failure load with increasing temperature was found.

It is expected that the decreasing failure load was caused by the changed type of bond failure above 50°C, as will be discussed in the next section, and the corresponding decreasing bond strength of the concrete-adhesive interface with increasing temperature (Section 5.2). The tendency of an increasing failure load with increasing temperatures up to T_g could have been related to the reduced Young's modulus of the adhesive and/or the difference in coefficient of thermal expansion between concrete and CFRP. These effects will be further discussed in Section 5.3.4 and 5.3.5.

5.3.3 Type of failure

The specimens that were tested at temperatures from -20°C up to +50°C failed in an explosive way by failure in the concrete adjacent to the interface with the adhesive, leaving a small layer of concrete attached to the adhesive (Figure 5-10a). The specimens that were tested at temperatures of 70°C and higher failed exactly in the interface in between the concrete and adhesive, without leaving any concrete attached to the adhesive (Figure 5-10b). This relation between the temperature and the type of failure is similar to what was found for the mode I fracture tests of the concrete-adhesive joint. The temperature, at which the type of failure changes, is also roughly the same in both types of tests.

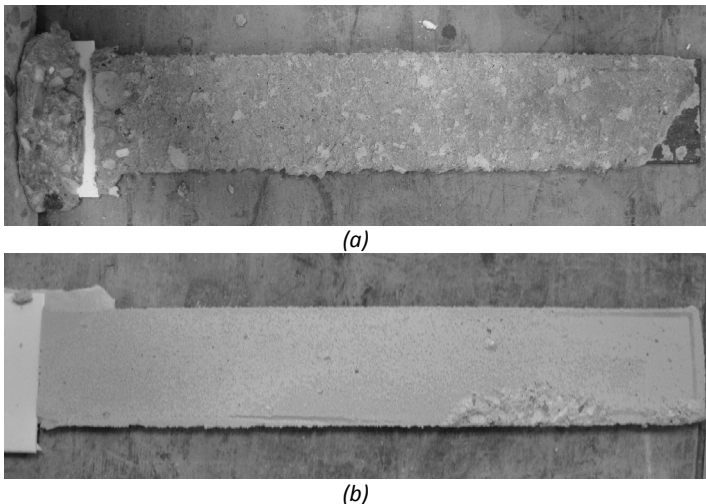


Figure 5-10: Failure in the concrete at 20°C (a) and in the adhesive at 70°C (b)

5.3.4 Thermal strain development

Four specimens were used to investigate the development of strains in the specimens during heating. Two specimens were heated in an oven up to 50°C, then cooled down to room temperature and heated up again to 50°C. The development of (thermal) strains in time in the CFRP laminate (a), the concrete-adhesive interface (b) and the concrete (c) is shown in Figure 5-11 for the lower strength concrete specimen. The strain in Figure 5-11 corresponds to the strain in the middle of the bonded length, at 150 mm from the plate-end. For the higher strength concrete specimen similar results were found (Appendix B.4.1). The strain measurements had to be corrected to be able to measure the correct thermal strains. The strain measurements were calibrated in such way that the strain in point c corresponded to the thermal expansion of concrete ($10.2 \cdot 10^{-6} / ^\circ\text{C}$ and $11.3 \cdot 10^{-6} / ^\circ\text{C}$ for the lower and higher strength concrete respectively).

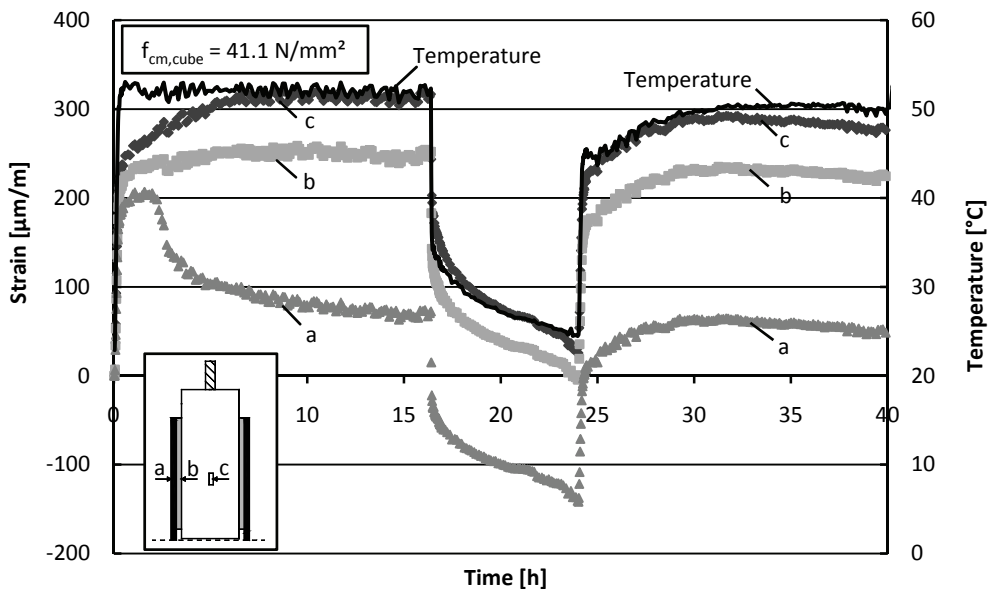


Figure 5-11: Strain development in the CFRP (a), concrete-adhesive interface (b) and concrete (c) due to heating and cooling down of a double-lap shear test specimen

The highest strains developed at the concrete surface that was not strengthened with the CFRP laminate (c). The strains in the concrete-adhesive interface (b) were slightly lower due to the fact that the CFRP laminate gives resistance to the thermal expansion of the concrete, due to its significant lower coefficient of thermal expansion. The strain in the CFRP laminate (a) initially followed to a large extent the expansion of the concrete, but, after about 1.5 h, started to decrease in time, while the temperature stayed constant. It is expected that this was caused by time dependent behavior of the adhesive (creep), which becomes more significant at elevated temperatures.

Thermal strains in the concrete and concrete-adhesive interface disappeared after cooling the specimen down to room temperature again. The CFRP laminate followed the shrinking of the concrete, which resulted in a negative residual strain after cooling down. This strain did not disappear in time, as was seen at elevated temperatures, probably because the adhesive regained its original material properties, including a high Young's modulus and low time dependent creep behavior. Heating the specimen up again till 50°C resulted in similar strains as just before cooling down.

Two other specimens, one of each concrete grade, were heated up in three steps, first to 40°C, then to 50°C and finally up to 70°C. The strain development during heating in the oven is shown in Figure 5-12 for the lower strength concrete specimen. Similar results were found for the higher strength concrete specimen (Appendix B.4.2). It can be seen that the CFRP strain did not decrease significantly in time at 40°C, after initially having followed the expansion of the concrete to a certain extent ($\pm 60\%$), while at 50°C and 70°C, it did decrease in time.

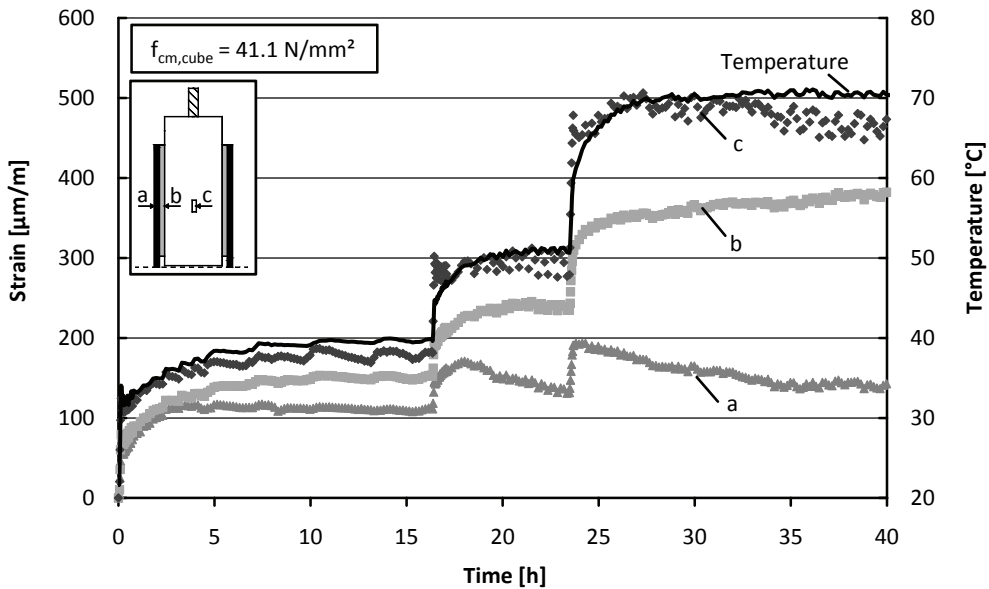


Figure 5-12: Strain development due to heating of the double-lap shear test specimen up to 40°C, 50°C and 70°C

Based on the strain measurements, it can be concluded that the strain in the CFRP laminate to a large extent follows the expansion of the concrete. The strain in the CFRP laminates does however decrease in time, due to the time dependent creep behavior of the adhesive. This behavior starts to become significant at 50°C and higher and results in residual stresses in the CFRP laminate after cooling down the specimens back to room temperature.

5.3.5 Strain development during loading

The strain distribution in the CFRP laminate due to loading of the specimens is shown in Figure 5-13 for the lower and higher strength concrete specimen at 20°C. The strain at 300 mm from the plate-end corresponds to the strain in the non-bonded part, which is not measured, but calculated from the applied load by;

$$\varepsilon_f = \frac{F_{\text{ext}}}{2 \cdot t_f \cdot b_f \cdot E_f} \quad (5.1)$$

where

- F_{ext} is the applied load
- t_f is the thickness of the CFRP laminate
- b_f is the width of the CFRP laminate
- E_f is the Young's modulus of CFRP

The strain measurements were connected with straight lines to visualize the tendency of the strain distribution. It should however be realized that the actual strain distribution is not necessarily linear distributed between two points.

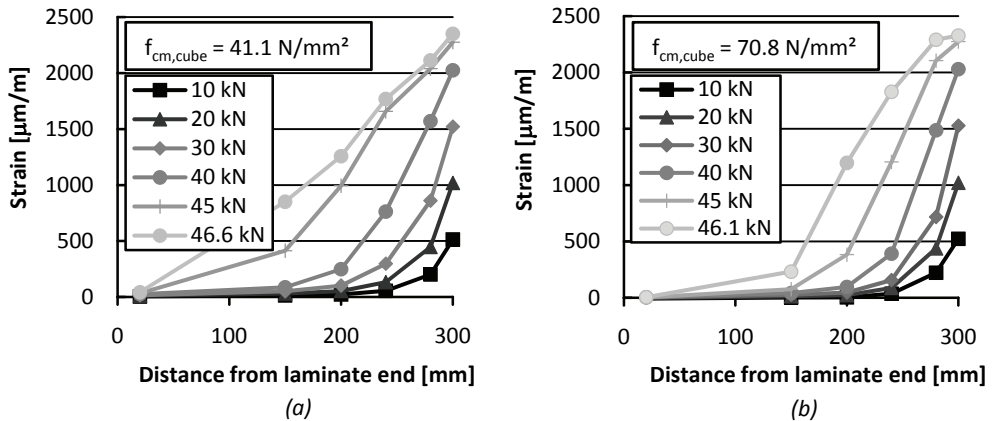


Figure 5-13: CFRP strain distribution at 20°C for the lower (a) and higher (b) strength concrete specimen at 20°C

At low load levels, the highest strains were concentrated in the first approximately 100 mm, measured from the end of the bonded length closest to the middle of the specimen (= 300 mm from the plate-end). This means that the CFRP force is mainly transferred to the concrete in this area, which implies that the shear (and normal) stresses in the concrete adjacent to the concrete-adhesive interface are concentrated in this area. Only just before reaching the failure load, strains start to increase in the rest of the laminate. At the failure load, debonding occurs in a very explosive way, which made it difficult to record the strain distribution exactly at the maximum load. This might explain the differences in the last recorded strain distributions between both concrete grades.

Figure 5-14 shows the mechanical strain distribution in the CFRP at 30 kN for the lower and higher strength concrete specimens at 20°C, 50°C and 70°C. The strain measurement just before applying the load was taken as reference, to make a clear distinction between the mechanical and thermal strains. At 20°C, strains were concentrated in the first approximately 100 mm of the bonded laminate closest to the middle of the specimen. At higher temperatures, strains were distributed more linear over the length of the laminate, which implies that the shear stresses in the concrete are more equally distributed, especially at 70°C. It is expected that this behavior was caused by the reduced Young's modulus of the adhesive at elevated temperatures. This is further investigated by means of finite element analyses in Chapter 6.

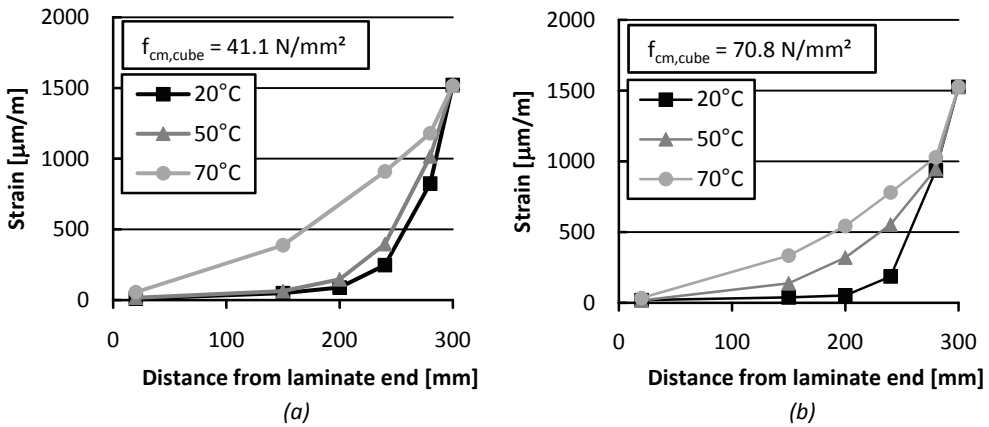


Figure 5-14: CFRP strain distribution at 30 kN for the lower (a) and higher (b) strength concrete specimen

5.4 Mode II bond fracture – Three-point bending test

5.4.1 Test setup

The mode II bond behavior of the concrete-adhesive-CFRP interface can also be investigated with flexural tests. Curvature of a beam in a flexural test causes small additional stresses perpendicular to the bonded area, which means that fracture of the concrete-adhesive-FRP joint is not pure mode II fracture. An advantage of flexural tests is that the load situation of the joint is more comparable to the load situation in normal structures like beams and slabs. It was therefore decided to also investigate the bond behavior in the longitudinal shear direction with three-point bending tests (Figure 5-15).

The specimens were produced in two series of twelve specimens, one of each concrete grade. The same concrete grades as for the double-lap shear tests were used. The specimens spanned 750 mm, were supported at one fixed hinge support and one roller support and were loaded at midspan. The specimens were cut in at midspan till half the height of the beam after curing of the concrete for 21 days (at 20°C and 60% R.H.). This was done to make sure that it breaks in two parts at that location. No internal reinforcement was applied. One CFRP laminate ($25 \times 1.2 \text{ mm}^2$) with a length of 650 mm was applied after 28 days to the sandblasted soffit of the specimen (formworked side). At each side of the saw cut, 25 mm remained unbonded to avoid local stress concentrations at the saw cut.

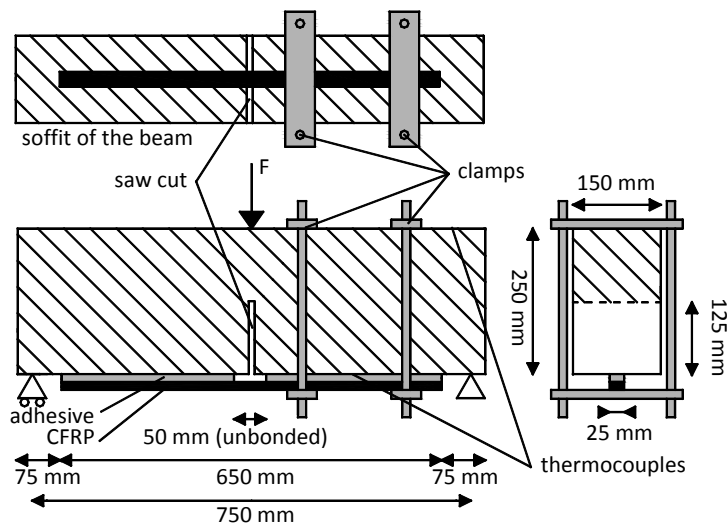


Figure 5-15: Three-point bending test setup

The specimens were tested in a 100 kN testing machine (Figure 5-16a) after being stored at 20°C and 60% R.H. for, on average, 63 days. They were not insulated during the tests, in order to have a clear view on the specimen during debonding. The temperature, which varied with a maximum of 5°C during the tests, was measured on the concrete surface and under the adhesive (Figure 5-15).

The vertical displacement was measured at midspan with LVDTs. Initially, one LVDT was used, but during the test program it was decided to use an extra LVDT, as some of the specimens showed some rotation over their longitudinal axis, which resulted in variations in displacement measurements (Appendix C.1). Strains in the CFRP laminate were again measured with strain gauges (measuring length 6 mm and 10 mm) at 20 mm, 150 mm 200 mm, 240 mm and 280 mm from the plate-end, similar to the double-lap shear tests, and at midspan, directly under the saw cut. Four specimens were supplied with additional strain gauges in the concrete-adhesive interface (measuring length 30 mm), also similar to the double-lap shear tests. Steel clamps were applied to make sure debonding occurred at the side with the strain gauges (Figure 5-16b).

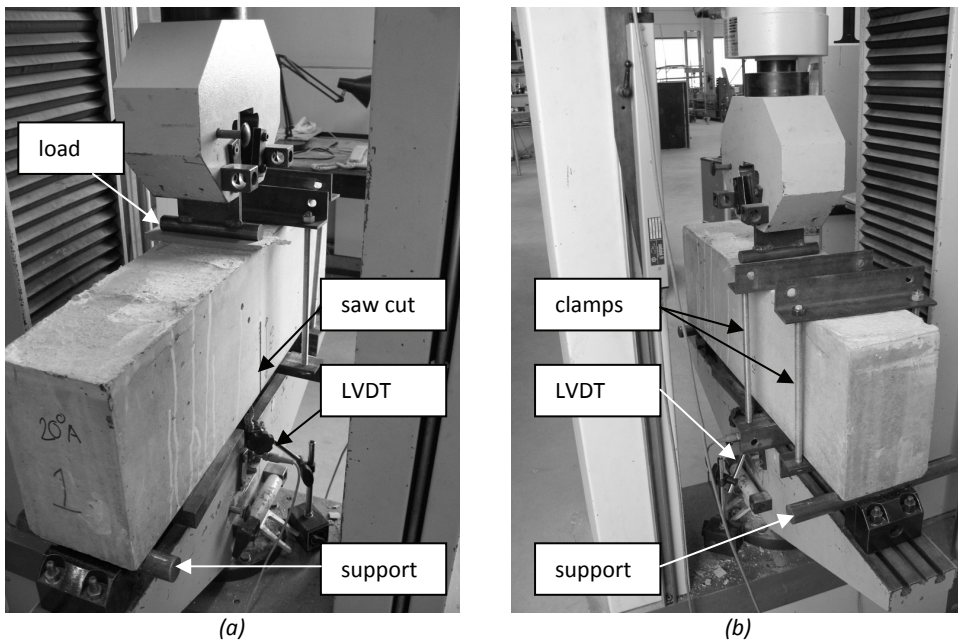


Figure 5-16: Non-clamped (a) and clamped (b) side of the three-point bending test specimen in the test setup

5.4.2 Failure load as function of temperature

The specimens were loaded by displacement controlled loading in approximately 10 minutes. All specimens failed by debonding of the CFRP, immediately followed by flexural failure of the concrete at midspan (Section 5.4.3). The corresponding failure loads as function of the applied temperature are plotted in Figure 5-17. The load-displacement curves are given in Appendix C.1 and Section 6.5.3, for the comparison with the results of the finite element analyses. For both concrete grades, a similar tendency was found. Again, the failure load first increased with increasing temperature, followed by a decrease while further increasing temperature. The transition between these two tendencies was at a temperature close to the glass transition temperature of the adhesive (T_g) for the lower strength concrete specimens. For the higher strength concrete specimens, the transition was around 50°C.

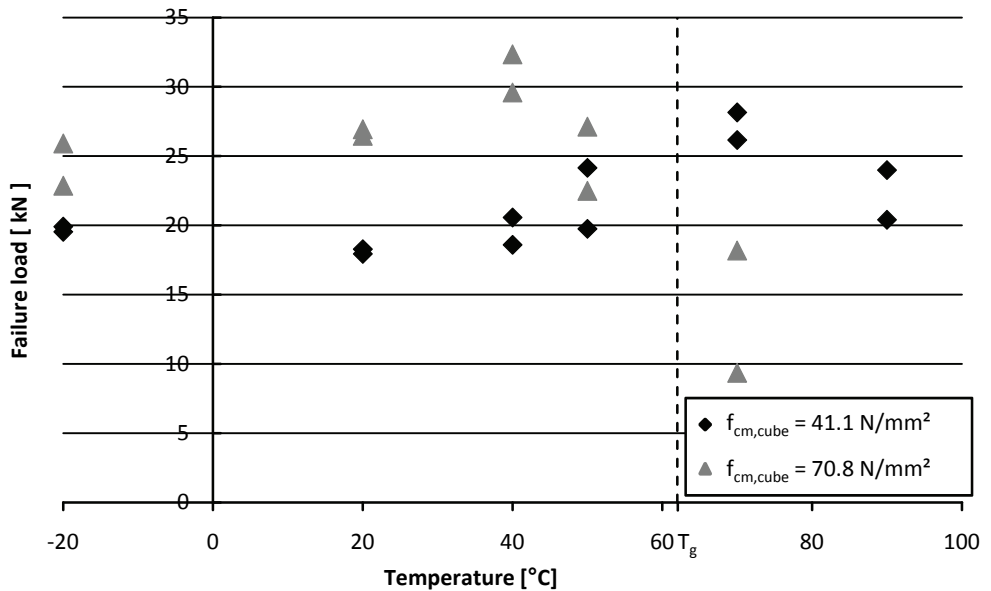


Figure 5-17: Failure load of the three-point bending tests as function of temperature

At temperatures above the glass transition temperature, the failure load of the higher strength concrete specimens was even lower than that of the lower strength concrete specimens. Moreover, two higher strength concrete specimens that were heated up to 90°C could not be tested, as the bond between the concrete and CFRP failed right after getting them out of the oven, even before applying a load. The lower strength concrete specimens could reach, at the same temperature, a load that was even higher than that at room temperature. No sound explanation can be given for this behavior, although Tadeu and Branco (2000) also showed that the effect of temperature was more significant for higher strength concrete (Section 3.2.1).

It is again expected that the decreasing failure load was caused by the changed type of failure at elevated temperatures and by the corresponding decreasing bond strength of the concrete-adhesive joint with increasing temperature (Section 5.2.2). The reduced Young's modulus and/or the differences in coefficient of thermal expansion could have caused the initial increasing failure load at moderate temperatures. This is further investigated by means of finite element analyses (Chapter 6).

5.4.3 Type of failure

The type of failure was affected by temperature in a similar way as for the double-lap shear tests. Up to about 50°C, bond failure was caused by failure of the concrete adjacent to the concrete-adhesive interface, leaving a thin layer of concrete attached to the adhesive (Figure 5-18a). At higher temperatures debonding occurred in the concrete-adhesive interface, leaving hardly any concrete attached to the adhesive (Figure 5-18b).

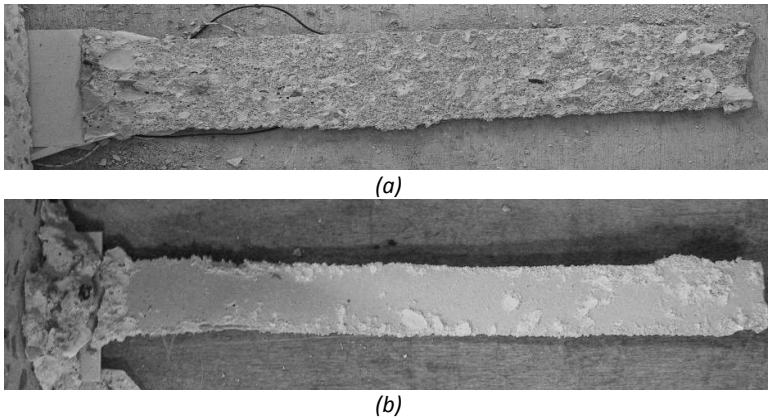


Figure 5-18: Cohesive failure in the concrete (a) and failure in the concrete-adhesive interface (b)

Debonding propagated from the saw cut towards the end of the laminate (Figure 5-19). The beam collapsed after cracking of the concrete above the saw cut, immediately after debonding of the CFRP laminate. In most cases, a small concrete corner broke off above the non-bonded part of the laminate.

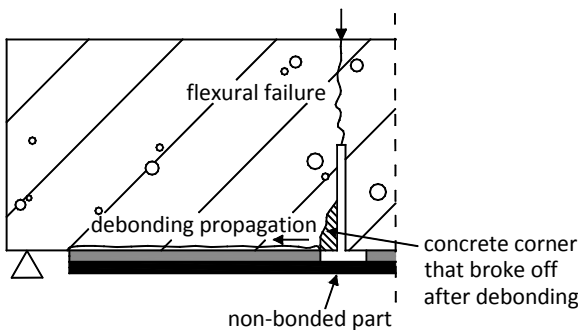


Figure 5-19: Debonding propagation in the three-point bending test

5.4.4 Thermal strain development

The strain development was again measured during heating in the oven. Two specimens, one of each concrete grade, were heated up to 50°C, then cooled down to room temperature and heated up again to 50°C, similar as for the double-lap shear tests. The surface with the CFRP laminate was faced upwards during heating in the oven and the specimens were supported over the entire length with rollers (Figure 5-20), which allowed the concrete to expand and bend freely. Figure 5-20 shows the strain development in time for the lower strength concrete specimen. For the higher strength concrete specimen, similar results were found (Appendix C.2.1). The strain measurements were corrected for temperature influences in the same way as for the double-lap shear test and correspond to;

- the strain in the non-bonded part of the CFRP laminate directly above the saw cut,
- the strain in the middle of the bonded part of the CFRP laminate, 150 mm from the plate-end,
- the strain in the bonded part of the CFRP laminate, 20 mm from the plate-end,
- the strain in the concrete at the interface with the adhesive, at the middle of the bonded length.

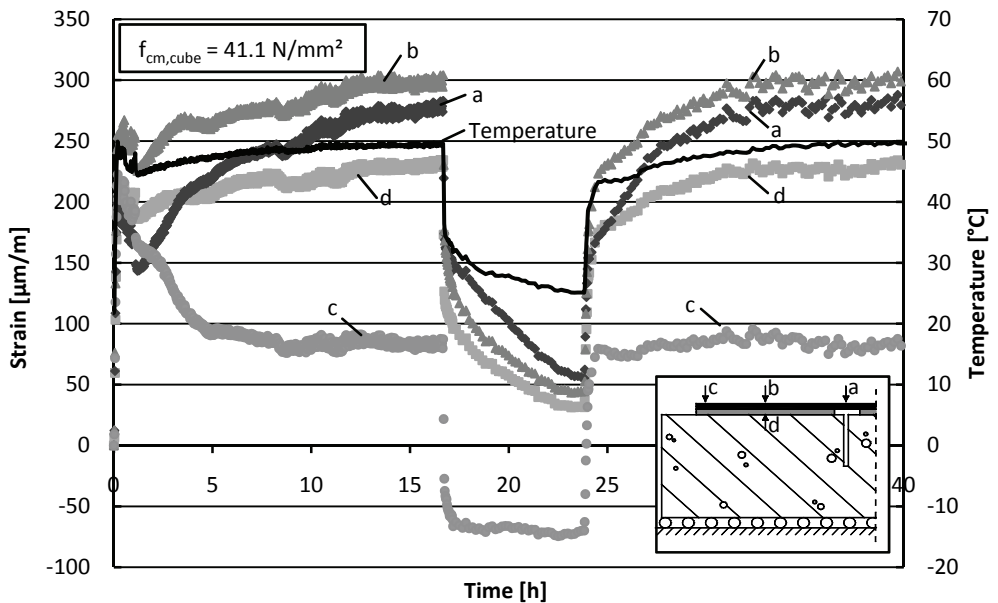


Figure 5-20: Strain development due to heating and cooling of the three-point bending test specimen

Strains developed in an almost similar way as for the double-lap shear tests (Section 5.3.4). The strain in the concrete-adhesive interface (d) followed the expansion of the concrete. The strain in the CFRP in the middle of the bonded (b) and non-bonded (a) part followed this expansion and even showed a slightly higher strain compared to the concrete-adhesive interface (d), which is opposite to what was shown in the double-lap shear tests. No sound explanation can be given for this difference, but is possibly an error in the measurement.

The strain in the non-bonded part above the saw cut (a) was slightly lower than the strain in the middle of the bonded part (b). It is expected that this is caused by curvature of the beam, which partly closes the saw cut and therefore reduces the strain in the non-bonded part. The strain in the CFRP laminate at 20 mm from the plate-end (c) initially also followed the expansion of concrete, but after a while started to decrease. This time dependent behavior was not observed in the middle of the bonded length (b), which is different compared to the double-lap shear tests. It is expected that this is related to the fact that the two bonded parts are connected to each other by the concrete below the saw cut at midspan, which is not the case for the double-lap shear tests. The two bonded parts of the CFRP laminate are pushed away from each other, due to the expansion of concrete, which results in a higher strain at the end of the bonded length near the saw cut, compared to the strain at the end of the bonded length near the middle of the specimen in the double-lap shear tests. This is further investigated by means of FE-analyses (Section 6.5.4).

Most thermal strains disappeared after cooling down the specimen back to room temperature, although the cooling down period was too short for the strains to completely return to zero. The strain in the CFRP at 20 mm from the end decreased (a) to a negative residual strain. Again, heating to 50°C resulted in similar strains as just before cooling down.

Two other specimens, one of each concrete grade, were heated up in three steps till 40°C, 50°C and finally till 70°C. Figure 5-21 shows the strain distribution for the lower strength concrete specimen. The higher strength concrete specimen again showed a similar behavior (Appendix C.2.2).

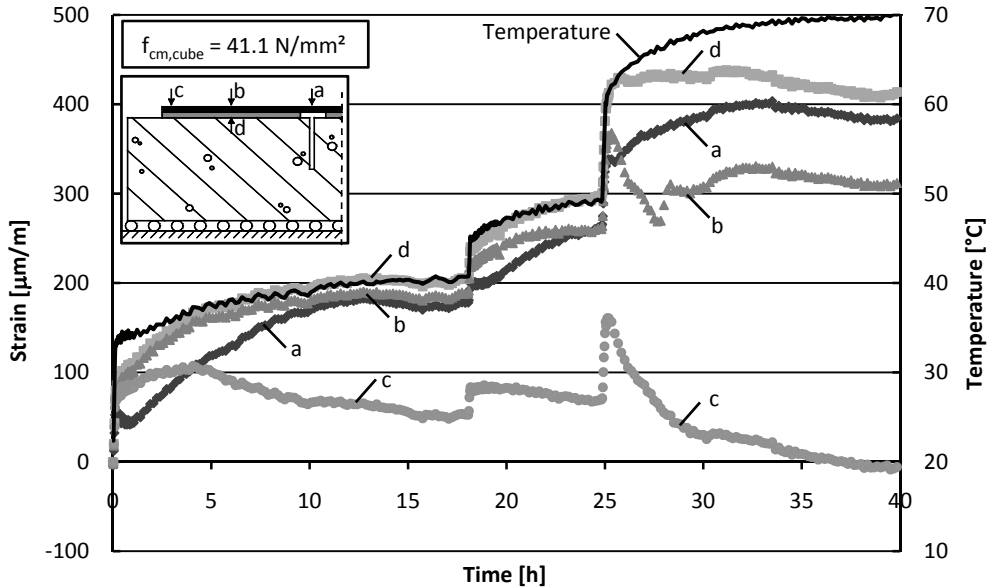


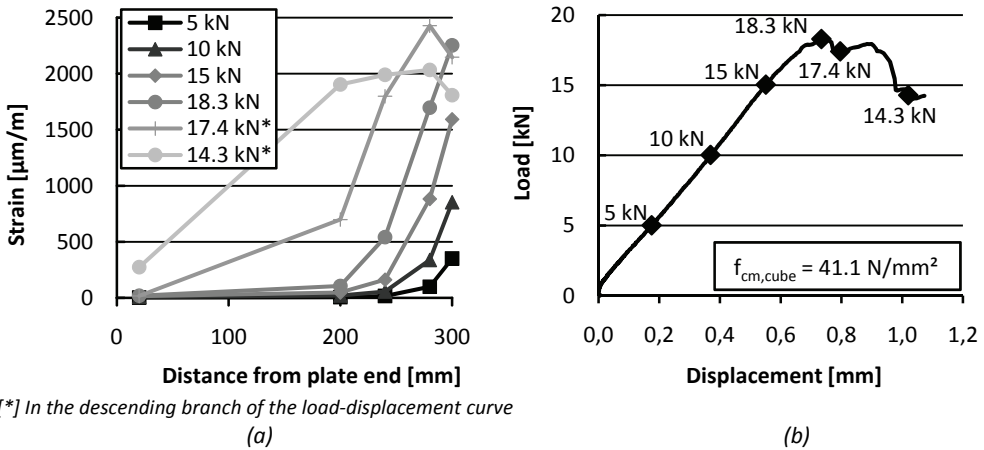
Figure 5-21: Strain development due to heating to 40°C, 50°C and 70°C of the three-point bending test specimen

The thermal strain development up to 50°C was almost similar as in Figure 5-20, although the CFRP strains were now lower than the strains in the concrete-adhesive interface, as could be expected. The strains in the middle of the bonded part (b) followed the expansion of the concrete-adhesive interface (d) at 40°C and 50°C. After increasing the temperature to 70°C, it showed a sudden reduction of the strain in time, although not as significant as at the end of the CFRP laminate (c). It can also be seen that the decrease in strain in time at 20 mm from the plate-end starts faster and is more significant with increasing temperature. It is expected that the time dependent behavior of the adhesive is mainly affecting the CFRP strain distribution at the end of the CFRP laminate at 40° and 50°C, while at 70°C, the strain distribution becomes affected over a longer length, seen from the plate-end, due to both the time dependent creep behavior and the reduced Young's modulus of the adhesive.

5.4.5 Strain development during loading

The strain development in the CFRP laminate due to loading of the specimens was measured at several temperatures. Only the mechanical strain due to the external loading is shown in this section, similar as was done for the double-lap shear tests. Figure 5-22a shows the strain distribution over the length of the CFRP laminate for the lower strength concrete specimen that was tested at room temperature.

For all load steps up to the maximum load (18.3 kN) strains were concentrated in the first approximately 100 mm of the bonded part, measured from the end near the saw cut. The two load steps indicated with a * are load steps in the post peak branch of the load-displacement curve (Figure 5-22b). In these load steps, strains start to increase significantly in the part towards the plate-end as well. This indicates that debonding has started at the end of the bonded length closest to the saw cut and has propagated towards the plate-end.



[*] In the descending branch of the load-displacement curve

Figure 5-22: Strain distributions in the CFRP at different loads (a) and the corresponding load-displacement curve (b) of the lower strength concrete specimen at 20°C

Figure 5-23 shows the strain distribution at 10 kN for the lower strength concrete specimens at different temperatures. Note that some of the strain gauges under the saw cut malfunctioned. It can be seen that, at 70°C and 90°C, strains were more linear distributed over the length of the laminate, which can be explained by the reduced Young's modulus at elevated temperatures. This will result in more equally distributed shear stresses over the length of the CFRP laminate.

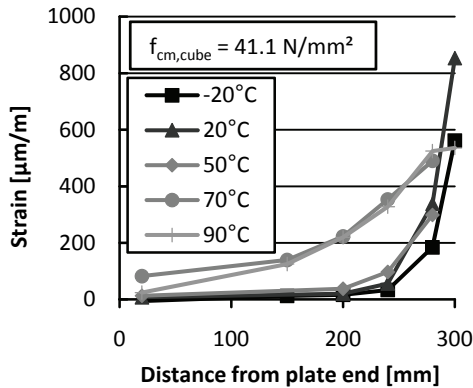


Figure 5-23: Strain distributions in the CFRP at 10 kN at different temperatures for the lower strength concrete specimen

An important difference compared to the double-lap shear tests is the fact that, at the same external load level, the CFRP strain in the non-bonded part directly under the saw cut, was not the same for each temperature. This effect is further investigated by means of finite element analyses in Chapter 6.

5.5 Effect of the angle of loading on the debonding of externally bonded CFRP

5.5.1 Test setup

During the research project, it was decided to investigate the effect of the angle of loading on the debonding of the externally bonded CFRP (see also Schettlers (2004)). At the tip of a shear crack, a CFRP laminate is loaded under a certain angle with the concrete surface, due to the difference in vertical displacement between the two sides of the crack (Figure 5-24). Investigating the effect of the angle of loading on the debonding of externally bonded CFRP could increase the insight in the debonding at shear cracks.

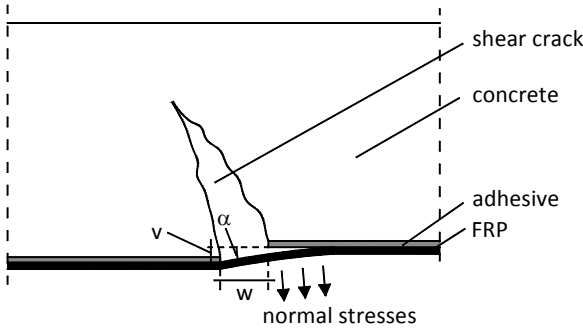


Figure 5-24: Peeling angle at a shear crack (fib 2001)

For the tests, concrete specimens were casted with a dimension of $400 \times 100 \times 100 \text{ mm}^3$, equal to one half of the double-lap shear test specimens. Two CFRP laminates (Sika CarboDur S812, $80 \times 1.2 \text{ mm}^2$) were bonded to the concrete over 300 mm, starting at 25 mm from the corner (Figure 5-25a), again similar as in the original double-lap shear tests. The other end of the CFRP laminate was clamped on a 100 mm wide steel profile. By using filling plates in between the CFRP and the steel profile, it was possible to vary the angle of loading (α) (Figure 5-25b and c).

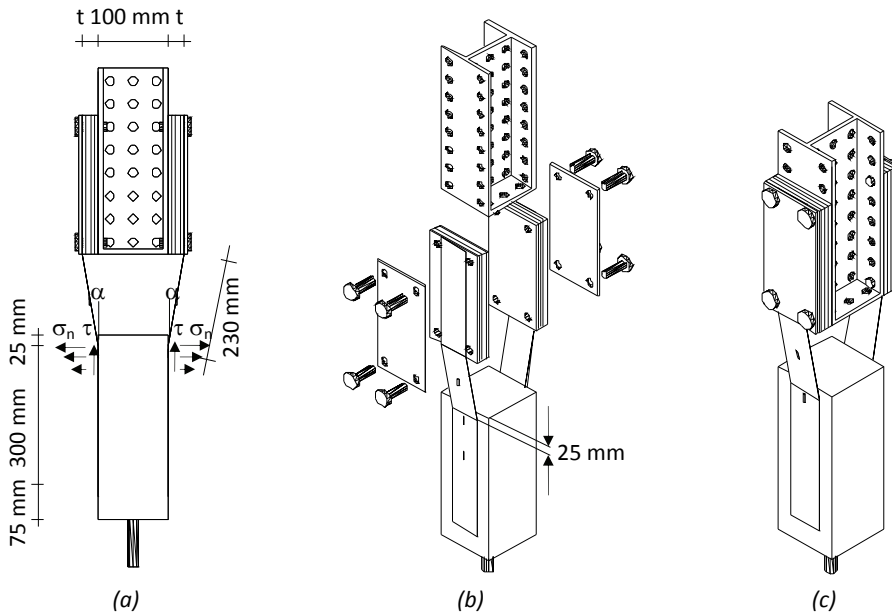


Figure 5-25: Test setup to determine the relation between the angle of loading and the debonding load (Schetters 2004)

The concrete specimens had a mean compressive strength of 46.5 N/mm^2 , a mean tensile splitting strength of 3.1 N/mm^2 and a mean concrete surface bond strength of 3.4 N/mm^2 . The individual results of the compressive, tensile splitting and bond tests are given in Appendix D.1.

The steel profile was pulled away from the concrete specimen with a hydraulic jack that reacted against an external reaction frame (Figure 5-26a). A load cell was applied in between the jack and the steel profile to measure the load. The threaded rod in the concrete specimen was connected to the reaction frame with a hinged connection. The steel profile was aligned with the concrete profile, before fixing the CFRP laminates to the steel profile, to make sure that the two angles of loading were the same. These angles were measured and checked after applying a small initial load (Figure 5-26b).

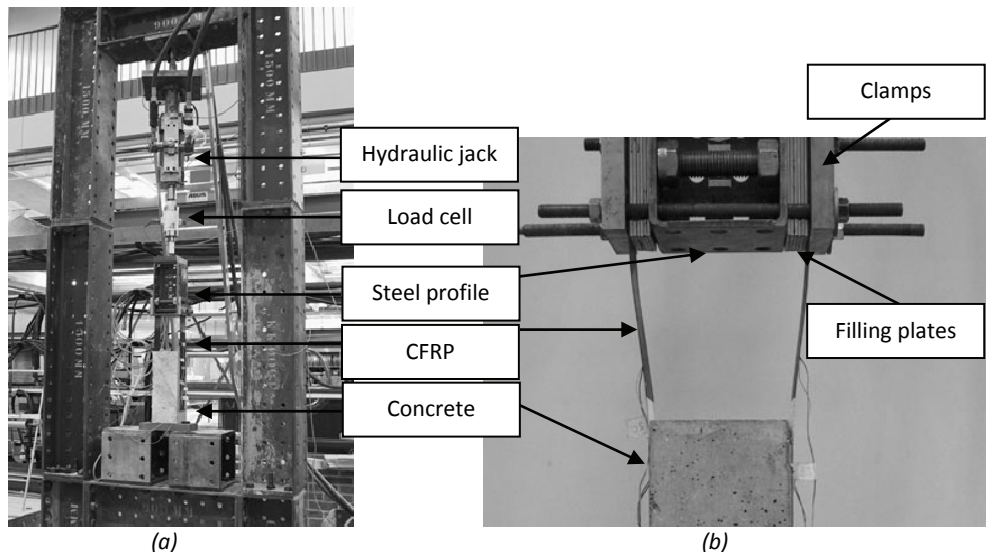


Figure 5-26: Test setup (a) and detail of the connection between the concrete specimen and the steel profile (b)

5.5.2 Failure load as function of the angle of loading

The relation between the failure load and the angle of loading has been plotted in Figure 5-27. It turned out that for an angle of loading of 1.5° and lower, the specimen immediately failed after initiation of the debonding, while the load was able to further increase for higher angles of loading. This is further explained in Section 5.5.3. Two (exponential) trend lines have been plotted to show the tendency of the failure and debonding load. A distinction has been made between angles of loading lower and higher than 1.5° .

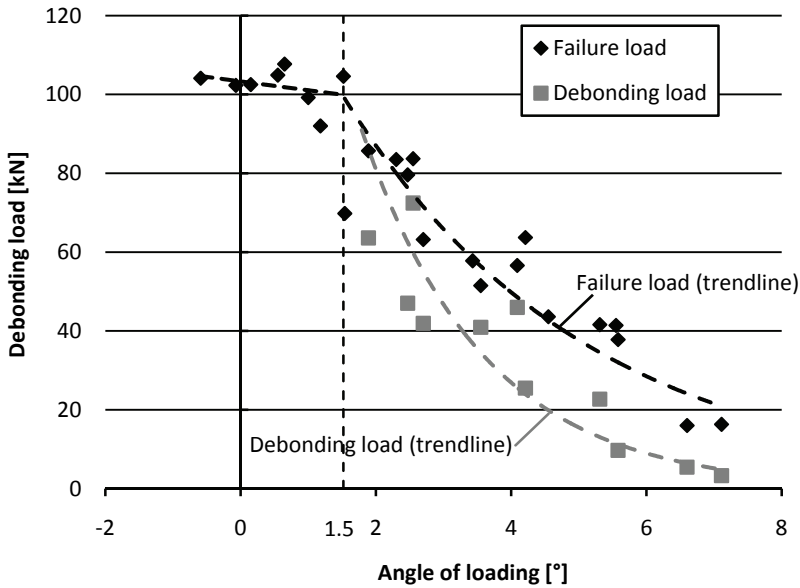


Figure 5-27: Relation between the angle of loading and the debonding/failure load

The results showed that the load at which debonding initiated decreased with an increasing angle of loading. This behavior can be explained by the higher concentrated stresses acting normal to the bonded concrete surface at the plate-end (σ_n in Figure 5-25) with an increasing angle of loading. At $\pm 7^\circ$ hardly any capacity was left.

5.5.3 Type of failure

The specimens loaded under a small angle ($\leq 1.5^\circ$) failed explosively, by failure of the concrete adjacent to the concrete-adhesive interface, similar as in the double-lap shear tests in Section 5.3.3. Again, a small corner broke off from the concrete at the non-bonded part of the CFRP laminate (Figure 5-28a).

The specimens that were loaded under a relatively large angle ($> 1.5^\circ$) failed by debonding in between the adhesive and the CFRP (Figure 5-28b and c). Debonding propagated in most of these specimens slowly, while the load was able to further increase with increasing debonded length. It is expected that this is caused by the reduction of the angle of loading after debonding over a certain length. Some of the specimens debonded in several steps, where, after each step, a line of the adhesive was left on the CFRP laminate at the locations where it had stopped (Figure 5-28c).

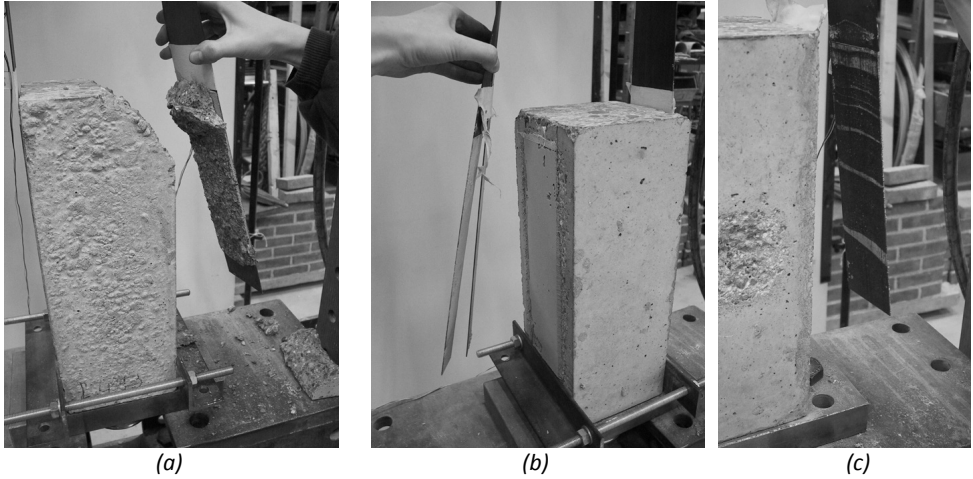


Figure 5-28: Debonding in the concrete, adjacent to the adhesive for angles $\leq 1.5^\circ$ (a) and debonding in the adhesive-CFRP interface for angles $> 1.5^\circ$ (b and c)

5.6 Summary

The bond tests have shown that temperature is affecting the bond behavior of a concrete-adhesive-CFRP joint in more than one way. Changing the temperature results in the development of thermal strains and stresses in the different materials, due to the difference in the coefficient of thermal expansion between concrete and CFRP. Time dependent creep behavior of the adhesive seems to reduce these thermal strains, especially at the plate-ends. This behavior becomes more significant and occurs over a longer length with increasing temperatures.

The strain distribution in the CFRP is also significantly affected by temperature, which is probably related to the reduced Young's modulus of the adhesive at temperatures above T_g . This results in a more linear strain distribution in the CFRP and more equally distributed shear stresses in the concrete adjacent to the concrete-adhesive interface, which could have affected the bond capacity.

Both types of bond tests in shear showed an increasing failure load with increasing temperature up to T_g , which is expected to be related to one or more of these effects. Close to the glass transition temperature of the adhesive, bond failure changes from failure in the concrete to failure in the concrete-adhesive interface. This change is accompanied by a significant reduction of the bond strength of the joint and consequently results in a decreasing failure load with increasing temperature above T_g .

6 Finite element analyses of bond shear tests

6.1 Introduction

A change in temperature affects the bond behavior of the CFRP strengthening in different ways, as has been shown in the previous chapters. A temperature increase reduces the Young's modulus of the adhesive and the bond strength of the concrete-adhesive interface, but also results in the development of thermal stresses due to the thermal mismatch between concrete and CFRP. In experiments, these effects generally occur simultaneously, due to the nature of an experiment.

The effect of temperature on the bond behavior can also be investigated numerically. Numerical analyses of structural engineering problems are often based on the finite element method. With finite element (FE) analyses, different effects of temperature can be investigated individually. Moreover, it becomes possible to compute, for example, the shear stresses in the concrete-adhesive interface, which cannot be measured easily in an experiment. It has, of course, to be kept in mind that the results of finite element analyses are in general an approximation of the reality and highly depend on a correct modeling of the problem. The finite element analyses in this section are carried out with DIANA 9.1 (TNO DIANA B.V. 2005). DIANA is a FE program that is widely used for numerical analyses of concrete structures, although other materials can be analyzed as well.

In the next section, first a short description of the finite element method is given. The approach that has been followed in the numerical simulations of the bond (shear) tests is explained in Section 6.3, followed by a description of the finite element analyses of the double-lap shear tests (Section 6.4) and the three-point bending tests (Section 6.5). In Section 6.6, the effect of temperature on the concrete-adhesive-CFRP joint in the direction perpendicular to the longitudinal direction is investigated.

6.2 Finite element method

The finite element method is a widely accepted and well documented method that can be used to analyze structural engineering problems (Cook, Malkus, and Plesha 1989; Bathe 1996). Structural engineering problems, like for example the calculation of stresses in a (strengthened) beam subjected to external loading, can, in theory, be solved exactly by setting up a set of differential equations. These equations have to cover the actual behavior of the structure (continuum), like the behavior of the materials, external loading, supports, etc. In most cases this leads to a very complex set of equations, which cannot be solved easily without significant simplification of the problem.

The finite element method is a method to approximate the solution of the differential equations by discretization of the continuous problem into a limited number of finite elements. For these elements the solution can be defined by a set of algebraic equations, which can be solved with the help of a computer. Extensive information about the finite element method can, for example, be found in Zienkiewicz (2000).

6.3 Modeling approach

The bond shear tests (Mode II fracture) that were used to investigate the debonding of the CFRP laminate from the concrete surface in the previous chapter were carried out in two steps. Firstly, the specimens were heated in the oven or cooled in the freezer to the required temperature, and secondly, the specimens were loaded in the testing machine. This sequence will also be adopted for the finite element analyses of the bond tests.

Heating and cooling of the specimens

In the finite element analyses, the temperature was first increased in a number of steps from room temperature (20°C) up to the required temperature. Temperature dependent material properties and coefficients of thermal expansion were applied for the different materials, to simulate the effect of a temperature change. The time-dependent behavior of the adhesive (creep) was neglected in the FE-analyses, as the time-dependent properties of the adhesive at different temperatures are not exactly known. Possible effects of this behavior on the results of the finite element analyses will however be explained when the numerical results are discussed.

Loading of the specimens

The stress state after heating or cooling will be the starting point in the second step of the analyses. The loading in the model was displacement controlled, which has the advantage that the post peak branch in the load-displacement curve can be found. The temperature remained constant during loading, which implies that the temperature dependent material properties were also kept constant in this second step.

6.4 Double-lap shear tests

6.4.1 Finite element model

The finite element model of the double-lap shear tests is shown in Figure 6-1. Only half the specimen was modeled because of symmetry. Although possible, it was decided not to use the other symmetry line, as the threaded rod, two supports and the external load were all located on the symmetry line. The model was vertically supported at the end of the bonded length of the CFRP laminates near the saw cut, which implies that the non-bonded part of the CFRP laminate till the symmetry line was not modeled, as it gave some numerical problems. The CFRP force in this part will however be constant and equal to the reaction force in the support. The elongation of this part, due to the external load, is indirectly taken into account, when computing the displacement between the two concrete parts (Section 6.4.3). The model was horizontally supported at both ends of the (embedded) reinforcement bar. The external load was applied at the top end of the reinforcement bar.

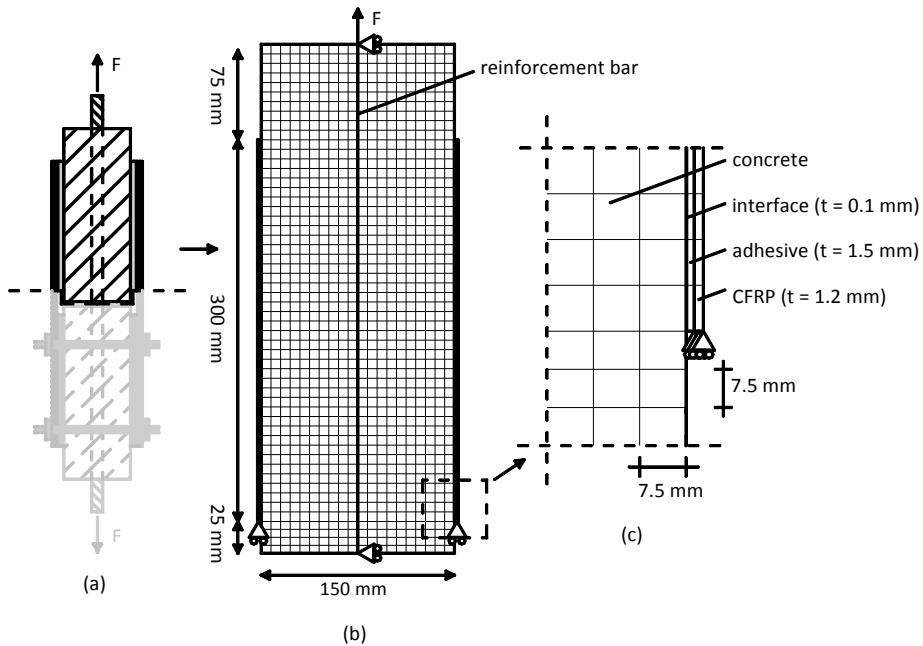


Figure 6-1: Finite element model of the double-lap shear test specimen (a) test setup, (b) finite element model and (c) detail of finite element model

The concrete, CFRP and adhesive were modeled with plane stress elements, which were eight-node quadrilateral isoparametric elements (TNO DIANA B.V. 2005). The default 2x2 Gauss integration scheme was used for these elements, with a quadratic interpolation. The element has sixteen degrees of freedom; two displacements in each node (u_x and u_y).

The threaded rod was modeled as an embedded reinforcement bar, which adds stiffness to the concrete elements in which it is embedded. This implies that perfect bond is assumed between the bar and the concrete elements, which is, for the purpose of this analysis, assumed to be adequate.

Perfect bond cannot be used for the interface between the concrete and the adhesive, as failure is expected to occur in the concrete, adjacent to this interface, or exactly in this interface. This bond behavior is modeled with interface elements with non-linear bond-slip properties, representing the mode II fracture of the concrete adjacent to the adhesive layer or of the concrete-adhesive interface. The interface elements had a dummy thickness of 0.1 mm.

An interface element consists of two lines with on each line three nodes (Figure 6-2a). These nodes are connected to the adjacent plane stress elements. The element describes the relation between the stresses t_n en t_t (also called tractions) and the relative displacements Δu_x en Δu_y (Figure 6-2b). The normal stress (t_n) is defined in the direction perpendicular to the x-axis of the interface element, while the shear stress (t_t) is defined parallel to x-axis of the interface element (Figure 6-2c). These stresses are not coupled. Stresses in the one direction do not affect the behavior in the other direction. The interface element is based on a quadratic interpolation. The default integration scheme was applied, which is a 4 point Newton-Cotes integration scheme (TNO DIANA B.V. 2005). Comparisons were made with the nodal lumping integration scheme, which is recommended for interface elements with a large dummy stiffness, but no significant differences were found in the results.

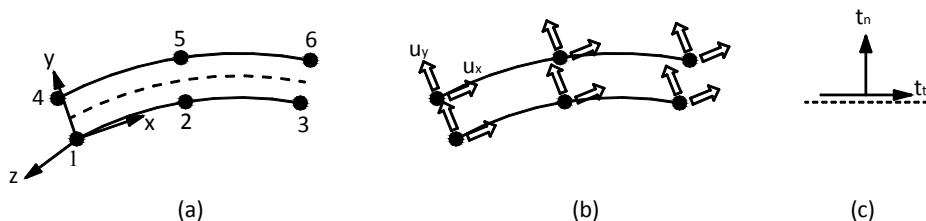


Figure 6-2: The topology (a), the displacements (b) and the tractions (c) of the applied interface element (TNO DIANA B.V. 2005)

6.4.2 Applied material properties

In the double-lap shear tests, no cracking, crushing or yielding was observed except for the concrete adjacent to the adhesive layer. It was therefore decided to apply linear elastic material properties to all plane stress elements and the reinforcement bar (Table 6-1), while non-linear material properties were applied to the interface elements in the bond layer in between the concrete and adhesive elements.

The Young's modulus and the coefficient of thermal expansion were determined experimentally for the concrete (Appendix B.1), adhesive (Section 4.5.4) and CFRP (Section 4.4.3), while the Poisson ratios of the adhesive and CFRP were taken according to the manufacturer's datasheets (Sika 2005; Sika 2009). The material properties of the steel reinforcement were taken according to Eurocode 2 (CEN 1997a), while the coefficient of thermal expansion was taken equal to that of concrete.

Table 6-1: Applied material properties of the plane stress elements and reinforcement bar at 20°C

Material property	Lower strength concrete	Higher strength concrete	Adhesive	CFRP	Reinforcement bar
Young's modulus (E_m) [N/mm ²]	26,800	31,100	12,800	165,000	210,000
Poisson ratio ν [-]	0.2	0.2	0.3	0.35	-
Coefficient of thermal expansion α [$\cdot 10^{-6}/^\circ\text{C}$]	10.2	11.3	26	-0.3	10.2 / 11.3

The applied temperature dependent material properties are shown in Figure 6-3. For the concrete elements, the relation between the Young's modulus and temperature according to Model Code 1990 (CEB 1993) was used. For the adhesive, the experimentally determined relation as given in Section 4.5.3 was used. The Young's modulus of the CFRP was assumed not to be affected by temperatures up to 100°C (Section 4.4.2.4) and therefore kept constant in the FE-analyses.

For the interface elements in between the concrete and adhesive, a non-linear bond-slip relation was applied to simulate the debonding behavior. One of the most widely used models to describe this debonding behavior is the fracture mechanics based model of Holzenkämpfer (1997), modified by Neubauer and Rostásy (1999). The model is based on a bilinear bond-slip (τ -s) relation (Figure 2-23) and relates the maximum FRP anchorage force ($N_{fa,max}$) to the mode II fracture energy (G_F^{II}) of concrete, which corresponds to the area under the bond-slip relation. Note that this model has been developed to describe the debonding due to bond shear failure (mode II fracture) of the concrete adjacent to the concrete-adhesive interface and not due to failure exactly in the concrete-adhesive interface, as was found in the experiment for temperatures above 60°C. Whether the model has to be replaced at these temperatures will be discussed later.

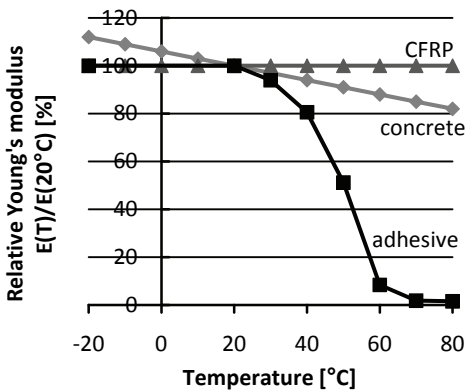


Figure 6-3: Young's modulus as function of temperature for the concrete, adhesive and CFRP

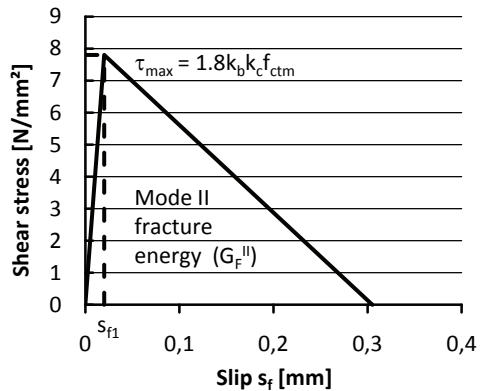


Figure 6-4: Bond slip relation according to Holzenkämpfer

The bond-slip relation in Figure 2-23 was used in the finite element analyses and is defined by three parameters, the mode II fracture energy (G_F^{II}), the shear strength (τ_{max}) and the slip at the shear strength (s_{f1}) (Holzenkämpfer 1997);

$$G_F^{II} = k_c^2 \cdot k_b^2 \cdot c_F \cdot f_{ctm} \quad (6.1)$$

$$\tau_{max} = k_b \cdot k_c \cdot 1.8 \cdot f_{ctm} \quad (6.2)$$

$$s_{f1} = \frac{\tau_{max}}{k_{Gc}} \quad (6.3)$$

where

f_{ctm} is the mean tensile strength of concrete
 C_F is a calibration factor
 k_c is the factor accounting for the state of compaction of concrete
 ≈ 1.0

k_b is the geometry factor

$$= 1.06 \sqrt{\frac{2 - \frac{b_f}{b_c}}{1 + \frac{b_f}{400 \text{ mm}}}} \geq 1$$

b_c, b_f is the width of the concrete and CFRP [in mm]

$$k_{Gc} = \frac{E_c(T)}{2 \cdot (1 + \nu_c) \cdot h_{c,ef}} \quad (\text{Section 3.5})$$

$E_c(T)$ is the Young's modulus of concrete at temperature T

ν_c is the Poisson ratio of concrete

$h_{c,ef}$ is the effective height of concrete
 $\approx 50 \text{ mm}$ or two times the maximum aggregate size

Based on calibrations with test results, values of $c_F = 0.092 \text{ mm}$ (Holzenkämpfer 1997) and $c_F = 0.202 \text{ mm}$ (Neubauer and Rostásy 1999) have been reported in literature for CFRP. The effect of stresses perpendicular to the bonded area, due to the distance between the CFRP and the concrete surface, are indirectly included in this calibration factor. The effective concrete height ($h_{c,ef}$) is similar as was defined in the model of Di Tommaso et al. (Section 3.5) and represents the height of the concrete that is contributing to the slip at the interface with the CFRP. In the FE-model, the behavior of the concrete is modeled with linear elastic plane stress elements, while the fracture behavior is concentrated in the interface elements. To compute the slip at $\tau_{max}(s_{f1})$ in the interface element, the effective height of the concrete had to be replaced with the thickness of the interface element.

The ascending branch of the bond-slip relation is temperature dependent as it is related to the Young's modulus of the concrete. The shear strength τ_{max} and the mode II fracture energy at 20°C are taken as starting point for the analyses, also for elevated temperature. Whether this is a correct assumption will be discussed later. The factor k_c was used to fit the finite element model to the experimental results at 20°C, where needed (Table 6-2). This factor was kept constant for all other temperatures. Linear elastic properties were applied to the interface elements in the direction perpendicular to the concrete surface. An overview of the applied material properties of the interface elements is shown in Table 6-2.

Table 6-2: Material properties of the interface element

Material properties	Lower strength concrete	Higher strength concrete
Tensile strength (f_{ctm})	3.07 N/mm ²	3.79 N/mm ²
Compaction factor (k_c)	1.0	0.925
Calibration factor (c_f)	0.092 mm	0.092 mm
Young's modulus (E_c) (at 20°C)	26,800 N/mm ²	31,100 N/mm ²
Poisson's ratio (ν_c)	0.2	0.2
Coefficient of thermal expansion (α_c)	$10.2 \times 10^{-6} / ^\circ\text{C}$	$11.3 \times 10^{-6} / ^\circ\text{C}$

6.4.3 Load-displacement curves

The experimental and numerical load-displacement curves of the double-lap shear tests ($f_{cm,cube} = 41.1 \text{ N/mm}^2$) are plotted in Figure 6-5 for -20°C, 20°C, 50°C and 70°C. Similar results were found for the higher strength concrete specimens (Appendix E.1.2). The displacement on the horizontal axis corresponds to the displacement between the two concrete parts (see LVDT in Figure 5-7) and is computed from the results of the FE-analyses and the elongation of the non-bonded part of the CFRP laminate.

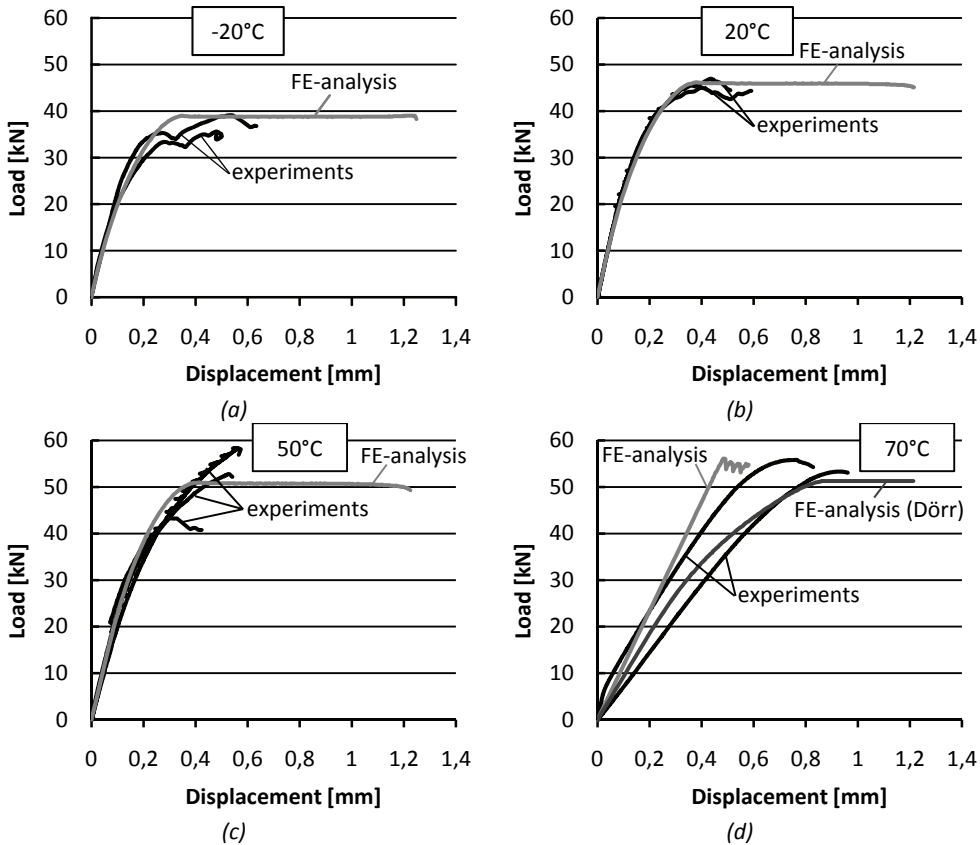


Figure 6-5: Load-displacement curves from the experiments and the FE-analyses for -20°C (a), 20°C (b), 50°C (c) and 70°C (d) for the lower strength concrete specimens

The displacement of the experiment in Figure 6-5 is the mean value of the two LVDT's. It can be seen that, up to 50°C, the load-displacement curves as well as the failure loads found with the FE-analyses corresponded remarkably well with the experimental results, by only applying temperature dependent material properties, without any fitting ($k_c = 1.0$). The main difference is the horizontal branch after reaching the maximum load, which is significantly longer for the FE-analyses. It is expected that this is caused by the explosive type of failure in the experiment, which made it impossible to measure these large displacements, as measurements were only recorded at certain time intervals.

The results of the finite element analyses showed an increasing failure load with increasing temperature, which is similar as the experimental results. At 70°C, the numerical load-displacement curve was different from the experimental load-displacement curves, especially for the higher strength concrete specimens (Appendix E.1.2). At this temperature, bond failure changed, in the experiments, from failure in the concrete to failure exactly in between the concrete and the adhesive. It can therefore be concluded that the applied bond-slip relation according to Holzenkämpfer (1997) was not valid anymore at this temperature. This is not a surprise, as the applied bond-slip relation was only developed for concrete bond failure.

To simulate the behavior of the specimens at 70°C, it was decided to apply a different bond-slip relation that describes the bond failure of the concrete-adhesive interface (at elevated temperature) rather than that of the concrete adjacent to the concrete-adhesive interface. By applying the bond-slip relation of Dörr (1980) (Figure 6-6) to the interface elements, it turned out that the results of the experiments were better approximated, especially for the higher strength concrete specimens (Figure 6-5).

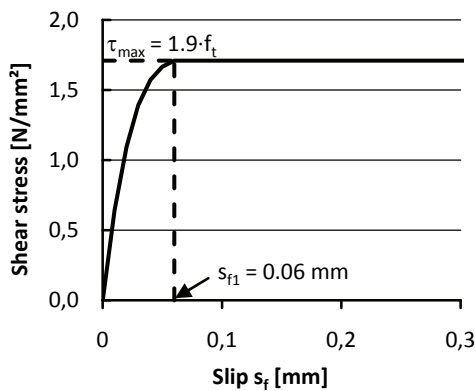


Figure 6-6: Bond slip relation according Dörr (1980)

The main variable in this model is the shear strength (τ_{max}), which is assumed to be related to the tensile strength. Initially, the tensile strength was taken equal to tensile strength of the adhesive at 70°C ($f_{atm}(70^\circ\text{C}) \approx 0.5 \cdot f_{atm,fl}(70^\circ\text{C}) = 7.7 \text{ N/mm}^2$), but this did not result in accurate results. Also taking the tensile strength equal to the bond strength of the concrete-adhesive interface at 70°C ($f_{cbm}(70^\circ\text{C}) = 1.13 \text{ N/mm}^2$ and 2.73 N/mm^2 for respectively the lower and higher strength concrete grade) (Section 5.2.2) did not provide accurate results.

It was therefore decided to determine the shear strength by fitting the numerical results to the experimental results. This resulted in a shear strength of 1.7 N/mm^2 and 1.4 N/mm^2 for respectively the lower and higher strength concrete specimens at 70°C. The slip at the shear strength (s_{fl}) was taken equal to the default value, 0.06 mm. It is expected that the fact that no clear relation was found between the shear strength on the one hand and the tensile and/or bond strength of the concrete-adhesive interface on the other hand was related to the wider scatter in bond strength at this temperature and possible effects of the heating curve before testing. The heating curve could have affected the glass transition temperature, and consequently the (bond) strength.

6.4.4 Heating and cooling of the specimens

Applying a temperature change to the finite element model resulted in thermal strains and stresses in the different materials. These strains were compared to the thermal strains as measured in the experiment (Figure 6-7). Note that the plotted experimental strain measurements correspond to the strain measurements just before increasing the temperature to the next temperature level (Figure 5-12), what implies that possible time dependent effects had occurred in the experiment. The thermal strains were also determined analytically with the model of Di Tommaso et al. (2001), as discussed in Section 3.5.

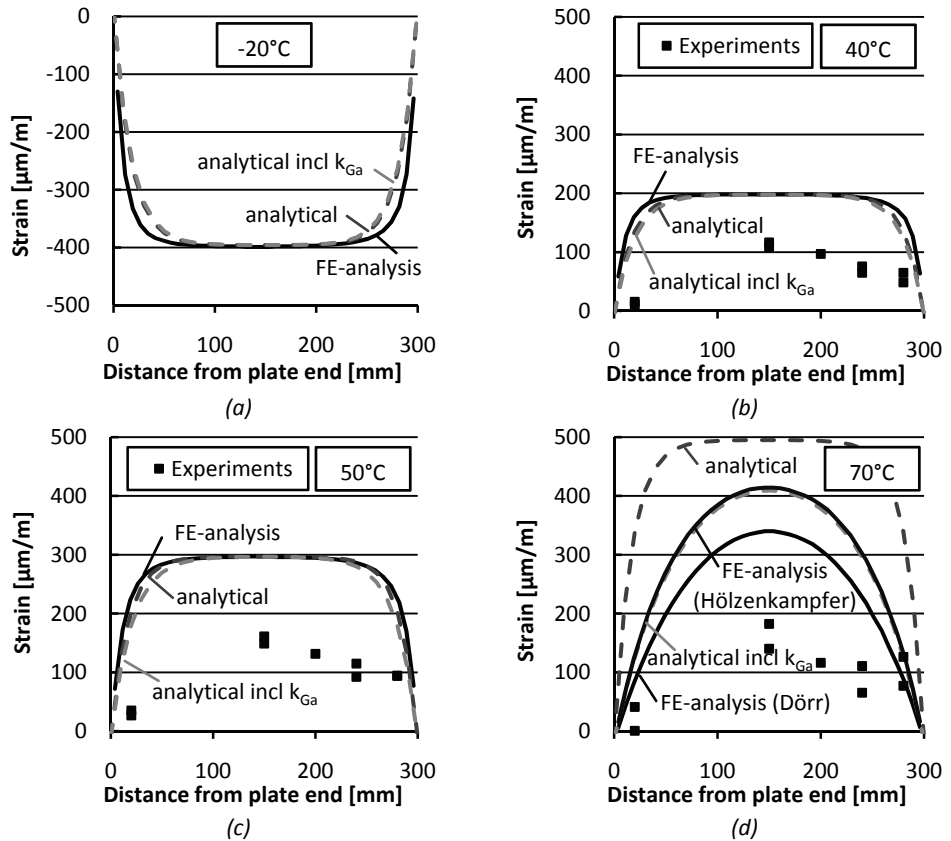


Figure 6-7: CFRP strain distributions for -20°C (a), 40°C (b), 50°C (c) and 70°C (d) for the lower strength concrete specimens

It can be seen that the analytical and numerical strain distributions were more or less the same for all temperatures up to 50°C. At 70°C, the numerical distribution was determined twice, once with the bond-slip relation according to Holzenkämpfer and once with the bond-slip relation according to Dörr, as has been explained in the previous section. Both distributions were significantly lower compared to the analytical distribution. This can be explained by the effect of the reduced Young's modulus of the adhesive layer, which was not taken into account in the analytical model. In order to take this effect into account, it was needed to modify the model by Di Tommaso et al. (2001) by adding the stiffness of the adhesive (k_{Ga}) to the stiffness of the concrete (k_{Gc});

$$\frac{1}{k_G} = \frac{1}{k_{Gc}} + \frac{1}{k_{Ga}} \quad (6.4)$$

where

$$k_{Gc} = \frac{E_c(T)}{2 \cdot (1 + \nu_c) \cdot h_{c,ef}}$$

$$k_{Ga} = \frac{E_a(T)}{2 \cdot (1 + \nu_a) \cdot t_a}$$

$E_c(T)$ is the Young's modulus of concrete at temperature T

ν_c is the Poisson ratio of concrete

$h_{c,ef}$ is the effective height of concrete

≈ 50 mm or two times the maximum aggregate size

$E_a(T)$ is the Young's modulus of adhesive at temperature T

ν_a is the Poisson ratio of the adhesive

t_a is the thickness of the adhesive

This modified analytical distribution is also plotted in Figure 6-7 (analytical incl k_{Ga}) and is, up to 50°C, almost similar to the original analytical distribution. For these temperatures, it is therefore allowed to neglect the adhesive layer. At 70°C, the modified analytical strain distribution becomes significantly lower than the original analytical distribution and is almost similar to the numerical distribution found with the finite element analysis with the bond-slip relation according to Holzenkämper. The results of the finite element analysis with the model of Dörr showed even lower strains in the CFRP laminate, but still overestimate the experimental strain measurements. It is expected that this is mainly due to the fact that the time-dependent behavior of the adhesive is not taken into account. The experimental strain measurements during heating showed that the strain in the CFRP decreased over time, especially at high temperatures.

The shear stress distributions in the concrete interface elements are plotted in Figure 6-8 for -20°C, 50°C and 70°C, according to the different analytical and numerical models. Shear stresses mainly developed at the ends of the bonded length, as expected, where the CFRP force is transferred to the concrete.

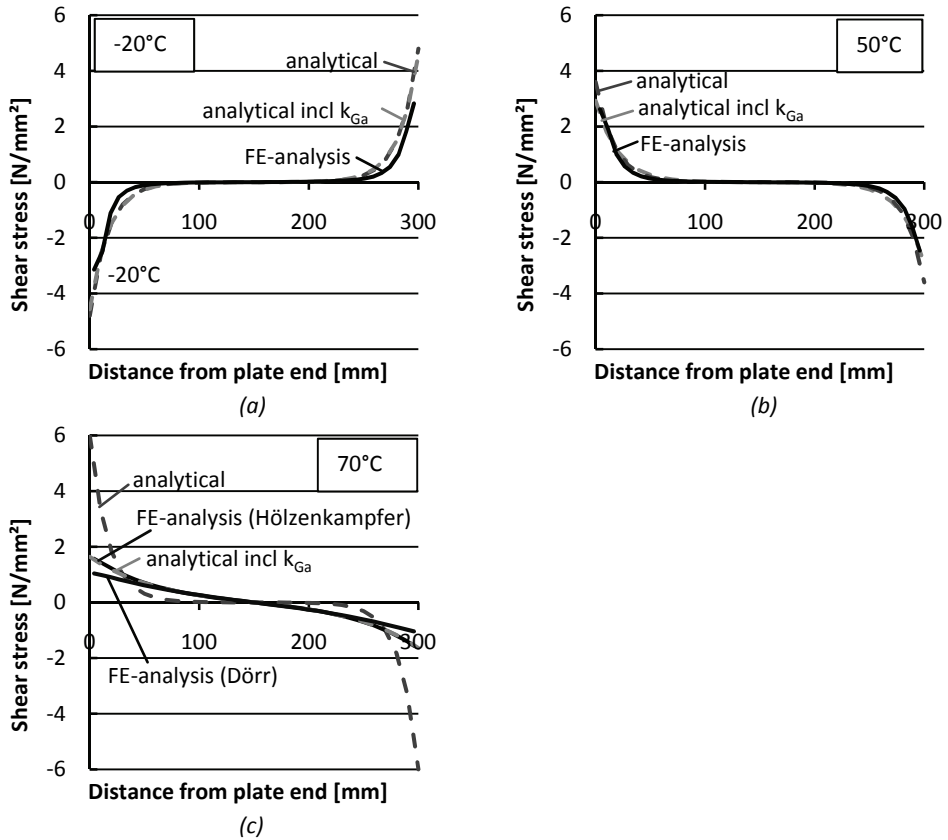


Figure 6-8: Shear stress distributions in the interface elements at -20°C (a), 50°C (b) and 70°C (c)

Up to 50°C, there is no significant difference between the analytical and numerical shear stress distributions. At 70°C, it was again significantly affected by the reduced Young's modulus of the adhesive, as can be seen by the difference between the two analytical shear stress distributions. The peak in shear stress at the end even became lower at 70°C compared to that at 50°C.

It can be concluded that the differences in the coefficient of thermal expansion of the different materials resulted in the development of thermal strains and stresses in the concrete and CFRP. Up to 50°C, there is no significant effect of the reduced Young's modulus of the adhesive on these strains and stresses. At 70°C, however, the reduction of Young's modulus of the adhesive results in lower strains and stresses in the CFRP and lower peaks in shear stresses in the concrete adjacent to the concrete-adhesive interface at the ends of the bonded length. The FE-analyses however still overestimate the thermal strains and stresses due to the time dependent behavior of the adhesive, which was not taken into account. Note however that shortly after increasing the temperature, thermal strains are significantly higher, as was shown in Section 5.3.4.

6.4.5 Loading of the specimens

After the change in temperature in the first part of the finite element analysis, load was applied on the model in several steps in the second part. The strain distribution in the CFRP laminate at an arbitrary chosen external load of 30 kN is plotted in Figure 6-9a for four different temperatures. The strain distribution at 70°C has been determined with the bond-slip relation of Dörr (1980), as bond failure was governed by bond failure in the concrete-adhesive interface and not in the concrete adjacent to the concrete-adhesive interface at this temperature. The strain distributions in Figure 6-9a include both the thermal strains due to the temperature change and the mechanical strains due to the external loading. To compare the experimental results (strain measurements were reset just before the start of the test) with the finite element analyses, it was needed to compute the mechanical strains (Figure 6-9b) by subtracting the thermal strain distribution (Figure 6-7) from the total strain distribution (Figure 6-9a). Note that the time-dependent material properties of the adhesive were less important during loading of the specimens, as the test was carried out in about 15 minutes.

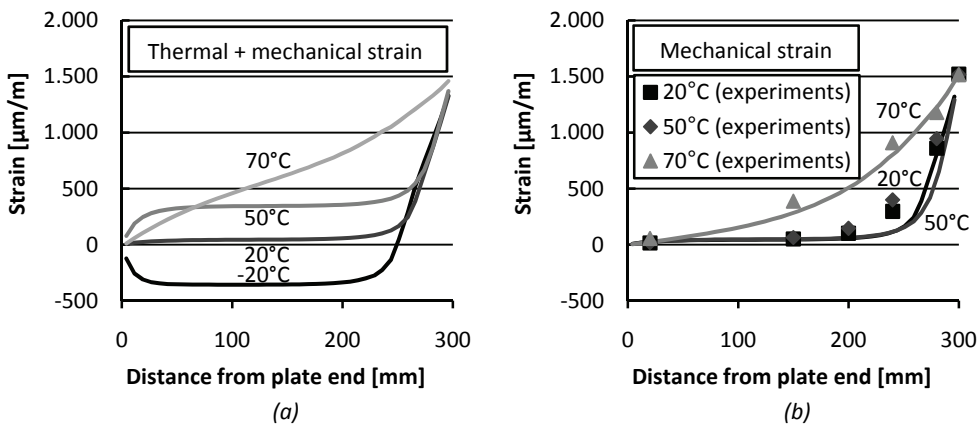


Figure 6-9: Total (a) and mechanical (b) CFRP strain distributions at 30 kN for the lower strength concrete specimens

The numerical strain distributions corresponded quite well to the experimental results. It can be seen that, at 20°C and 50°C, the strains due to loading of the specimen were mainly concentrated at the end of the bonded length near the middle of the specimen (between 200 mm and 300 mm). This means that the stresses in the CFRP are mainly transferred to the concrete by means of shear stresses in this area. In the remaining part of the CFRP, strains are almost equal to the initial thermal strains caused by the temperature in- or decrease. At 70°C, the mechanical strain is more linear distributed over the bonded length, due to the reduced Young's modulus of the adhesive. The corresponding shear stress distributions are plotted in Figure 6-10 for 0 kN, 10 kN, 30 kN and the maximum load.

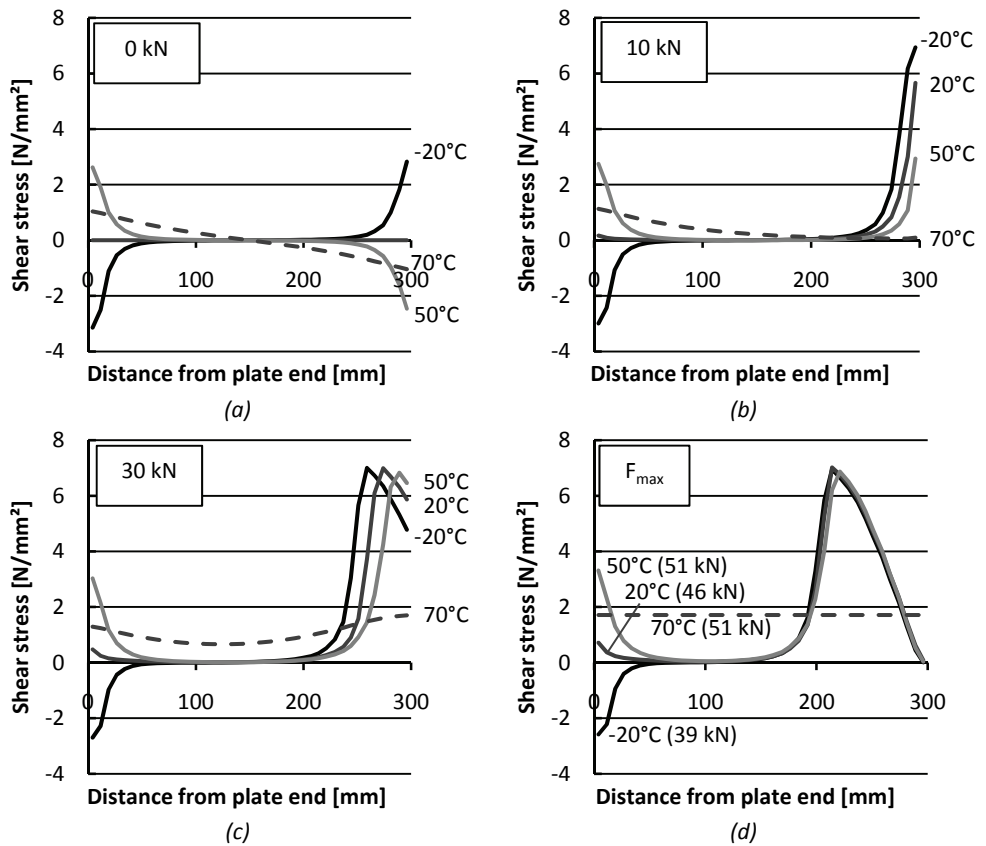


Figure 6-10: Shear stresses in the interface elements at 0 kN (a), 10 kN (b), 30 kN (c) and the failure load (d)

It can be seen that, at the end of the bonded length near the middle of the specimen (300 mm), the direction of the shear stress due to a temperature increase (Figure 6-10a) is opposite to the direction of the shear stress due to loading (Figure 6-10b and c). Shear stresses due to loading will first have to compensate the thermal shear stresses at this end. As a result, the peak in shear stress is lower at this end with increasing temperature (Figure 6-10b), which explains the increasing failure load with increasing temperature (Figure 6-10d). For the specimen at -20°C , the initial thermal stress is acting in the same direction as the shear stress due to loading, resulting in the highest peak at 10 kN.

6.4.6 Effects of temperature on the failure load

As mentioned before, one of the advantages of finite element analyses is that different effects of temperature can be investigated individually. Figure 6-11 shows the effect of (separately) changing the Young's modulus of the adhesive (E_a) and the concrete (E_c) on the failure load. With the relation between temperature and the Young's moduli (Figure 6-3), the effect of the change in Young's moduli of the adhesive and the concrete on the failure load can be given individually at different temperatures (E_a and E_c in Figure 6-12).

It can be seen that changing the Young's modulus of concrete (E_c) did not significantly affect the failure load in the temperature range from -20°C to 80°C . The decreasing Young's modulus of the adhesive (E_a) with increasing temperature resulted in a slowly decreasing failure load, although at 60°C , the failure load suddenly started to increase with increasing temperature. At this temperature, the Young's modulus was about 8% of the Young's modulus at 20°C . For lower Young's moduli, an increasing load was found (Figure 6-11), due to the change in shear stress distribution in the concrete adjacent to the concrete-adhesive interface.

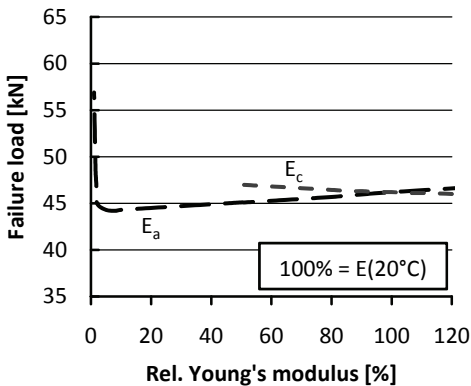


Figure 6-11: Failure load as function of the Young's modulus of concrete and adhesive

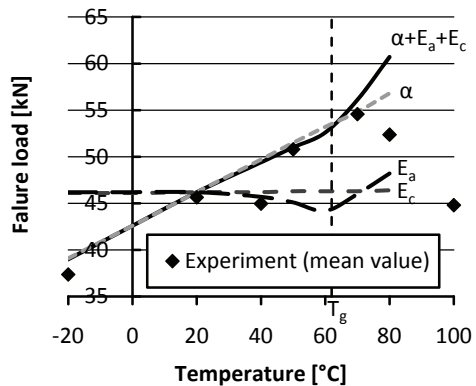


Figure 6-12: Failure load as function of temperature

It turned out however that the failure load was affected the most by the differences in the coefficient of thermal expansion between concrete and CFRP (α), as can be seen in Figure 6-12. The effect of temperature on the failure load, taking all effects into account, is also plotted in Figure 6-12 ($\alpha+E_a+E_c$) and compared with the experimental failure loads. It can be seen that the results of the finite element analyses approximate the average experimental failure loads rather well for temperatures up to 50°C, except at 40°C. At this temperature, the failure load was unfortunately determined with only one specimen. At 70°C and higher, large differences were found, as the results of the finite element analyses were determined with the bond-slip model of Holzenkämpfer.

6.4.7 Summary

Based on the analyses, it can be concluded that the increasing failure load with increasing temperatures up to 50°C is mainly due to the effect of the differences in the coefficient of thermal expansion between concrete and CFRP (Figure 6-12). Above this temperature, a different type of failure occurs, for which the applied bond-slip relation according to Holzenkämpfer is not valid anymore. It is expected that the failure load highly depends on the (bond) properties of the concrete-adhesive interface at these temperatures. It was however not possible to find a direct relation between the failure load and the (reduced) bond strength of the concrete-adhesive interface or the (reduced) tensile strength of the adhesive at elevated temperature. Nevertheless, the overall tendency above the glass transition temperature of the adhesive is a decreasing bond strength and decreasing failure load with increasing temperature.

6.5 Three-point bending tests

6.5.1 Finite element model

The three-point bending tests were analyzed in a similar way as the double-lap shear tests. The finite element model of the tests is shown in Figure 6-13. For the analyses, a fixed hinge support (left) and a roller support (right) were modeled at the soffit of the beam and a load was applied at midspan on top of the beam. There were no elements over the lower half of the midspan cross-section, in order to model the saw cut at this location. The non-bonded part between the concrete and the CFRP, 25 mm at each side of the saw cut, was modeled in the same way (Figure 6-13). The concrete, adhesive, CFRP and bond layer were modeled with the same elements as have been used in the double-lap shear tests (Section 6.4.1). Interface elements were used at the upper half of the midspan cross-section to model the (discrete) cracking of the concrete at this location.

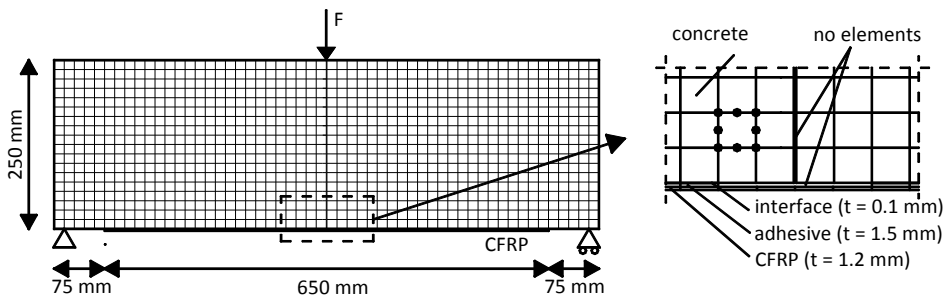


Figure 6-13: Finite element model for loading of the three-point bending test specimen

For the simulation of the heating of the specimen, the FE-model was slightly changed. It was turned up-side-down and supported over the entire length of the specimen with springs (Figure 6-14), similar as the situation in the oven in the experiment. A very high stiffness was applied to the springs in compression, while no stiffness was applied in tension. In this way, the specimen was able to bend upwards, e.g. due to the difference in coefficient of thermal expansion between the concrete and CFRP.

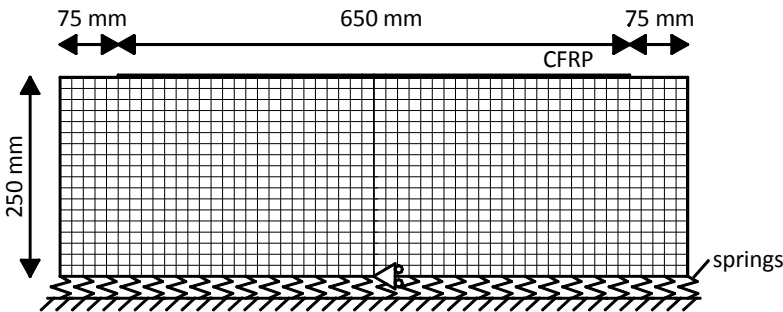


Figure 6-14: Finite element model for heating of the three-point bending test specimen

6.5.2 Applied material properties

For the plane stress elements and the interface elements of the bond layer, the same material properties were applied as for the elements in the double-lap shear tests. The factor k_c , which was a parameter in the bond-slip relation according to Holzenkämpfer, was adjusted for the higher strength concrete specimens, to fit the experimental results at 20°C. This factor turned out to be 1.35 for the higher strength concrete specimens, which is probably caused by the higher age at testing, compared to the double lap shear tests. It was kept constant for all temperatures up to 50°C. At 70°C, the bond-slip model of Dörr was used, which was expected to describe the bond-slip behavior of the concrete-adhesive interface at this temperature better, similar as in the double-lap shear tests.

For the interface elements of the discrete crack in the concrete at midspan above the saw cut, a brittle stress-relative displacement relation (strain divided by the thickness of the element) was defined to simulate the cracking at this location (Figure 6-15). The shear stiffness of these elements was reduced to zero when the normal stress in the interface element reached the tensile strength of concrete (f_{ctm}). The material properties in compression were kept linear elastic, as the compressive stress was not expected to reach the compressive strength of concrete.

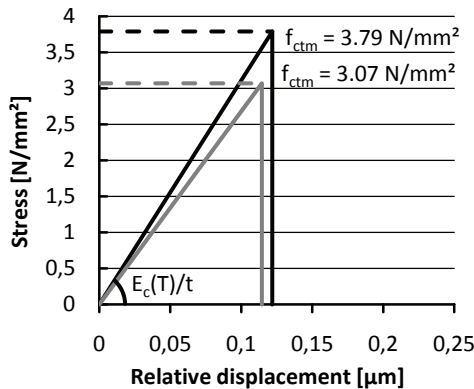


Figure 6-15: Stress-relative displacement relations of the discrete crack representing the concrete at midspan in tension

6.5.3 Load-displacement curves

The load-displacement curves of the higher strength concrete specimens are plotted in Figure 6-16 for -20°C, 20°C, 40°C and 70°C (see Appendix E.2.1 for the lower strength concrete specimens). The displacement on the horizontal axis corresponds to the vertical displacement at midspan. It was decided to use the load-displacement curves of the higher strength concrete specimens as the displacement of these specimens were measured with two LVDTs in the experiment (Section 5.4.1). The displacement in Figure 6-16 corresponds to the mean value of these two measurements.

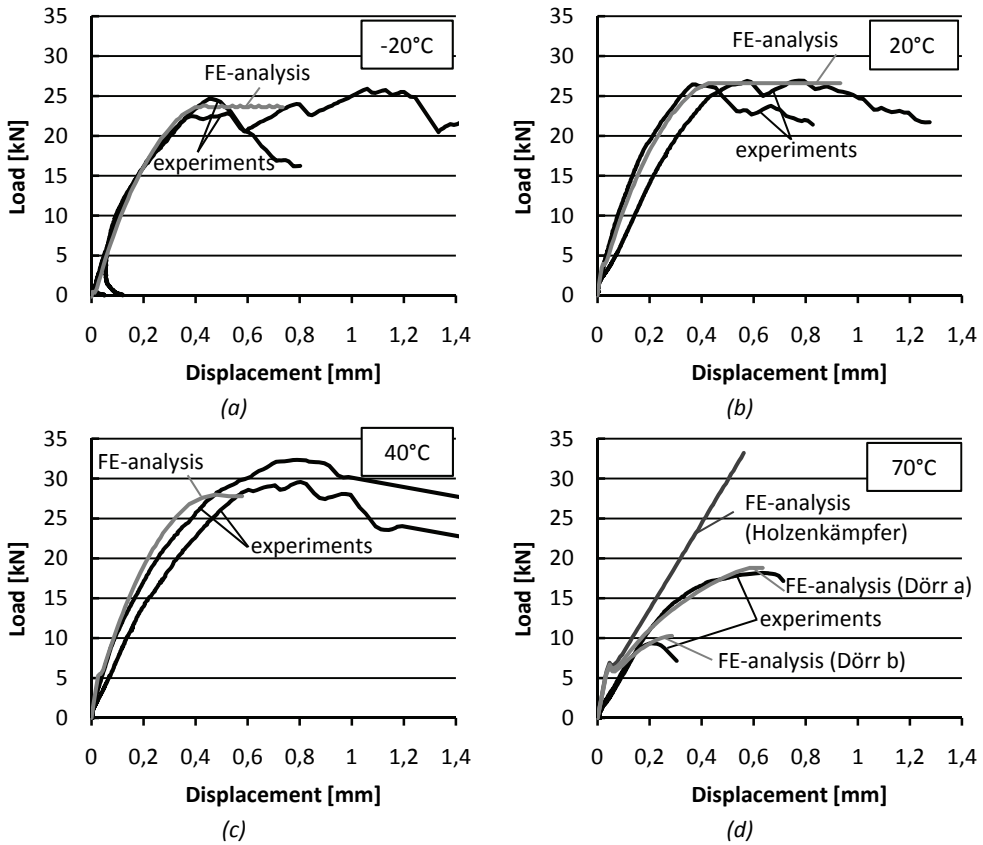


Figure 6-16: Load-displacement curves from the experiments and FE-analyses for -20°C (a), 20°C (b), 40°C (c), and 70°C (d) for the lower strength concrete specimens

The tendency in the results is similar to the results of the double-lap shear tests. Up to 40°C , the numerical results showed good similarity with the experimental results. In this temperature range, an increasing failure load was found with increasing temperatures, similar as in the experiments.

At 70°C , the results of the FE-analysis with the bond-slip model of Holzenkämpfer did not correspond to the experimental results, as expected, because (bond) failure had changed in the experiment from failure in the concrete adjacent to the concrete-adhesive interface to failure exactly in the concrete-adhesive interface. Again, the bond-slip relation according to Dörr (1980) gave better results at this temperature, although the shear strength had to be adjusted to fit the numerical results with the experimental results (Figure 6-16d).

A shear strength of 1.3 N/mm^2 was used for the lower strength concrete and 0.5 N/mm^2 (FE-analysis Dörr a) and 0.9 N/mm^2 (FE-analysis Dörr b) for the higher strength concrete. Again, no clear relation was found between the shear strength and the tensile strength of the adhesive or the bond strength of the concrete-adhesive interface at 70°C . The shear strength was however significantly lower than the shear strength that was used in the model of Holzenkämpfer for concrete bond failure ($\tau_{\text{max}} = 7.7 \text{ N/mm}^2$ and 12.3 N/mm^2 for the lower and higher strength concrete).

6.5.4 Heating and cooling of the specimens

The three-point bending test specimens were heated in the experiment with the CFRP faced upwards (Figure 6-14). The strain distribution in the CFRP laminate after changing the temperature to -20°C , 50°C and 70°C is plotted in Figure 6-17a, both according to the finite element analyses and as was measured in the experiment. The experimental strain measurements showed good correspondence with the numerical results at 50°C but are overestimated by the numerical analyses at 70°C , probably due to time-dependent behavior of the adhesive.

It can be seen that the bond-slip relations according to Holzenkämpfer and Dörr resulted in a similar strain in the CFRP laminate near midspan. The strain was not decreasing to zero at the end of the bonded length near midspan (at 300 mm), as was seen in the double-lap shear tests, because the two bonded parts of the laminate were connected to each other by the concrete below the saw cut and, as a result, moved away from each other due to the expansion of concrete. The strains in the non-bonded part of the CFRP laminate at midspan were slightly lower than in the bonded part, probably due to curvature of the beam.

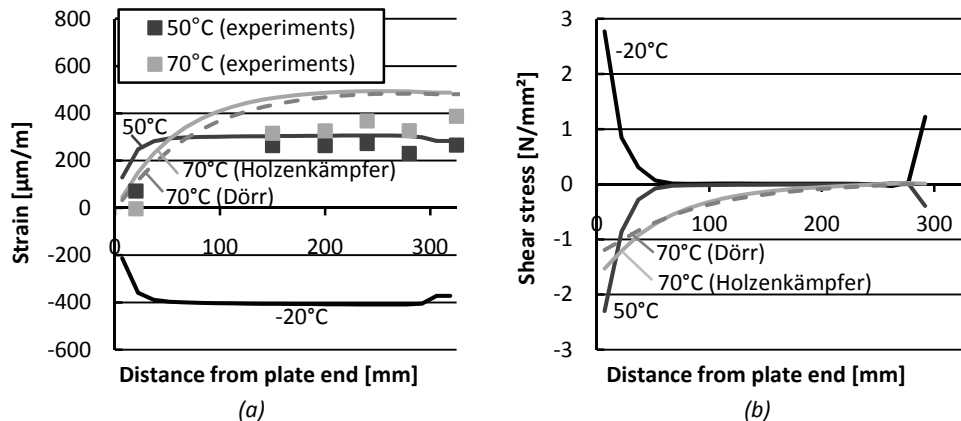


Figure 6-17: Thermal strains in the CFRP (a) and shear stresses in the interface elements (b) for the lower strength concrete specimens

The shear stresses in the concrete at the end of the bonded length near the support were similar to those found for the double lap shear tests (Figure 6-17b). However, at the end of the bonded length near midspan, significantly lower shear stresses were found, due to the fact that similar strains developed in the bonded and non-bonded part of the CFRP.

6.5.5 Loading of the specimens

The specimens were loaded with the CFRP laminate faced downwards (Figure 6-13). Turning the specimen from the position during heating (CFRP upwards) to this position (CFRP downwards) slightly affected the thermal strains in the non-bonded part at midspan (Figure 6-18a). The strain distribution due to the temperature change and due to loading (10 kN) is shown in Figure 6-18b for four different temperatures. The mechanical strain distribution (Figure 6-18c), which was needed to make a comparison with the experimental strain measurements, was determined in the same way as for the double-lap shear tests. The strain distributions at 70°C have been calculated with the bond-slip relation according to Dörr.

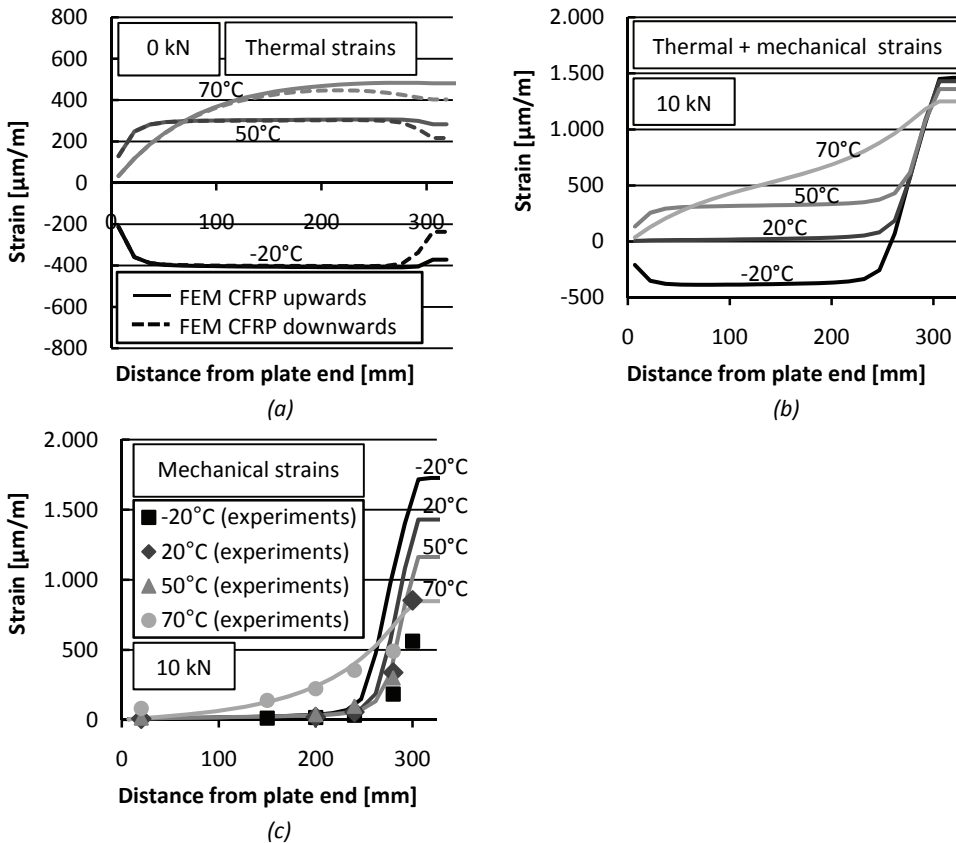


Figure 6-18: Thermal (a), total (b) and mechanical (c) strain distributions for different temperatures for the lower strength concrete specimens

It can be seen that, at a certain load level, the strain (Figure 6-18b) in the non-bonded part was not the same for the different temperatures, as was also observed in the experiments. Due to the lower Young's modulus of the adhesive at elevated temperatures, less stresses were transferred to the CFRP laminate, which resulted in a different equilibrium in the midspan cross-section with more tensile stresses in the concrete, above the saw cut. The corresponding shear stress distributions in the concrete adjacent to the concrete-adhesive interface are plotted in Figure 6-19 for 0 kN, 5 kN, 10 kN and 15 kN.

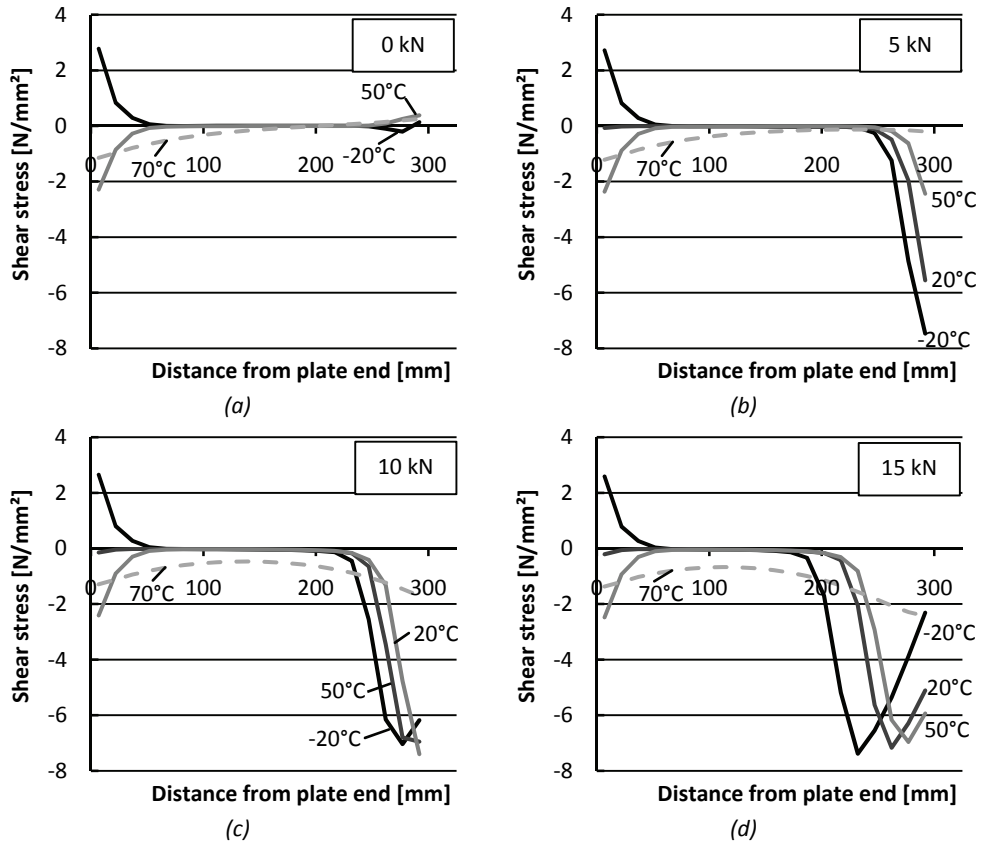


Figure 6-19: Shear stresses in the concrete adjacent to the concrete-adhesive interface at 0 kN (a), 5 kN (b), 10 kN (c) and 15 kN (d) at different temperatures for the lower strength concrete specimens

It can be seen that debonding initiated at the end of the bonded length near midspan. At this location, the shear strength ($\tau_{\max} = 7.7 \text{ N/mm}^2$) was first reached at about 5 kN for the specimen at -20°C (Figure 6-19b), while the specimen at 50°C reached the shear strength at about 10 kN (Figure 6-19c). At 70°C, significant lower peaks and more equally distributed shear stresses were found due to the reduced Young's modulus of the adhesive. The shear strength is, however, also significantly reduced, due to the changed type of bond failure, as has been explained before.

6.5.6 Temperature effects on the failure load

Again, additional calculations have been made to investigate the different effects of temperature, like the change in Young's moduli (E_a+E_c) and the differences in the coefficient of thermal expansion (α), individually and combined ($\alpha+E_a+E_c$). Figure 6-20 shows the results for the lower (a) and higher (b) strength concrete specimens, as well as the mean experimental failure loads. All numerical calculations in these figures, also for 70°C, were based on the bond-slip according to Holzenkämpfer.

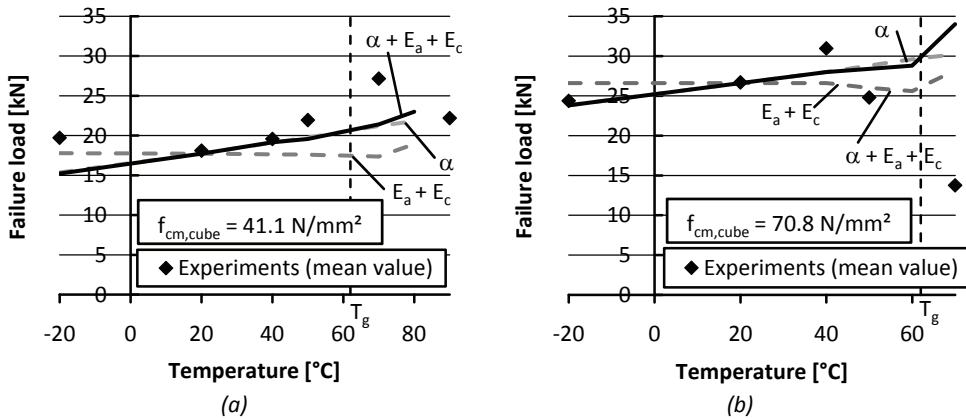


Figure 6-20: Effects of the reduced Young's moduli and the differences in coefficient of thermal expansion on the failure load for the lower (a) and higher (a) strength concrete specimens

The tendency in the numerical results up to 50°C corresponded to the tendency in the experimental data, although some small differences were found, for example at -20°C for the lower strength concrete specimens. Again, the increase in failure load up to 50°C can mainly be subscribed to the difference in the coefficient of thermal expansion between concrete and CFRP. At higher temperatures, the results of the finite element analyses did not correspond to the experimental results anymore, as the type of bond failure had changed in the experiment.

6.6 Bond behavior in the perpendicular shear direction

6.6.1 General

A temperature change also causes thermal strains and stresses in the concrete-adhesive-CFRP joint in the (shear) direction perpendicular to the longitudinal laminate direction (further called perpendicular direction). In the experiments, changing the temperature did not lead to debonding or cracking of the concrete at the sides of the CFRP laminate. Nevertheless, it was decided to investigate the effect of temperature on the development of thermal stresses in this direction by means of finite element analyses.

CFRP has a positive coefficient of thermal expansion in the perpendicular direction ($\alpha_f = 33 \cdot 10^{-6} / ^\circ\text{C}$ for Sika Carbodur), which is higher than that of concrete ($\alpha_c \approx 10 \cdot 10^{-6} / ^\circ\text{C}$). The bonded length is relatively small and the Young's modulus of the CFRP is significantly lower in this direction, compared to the longitudinal direction. It is expected that the development of thermal stresses in the perpendicular direction are lower compared to the longitudinal direction, due to these aspects. Moreover, time dependent creep behavior of the adhesive also reduces the effects of the thermal mismatch, as it mainly decreases the thermal strains in the CFRP close to the plate-ends, in the anchorage zones. As the anchorage zones are overlapping due to the short bonded length in the perpendicular direction, thermal strains are expected to reduce over the entire width due to the creep of the adhesive.

6.6.2 Finite element model

The development of thermal stresses in the perpendicular direction was analyzed with a finite element analysis of the cross-section of the three-point bending test specimen. The FE analysis has been carried out for a CFRP laminate with a width of respectively 25 mm and 100 mm (Figure 6-21). Time dependent behavior of the adhesive as well as the effect of loading in the longitudinal direction on the stresses in the perpendicular direction have been neglected, but will be taken into account when discussing the results of the finite element analyses.

The finite element model was modeled in the same way as in the previous analyses, although plane strain elements have been used instead of plane stress elements, as recommended for the analysis of a cross-section of a (long) beam (TNO DIANA B.V. 2005). The strengthened side was faced upwards, in the same position as in the experiment during heating in the oven, and was supported on springs, in the same way as for the three-point bending tests.

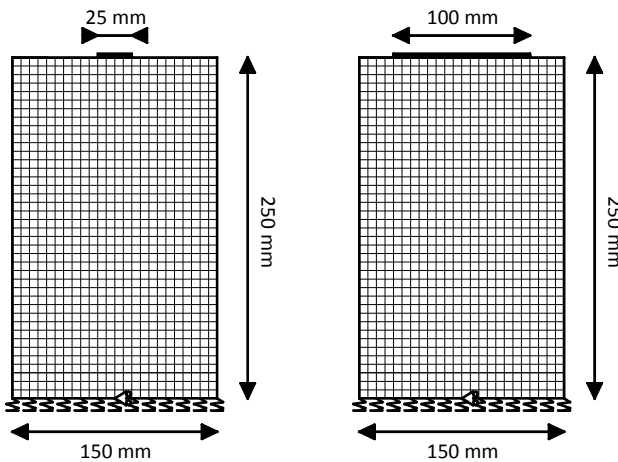


Figure 6-21: Finite element model of the beam cross-section

6.6.3 Material properties

For the concrete and adhesive elements, the same (temperature dependent) material properties were applied as in the previous analyses. For CFRP, different properties had to be applied as it is an orthotropic material. The CFRP laminates that were used in the experiments have a Young's modulus of 3000 N/mm² (Sika 2007) and a coefficient of thermal expansion of $33 \cdot 10^{-6}$ /°C in the direction perpendicular to the fiber direction (Table 4-6). The CFRP properties were taken as temperature independent for the analyses, although it is likely that the Young's modulus will decrease with increasing temperature, due to the effect of temperature on the matrix material properties. This is a conservative approach, as thermal stresses are smaller for a reduced CFRP Young's modulus. For the interface elements, linear elastic material properties were applied in the normal and shear direction as it was expected that the shear strength will not be exceeded.

6.6.4 Thermal strains and stresses

The normal stress in the CFRP laminate over its width (a) and the shear stress in the concrete adjacent to the concrete-adhesive interface (b) are plotted in Figure 6-22, after increasing the temperature up to 50°C and 70°C.

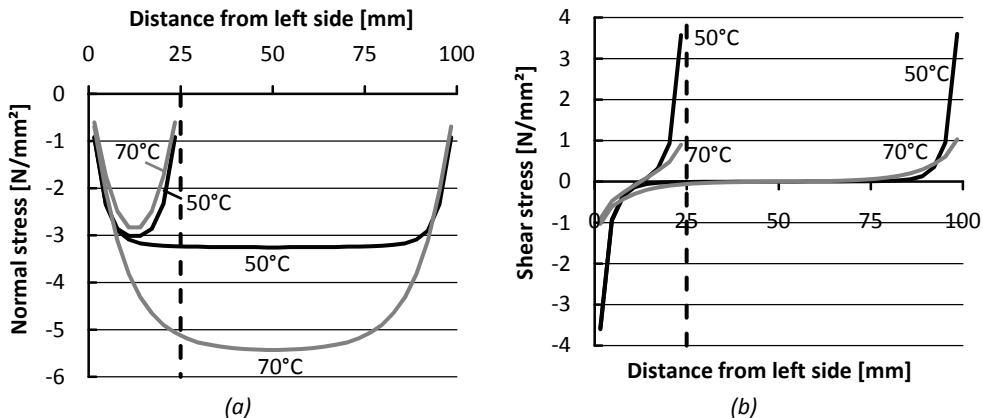


Figure 6-22: Normal stress in the CFRP (a) and shear stress in the concrete at the interface with the adhesive (b) at 50°C and 70°C

The temperature increase up to 50°C resulted in a compressive stress in the CFRP laminate of about 3 N/mm². At 70°C, a slightly lower compressive stress was found for the CFRP laminate of 25 mm width, while for the 100 mm wide CFRP laminate, a higher compressive stress was found. This can be explained as follows. Seen from the sides of the laminate, stresses are building up faster at 50°C, compared to 70°C, due to the higher Young's modulus of the adhesive. In the small CFRP laminate, stresses cannot fully develop to their maximum ($\approx E_f \alpha_c \Delta T$), as the two anchorage lengths are overlapping each other, resulting in lower stresses in the middle at 70°C, compared to 50°C. In the wide CFRP laminate, stresses can (almost) fully develop, resulting in higher stresses in the middle at 70°C.

The reduced Young's modulus of the adhesive at 70°C resulted in lower shear stresses near the sides of the laminate, compared to 50°C, similar as in the previous analyses. No significant differences were found for the 25 mm and 100 mm wide CFRP laminate. The shear stresses at 50°C were still below the shear strength of the concrete (6 à 8 N/mm²). It could, however, be possible that the additional thermal shear stresses in the perpendicular direction affect the debonding behavior in the longitudinal direction. However, based on the fact that thermal stresses will reduce due to creep and the reduced Young's modulus of the adhesive, especially in the end anchorage zone (Section 5.3 and 5.4) and the fact that the laminate length is very short in the perpendicular direction (overlapping anchorage zones), it can be expected that the thermal stresses will almost completely disappear. It is therefore expected that the effect of the thermal mismatch in the perpendicular direction will not (significantly) affect the debonding behavior in the longitudinal direction.

6.7 Summary

The bond behavior of the concrete-adhesive-CFRP joint in the longitudinal shear direction has been analyzed with finite element simulations of both the double-lap shear test and the three-point bending test. The bond behavior is affected by temperature in a similar way in both tests. Two tendencies can be distinguished. Up to around the glass transition temperature of the adhesive, an increasing failure load was found with increasing temperature. This was mainly caused by the differences in the coefficient of thermal expansion between concrete and CFRP. The bond-slip relation according to Holzenkämpfer can be applied for this temperature range to simulate the bond behavior of the concrete adjacent to the concrete-adhesive interface. The effect of the reduced Young's moduli of concrete and adhesive on the bond behavior up to 50°C is negligible.

Above the glass transition temperature, a decreasing failure load was found with increasing temperature in the experiments. It turned out that the bond-slip relation according to Holzenkämpfer was not valid anymore in this temperature range, as the type of failure had changed, in the experiment, from failure in the concrete adjacent to the concrete-adhesive interface to failure exactly in between the concrete and adhesive. Both a different bond-slip relation and the reduced Young's modulus of the adhesive had to be taken into account to simulate the tests in this temperature range. With the bond-slip relation according to Dörr it was possible to simulate the load-displacement behavior, although the shear strength in this model had to be adjusted to fit the numerical results to the experimental results. It turned out that, above the glass transition temperature, there was no clear relation between the shear strength in the model and the strength of the adhesive or (mode I) bond strength of the concrete-adhesive interface at elevated temperature. The overall tendency is however a decreasing shear strength with increasing temperature.

7 Effect of temperature on full scale CFRP strengthened beams

7.1 Test program

Experimental research into the effect of elevated temperature on CFRP strengthened concrete structures has so far only been carried out with small scale bond tests. In these tests, failure is generally governed by mode II fracture (debonding) of the concrete adjacent to the adhesive layer. In full scale flexural CFRP strengthened structures, like beams and slabs, failure can be initiated by different debonding mechanisms, as has been discussed in Section 2.4. Debonding can initiate at different locations along the length of the CFRP laminate and is affected by cracks in the concrete perpendicular to the bonded area, which generally do not occur in small scale bond tests. Moreover, failure can also initiate at the plate-end by the development of a vertical crack that propagates further along the level of the internal steel reinforcement or as a shear crack. These types of (debonding) failure may all be affected by temperature in a different way. It was therefore decided to set up a test program in which the influence of temperature is investigated on full scale beams that are strengthened with externally bonded CFRP (Hermes (2006)).

Four different beams were designed in such way that the four most important debonding mechanisms were most probably covered at room temperature (Figure 7-1 and Table 7-1). 'Debonding at flexural cracks' and 'debonding due to the unevenness of the concrete surface' were not investigated due to the fact that the first only leads to local debonding (Section 2.4.3.1), while the second can easily be prevented by removing the unevenness before applying the CFRP laminate (Section 2.4.3.6). Concrete cover rip-off and plate-end shear failure are expected to initiate in the same way, and are therefore investigated with only one beam. Given the amount of shear reinforcement, it was expected that beam D would fail by concrete cover rip-off.

It was decided to only vary the concrete grade and the CFRP dimensions, which had the advantage that the same test setup could be used for all tests. The design of the beams was based on the models in the Dutch CUR Recommendation 91 (first edition (CUR 2002)), which is mainly based on *fib*-Bulletin 14 (*fib* 2001). Note that this CUR Recommendation has been replaced with the second edition in 2007 (CUR 2007).

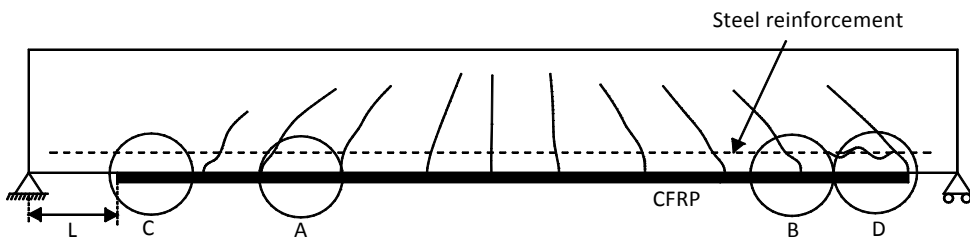


Figure 7-1: The debonding mechanisms that were investigated with the full scale experiments

Table 7-1: Experimental full scale test program

Beam	Designed debonding mechanism at room temperature	Concrete grade	Width of CFRP (b_f)	Distance plate-end-support (L)
A	Debonding due to high shear stresses	C20/25	50 mm	100 mm
B	Debonding at shear cracks	C45/55	80 mm	100 mm
C	Debonding at the end anchorage	C45/55	80 mm	300 mm
D	Concrete cover rip-off	C20/25	150 mm	100 mm

For each debonding mechanism, three similar beams were made that were tested at three different temperatures; 20°C, being the reference beam, and 50°C and 70°C, which is respectively just below and just above the glass transition temperature of the adhesive ($T_g = 62^\circ\text{C}$).

7.2 Test setup

The beams were loaded in four point bending (Figure 7-2) with two loading points at 650 mm from midspan. The beams measured $200 \times 450 \times 4000 \text{ mm}^3$ and spanned 3800 mm. The same reinforcement was applied for all beams. Four bars $\varnothing 12 \text{ mm}$ (Feb 500 HWL, HK) were applied in the tensile zone and two bars $\varnothing 8 \text{ mm}$ in the compressive zone. Stirrups $\varnothing 8 \text{ mm}$ were applied at a 100 mm centre-to-centre distance, except for the part at midspan.

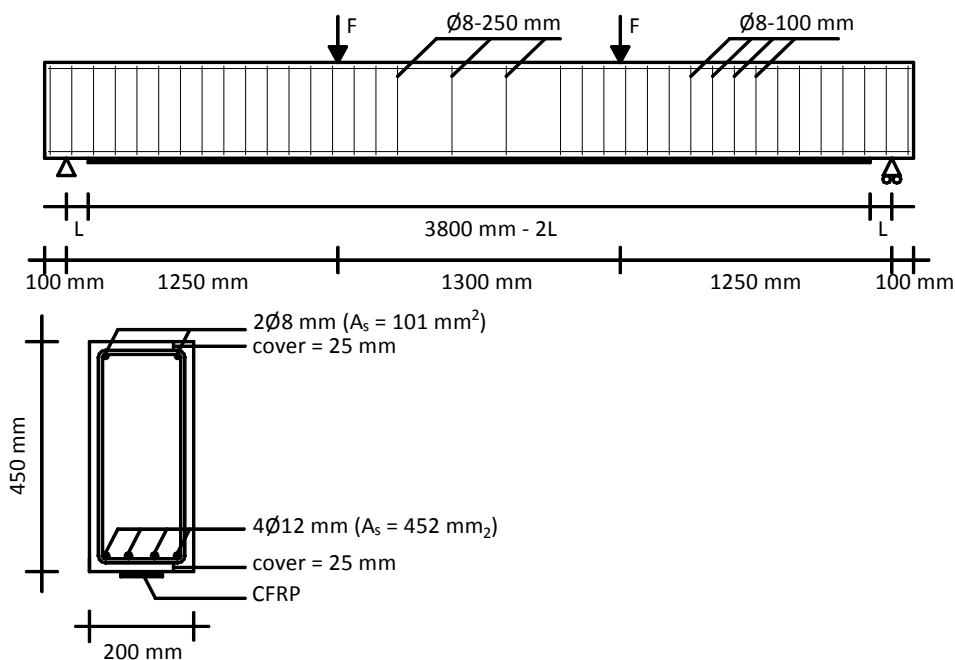


Figure 7-2: Dimensions of the full scale beams

After sandblasting and cleaning of the concrete surface, a CFRP laminate (SIKA Carbodur) of 1.2 mm thickness was glued to the soffit of the beam. The applied width and length of the laminates are given in Table 7-1. A 2-component epoxy adhesive (SikaDur 30) with a thickness of approximately 1.5 mm was used to glue the CFRP laminates to the concrete surface. Both the CFRP and the adhesive were the same as the ones that were used for the small scale bond tests (Chapter 5).

A temporary isolated chamber was designed for testing of the beams at elevated temperature (Figure 7-3a). Small windows were applied to be able to inspect the beams during the tests. The isolated chamber could be opened and closed after each test for removing and replacing of the beams and the measurement equipment (Figure 7-3b).

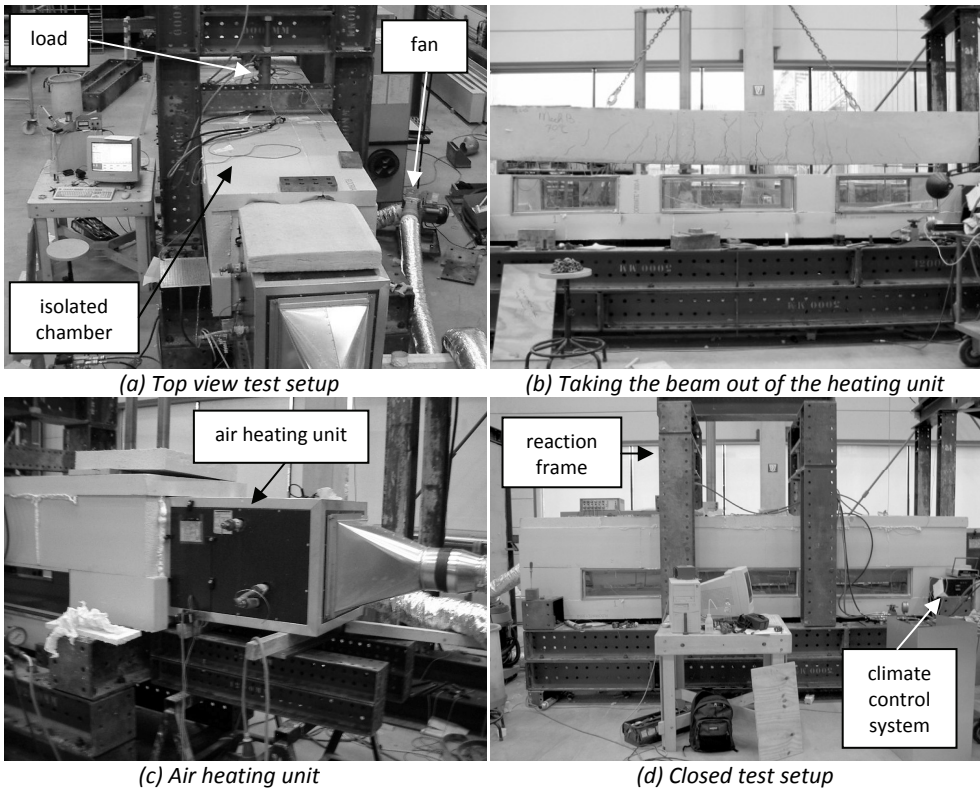


Figure 7-3: Test setup of the full scale beams

The isolated chamber was part of a closed air circuit, in which the air was circulated by means of an air-fan. The air was circulated through an air-heating unit (6.6 kW) (Figure 7-3c) and subsequently through the isolated chamber. Additional small fans were placed in the isolated chamber to make sure that the temperature was the same between the bottom and the top of the beam. Air temperature and pressure were measured by a climate control system (Figure 7-3d), while the concrete temperature was measured by thermocouples at various locations, including in the core of the beam (Figure 7-4).

The vertical displacement of the beam was measured with LVDTs at five different points. This was at the supports to measure any accidental displacement of the supports, at the cross-section where the loads were applied, and at midspan. Eleven strain gauges were applied on the CFRP laminate to measure the strain distribution in the CFRP laminate, both during heating and during loading of the beam (Figure 7-4).

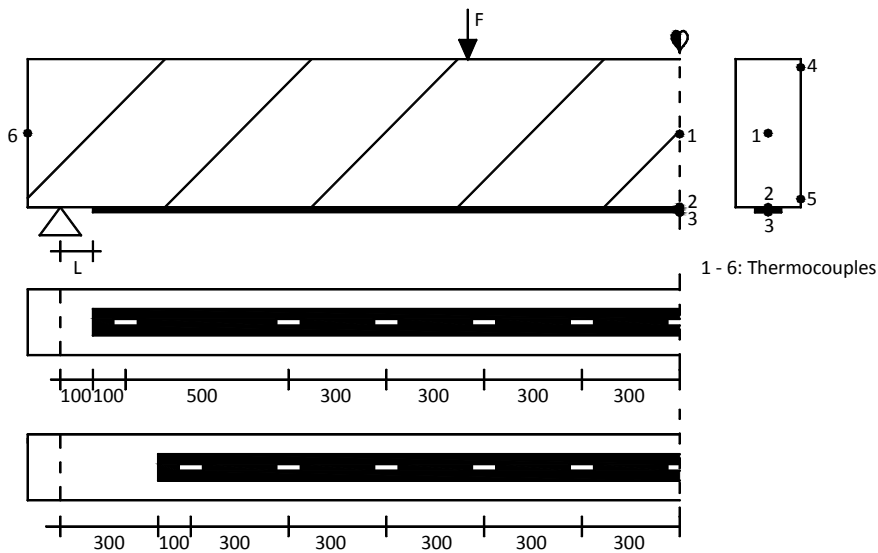


Figure 7-4: Location of the thermocouples and the strain gauges on the CFRP laminate for $L=100$ mm and $L=300$ mm

The beam was first heated in the isolated chamber until the entire beam reached the required temperature. This took about 6 hours for the beams tested at 50°C and 30 hours for the beams tested at 70°C . The significant difference in heating time was caused by the fact that heating of the specimens was not allowed during night, because of safety regulations. After heating of the beams, the maximum temperature variation between the core and the surface of the concrete was approximately 5°C , which was regarded acceptable. After heating, the beams were loaded by two hydraulic jacks at a rate of 6.6 kN/min until yielding of the internal steel reinforcement occurred. This was determined by the slope of the load-deflection diagram. From that point on, the loading rate was reduced to 3.3 kN/min until failure of the beam occurred.

7.3 Material properties

Due to the relatively long preparation time that was needed for each test, it was decided to cast the beams at different points in time. In this way it was possible to have, on average, an almost similar age at testing (49 days on average) (Table 7-2). One of the beams B and D were produced from another concrete cast as the other two in the series, due to problems with the delivery of the concrete (Table 7-3). The differences in the material properties between the two casts are rather small for C20/25 and negligible for C45/55 (Appendix F).

Table 7-2: Concrete grade of the tested beams and (age at test date)

Beam	20°C	50°C	70°C
A	C20/25a (56 d)	C20/25a (51 d)	C20/25a (59 d)
B	C45/55b (41 d)	C45/55a (43 d)	C45/55b (49 d)
C	C45/55a (46 d)	C45/55a (49 d)	C45/55a (48 d)
D	C20/25b (40 d)	C20/25a (66 d)	C20/25b (44 d)

Table 7-3: Mean values of the measured concrete material properties at room temperature

Material properties	C20/25a [N/mm ²]	C20/25b [N/mm ²]	C45/55a [N/mm ²]	C45/55b [N/mm ²]
Cube compressive strength ($f_{cm,cube}$)	27.7	36.0	51.2	52.3
Tensile splitting strength ($f_{ctm,sp}$)	2.3	3.0	3.7	3.6

The bond strength of the concrete surface in the direction perpendicular to the bonded area was experimentally determined by pulling-off a glued steel cylinder Ø50 mm from the concrete surface according to CUR Recommendation 20 (CUR 1990), similar as described in Section 5.2.2. The bond strength was determined at 20°C, 50°C and 70°C (Appendix F). The mean values are shown in Table 7-4. The individual test results are plotted in Figure 7-5. The material properties of the CFRP laminates (SIKA Carbodur) and the adhesive (SikaDur-30) have been given in Section 4.4 and 4.5.

Table 7-4: Mean concrete surface bond strength (f_{cbm}) at different temperatures

Temperature	C20/25a [N/mm ²]	C20/25b [N/mm ²]	C40/45a [N/mm ²]	C40/45b [N/mm ²]
20°C	2.6	2.8	4.5	4.8
50°C	1.8	2.2	3.9	3.8
70°C	n/a	1.3	2.4	2.9

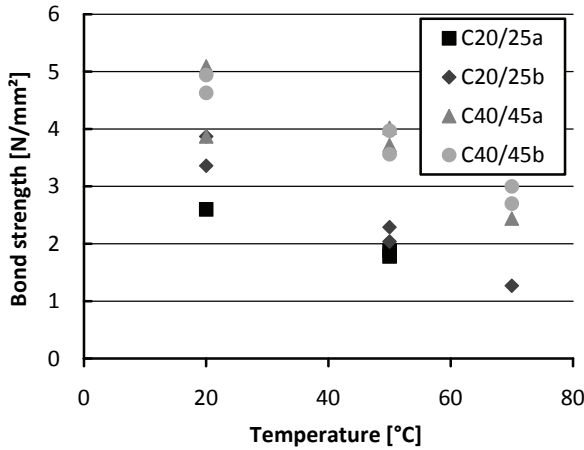


Figure 7-5: Test results of the concrete surface bond tests at 20°C, 50°C and 70°C for the different concrete grades

7.4 Heating of the beams

The measured strains along the length of the CFRP laminate after heating of beams A and D (C20/25) are shown in Figure 7-6. Similar results were found for beams B and C (C45/55) (Appendix G.1). Indication (I) represent the measurements on the beams that were tested 50°C, while indication (II) represents the measurements at 50°C on the beams that were later heated up to 70°C. The strain distributions according to the modified model of Di Tommaso et al. (Section 6.4.4) are also given in Figure 7-6 for comparison. The coefficient of thermal expansion of concrete was taken equal to $10 \cdot 10^{-6} / ^\circ\text{C}$ and the effective concrete height equal to 50 mm. Note that the analytical model neglects the time-dependent creep behavior of the adhesive, but also the effect of curvature of the beam, due to the difference in thermal expansion between concrete and CFRP.

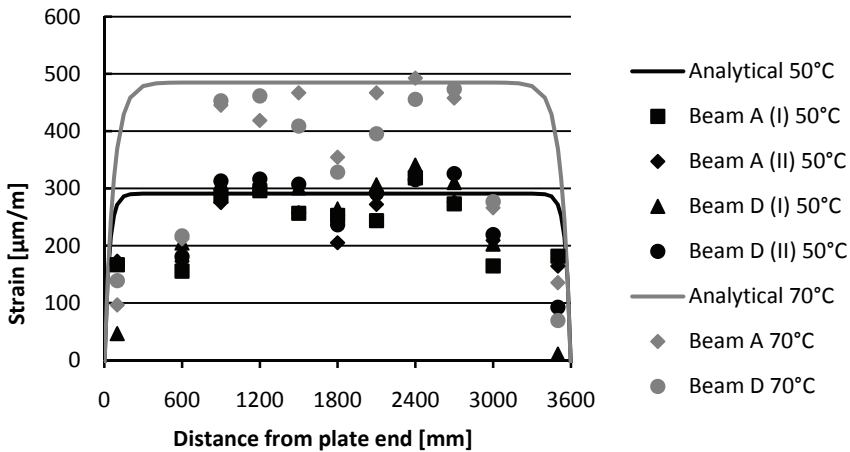


Figure 7-6: Thermal strains in the CFRP laminate after heating of beams A and D up to 50°C and 70°C

It can be seen that there is a similar tendency for the analytical and experimental strain distributions. The CFRP strain is approaching to zero close to the plate-end and is almost equal to the thermal expansion of concrete further away from the end, as could be expected. However, starting from the plate-end, the CFRP strains build up in a faster way in the analytical model compared to what was measured in the experiments, despite the fact that the reduced Young's modulus of the adhesive was taken into account in the analytical model. It is expected that this was caused by the time-dependent behavior of the adhesive, which reduced the thermal strains in the anchorage zone in time. This time-dependent behavior can clearly be seen in Figure 7-7. The strains at 100 mm from the plate-ends initially followed the expansion of the concrete, but after about 1 hour started to decrease in time. Also at 600 mm from the plate-end, strains decreased in time, although the reduction was significantly smaller. Further away from the plate-end, no reduction in time was found. The decreasing strains at the plate-ends implied that the anchorage length, over which the stresses were transferred from the concrete to the CFRP, increased in time.

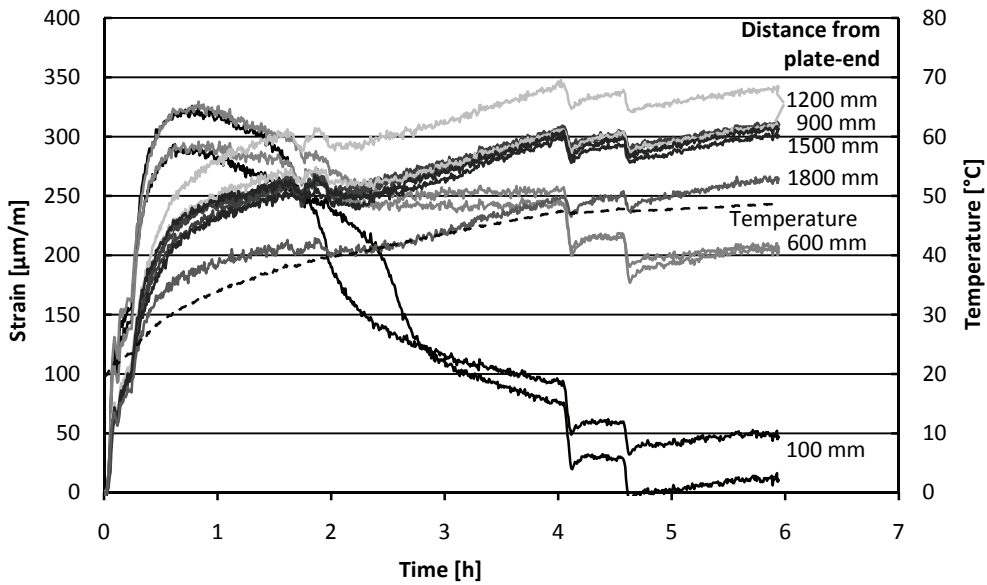


Figure 7-7: Thermal strain development in time for beam A during heating up to 50°C

The strain in the middle of the beam (1800 mm) was slightly lower compared to the strain further away from the middle (see also Figure 7-6). This behavior was observed for all beams (Appendix G.1) (Hermes 2006) and is expected to be related to curvature of the beams due to the lower thermal expansion of the CFRP laminate compared to that of the concrete.

The shear stress distribution in the concrete adjacent to the concrete-adhesive interface, can also be calculated with the modified model of Di Tommaso et al. (2001) (equation 3.2) (assuming that no non-linear bond-slip behavior has occurred). Note however, that it is likely that these shear stresses initially will develop, but will decrease in time, due to the time dependent behavior of the adhesive. Figure 7-8 shows the analytical shear stress distributions in the concrete adjacent to the concrete-adhesive interface of beam A over the length of the CFRP laminate and, in detail, at the plate-end for 50°C and 70°C. For the other beams, similar results were found (Appendix G.2).

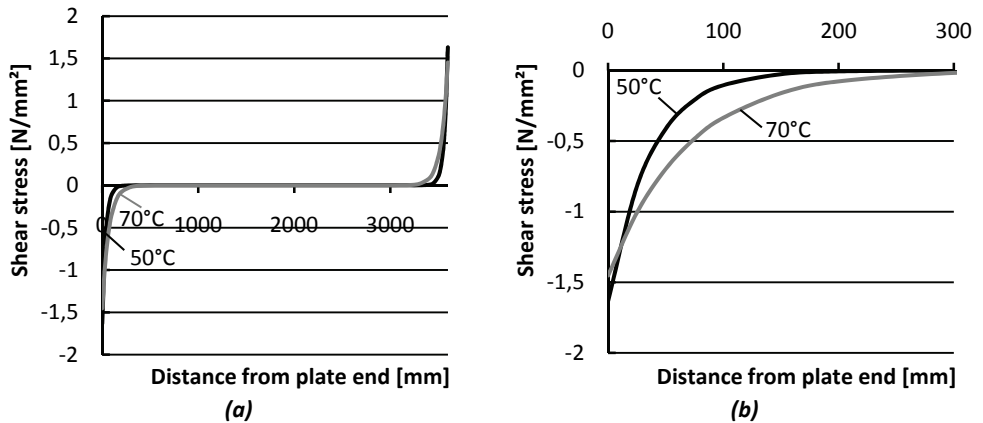


Figure 7-8: Analytical thermal shear stresses in the concrete adjacent to the concrete-adhesive interface over the length of the CFRP laminate (a) and, in detail, at the plate-end (b) for beam A

It can be seen that shear stresses mainly develop in the end anchorage zone. The peak in shear stress at the plate-end turned out to be lower at 70°C, compared to 50°C, despite the higher temperature, due to the reduced Young's modulus of the adhesive. Compared to the bond (shear) strength (± 4 à 5 N/mm^2 for beam A), the shear stress is still relatively low, which indicates that it is not likely that non-linear bond-slip behavior has occurred.

7.5 Loading of the beams

7.5.1 Beam A

The beams A that were designed to fail by ‘debonding due to high shear stresses’ showed hardly any differences in the load-displacement response between the different applied temperatures (Figure 7-9). The failure load was also similar (102 – 104 kN) for all tested temperatures.

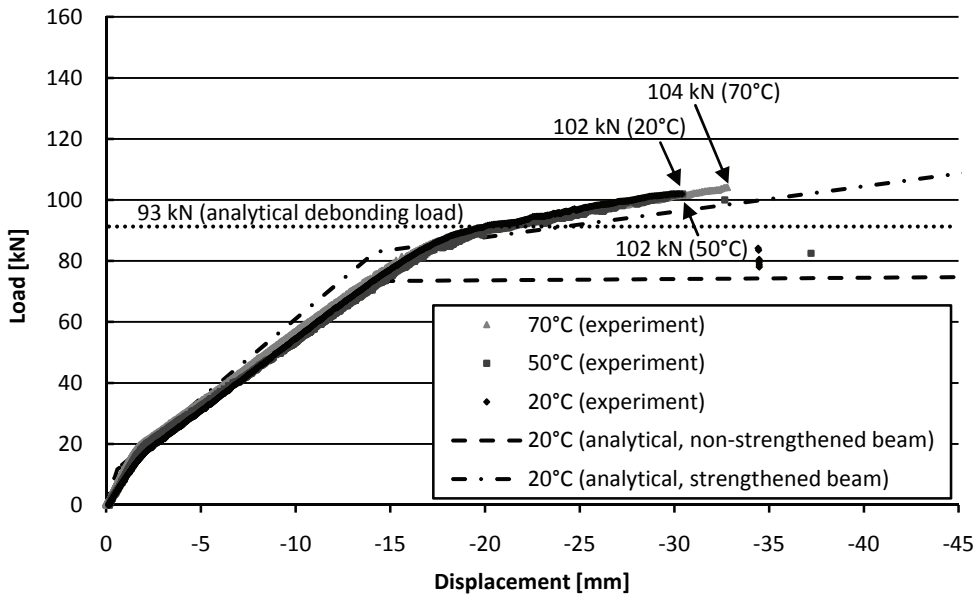


Figure 7-9: Load-displacement curves for beam A at 20°C, 50°C and 70°C

For comparison, the load-displacement behavior was also analytically determined with a cross-sectional analysis according to Eurocode 2 (CEN 1997a) (Appendix H). In the cross-section analysis, the load and corresponding displacement are determined at cracking, yielding and failure (concrete, steel or CFRP failure). These points are connected with straight lines. The analysis has been performed for both a strengthened beam (at 20°C) and for a non-strengthened beam (with the same material properties as the strengthened beam). It can be seen that some small differences were found between the analytical and experimental load-displacement curves of the strengthened beam. This is related to the simplifications that were made in the analysis (CFRP over entire length beam, no tension in concrete after cracking, etc., see Appendix H). Moreover, the material properties after 28 days were used in the analysis, while the beam was tested after 56 days. The overall tendency of both load-displacement curves is, nevertheless, similar.

The beams that were tested at 20°C and 50°C showed a few load steps after failure at about 80 kN, which indicates that the capacity of the non-strengthened beam (76 kN) is predicted well. Compared to the non-strengthened beam, an increase in capacity of 34% was achieved by strengthening of the beam.

The load at which debonding was expected to occur is also indicated in Figure 7-9 and is based on the model for ‘debonding due to high shear stresses’ by Matthys (2000), as described in Section 2.4.3.2. The analytical debonding load has been computed by applying mean material properties (at 28 days) and safety and material factors equal to 1.0 (Appendix I.1). The failure load in the experiment was about 10% higher than the analytical debonding load according to the model by Matthys (2000).

Based on the observations during the tests, it seemed that debonding of the externally bonded CFRP initiated, at all temperatures, in the region away from the plate-end, just outside the constant moment region, and propagated towards the plate-end. It was however difficult to indicate the exact location due to the explosive behavior of the debonding. Outside the constant moment region, cracks were mainly inclined, which might have negatively affected the debonding load due to the differences in vertical displacement between the two sides of an inclined (shear) crack. No significant differences were found in the crack patterns of the beams after failure between the different temperatures (Figure 7-10). Visual inspections of the specimens during the tests did also not show significant differences in the crack patterns just before failure. It can be seen that cracks had not developed over the entire bonded length of the CFRP laminate.

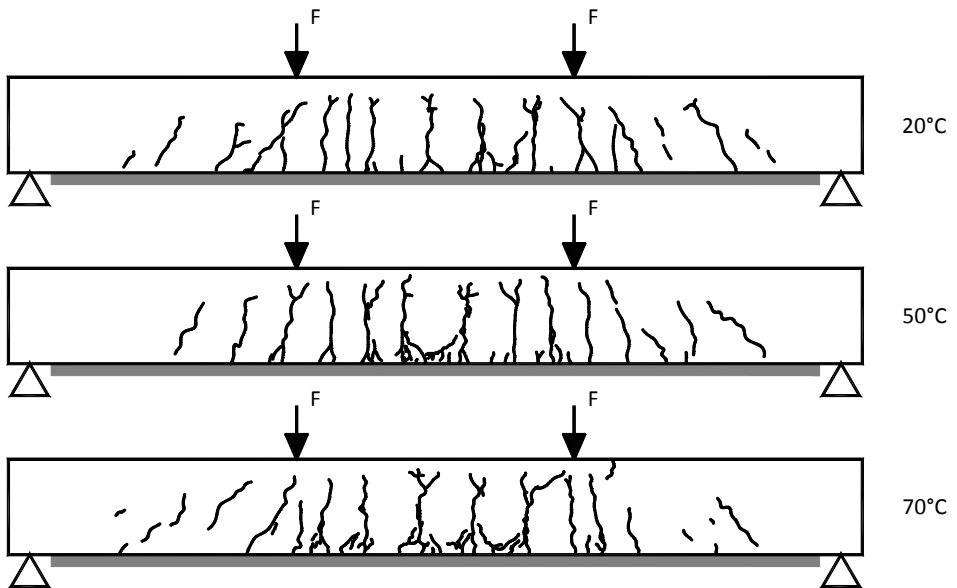


Figure 7-10: Crack patterns after failure of beam A at 20°C, 50°C and 70°C

At 20°C and 50°C, debonding propagated in the concrete, leaving a small layer of concrete remaining attached to the adhesive after debonding (Figure 7-11). Also at 70°C, concrete remained attached to the adhesive after debonding at several parts along the length of the CFRP laminate, while in the other parts, no concrete remained attached (Figure 7-11). This seems to indicate that debonding was shifting from concrete bond failure to interfacial failure exactly in between the concrete and the adhesive. This debonding behavior was different compared to what was found in the small scale bond tests at 70°C, where no concrete remained attached to the adhesive after debonding.

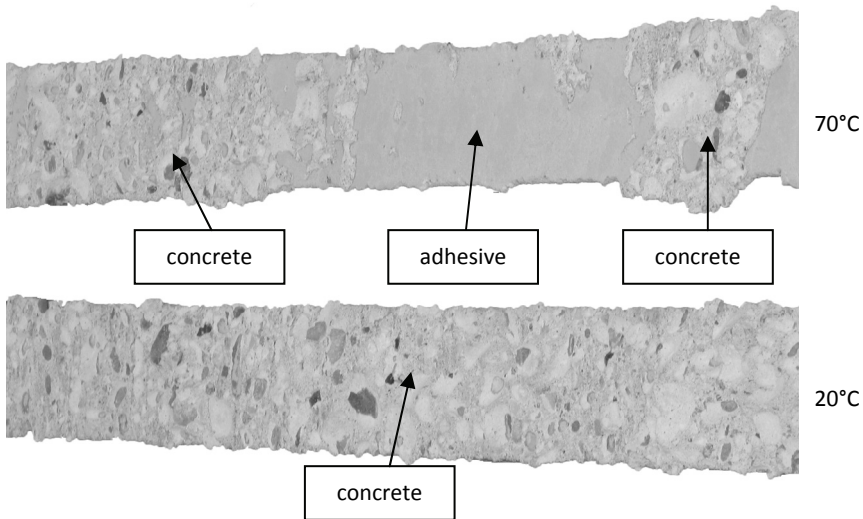


Figure 7-11: Failure surface after debonding of beam A at 20°C (bottom) and 70°C (top)

The strain distributions in the CFRP laminate at 50 kN and 100 kN are plotted in Figure 7-12 for 20°C, 50°C and 70°C. The strain in the CFRP laminate corresponds to the strains due to heating plus the strain due to loading of the beam. It can be seen that there is, at the same external load, a tendency of slightly higher strains with increasing temperature. This can be explained by the initial thermal strains that had developed in the CFRP after heating of the beams (Section 7.4) and that acted in the same direction as the mechanical strains due to loading of the beam.

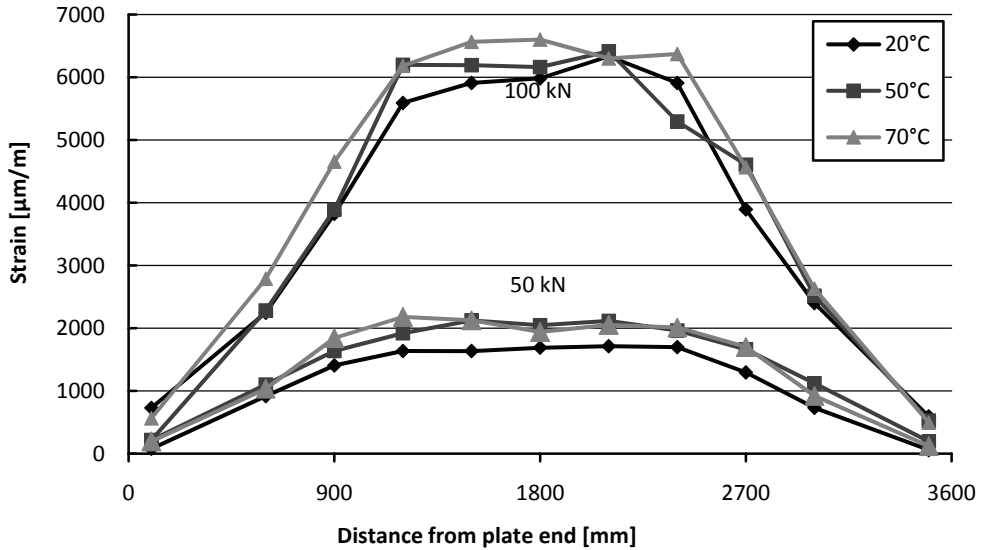


Figure 7-12: Normal strains in the CFRP laminate of beams A at 50 kN and 100 kN

In the small bond tests, the strain distribution was significantly affected by the reduced Young's modulus of the adhesive at 70°C. This was not observed in the full scale beam at 70°C. It is expected that the reduced Young's modulus mainly affects the distribution close to the ends of the laminate, while it has no significant effect on the strain distribution further away from the plate-end. Only one strain gauge was applied in the anchorage zone, so the strain distribution in the anchorage zone itself was not determined. It can however be concluded that, at all temperatures, strains could build up to the same level due to the relatively long available anchorage length.

The effect of the thermal mismatch between concrete and CFRP, which was affecting the failure load of the small scale tests, turned out to be negligible for the full scale beams. This can be explained by the fact that shear stresses in the concrete due to the thermal mismatch between concrete and CFRP mainly develop near the plate-end, as was shown in Figure 7-8a, and not at the location where debonding was expected to have initiated. It can therefore be concluded that both the reduced Young's modulus and the thermal stresses did not significantly affect this debonding mechanism.

The failure load of the beam at 70°C was also not affected by the expected reduced bond strength of the concrete-adhesive-CFRP joint at this temperature. This might be related to the fact that the beam was heated up to 70°C with a heating cycle, as heating was not allowed during the night. This could have increased the glass transition temperature of the adhesive (Section 4.5.3) and therefore have increased the bond strength at 70°C. This might also explain the fact that significant more concrete remained attached to the adhesive at this temperature, compared to the small scale bond tests.

7.5.2 Beam B

The beams B were strengthened with a wider CFRP laminate (80 mm) and produced with a higher concrete grade (C45/55) compared to beams A (50 mm and C20/25 respectively). The beams were designed to fail by ‘debonding at shear cracks’ and showed almost similar load-displacement curves at 20°C, 50°C and 70°C (Figure 7-13), similar as beam A.

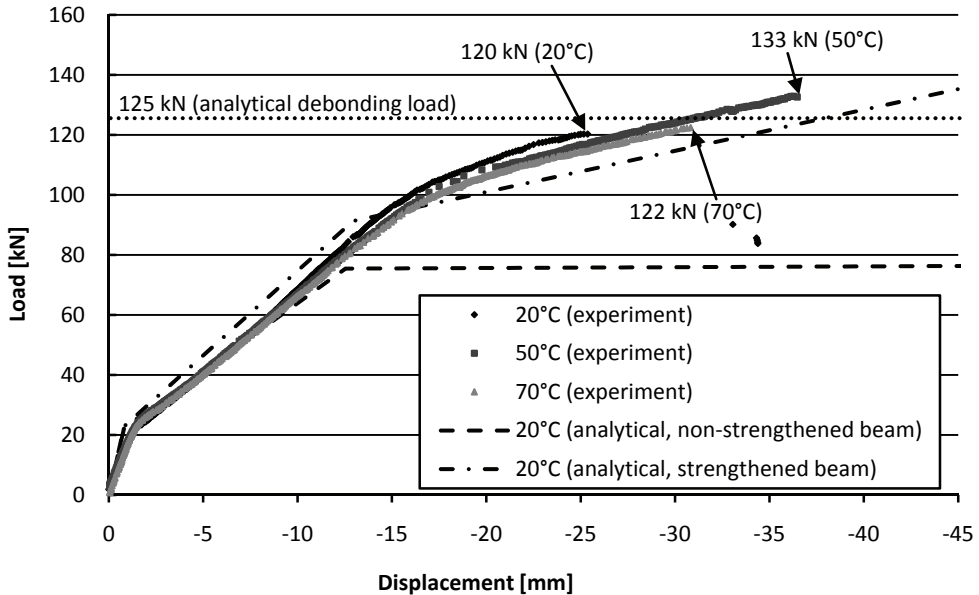


Figure 7-13: Load-displacement curves for beam B at 20°C, 50°C and 70°C

A slightly decreasing stiffness was observed with increasing temperature, which can be explained by the reduced Young’s modulus of the concrete and the adhesive at elevated temperature. The failure load at 50°C was about 10% higher compared to 20°C and 70°C. This is possibly related to the concrete type that was used for the beam at 50°C, which was different compared to what was used for the beams that were tested at 20°C and 70°C. Moreover, the thermal stresses will result in a “pretensioned” beam at elevated temperature, which could explain a part of the higher failure load (± 1.5 kN according to calculations). All failure loads were higher compared to beam A, as expected, due to the wider CFRP laminate and higher concrete grade.

Again, small differences were found between the analytical and experimental load-displacement curves, due to the same reasons as for beam A. The failure load of the strengthened beam at 20°C (120 kN) was 52% higher compared to the (analytical) failure load of a similar non-strengthened beam (79 kN) (Appendix H.4). The debonding load was also analytically determined according to the model for ‘debonding at shear cracks’ by Matthyss (2000) (Section 2.4.3.3 and Appendix I.2) and turned out to be slightly higher (125 kN) compared to the failure load in the experiment (120 kN).

Based on the observations during the test, it seemed that debonding of the externally bonded CFRP initiated at about the same location as for beam A, away from the plate-end, but outside the constant moment region. Debonding seemed to have propagated in the concrete adjacent to the concrete-adhesive interface towards the plate-end. A thin layer of concrete remained attached to the adhesive after debonding, also at 70°C. Again, it was difficult to indicate the exact location where debonding had initiated due to the explosive debonding behavior. It was therefore not possible to indicate whether the beam failed due to 'debonding at shear cracks' or 'debonding due to high shear stresses'. In both debonding mechanisms, debonding is expected to be mainly related to high shear stresses in the concrete adjacent to the concrete-adhesive interface, as explained in Section 2.4.3.2. Normal stresses due to the difference in vertical displacement between the two sides of a shear crack will, most likely, have negatively affected the debonding load.

Similar crack patterns were observed for the three beams after failure (Figure 7-14). Compared to beam A, cracking had occurred over a wider part of the beam, although the end anchorage zone still remained uncracked.

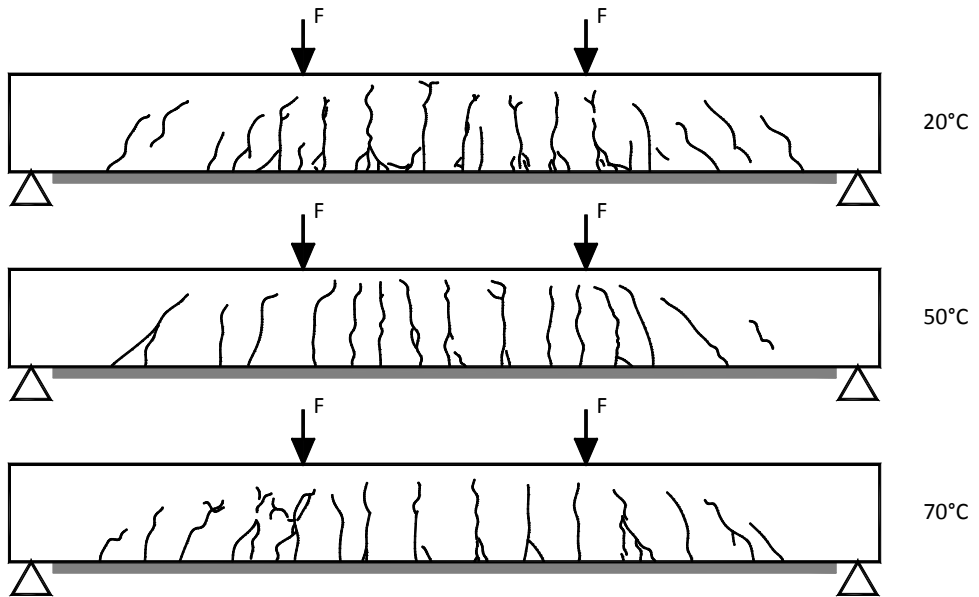


Figure 7-14: Crack patterns after failure of beam B at 20°C, 50°C and 70°C

The normal strain distribution in the CFRP laminate at 50 kN and 100 kN is shown in Figure 7-15 for the different temperatures. Again, the tendency was a slightly higher strain distribution with increasing temperature, which is expected to be a result of the initial thermal strains in the CFRP laminate. Strains in the CFRP laminate were lower compared to those in beam A at the same load, due to the wider CFRP laminate that has been used for beam B.

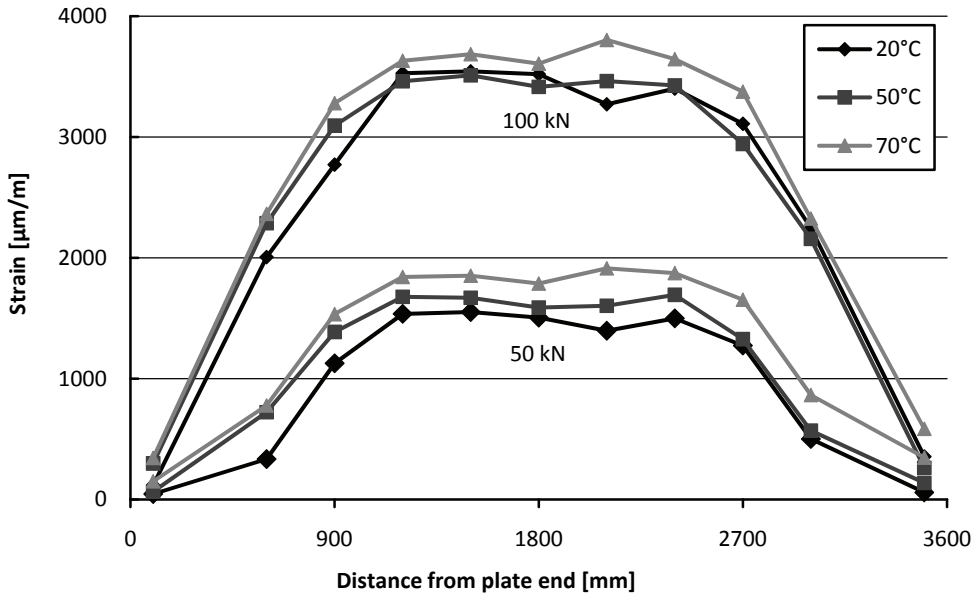


Figure 7-15: Normal strains in the CFRP laminate of beam B at 50 kN and 100 kN

It can be concluded that beam B was not significantly affected by temperature, due to the same reasons as for beam A. Debonding in both beam A and B is expected to be mainly related to high shear stresses in the concrete adjacent to the concrete-adhesive interface. Like for beam A, thermal stresses in the CFRP laminate and the reduced Young's modulus of the adhesive are mainly affecting the shear stresses in the anchorage zone, and not (significantly) further away from the plate-end, where debonding seemed to have initiated. Moreover, the type of bond failure was not significantly affected at elevated temperature and was still governed by failure of the concrete at 70°C, possibly due to an increase of T_g due to the heating cycle during heating of the beam.

7.5.3 Beam C

Beam C was designed to fail by ‘debonding at the end anchorage’ and was therefore strengthened with a shorter CFRP laminate compared to beam B. At 20°C, the beam failed at 132 kN, which was about 69% higher than the (analytical) failure load of a similar non-strengthened beam (78 kN) (Figure 7-16). The failure load was also higher than that of beam B at 20°C (120 kN), despite the shorter laminate length. It was however similar to the failure load of beam B at 50°C (133 kN), which was produced with the same concrete as beams C. This might indicate that the bond strength of this type of concrete (C45/55a) was slightly higher compared to that of beam B at 20°C and 70°C (C45/55b). This was, however, not observed in the concrete surface bond tests (Table 7-4).

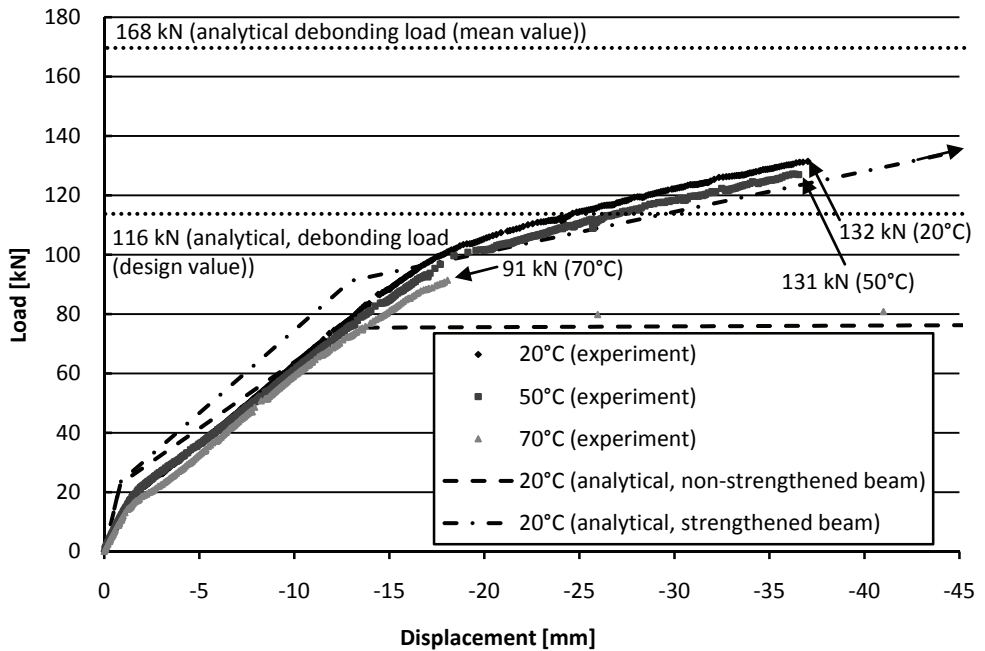


Figure 7-16: Load-displacement curves for beam C at 20°C, 50°C and 70°C

The load-displacement curves at 50°C and 70°C showed a slightly less stiff behavior compared to room temperature, similar to what was observed for beam A and B. The failure load at 50°C (131 kN) was about the same as the failure load at 20°C (132 kN). The beam that was tested at 70°C failed at a significant lower failure load (91 kN), just after the internal steel reinforcement started to yield at midspan. A possible explanation for this lower failure load will be given at the end of this section.

The analytical debonding load that has been determined according to the model for 'debonding at the end anchorage' by Holzenkämpfer (1997), modified by Neubauer and Rostásy (1999) (Appendix I.3) turned out to result in a relatively high failure load (168 kN), compared to the experimental failure load (132 kN), when using mean material properties and safety factors equal to 1.0. The design value according to this analytical model (116 kN) was, however, lower than the actual experimental failure load and therefore on the safe side (Appendix I.3).

The crack pattern of beam C was different compared to beam A and B. Cracks had developed over the entire bonded length of the CFRP laminate, also in the end anchorage zone and at the end of the CFRP laminate (Figure 7-17).

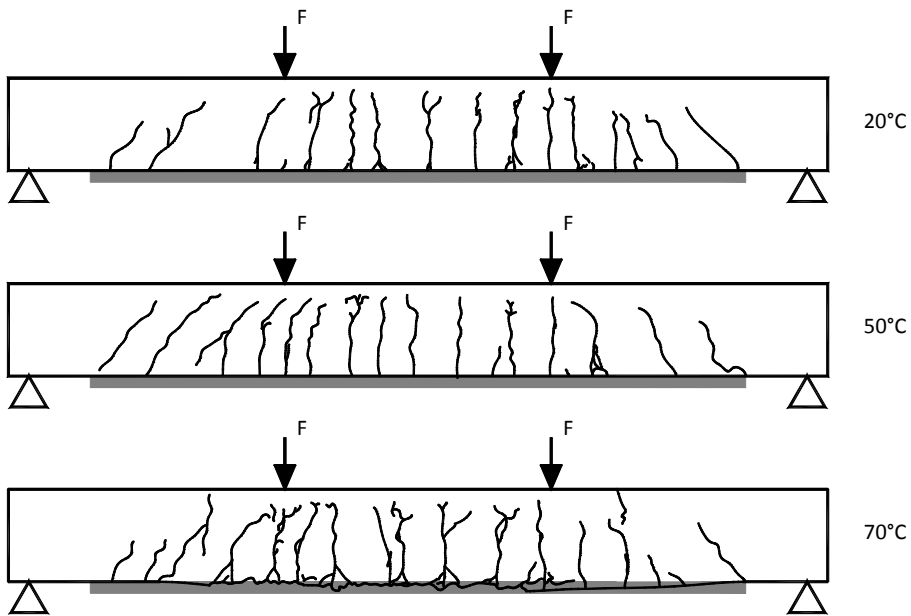


Figure 7-17: Crack patterns of beam C after failure at 20°C, 50°C and 70°C

At 20°C and 50°C, debonding initiated at the end of the CFRP laminate and propagated in the concrete adjacent to the concrete-adhesive interface towards midspan, which is in the other direction as was seen in beam A and B. At 70°C, debonding initiated in a similar way, but, after debonding over about 500 mm, started to rip-off parts from the concrete cover, leaving large pieces of concrete attached to the adhesive after debonding (Figure 7-18). Debonding turned out to be less explosive compared to what was seen during debonding in beam A and B.

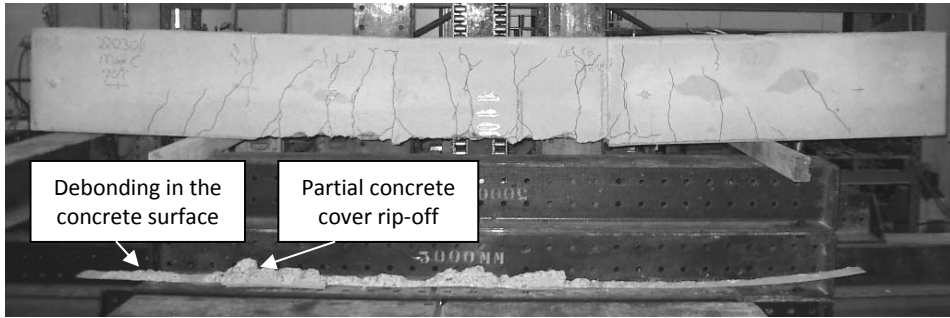


Figure 7-18: Large pieces of concrete remained attached to the adhesive after debonding at 70°C

The normal strains at 50 kN and 100 kN have been plotted in Figure 7-19. The strain distribution at 100 kN has not been plotted for 70°C as the beam already failed at 91 kN. Again, the same tendency of larger strains with increasing temperature can be seen.

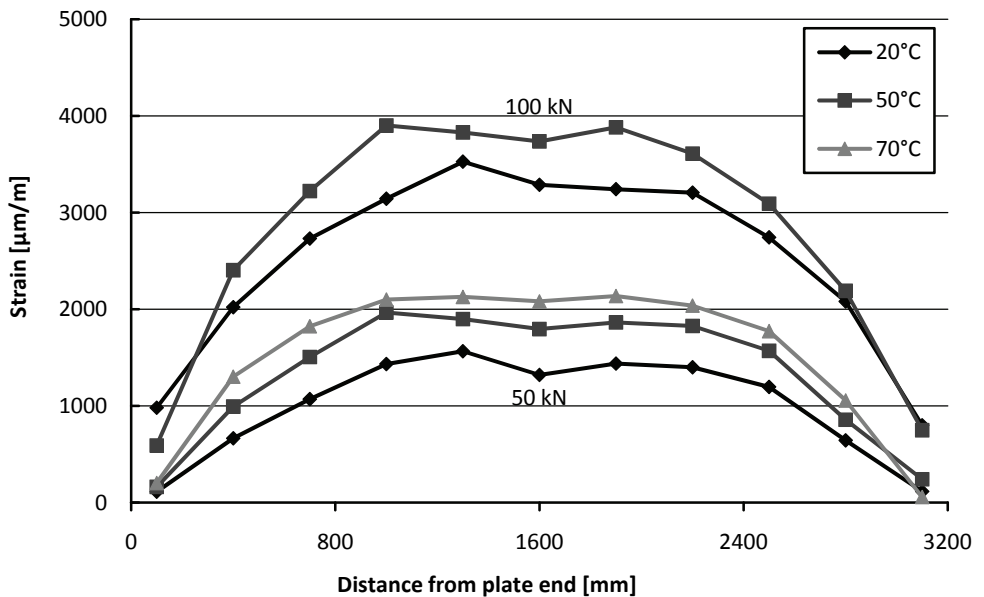


Figure 7-19: Normal strains in the CFRP laminate of beam C at 50 kN and 100 kN

Failure of this beam is closely related to the capacity of the end anchorage zone. It is expected that the capacity of this end anchorage zone is affected by temperature in three different ways at 70°C. First of all, the capacity of the anchorage zone is likely to reduce due to the reduced bond strength of the concrete-adhesive-CFRP joint at elevated temperatures, as was shown with the small scale bond test (Chapter 5). However, bond failure is still mainly governed by failure of the concrete adjacent to the concrete-adhesive interface at 70°C in the experiment and not by failure exactly in the concrete-adhesive interface. It is therefore expected that this aspect will only result in a small reduction in bond capacity of the anchorage zone.

The second aspect is the reduced Young's modulus of the adhesive at elevated temperature, which is expected to have two different effects. The first effect is a more linear strain distribution in the end anchorage zone, which reduces the peak in shear stresses at the end of the laminate and therefore affects the anchorage capacity positively. The second effect is an increase in the (needed) anchorage length. If this anchorage length is not available, the capacity of the anchorage zone will reduce. These effects will be further investigated by means of finite element analyses in Chapter 8.

The third aspect is the difference in the coefficient of thermal expansion between concrete and CFRP. This results in the development of thermal stresses in the CFRP and shear stresses in the concrete adjacent to the concrete-adhesive interface in the end anchorage zone. It is expected that these stresses reduce the capacity of the end anchorage zone, as they act in the same direction as the stresses due to loading. Based on the difference in failure load between 20°C and 50°C, it is however expected that this effect is only small.

Based on the experimental results, it is expected that the reduced failure load at 70°C is caused by a combination of aspects; the reduced bond strength of the concrete-adhesive-CFRP joint, the increased anchorage length and the development of thermal stresses. Another possible explanation could be a difference in the roughness of concrete surface between the beam at 70°C and the beams at 20°C and 50°C. The contribution of each of the thermal aspects to the reduction in failure load will be investigated by means of finite element analyses of the beams in Chapter 8.

7.5.4 Beam D

Beam D was strengthened with a 150 mm wide CFRP laminate and was designed to fail by ‘concrete cover rip-off’ or ‘plate-end shear failure’. The beam that was tested at 20°C was unloaded and reloaded at ± 50 kN (Figure 7-20), as one of the measurement devices was not working correctly. Again, some differences were found between the analytical and experimental load-displacement curves, due to the same reasons as for the other beams.

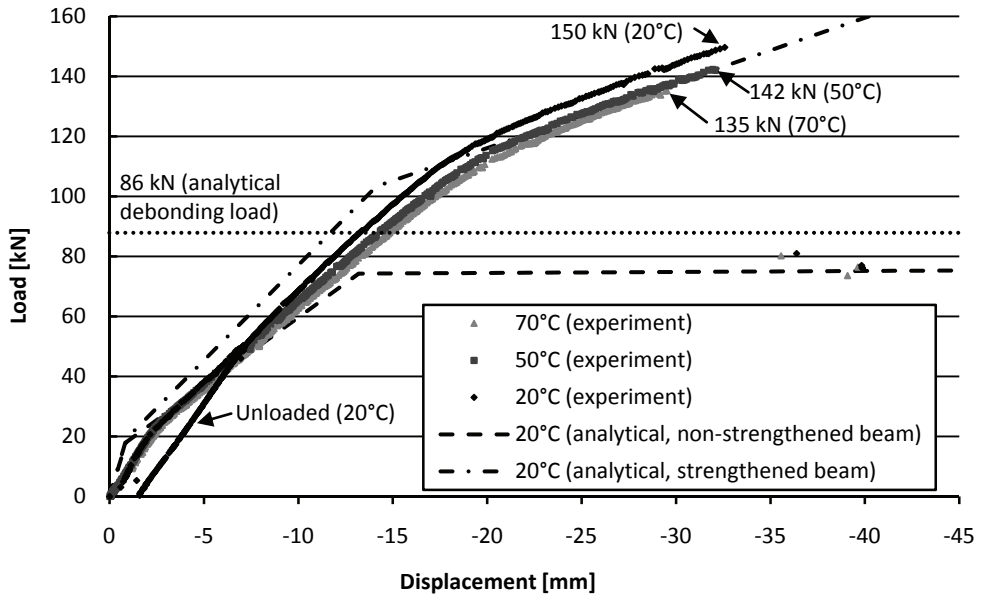


Figure 7-20: Load-displacement curves for beam D at 20°C, 50°C and 70°C

The failure load decreased by 5% at 50°C and 10% at 70°C, both compared to that at 20°C. Beam D failed at the highest load compared to the other beams, despite the lower concrete strength, due to the wide (150 mm) CFRP laminate that was applied. Compared to the (analytical) failure load of a non-strengthened beam (77 kN), an increase of 94% in failure load was achieved by strengthening of the beam (150 kN). Again, some load steps were found in the experiment after failure of the strengthened beam (± 79 kN), which were all close to the analytical failure load of the non-strengthened beam (77 kN).

The analytical failure load of the strengthened beam was also predicted with the model of Jansze (1997) for ‘concrete cover rip-off’ and ‘plate-end shear failure’ (Appendix I.4) and turned out to be relatively low (86 kN) compared to the actual failure load in the experiment (150 kN). Also for the other beams, the model of Jansze tuned out to result in relatively low values for the debonding load, while these beams didn’t even fail by this type of debonding.

All beams D showed significant more cracks at the failure load than the previous beams (Figure 7-21), due to the higher failure load. All beams failed after concrete cover rip-off had occurred. This is not clearly visible in Figure 7-21, as the concrete cover was, at some places, not ripped-off over the entire width of the beam, but only over the width where the CFRP was bonded to the concrete.

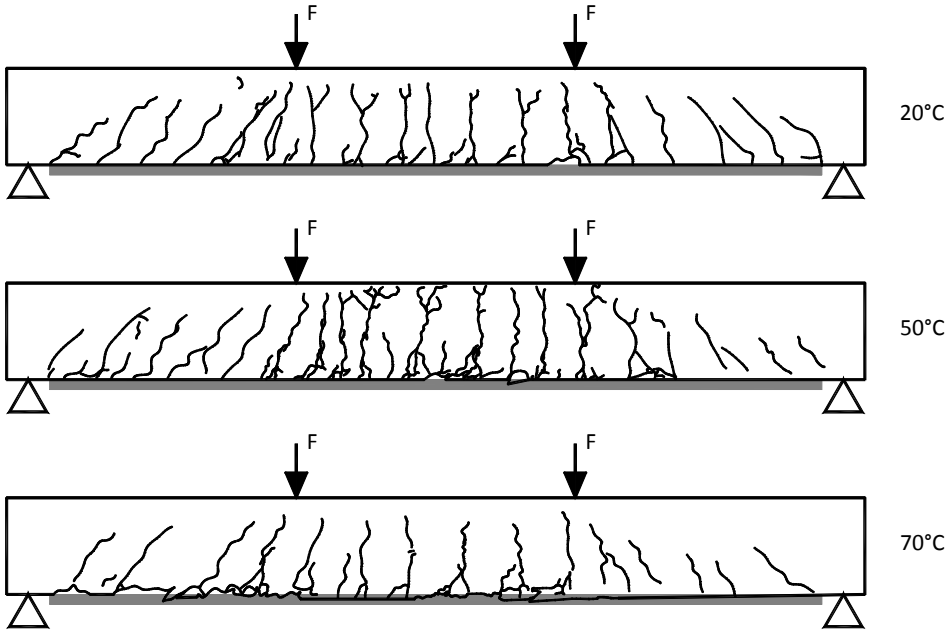


Figure 7-21: Crack patterns of beam D after failure at 20°C, 50°C and 70°C

Figure 7-22, however, clearly shows the internal steel reinforcement that was visible after failure of the beam. This different type of failure can be explained with the wider CFRP laminate (150 mm) compared to the other beams. The wide CFRP laminate results in relatively small (shear) stresses in the concrete at the interface with the adhesive, which makes concrete cover rip-off the governing type of failure over the debonding mechanisms that are related to bond failure.



Figure 7-22: Internal steel reinforcement is clearly visible after concrete cover rip-off

The normal strain distributions in the CFRP laminate at 50 kN and 100 kN (Figure 7-23) showed similar results as for the previous beams, increasing strains with increasing temperature due to the initial thermal strains after heating of the beams. Strains in the CFRP laminate were again lower compared to the other beams, as a wider CFRP laminate was applied.

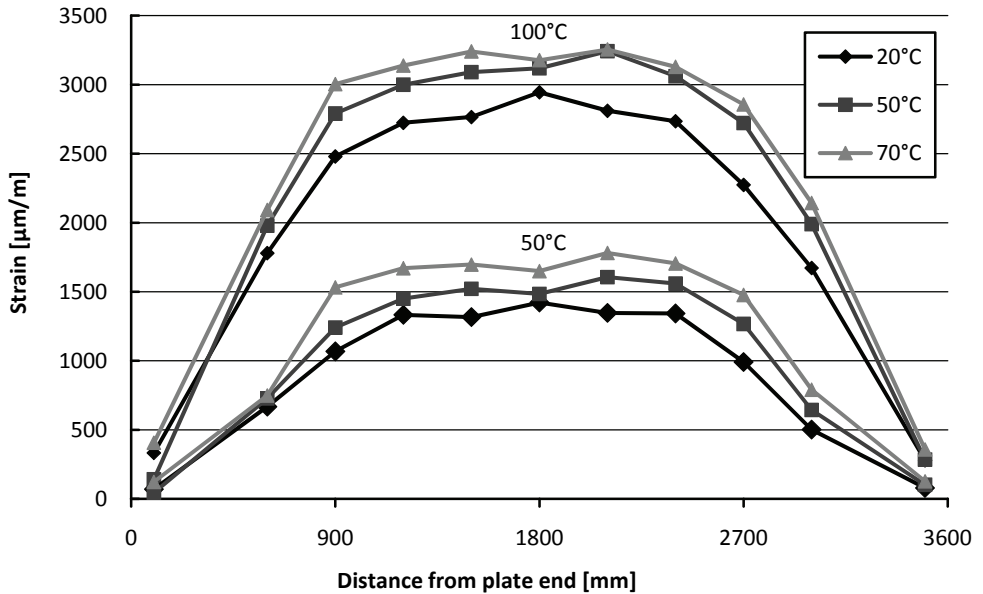


Figure 7-23: Normal strains in the CFRP laminate of beam D at 50 kN and 100 kN

The normal strain distributions due to heating and due to loading of the beam acted in the same direction, as can be seen by comparing Figure 7-6 and Figure 7-23. It can therefore be concluded that the stress concentrations at the plate-end due to heating also act in the same direction as the stress concentrations due to loading. Failure is initiated at the plate-end and is therefore expected to be negatively affected by the thermal stresses.

The effect on the failure load turned out to be small, as can be seen in Figure 7-20. This is also related to the fact that reduced Young's modulus and the time dependent creep behavior of the adhesive at elevated temperature reduce the stress concentrations at the plate-end and therefore reduce the negative effect of the thermal mismatch. This is further investigated by means of finite element analyses in Chapter 8.

The reduced bond strength will not affect the failure load of this debonding mechanism, as failure is governed by cracking of the concrete at the end of the laminate and not by bond failure of the concrete adjacent to the concrete-adhesive interface. Based on the experimental results, it can be concluded that the bond strength at 70°C was still sufficient to prevent one of the other debonding mechanisms to occur.

7.6 Conclusions

In the full scale experiments, four different debonding mechanisms have been investigated at 20°C, 50°C and 70°C. For all the beams tested at 50°C, no change in the type of bond failure was observed, compared to that of the beams tested at 20°C. The failure load was also not significantly affected at 50°C. Only the failure load of beam D was slightly reduced, probably due to the development of thermal stresses in the concrete at the plate-end, which acted in the same direction as the stresses at the plate-end due to loading of the beam. The effect on the failure load was however small, both at 50°C (-5%) and 70°C (-10%).

At 70°C, the type of bond failure of the concrete-adhesive-CFRP joint only changed for beam A from concrete bond failure to a mixed type of failure, in which less concrete remained attached to the adhesive. Debonding in beam A and B seemed to have initiated away from the plate-end and propagated towards the plate-end. The failure loads of these beams were not significantly affected at 70°C, because thermal shear stresses in the concrete adjacent to the concrete-adhesive interface mainly developed in the anchorage zone and not at the location where debonding initiated. The bond strength is expected not to be significantly reduced at 70°C, as bond failure was still, to a large extent, governed by concrete bond failure, and not by failure exactly in the concrete adhesive-interface. This is probably related to an increase in T_g as a result of the heating cycle during heating of the beam.

The failure load of beam C at 70°C was significantly lower compared to that at room temperature. For this beam, which had a short laminate length, debonding was closely related to the capacity of the anchorage zone. The reduction of the anchorage capacity is expected to be related to the increased required anchorage length, due to the reduced Young's modulus of the adhesive, and the development of thermal (shear) stresses in the anchorage zone, which acted in the same direction as the shear stresses due to loading.

8 Finite element analyses of the full scale experiments

8.1 Introduction

To gain better insight into the effect of temperature on the debonding of externally bonded CFRP in full scale concrete structures, it was decided to simulate the full scale experiments by means of finite element analyses. Simulating the full scale beams is more complicated than simulating the small scale bond tests, as more aspects have to be taken into account, like cracking of the concrete and yielding of the internal steel reinforcement. It was therefore needed to apply a slightly different modeling approach (Section 8.2) and modified material properties (Section 8.3), compared to what was used in the simulations of the small scale bond tests.

8.2 Finite element model

The finite element model, as shown in Figure 8-1, was used for all beams. The only differences between the beams A to D were the material and geometry properties of the elements and the length L (Table 8-1). Only half of the beam was modeled because of symmetry. For the concrete, six-node triangular plane stress elements (CT12M) were used, which are based on quadratic interpolation and area integration. The default three-point integration scheme was applied for these elements.

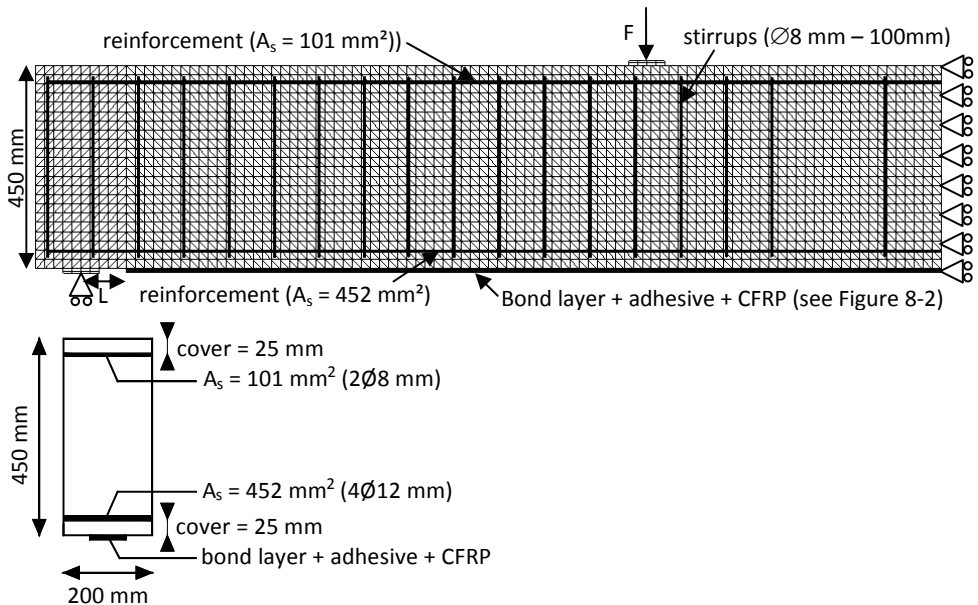


Figure 8-1: Finite element model and (schematic) cross-section of the model

Table 8-1: Concrete grade and geometrical properties of the CFRP for the different beams

Beam	Designed debonding mechanism at room temperature	Concrete grade	Width of CFRP (b_f)	Distance plate-end-support (L)
A	Debonding due to high shear stresses	C20/25	50 mm	100 mm
B	Debonding at shear cracks	C45/55	80 mm	100 mm
C	Debonding at the end anchorage	C45/55	80 mm	300 mm
D	Concrete cover rip-off	C20/25	150 mm	100 mm

The bond layer in between the concrete and the adhesive was first modeled with interface-elements, in the same way as for the finite element models of the small scale bond tests (Figure 8-2). It turned out, however, that the analyses with these elements did not provide adequate results, as the computation most of the times stopped far before yielding of the internal steel reinforcement. It is expected that this was due to numerical problems with the interface elements. This is possibly related to the fact that non-linear material behavior in the interface elements can only be defined in the normal direction, perpendicular to the bonded area, or in the shear direction, parallel to the bonded area, and not as a combination of both.

In the full scale beams, the concrete-adhesive interface is subjected to loading in both the normal and the shear direction. Normal stresses, for example, develop at the tip of a shear crack, due to the difference in vertical displacement between the two sides of the crack (2.4.3.3), while shear stresses develop due to a change in the CFRP force along the length of the CFRP laminate (Section 2.4.3.2) and in the end anchorage zone, where stresses have to be transferred from the CFRP to the concrete (Section 2.4.3.4). It was therefore decided to apply plane-stress elements for the bond layer in between the concrete and the adhesive. In plane stress elements, normal and shear stresses are coupled, resulting in principle stresses.

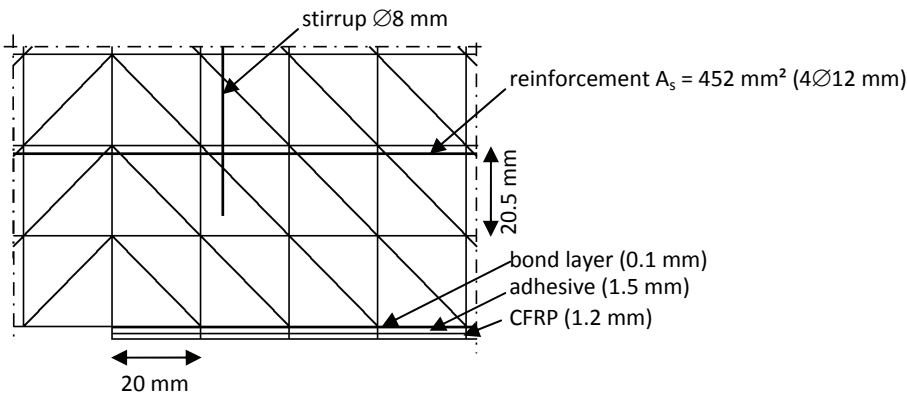


Figure 8-2: Detail of FE-model at the end of the CFRP laminate

Applying plane stress elements in the bond layer between the concrete and the adhesive introduces the question what height should be used for these elements. Unlike interface elements, plane stress elements should have an aspect ratio (shortest side divided by the longest side) that is not too small. Applying elements with small aspect ratios could result in deviations of the result from the theoretical ideal (TNO DIANA B.V. 2005). Applying a large height for these elements results, however, in a large distance between the CFRP and concrete, which does not correspond with reality. An option is applying a smaller element width, but this has the disadvantage that significantly more elements are needed, which strongly increases the computation time. All options therefore have their drawbacks.

Finally, it was decided to apply a height of 0.1 mm to the elements in the bond layer (Figure 8-2), similar to the height applied in the analyses of the small scale bond tests. Increasing the height to, for example, 1 mm did not result in significant different results. The small aspect ratio was therefore regarded to be acceptable for the purpose of the analyses. The depth (width in the direction perpendicular to the beam axis) of the bond layer was taken equal to the depth of the CFRP laminate and of the adhesive. The adhesive and CFRP elements were modeled with 8-node plane stress elements (CQ16M), similar as in the small scale bond tests.

8.3 Material properties

8.3.1 Concrete and bond layer

There are several ways to model cracking of concrete. Generally, distinction is made between the smeared crack approach and the discrete crack approach (Feenstra 1993; De Borst and Sluys 2002). For the discrete crack approach, it is required that the locations of the cracks are known in advance. The discrete crack approach was, for example, applied in the small scale three-point bending tests (Section 6.5), as it was known in advance that a crack will develop in the cross-section above the saw cut. For the full scale beams, the locations of the cracks are not known in advance. It was therefore decided to adopt the smeared crack approach.

Two crack models are generally distinguished within the smeared crack approach, the fixed and rotating crack model (De Borst and Sluys 2002). The fixed crack model can be subdivided into the *“Total Strain Fixed crack model”* and the *“Multi-directional Fixed crack model”*. In the first, the direction of the normal to the crack is fixed when a crack is initiated and is the same as the direction of the principle stress in the load step when cracking initiates. This direction does not change with further loading.

The direction of the principle stress will, in reality, change after the initiation of a crack, e.g. due to increased shear stresses in a crack. This can result in violation of a failure criterion in a new direction. A second fixed crack model was therefore introduced in which the total strain is decomposed into an elastic part and a cracking part. Each load step can contribute to the cracking strain, even if the direction of the principle stress has changed. This model is referred to as the *“Multi-directional Fixed crack model”*. Both fixed crack models apply a shear retention factor that defines the reduction of the shear stiffness after cracking. It turns out that it is quite complicated to find a suitable shear retention factor, as the shear stiffness of cracked concrete highly depends on the crack opening (De Borst and Sluys 2002).

In the rotating crack model, the normal to the crack is allowed to rotate during the fracture process. This means that in every new load step, a new crack will arise, while the old existing crack is erased from memory. Only the damage (degradation of the tensile strength) is transferred to the new crack. So, the normal to the crack stays aligned to the major principle stress in every load step. This model is referred to as the *“Total Strain Rotating crack model”* and has the advantage that it eliminates the difficulty of choosing a proper shear retention factor, as the stress only has to be evaluated in the direction of the principle stress. It was decided to apply the Total Strain Rotating crack model for the analyses of the full scale beams.

Figure 8-3 shows the stress-strain relations that were applied to the concrete elements in tension (a) and in compression (b). In tension, the applied linear softening relation was defined by the mean tensile strength (f_{ctm}), the mean Young’s modulus (E_{cm}), the fracture energy (G'_F) and the crack band width (h). In compression, a bi-linear compressive stress-strain relation was applied that is defined by the mean compressive strength (f_{cm}) and the mean Young’s modulus (E_{cm}).

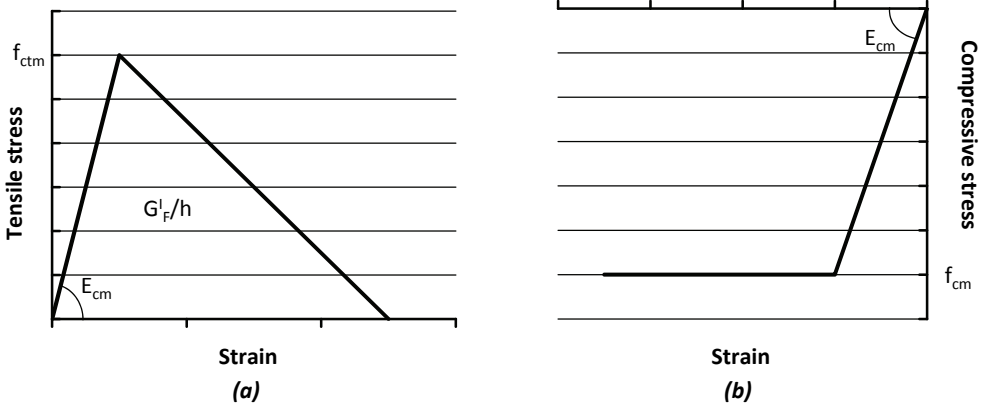


Figure 8-3: Linear tension-softening (a) and ideal compressive (b) behavior of concrete

The mean (uni-axial) tensile strength was determined from the experimental tensile splitting strength (Appendix F) with $f_{ctm} = 0.9 \cdot f_{ctm,sp}$, according to Eurocode 2 part 1-1 (CEN 1997a). The mean (uni-axial) compressive strength was taken equal to $f_{cm} = 0.8 \cdot f_{cm,cube}$ with $f_{cm,cube}$ being the experimental mean cube compressive strength, also according to Eurocode 2 part 1-1. The mean Young's modulus and the fracture energy were computed with the relations as given by Bažant (1992).

$$G_F^I = 58,400 \cdot f_{ctm} \cdot d_a / E_{cm} \quad (G_F^I \text{ in J/m}^2) \quad (8.1)$$

$$E_{cm} = 4733 \cdot \sqrt{f_{ctm}} \quad (E_{cm} \text{ in N/mm}^2) \quad (8.2)$$

where

f_{ctm} is the mean tensile strength of concrete (in N/mm²)

d_a is the maximum aggregate size (in mm)
= 16 mm

f_{cm} is the mean compressive strength of concrete (in N/mm²)

The relation between the temperature and the material properties of concrete was taken into account with the relations as given in Model Code 1990 (CEB 1993) for dry concrete, (equation 4.1, 4.2, 4.3 and 4.6). The crack band width (h) represents the width over which the fracture energy is smeared out. This value is determined automatically by DIANA and is equal to a width of the square root of the surface area of an element. For the triangular concrete element in the FE-model, this is approximately $\frac{1}{2}\sqrt{2}$ times the width of the element. It turned out that applying the default value was appropriate for the concrete elements.

For the bond layer, the same material properties as for the concrete elements were applied, except for the crack band width. Due to the high aspect ratio, it was not possible to use the default value of DIANA, as this would result in a relatively high value for the crack band width. The crack most likely propagates horizontally in the bond layer. The fracture energy therefore had to be smeared out over one integration point over the height of the element. This is equal to half the height of the element (0.05 mm). Small variations in the crack band width did not result in significant different results. The material properties of the concrete and interface elements have been summarized in Table 8-2 for the different beams.

Table 8-2: Concrete material properties applied to the concrete and interface elements

	Beam A	Beam B	Beam C	Beam D
Density (ρ_c) [kg/m ³]	2400	2400	2400	2400
Young's modulus (E_{cm}) (eq. 8.2) [N/mm ²]	22,300	30,600	30,300	25,400
Poisson ratio (ν_c) [-]	0.2	0.2	0.2	0.2
Tensile strength (f_{ctm}) [N/mm ²]	2.11	3.27	3.33	2.70
Fracture energy (G_F^I) (eq. 8.1) [J/m ²]	88,3	99.7	102,7	99,3
Compressive strength (f_{cm}) [N/mm ²]	22.2	41.8	41.0	28.8

8.3.2 Steel reinforcement, adhesive and CFRP

The material properties of the steel reinforcement, the adhesive and the CFRP were taken almost equal to the material properties applied for the small scale bond tests (Table 8-3). The only difference was that, for the adhesive and the steel reinforcement, bi-linear stress-strain relations were applied instead of linear-elastic relations. The yield strength of the steel reinforcement was taken equal to 560 N/mm² (Figure 8-4a) while that of the adhesive was taken equal to 28 N/mm² (at 20°C), according to the datasheet of the manufacturer (Sika 2009). The reduction of the tensile strength with increasing temperature was taken proportional to the reduction in the flexural strength with increasing temperature, as described in Section 4.5.2 (Figure 8-4b and Table 8-3). The temperature dependent Young's modulus of the adhesive was taken similar as in the analyses of the small scale bond tests. The stress-strain relation of the CFRP laminate was assumed to be temperature independent and linear elastic up to the tensile strength (2800 N/mm²).

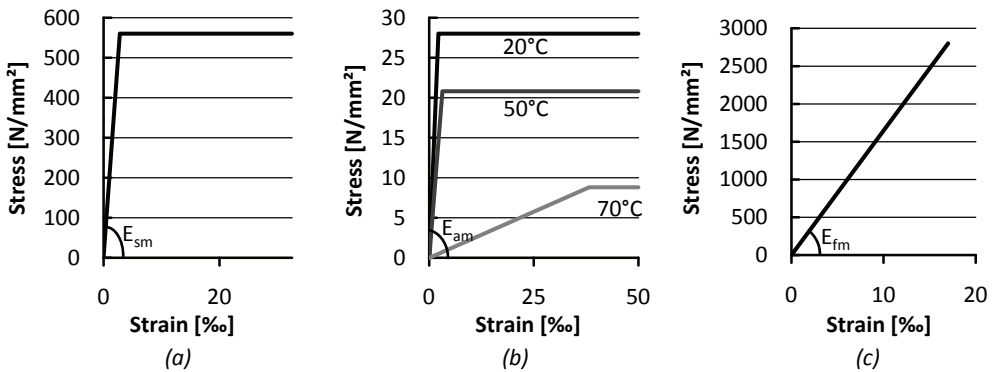


Figure 8-4: Applied stress-strain relation of steel reinforcement (a), adhesive (b) and CFRP (c)

Table 8-3: Applied material properties of the reinforcement, adhesive and CFRP

Property	Reinforcement	Adhesive	CFRP
Density (ρ) [kg/m ³]	7600	1650	1600
Mean Young's modulus (E_m)			
- 20°C [N/mm ²]	200,000	12,800	165,000
- 50°C [N/mm ²]	200,000	6565	165,000
- 70°C [N/mm ²]	200,000	230	165,000
Poisson ratio (ν) [-]	0.3	0.3	0.35
Mean tensile stress (f_m)			
- 20°C [N/mm ²]	560	28.0	2800
- 50°C [N/mm ²]	560	20.8	2800
- 70°C [N/mm ²]	560	8.8	2800

8.3.3 Coefficient of thermal expansion

A disadvantage of applying the Total Strain Rotating crack model to the concrete elements is the fact that, in DIANA version 9.1, it was not possible to combine it with environmental effects, like a temperature change. As a result, a temperature change cannot be applied to the concrete elements. In order to be able to simulate the development of thermal stresses due to thermal mismatch between the different materials, it was decided to adopt the following approach. The development of thermal stresses is not defined by the thermal expansion of the different materials in an absolute sense, but by the differences in expansion between the different materials. A temperature change results in the same thermal stresses, as long as the differences between the coefficients of thermal expansion are kept the same. By using zero for the coefficient of thermal expansion of the concrete elements, and adjusting it for the other materials such that the differences stay the same, it becomes possible to apply a temperature change to the model, without having to apply a temperature change to the concrete elements. In this way, the thermal stresses can be computed. The modified coefficients of thermal expansion are shown in Table 8-4.

Table 8-4: Actual and modified coefficient of thermal expansion

Material	Actual coefficient of thermal expansion [10⁻⁶/°C]	Modified coefficient of thermal expansion [10⁻⁶/°C]
Concrete (α_c)	10	0
Reinforcement (α_s)	10	0
Adhesive (α_a)	26	16
CFRP (α_f) (longitudinal direction)	-0.3	-10.3

Unlike the thermal stresses, thermal strains are not represented correctly by this approach. These strains are, however, small compared to the strains due to loading. The effect of the deviation in the thermal strains on the results of the analyses can therefore be neglected.

8.4 Results of the finite element analyses

8.4.1 General

The finite element model was first loaded by the dead weight of the beam. Then, a temperature change was applied to simulate the heating of the beam to 50°C and 70°C. Finally, the model was loaded until failure. In the small scale bond tests, a displacement controlled solution procedure (Figure 8-5b) was used. It turned out that this was not possible for the full scale experiments, as convergence could not be reached when cracking of the concrete occurred. Also with load-control (Figure 8-5a) it was not possible to reach convergence, which made it necessary to apply the arc-length method (Figure 8-5c). The arc-length method is a modification of load control loading that can be used in situations where neither load- nor displacement-control can be used, for example when snap back behavior occurs. This technique is also referred to as the path following technique and can compute the correct solution even if there are two or more solutions at one load- or displacement step. Extensive information about the arc-length method can be found in Zienkiewicz and Taylor (2000) and De Borst and Sluys (2002). The applied convergence criterion for the analyses is based on energy.

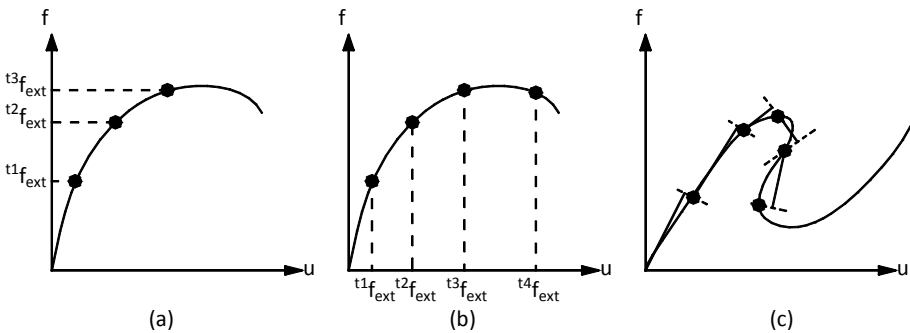


Figure 8-5: Load-control (a), displacement-control (b) and arc-length control (c) (TNO DIANA B.V. 2005)

The simulations of the beams were carried out for 20°C, 50°C and 70°C, the same temperatures as in the experiments. The results of these simulations will be discussed for each beam configuration individually in the following sections. In each section, first, detailed results of the simulation at 50°C will be presented, to show the effect of heating and loading of the beam, followed by a comparison of the results at the different temperatures and a comparison with the experiments.

8.4.2 Beam A

8.4.2.1 Results of the analysis at 50°C

Beam A was strengthened with a 50 mm wide CFRP laminate that ended at 100 mm from the support. The numerical and experimental load-displacement curves of this beam are plotted in Figure 8-6 for 50°C. It can be seen that there is a good agreement between the load-displacement curves, although a slightly higher maximum load was found in the FE-analysis (111 kN), compared to the experimental failure load (102 kN). Cracking of the concrete (at ± 20 kN) and yielding of the steel reinforcement (at ± 90 kN) occurred at about the same load as in the experiments.

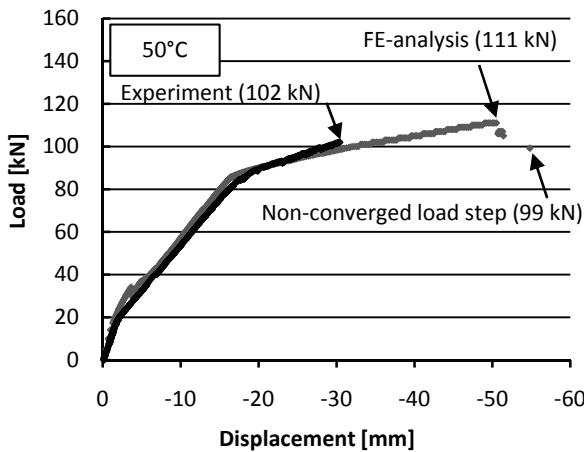


Figure 8-6: Numerical and experimental load-displacement curves of beam A at 50°C

The beam slightly bended upwards after increasing the temperature, but this effect was very small. According to the FE-analysis, the displacement at midspan was 0.03 mm (upwards) after increasing the temperature to 50°C. The maximum load turned out to be slightly dependent on the size of the applied load steps. Applying a different step size sometimes resulted in a slightly different crack pattern, which caused small variations in the maximum load (± 5 kN). After the maximum load, the FE-analysis was able to continue for eight more load steps in which the load decreased. These load steps will be indicated as “post peak” throughout this chapter. The last plotted load step at 99 kN did not converge within the applied maximum number of iterations. Whether these decreasing load steps and non-converged load step are indeed related to (debonding) failure of the beam or are only the result of numerical problems will be discussed later.

The crack pattern at the maximum load is shown in Figure 8-7, by plotting the crack strains as vectors. For the sake of clarity, only crack strains in the concrete elements have been plotted and not in the elements in the bond layer. Cracks in the concrete occurred over almost the entire length of the CFRP at the maximum load. The flexural cracks in and close to the constant moment region showed significant larger crack strains compared to the shear cracks closer to the support, due to the higher bending moment and yielding of the internal steel reinforcement in this region.

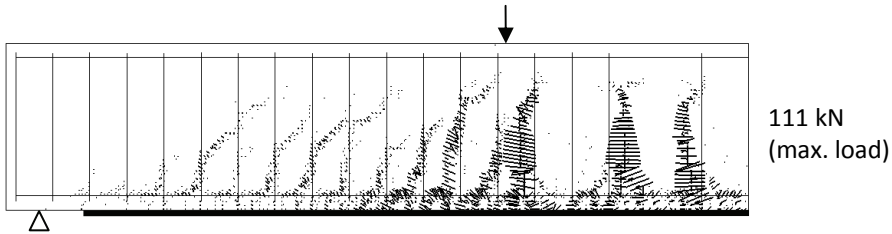


Figure 8-7: Crack pattern of beam A at 50°C at the maximum load

Figure 8-8 shows the crack strains, again plotted as vectors, but now in both the concrete and the bond layer together. A different scale was used for this figure, as the crack strains in the bond layer were significantly larger than the crack strains in the concrete after the maximum load. The latter are therefore (almost) invisible.

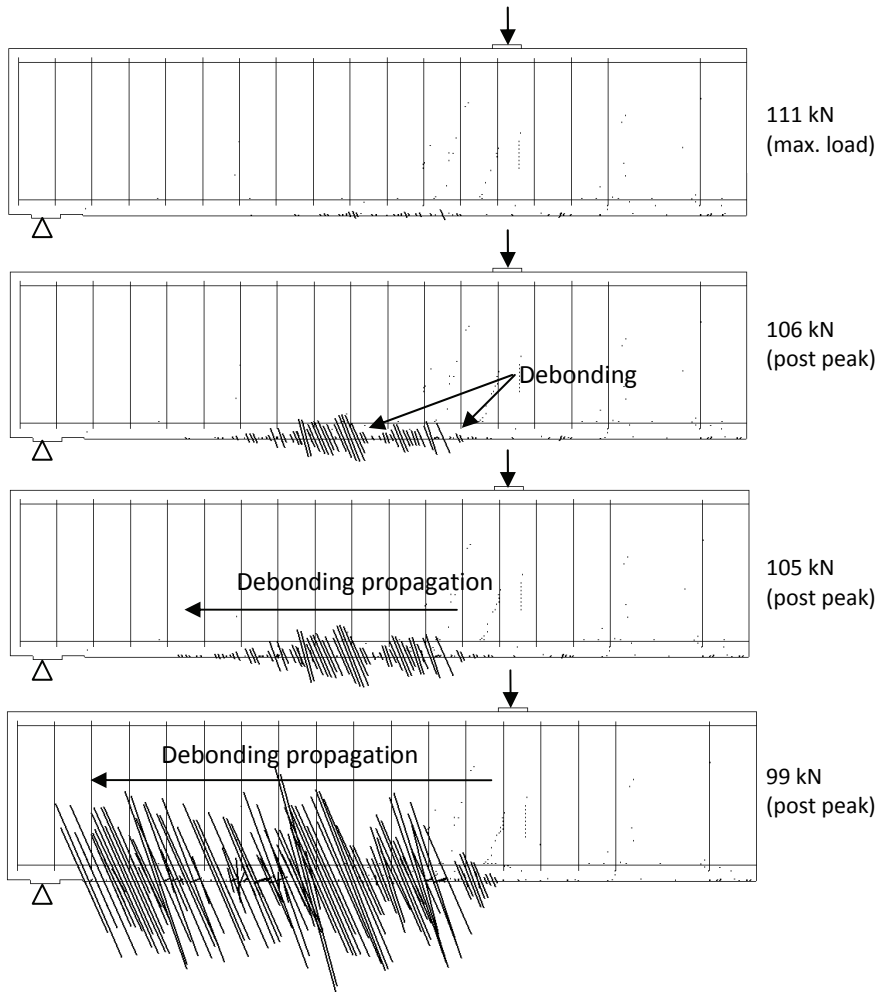


Figure 8-8: Debonding of the CFRP laminate of beam A at 50°C

It can be seen that, in the first load step after the maximum load (106 kN), significant crack strains developed in the bond layer, just outside the constant moment region, which can be regarded as the initiation of debonding. In the following load steps (105 kN) crack strains increased further but also developed in more elements at the left side of the location where debonding was initiated first. This indicates that debonding is propagating towards the plate-end.

In the last load step (99 kN), the analysis did not converge anymore within the maximum number of iterations. The crack strains do however clearly show that debonding has propagated until the plate-end, which probably explains why the analysis did not converge anymore. Debonding initiated at about the same location as it was thought to have initiated in the experiment and also propagated in the same direction. Based on these findings, it is assumed that the debonding mechanism has been simulated correctly and so, the maximum load (111 kN) can be regarded as the failure load found by the numerical analysis.

Figure 8-9 shows the normal stress distribution in the CFRP laminate and the shear stresses in the concrete adjacent to the concrete-adhesive interface (in the bond layer) after loading the beam with the dead weight and after increasing the temperature to 50°C. The stress distribution corresponds to the average normal stresses in the elements along the length of the laminate. It can be seen that both the dead weight and the temperature increase resulted in a tensile stress in the CFRP laminate, as expected. The maximum normal stress in the CFRP laminate due to the temperature increase is equal to the analytical thermal stress ($\sigma_{f,\Delta T} \approx E_f \cdot \alpha_c \cdot \Delta T = 50 \text{ N/mm}^2$), which confirms that the thermal stresses are computed correctly with the modified coefficients of thermal expansion (Section 8.3.3). Shear stresses in the concrete bond layer are mainly concentrated at the plate-end, as the normal stresses in the CFRP are transferred to the concrete in this area, similar as in the small scale bond tests.

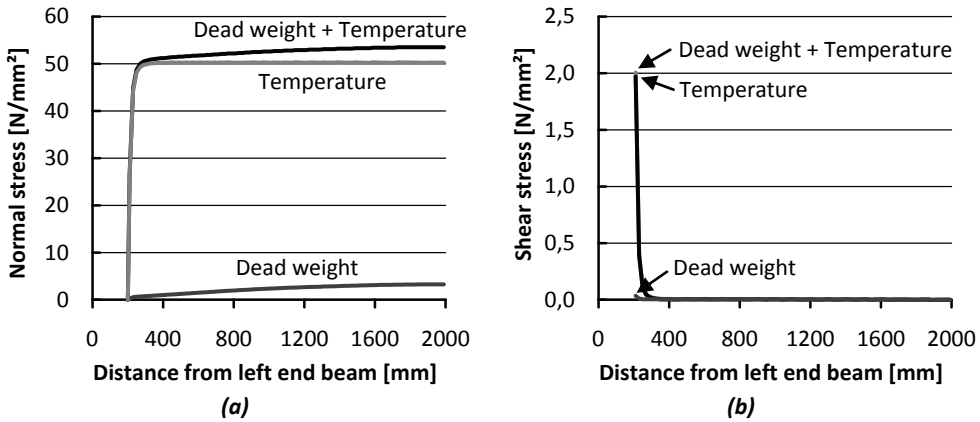


Figure 8-9: Normal stresses in the CFRP (a) and shear stresses in the concrete adjacent to the concrete-adhesive interface (b) due to the dead weight and the temperature increase to 50°C for beam A

The development of the normal stress distribution in the CFRP laminate during loading is plotted in Figure 8-10 for every load step of 10 kN and for the failure load. Loading of the beam resulted, just like heating of the beam (ΔT), in the development of tensile stresses in the CFRP laminate. Up to 20 kN, the tensile stresses in the CFRP laminate remain rather small, because the concrete is not cracked. Above 30 kN, after cracking of the concrete at midspan, CFRP stresses are increasing faster with increasing loads. The contribution of cracked concrete to the tensile component in the equilibrium in the beam cross-section is significantly lower compared to that in uncracked concrete, which implies that the contribution of the CFRP and steel reinforcement had to increase. Above 90 kN, the tensile stress in the CFRP increased even faster, due to yielding of the internal steel reinforcement. For these loads, the increase in the tensile component as a result of the increased bending moment is almost solely taken by the CFRP laminate.

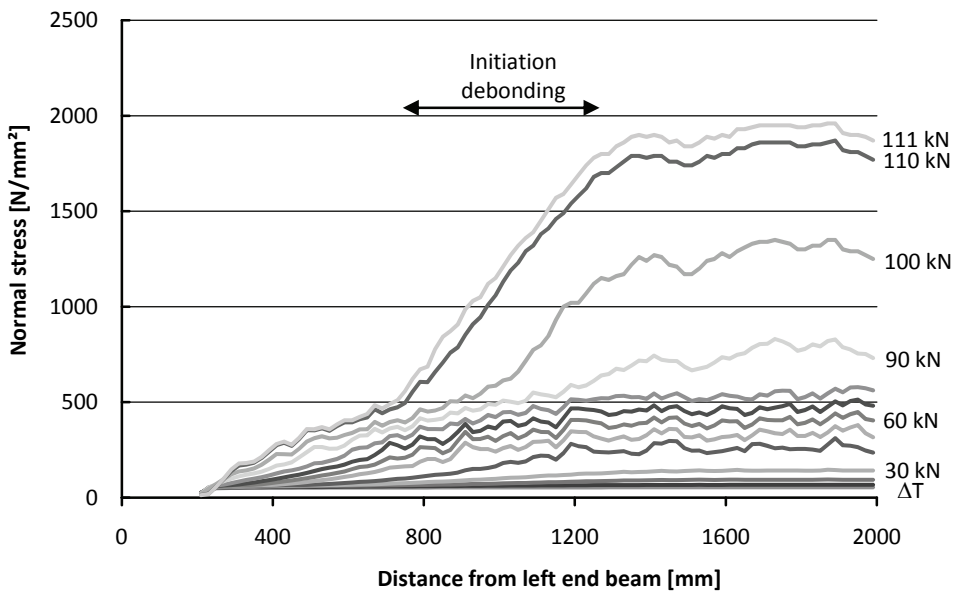


Figure 8-10: Normal stress distributions in the CFRP laminate of beam A at 50°C

The change in normal stress in the CFRP laminate per unit length is a size for the shear stress in the concrete bond layer. So, a higher tangent to the normal stress distribution in Figure 8-10 corresponds to higher shear stresses in the concrete bond layer. In the constant moment region, the normal stress is more or less constant, which implies that shear stresses in the concrete bond layer are relatively small. Outside the constant moment region, normal stresses in the CFRP laminate are decreasing towards the plate-end. After yielding of the internal steel reinforcement, the tangent to the normal stress distribution first starts to increase significantly in the area just outside the constant moment region.

At the failure load (111 kN), the area with a high tangent has expanded further to the left (between 800 mm and 1200 mm from the left end of the beam). The tangent in this area corresponds, at the failure load, to a shear stress of approximately $\tau = \Delta\sigma \cdot t_f / \Delta x \approx 4 \text{ N/mm}^2$, which is almost equal to the shear strength of concrete ($\tau_{\max} \approx 1.8 \cdot f_{ctm} = 3.8 \text{ N/mm}^2$). In the next load step, large crack strains developed in the bond layer, which propagate to the plate-end (progressive debonding). This confirms that the beam has failed due to the debonding mechanism 'debonding due to high shear stresses'.

The normal stress distribution in the tensile steel reinforcement is plotted in Figure 8-11. Cracks in the concrete caused an irregular stress distribution, similar as in the CFRP laminate. The steel reinforcement started to yield in the constant moment region ($f_{ym} = 560 \text{ N/mm}^2$) at about 90 kN.

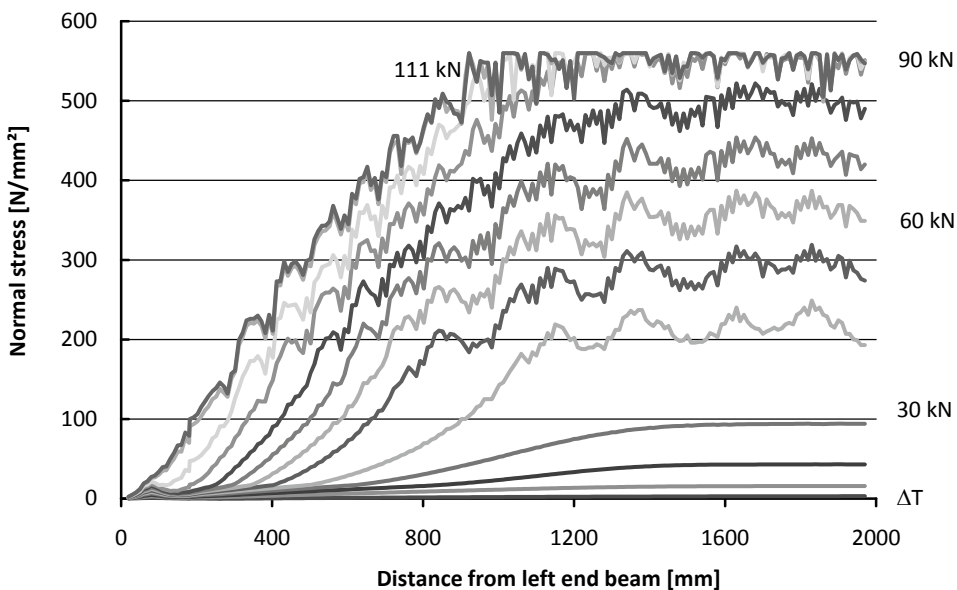


Figure 8-11: Normal stress distributions in the tensile reinforcement of beam A at 50°C

8.4.2.2 Comparison of the analyses at the different temperatures

The numerical and experimental load-displacement curves for beam A are plotted in Figure 8-12 for the different temperatures. The numerical load-displacement curve of a non-strengthened beam with the same material properties as the strengthened beam at 20°C is also plotted, for comparison. The experimental and numerical failure loads are given in Table 8-5.

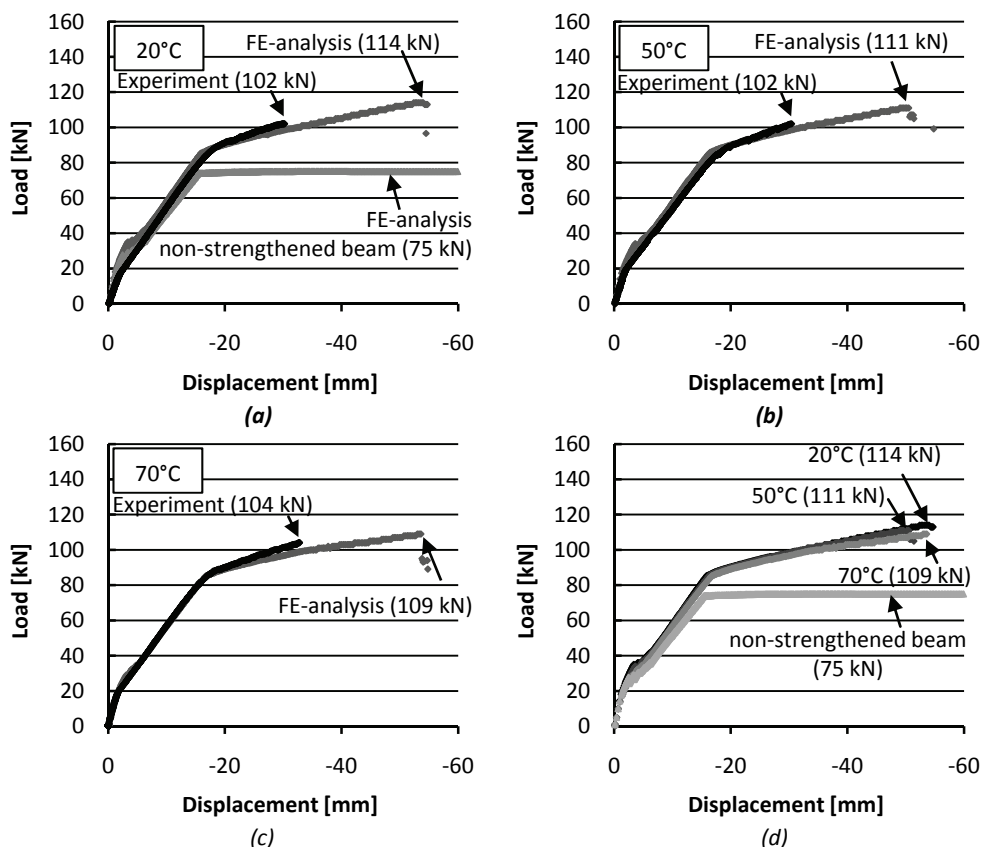


Figure 8-12: Load-displacement curves from the experiments and FE-analyses of beam A at 20°C (a), 50°C (b) and 70°C (c) and a comparison of the numerical load-displacement curves (d)

Table 8-5: Maximum load found for beam A in the numerical analyses and the experiments

Strengthening	Temperature [°C]	Experimental [kN]	FE-analysis [kN]
non-strengthened	20	± 80	75
strengthened	20	102	114
strengthened	50	102	111
strengthened	70	104	109

The load-displacement curves corresponded well to the experimental ones, although, at all temperatures, the numerical failure loads were slightly higher than the experimental ones. In the comparison of the numerical load-displacement curves (Figure 8-12d), it can be seen that the stiffness slightly reduced with increasing temperature. The reduction is however very small and only visible in the part of the load-displacement curve after yielding.

With separate analyses, in which the Young's modulus of the adhesive and concrete were varied individually, it was found that the reduction in stiffness is mainly related to the reduced Young's modulus of the adhesive at elevated temperatures. Only a small reduction in failure load was observed in the FE-analyses with increasing temperature, probably due to the slightly lower concrete strength and fracture energy at elevated temperature. The numerical failure load of the non-strengthened beam (75 kN) was significantly lower, as expected, and similar to the analytical failure load (± 80 kN) (Section 7.5.1).

The crack patterns of the beam at the different temperatures (Figure 8-13) did not show significant differences, as they failed at almost the same load.

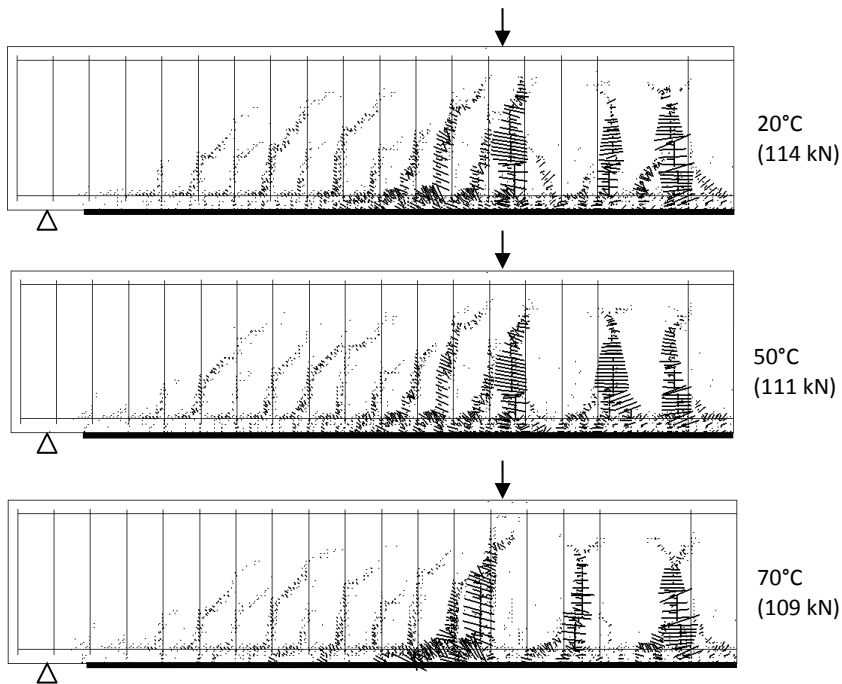


Figure 8-13: Crack pattern of beams A at the failure load for 20°C, 50°C and 70°C

All beams failed in a similar way as the beam at 50°C, due to debonding of the CFRP laminate. Debonding initiated in all beams just outside the constant moment region and propagated towards the plate-end (Figure 8-14). Note that the figures cannot be compared directly, as the load in the last, non-converged, load step was not the same for the different temperatures. It does however show that the type of failure was the same for the different beams.

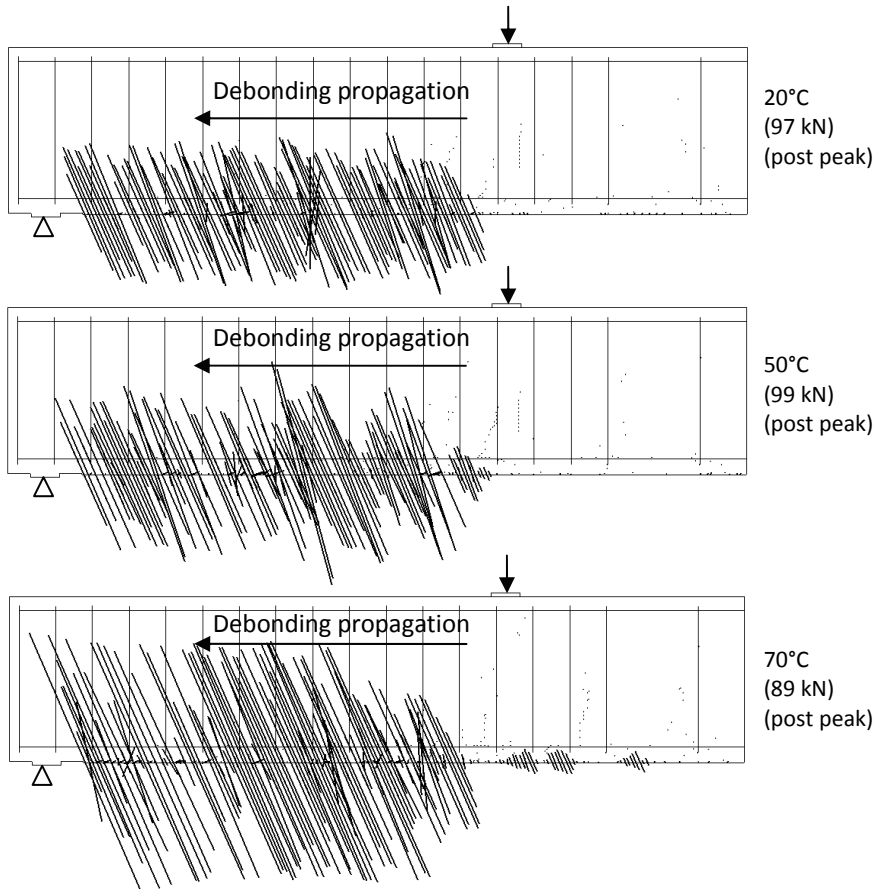


Figure 8-14: Debonding of the CFRP laminate of beams A at 20°C, 50°C and 70°C

Figure 8-15 shows a comparison of the numerical and experimental normal stresses in the CFRP laminate at the different temperatures. The stresses have been plotted after applying the temperature increase (ΔT), and for 50 kN and 100 kN. To make a comparison between the experimental and numerical stress distributions in the CFRP laminate, some modifications had to be made. The experimental stresses were calculated from the strain measurements in the experiment (Section 7.4). The numerical stresses had to be corrected, as they include the stresses due to the dead weight of the beam, which were not included in the strain measurements in the experiment. The numerical stresses in Figure 8-15 were therefore determined by subtracting the stresses due to the dead weight from the total computed stresses.

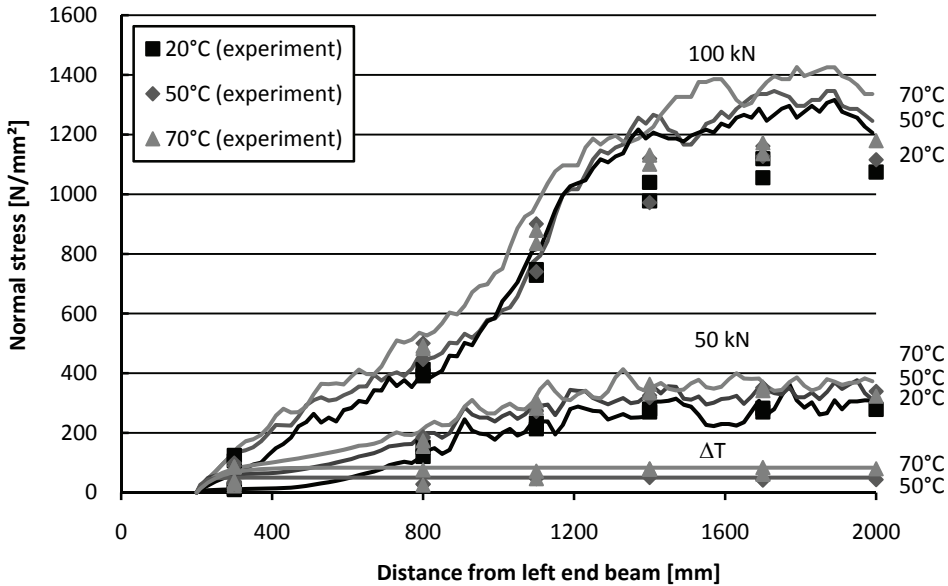


Figure 8-15: Comparison of the experimental and numerical normal stress distributions in the CFRP laminate of beam A at 20°C, 50°C and 70°C

It can be seen that there is a good agreement between the experimental and numerical stress distributions. Higher temperatures resulted in the analyses in a higher normal stress in the CFRP laminate due to the initial thermal stresses (ΔT), similar as in the experiment. No significant effects of the reduced Young's modulus were observed. In the constant moment region, the stresses according to the FE-analyses were slightly higher compared to the experimental stresses at 100 kN. It turned out that the CFRP stresses at this load highly depended on the load at which yielding of the internal reinforcement had started (see also Section 8.4.2.1 and Figure 8-10).

It can be concluded that debonding of the CFRP in beam A is initiated at a location away from the plate-end, just outside the constant moment region. At this location, the tangent to the normal stress distribution was relatively high at the failure load, which resulted in high shear stresses in the concrete adjacent to the concrete-adhesive interface. The temperature increase did result in higher normal stresses in the CFRP laminate, but did not significantly affect the slope of the normal stress distribution in the area where debonding was initiated. This means that the shear stresses were not (significantly) affected by the thermal mismatch between concrete and CFRP. Note that time dependent material properties of the adhesive were not taken into account in the analyses. However, based on the fact that the experiment was carried out in about half an hour, it can be expected that the effect on the mechanical strains is negligible, as it takes several hours before strains were significantly reduced (see e.g. Figure 5-12 and Figure 5-21).

The reduced Young's modulus of the adhesive did also not significantly affect the slope of the normal stress distribution in this area. The small reduction in failure load with increasing temperature is therefore probably related to the small reduction in concrete strength, which was included in the FE-model. It can be concluded that a temperature increase does not significantly affect this type of debonding. Note however that, in the analyses, it was assumed that bond failure is governed by concrete failure and not by failure of the adhesive or the concrete-adhesive interface. The experiments have shown that even at 70°C, bond failure was still to a large extent related to failure of the concrete surface. It can however be expected that further increasing the temperature will result in a different type of bond failure, with corresponding reduced bond strength.

8.4.3 Beam B

8.4.3.1 Results of the analysis at 50°C

Beam B was strengthened with a wider CFRP laminate (80 mm versus 50 mm) and produced with concrete of a higher concrete grade (C45/55 versus C20/25) compared to beam A. The heating and loading of this beam was simulated in the same way as for beam A. The numerical and experimental load-displacement curves are plotted in Figure 8-16 for 50°C.

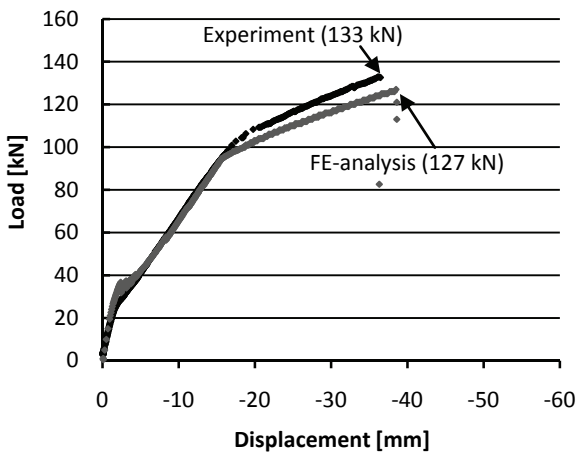


Figure 8-16: Numerical and experimental load-displacement curves of beam B at 50°C

The load-displacement curves showed a similar tendency, although the maximum load and the load at which the internal steel reinforcement started to yield were both slightly lower in the FE-analysis. The maximum load was again slightly dependent (± 5 kN) on the size of the applied load steps, due to the same reasons as for beam A.

Cracks in the concrete occurred over a smaller part of the CFRP laminate at the failure load (Figure 8-17 (127 kN)), compared to beam A, despite the higher maximum load. This is probably related to the higher concrete grade and the wider CFRP laminate of beam B. Large crack strains had developed in the bond layer at the tips of several flexural cracks in the constant moment region. These crack strains were initiated at a lower load level and did not lead to failure of the beam. This seems to confirm that debonding at flexural cracks only leads to local debonding close to the crack tip and not to complete debonding and failure of the beam, as discussed in Section 2.4.4.2 (Matthys 2000).

In the load steps after the maximum load, large crack strains developed in the bond layer, just outside the constant moment region, which can be regarded as the initiation of debonding (Figure 8-17 (113 kN)). In the last, non-converged, load step, debonding had propagated over the entire length from the crack tip till the plate-end (Figure 8-17 (83 kN)).

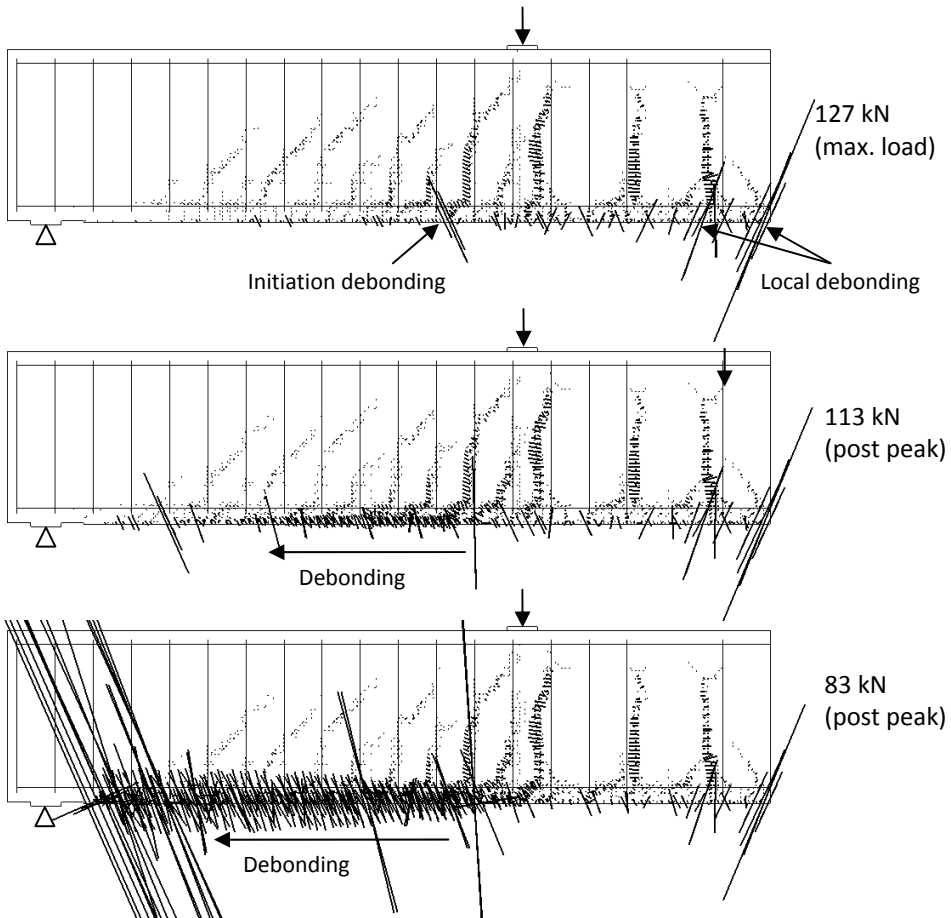


Figure 8-17: Debonding of the CFRP laminate of beam B at 50°C

Figure 8-18 shows the normal stress distribution in the CFRP laminate after heating (ΔT) and after loading of the beam. The temperature increase resulted in tensile stresses in the CFRP laminate, similar as in beam A. Again, stresses started to increase faster with increasing loads after cracking of the concrete and after yielding of the internal steel reinforcement. Yielding started in the constant moment region at about 100 kN, which was slightly higher compared to beam A. The normal stresses in the CFRP laminate at an arbitrary external load were smaller compared to beam A. Both are the result of the wider CFRP laminate that has been applied for beam B.

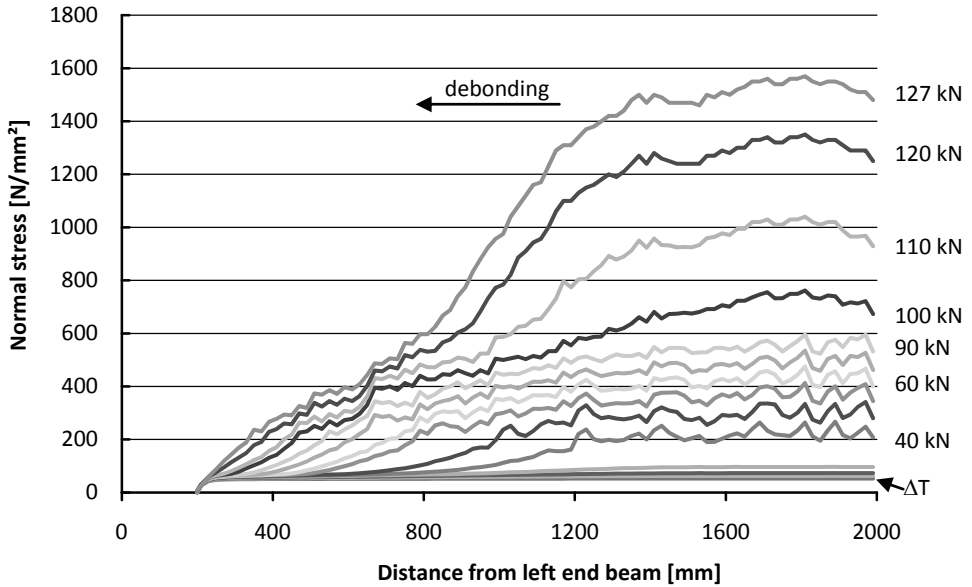


Figure 8-18: Normal stress distributions in the CFRP laminate of beam B at 50°C

The slope of the normal stress distribution is relatively high in the region where debonding was expected to have initiated, resulting in relatively high shear stresses in the concrete bond layer in this region. However, opposite to beam A, the shear stress in this region ($\tau = \Delta\sigma \cdot t_f / \Delta x \approx 3 \text{ N/mm}^2$) has not reached the shear strength ($\tau_{\max} \approx 1.8 \cdot f_{ctm} = 5.9 \text{ N/mm}^2$) at the failure load. Possibly, debonding initiated before the shear strength was reached due to the negative effect of the vertical displacement between the two sides of a shear crack. It can unfortunately not be seen to what extent the difference in vertical displacement between the two sides of the shear cracks has affected this type of debonding. The adopted smeared crack approach implied that the “crack” and thus the vertical displacements between both sides of a crack are “smeared out” over the crack band width. This, most likely, results in different stress concentrations at both sides of the crack tip compared to reality.

8.4.3.2 Comparison of the analyses at the different temperatures

The experimental and numerical load-displacement curves are plotted in Figure 8-19 for 20°C, 50°C and 70°C. Again, also the numerical load-displacement curve of a non-strengthened beam with the same material properties as the strengthened beam at 20°C has been plotted for comparison.

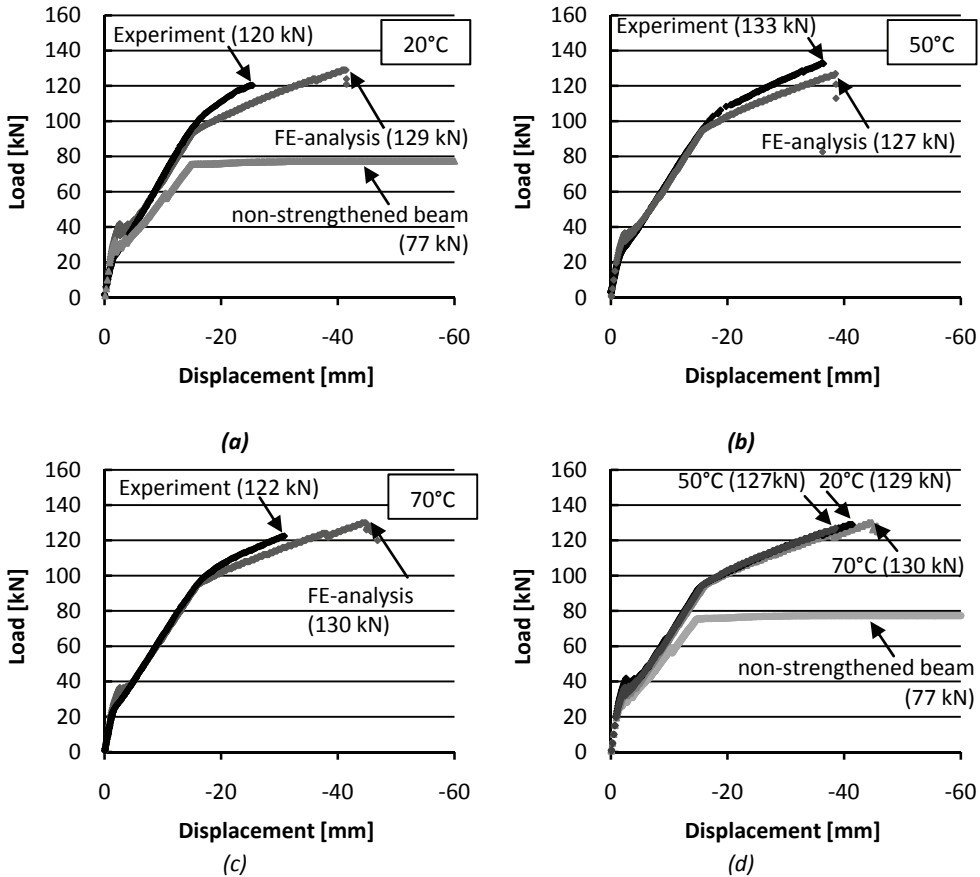


Figure 8-19: Load-displacement curves from the experiments and FE-analyses of beam B at 20°C (a), 50°C (b) and 70°C (c) and a comparison of the numerical load-displacement curves (d)

Table 8-6: Maximum load found for beam B in the numerical analyses and the experiments

Strengthening	Temperature [°C]	Experimental [kN]	FE-analysis [kN]
non-strengthened	20	± 80	77
strengthened	20	120	129
strengthened	50	133	127
strengthened	70	122	130

No significant difference in failure load was found in the FE-analyses between the different temperatures (Table 8-6). At 20°C and 70°C, the numerical failure loads were slightly higher compared to the experimental failure load, while at 50°C, it was slightly lower. For all beams, yielding started at a slightly lower load in the FE-analyses, compared to the experiment. Compared to the (numerical) failure load of the non-strengthened beam (77 kN) a significant higher failure load was reached at all temperatures by strengthening of the beam.

The crack strains in the last, non-converged, load step are plotted in Figure 8-20. Note that this load step is not necessarily the load step when complete debonding has occurred. Especially at 20°C, the finite element analysis was not able to continue until complete debonding until the plate-end has occurred, probably due to numerical problems. It is therefore not possible to directly compare the crack patterns, but it does give an indication of the type of (debonding) failure that has occurred.

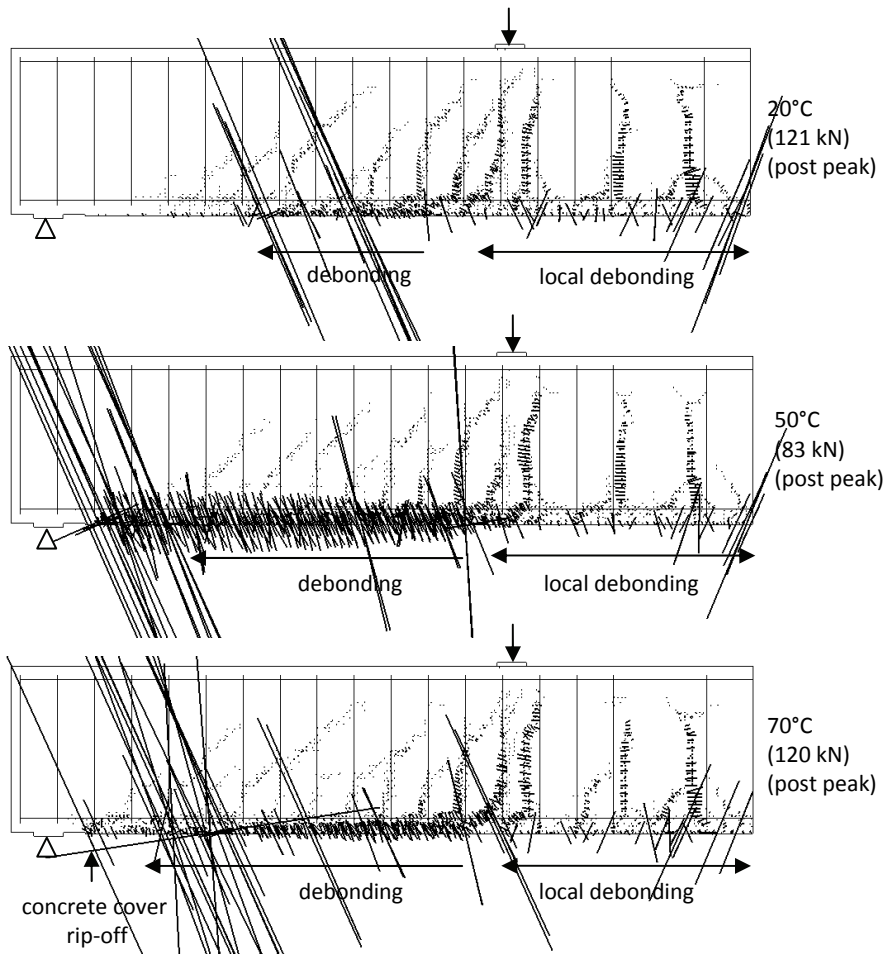


Figure 8-20: Debonding of the CFRP laminate of beams B at 20°C, 50°C and 70°C

At 20°C, in the last, non-converged, load step, suddenly large crack strains developed in the bond layer at three locations outside the constant moment region. Also smaller crack strains developed in the bond layer in between these locations. This seems to indicate that debonding initiated in a similar way as in the beam at 50°C. Again, large crack strains had also developed at the tips of several flexural cracks in the constant moment region at a lower load level, but only resulted in local debonding just next to the crack tip. At 70°C, large crack strains suddenly developed in the bond layer in the load step after the maximum load at about the same location as in the beam at 50°C, but also at the plate-end. At the plate-end, an inclined crack developed from the plate-end towards the internal steel reinforcement and then further towards midspan, along the level of the internal steel reinforcement. This seems to indicate that both debonding as well as (the initiation of) concrete cover rip-off occurred in the same load step. This is probably related to the additional thermal stresses at the plate-end, due to heating of the beam.

In Figure 8-21, the comparison of the experimental and numerical stress distributions in the CFRP laminate is plotted for 20°C, 50°C and 70°C. The comparison has been made after the temperature increase (ΔT) and at 50 kN and 100 kN, in a similar way as for beam A.

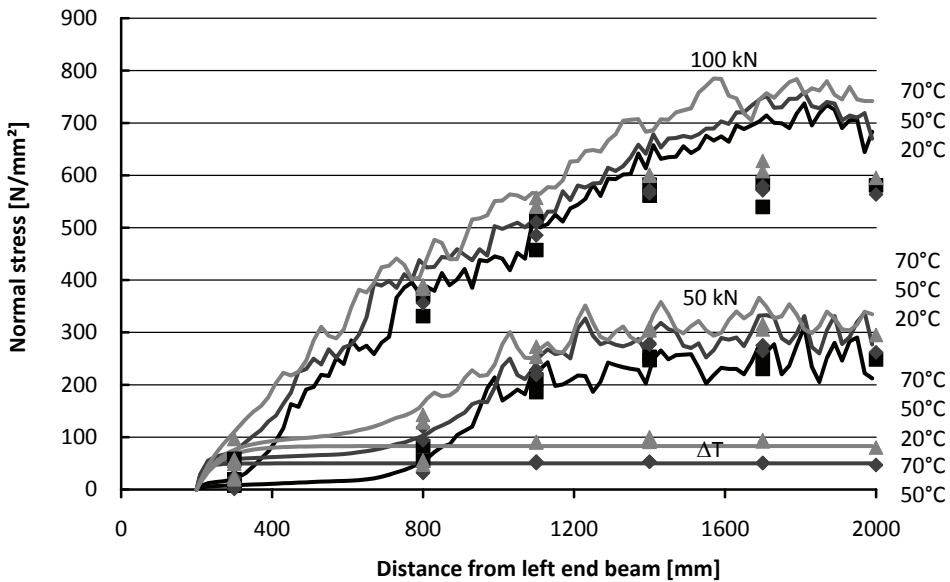


Figure 8-21: Comparison of the experimental and numerical normal stress distributions in the CFRP laminate of beam B at 20°C, 50°C and 70°C

The numerical and experimental stress distributions correspond quite well, although again slightly higher stresses were found in the constant moment region at 100 kN, due to the same reason as for beam A. Again, higher stresses were found with increasing temperatures. The slope to the normal stress distribution in the region where debonding initiated, was however not significantly affected by these additional thermal stresses and/or the reduced Young's modulus of the adhesive, similar as for beam A. It can also be seen that the higher normal stresses at 70°C resulted in a higher slope at the plate-end, especially compared to 20°C. This could explain, in combination with the (slightly) reduced concrete strength at elevated temperature, the initiation of concrete cover rip-off at this temperature. It can however be concluded that the effect of temperature is small for beam B.

8.4.4 Beam C

8.4.4.1 Results of the analysis at 50°C

Beam C was strengthened with an 80 mm wide CFRP laminate, similar as beam B, but was ended at a larger distance (300 mm) from the support. The experimental and numerical load-displacement curves at 50°C were in good agreement with each other (Figure 8-22). The maximum load according to the FE-analysis (127 kN) also corresponded well to the experimental failure load (127 kN).

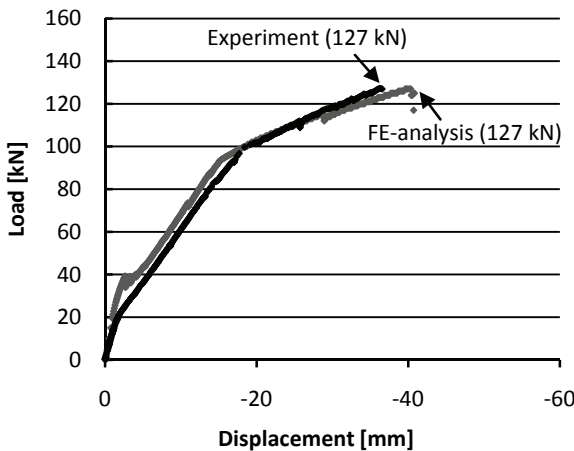


Figure 8-22: Numerical and experimental load-displacement curve of beam C at 50°C

At the failure load, cracks had developed over the entire length of the CFRP laminate, due to the shorter laminate length (Figure 8-23). A large shear crack developed exactly at the plate-end at ± 90 kN, which seems to correspond to the initiation of 'plate-end shear failure'. The load was, however, able to further increase to 127 kN, where after convergence could not be reached anymore.

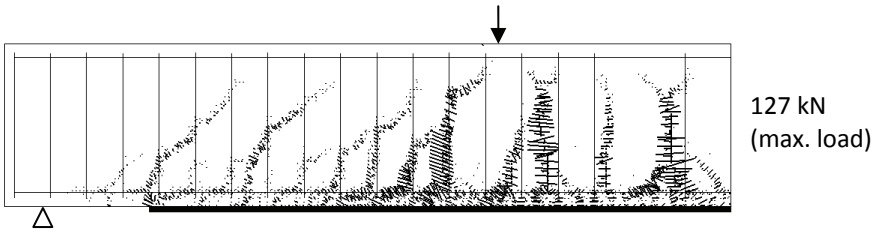


Figure 8-23: Crack pattern at the failure load of beam C

In the last, non-converged, load step (Figure 8-24, 117 kN) significant crack strains developed in the bond layer close to the plate-end. This corresponds to “debonding in the end anchorage zone”, which is the same type of (debonding) failure that was observed in the experiment. This seems to confirm that the finite element analysis has simulated the type of failure correctly. The maximum load (127 kN) can therefore be regarded as the failure load of the beam.

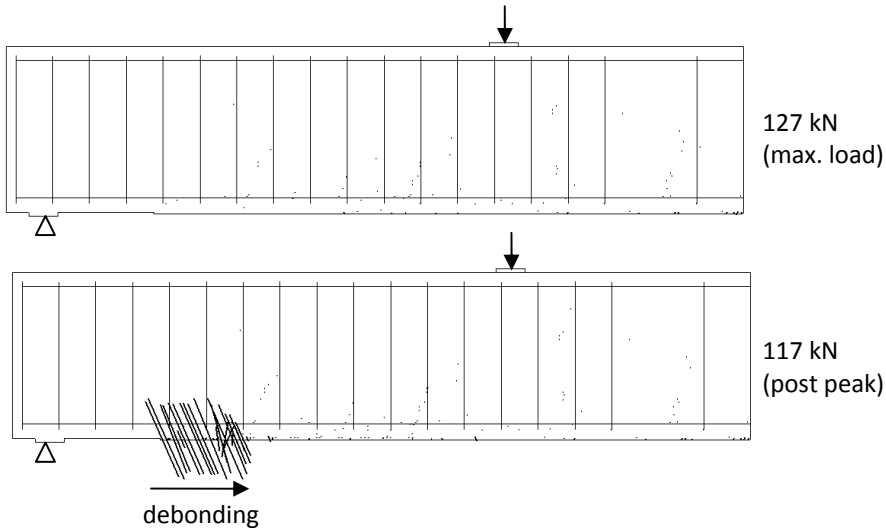


Figure 8-24: Debonding of the CFRP laminate of beam C at 50°C

The normal stresses in the CFRP laminate are plotted in Figure 8-25. The normal stresses in the constant moment region are similar as for beam B, as the same CFRP width and concrete grade have been applied. Yielding of the internal steel reinforcement also started at about the same load (± 100 kN) at midspan.

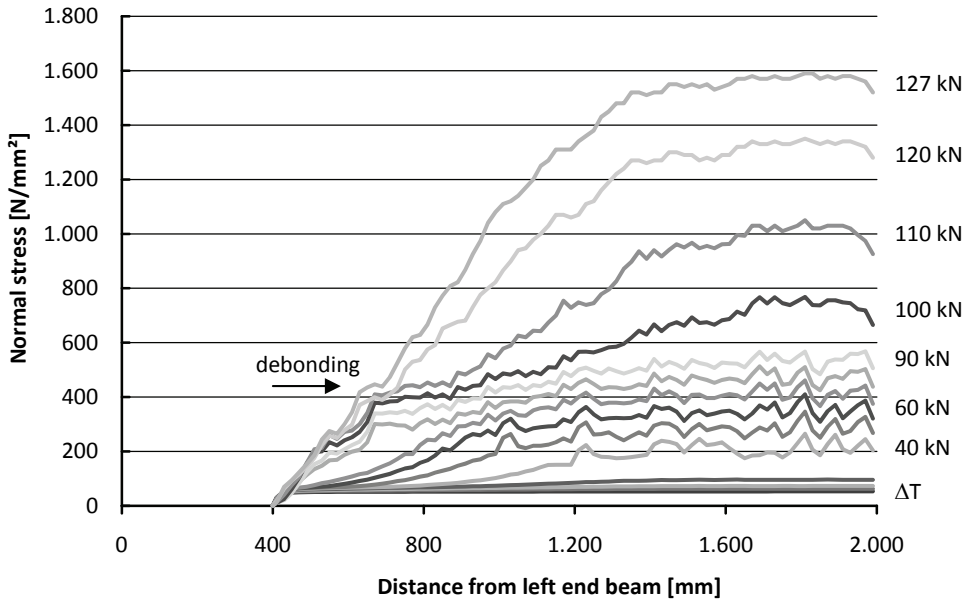


Figure 8-25: Normal stress distributions in the CFRP laminate of beam C at 50°C

At the failure load, the tangent to the normal stress distribution is the highest at the plate-end, although the difference with the tangent in the region just outside the constant moment region is small. The high tangent at the plate-end caused high shear stresses in the bond layer near the plate-end, which has resulted in the initiation of debonding in the anchorage zone. The high tangent to the normal distribution at the plate-end can be explained by the shorter CFRP length that has been applied. As a result, CFRP stresses had to be transferred to the concrete over a shorter (anchorage) length.

8.4.4.2 Comparison of the analyses at the different temperatures

The experimental and numerical load-displacement curves are plotted in Figure 8-26 for the different temperatures. At 20°C and 50°C, similar maximum loads were found in the FE-analysis and the experiment. The maximum load according to the FE-analyses was, at 70°C, similar as at 20°C and 50°C, while in the experiment, the beam failed right after the start of yielding of the internal steel reinforcement at midspan (Table 8-7).

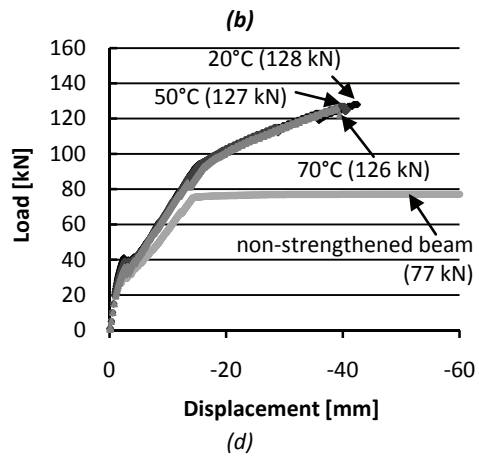
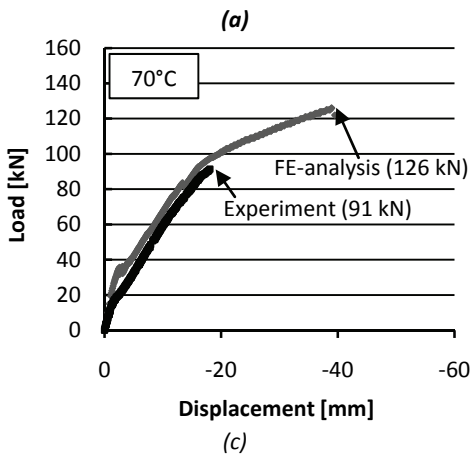
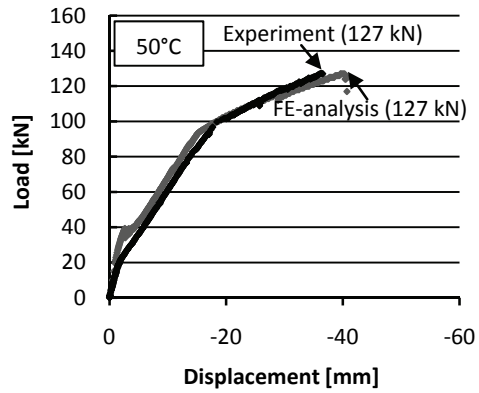
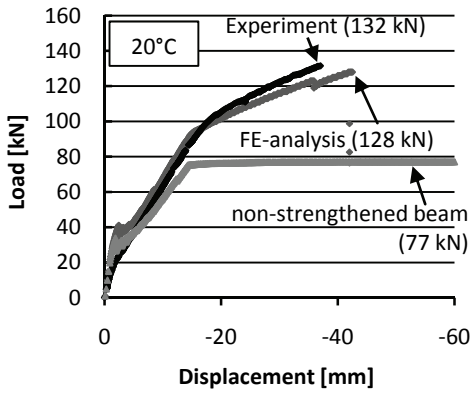


Figure 8-26: Load-displacement curves from the experiments and FE-analyses for beam C at 20°C (a), 50°C (b) and 70°C (c) and a comparison of the numerical load-displacement curves (d)

Table 8-7: Maximum load found for beam C in the numerical analyses and the experiments

Strengthening	Temperature [°C]	Experimental [kN]	FE-analysis [kN]
non-strengthened	20	± 80	77
strengthened	20	132	128
strengthened	50	127	127
strengthened	70	91	126

The beams failed, at all temperatures, by debonding in the end anchorage zone, as can be seen in Figure 8-27. Large crack strains developed in the bond layer in the end anchorage zone in the load steps after the maximum load. This is the same type of failure as was observed in the experiment.

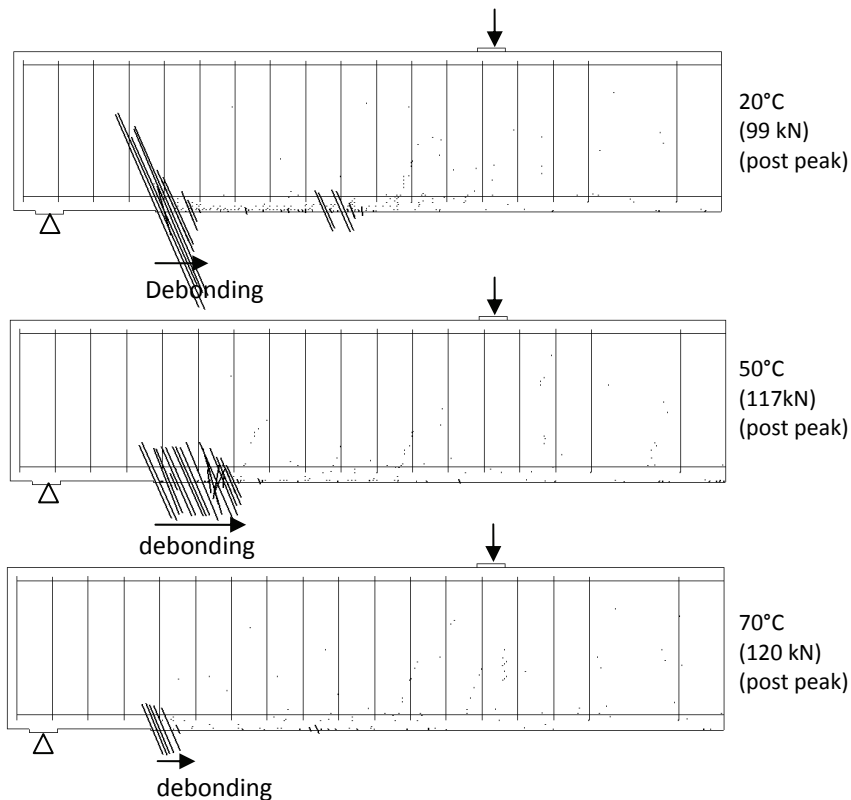


Figure 8-27: Debonding of the CFRP laminate of beams C at 20°C, 50°C and 70°C

The comparison of the experimental and numerical stress distributions in the CFRP laminate, after heating (ΔT) and after loading of the beams to 50 kN and 90 kN, is plotted in Figure 8-28 for the different temperatures. Like for beam A and B, there is a good agreement between the experimental and numerical stress distributions. Again, higher stresses were found with increasing temperatures, due to the initial thermal stresses.

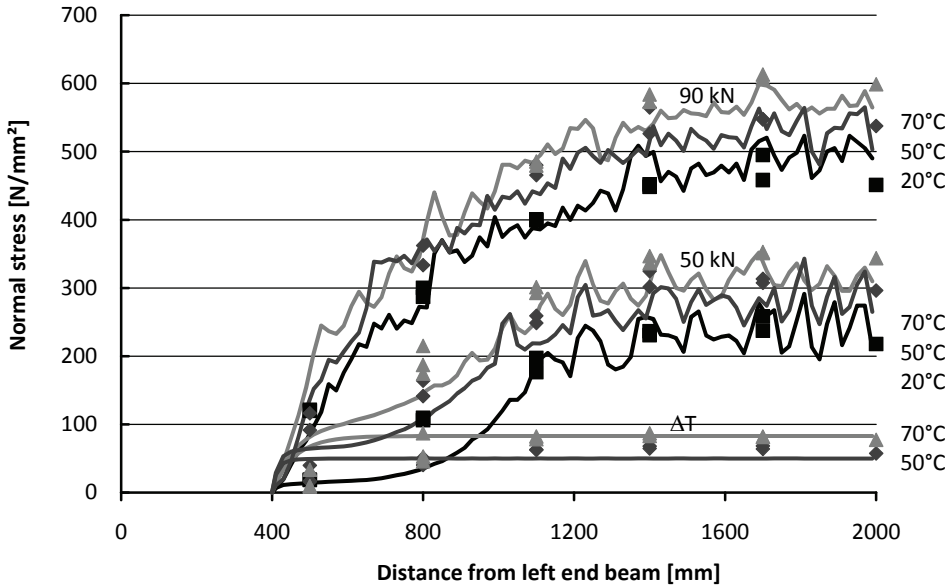


Figure 8-28: Comparison of the experimental and numerical normal stress distributions in the CFRP laminate of beam C at 20°C, 50°C and 70°C

The short laminate length resulted in a relatively high tangent to the normal stress distribution at the plate-end, and consequently in high shear stresses in the anchorage zone, which explains why the beam failed by “debonding at the end anchorage”. The additional thermal stresses due to the temperature increase resulted in a higher tangent to the normal stress distribution at the plate-end. This did however not result in a significant reduction of the failure load with increasing temperature, possibly due to the effect of the reduced Young’s modulus of the adhesive at this temperature. It is expected that the reduced Young’s modulus will decrease the tangent to the normal stress distribution in the anchorage zone, as was observed in the finite element analyses of the small scale tests. However, this effect was not clearly visible in the finite element analysis of beam C. Also note that, in reality, the tangent to the normal stress distribution at the plate-end will also reduce as a result of the time-dependent material properties of the adhesive.

8.4.5 Beam D

8.4.5.1 Results of the analysis at 50°C

Beam D had a lower concrete quality (C20/25) compared to beam B and C and was strengthened with a wider CFRP laminate (150 mm) that ended at 100 mm from the support. The numerical and experimental load-displacement curves at 50°C are plotted in Figure 8-29. The numerical load-displacement curve again corresponded well to the experimental one, although the maximum load found with the FE-analysis (130 kN) was slightly lower compared to the experimental failure load (142 kN).

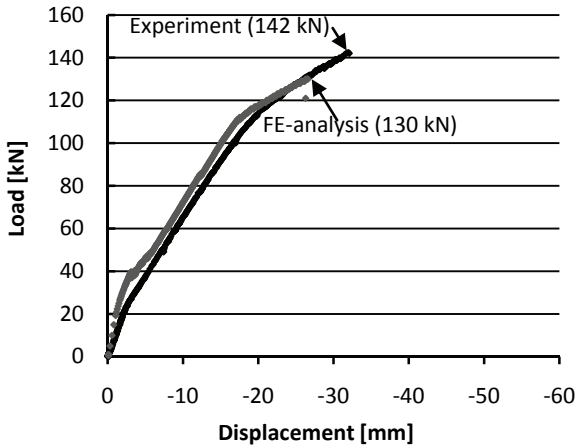


Figure 8-29: Load-displacement curve of beam D at 50°C

It turned out that the maximum load of this beam was highly dependent on the applied fracture energy of concrete, probably because failure of this beam was related to failure in the concrete (concrete cover rip-off), as can be seen in Figure 8-30. In the last, non-converged, load step (121 kN), crack strains suddenly increased significantly in the concrete elements in between the plate-end and the internal steel reinforcement and then towards midspan along the level of the internal steel reinforcement. This type of failure is the same as in the experiment. At the same time, also debonding initiated in the bond layer. Both initiated in the same load step, after the maximum load, which makes it difficult to indicate which one has caused the failure of the beam, or whether one is the result of the other.

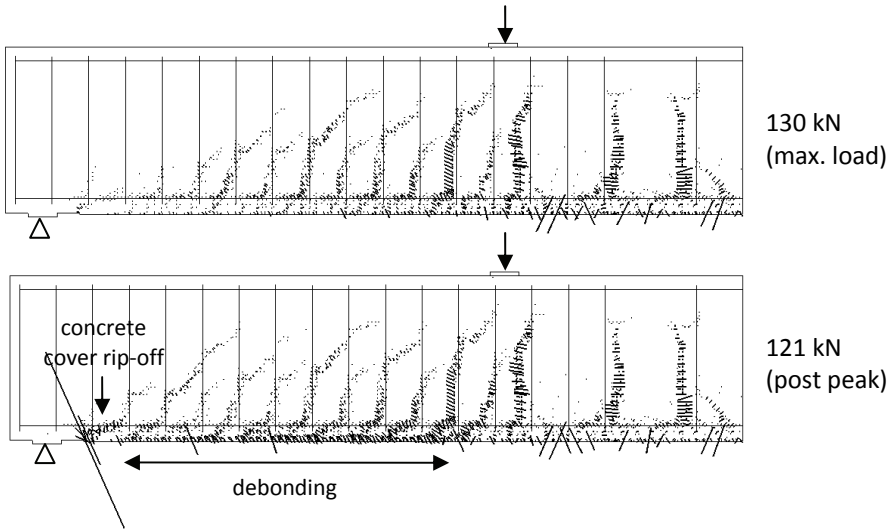


Figure 8-30: Concrete cover rip-off/debonding in beam D at 50°C

Figure 8-31 shows the normal stress distributions in the CFRP laminate at 50°C, again after increasing the temperature (ΔT) and after loading of the beam.

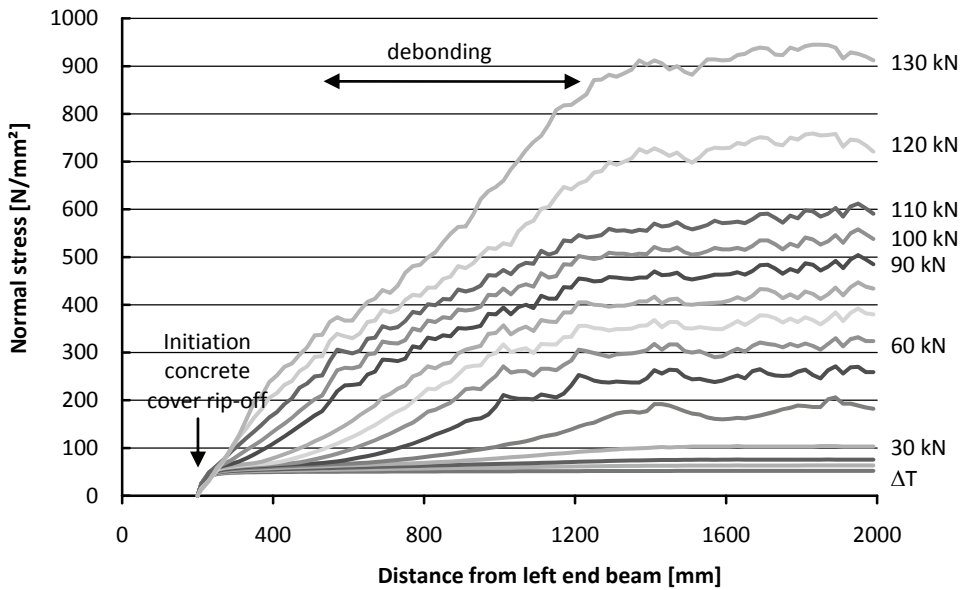


Figure 8-31: Normal stress distributions in the CFRP laminate of beam D at 50°C

The normal stresses in the CFRP laminate due to loading of the beam were lower compared to the other beams, due to the wider CFRP laminate (150 mm). Yielding of the internal steel reinforcement also started at a higher load. The tangent to the normal stress distribution at the failure load turned out to be relatively high at the plate-end. High stress concentrations are therefore expected to develop at this location, similar as for beam C, and are expected to have resulted in the initiation of concrete cover rip-off at this location.

8.4.5.2 Comparison of the analyses at the different temperatures

Figure 8-32 shows the comparison of the numerical and experimental load-displacement curves for 20°C, 50°C and 70°C. Like for the other beams, the load-displacement curve of a non-strengthened beam, with the same material properties as the strengthened beam at 20°C, has also been plotted.

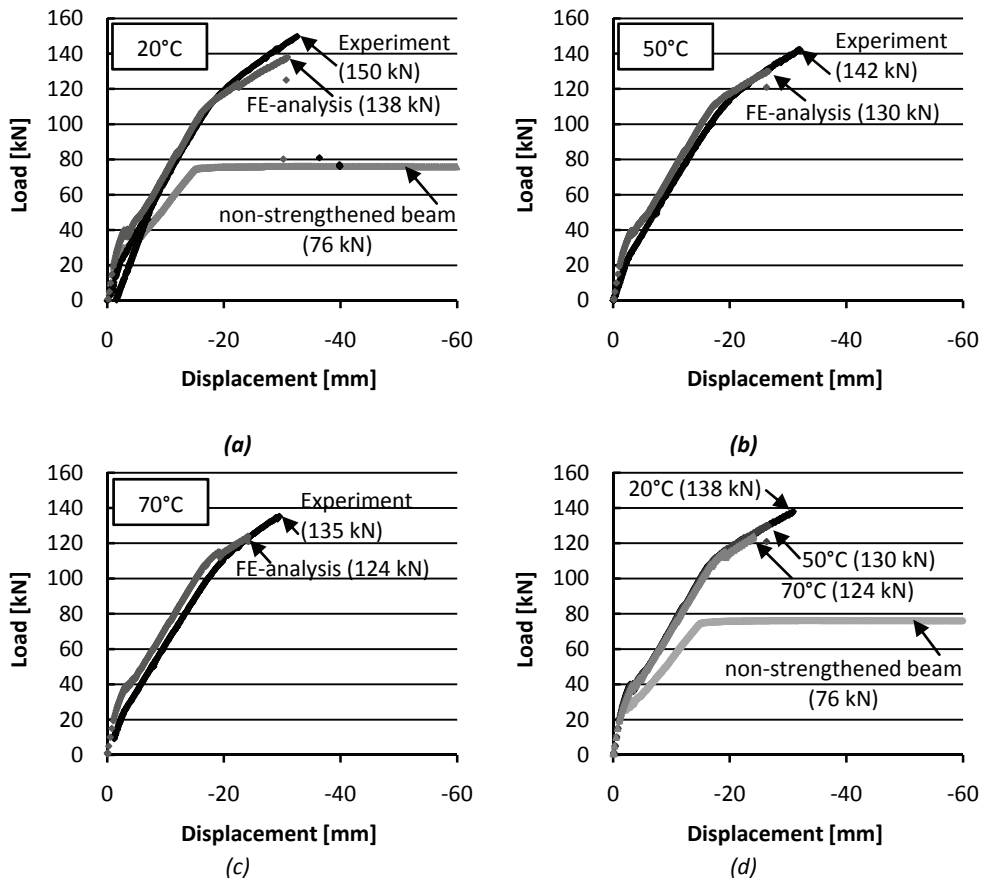


Figure 8-32: Load-displacement curves from the experiments and FE-analyses of beam D at 20°C (a), 50°C (b) and 70°C (c) and a comparison of the numerical load-displacement curves (d)

Table 8-8: Maximum load found for beam D in the numerical analyses and the experiments

Strengthening	Temperature [°C]	Experimental [kN]	FE-analysis [kN]
non-strengthened	20	± 80	76
strengthened	20	150	138
strengthened	50	142	130
strengthened	70	135	124

The beam was slightly bended upwards due to the temperature increase. The displacement at midspan was 0.16 mm upwards after increasing the temperature to 70°C. In the FE-analyses, a slightly reducing maximum load was found with increasing temperature, which was also found in the experiment (Table 8-8). The beams at 20°C and 50°C showed both concrete cover rip-off and debonding in the last, non-converged, load step (Figure 8-33). At 70°C, only concrete cover rip-off was found, probably due to the higher stress concentrations at the plate-end due to the thermal mismatch. Again, local debonding occurred at the tips of several flexural cracks, but this did not lead to complete debonding or failure of the beam.

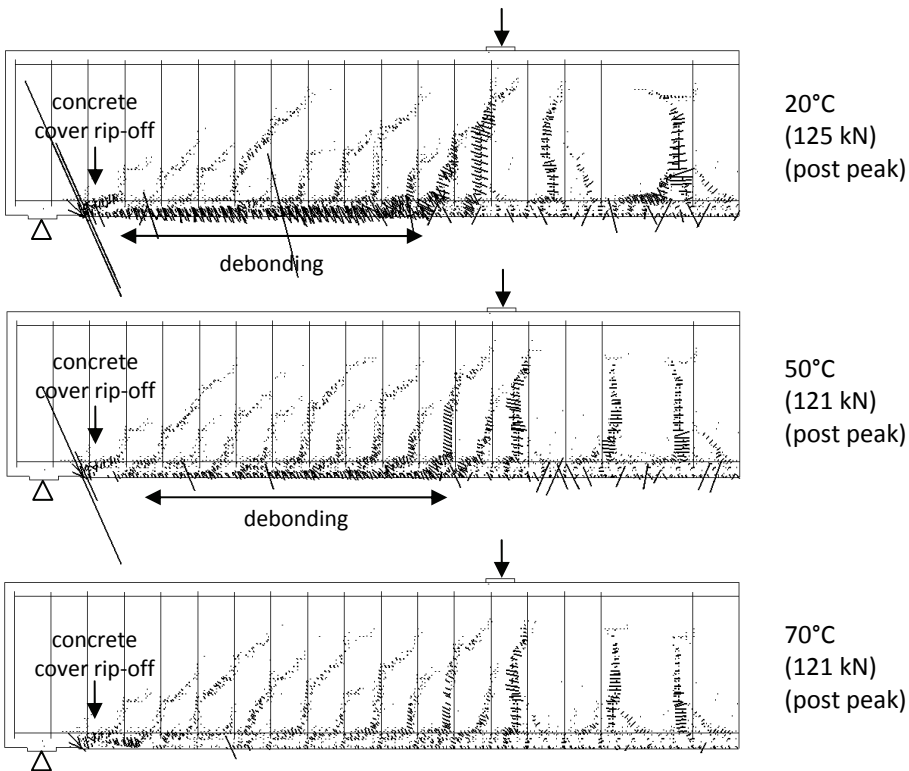


Figure 8-33: Concrete cover rip-off in beam D at 20°C, 50°C and 70°C

Like for the other beams, a comparison of the numerical and experimental normal stress distributions has been made after heating (ΔT) and after loading of the beam (50 kN and 100 kN) (Figure 8-34). Again, the numerical and experimental distributions corresponded quite well to each other.

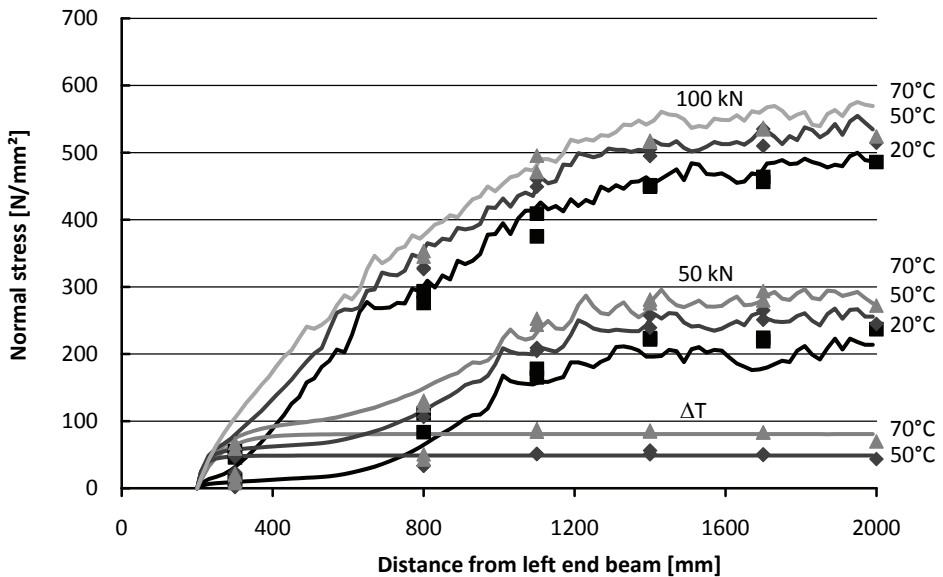


Figure 8-34: Comparison of the experimental and numerical normal stress distributions in the CFRP laminate of beam D

It can also again be seen that increasing the temperature to 50°C and 70°C resulted in the development of thermal stresses in the CFRP laminate. These thermal stresses resulted, as expected, in higher normal stresses in the CFRP laminate with increasing temperature. As a result, more stresses have to be transferred from the CFRP to the concrete at the plate-end, which causes higher shear stresses in the bond layer in the anchorage zone at elevated temperatures, but also in higher stress concentrations at the plate-end. It is expected that the reduced Young's modulus of the adhesive will reduce the tangent to the normal stress distribution at the plate-end, similar as in the small scale bond tests, but this is not clearly visible in Figure 8-34. Note that, in reality, the thermal stresses at the plate-end will further decrease, due to the time-dependent behavior of the adhesive. Separate analyses, in which only the reduced concrete strength and reduced fracture energy of concrete at elevated temperatures have been taken into account, and not the difference in the thermal expansion between concrete and CFRP, have shown that the reduction in the failure load with increasing temperature is mainly related to the reduction of the concrete material properties.

8.5 Summary

All full scale beams that were investigated experimentally, as described in Chapter 7, were numerically simulated by means of finite element analyses at three different temperatures, 20°C, 50°C and 70°C. The simulations have shown that, for beams that are strengthened with a relatively small and long CFRP laminate, failure is governed by debonding of the CFRP laminate that initiates just outside the constant moment region and propagates towards the plate-end. Applying a relatively short laminate resulted in a change in the type of failure. For these beams, failure was governed by debonding in the end anchorage zone. Applying a relatively wide CFRP laminate resulted in concrete cover rip-off, although two of the beams also showed debonding of the CFRP laminate in the same load step. The numerical load-displacement curves of all beams corresponded well to the experimental load-displacement curves. The CFRP stress distributions were also computed accurately with the analyses for all beams at all temperatures.

The finite element analyses have shown that there are different effects of an increasing temperature on the CFRP strengthened structure. First important effect of a temperature change is the development of thermal stresses in the CFRP laminate due to the difference in the coefficient of thermal expansion between concrete and CFRP. This results, at an arbitrary load level, in higher normal stresses in the CFRP laminate with increasing temperature, which causes a higher tangent to the normal stress distribution at the plate-ends. This causes higher shear stresses in the bond layer in the anchorage zone and higher stress concentrations at the plate-end. Both the debonding mechanisms 'debonding in the end anchorage zone' and 'concrete cover rip-off' are therefore expected to be affected negatively by these thermal stresses, although it turned out that the effect was relatively small (less than 1% reduction). The debonding mechanisms that initiated away from the plate-end were not significantly affected by the additional thermal stresses, as the tangent to the normal stress distribution, and thus the shear stresses in the concrete bond layer, did not significantly change at the location where debonding was initiated.

It turned out that the reduction of the failure load of beam D was mainly related to the applied reduced strength and fracture energy of the concrete at elevated temperatures. This effect was significantly smaller for the other beams, which all failed by debonding. It is expected that this is related to the fact that failure of beam D occurred in the concrete and not in the bond layer, as was the case for the other beams. The failure load of beam D was therefore more related to the concrete material properties, while the failure load of the other beams was more related to the shear stress distribution in the bond layer.

The third effect of temperature is the reduced Young's modulus of the adhesive at elevated temperature, especially at 70°C. This affects the tangent to the normal stress distribution and therefore reduces the stress concentrations and shear stresses in the bond layer at the plate-end. The effect on the failure load was however small.

Note that the finite element model has been developed for concrete (bond) failure only and not for failure of the adhesive or failure of the concrete-adhesive interface. The concrete (bond) properties were only slightly reduced with increasing temperature in the model. It is however likely that further increasing the temperature above 70°C will result in adhesive or interfacial failure, which is accompanied by a significant reduction in bond strength, but also in a wider scatter of bond strength. The latter makes it difficult to correctly simulate the behavior of a beam that fails by one of these changed types of bond failure. The experimental research on the full scale beams has however shown that, at 70°C, failure was still mainly governed by concrete bond failure.

9 Discussion

9.1 Introduction

The design of a CFRP strengthened structure at room temperature is generally governed by the debonding of the externally bonded CFRP (Chapter 2). So far, only a limited amount of research has been carried out into the effect of temperature on the debonding behavior (Chapter 3). It was therefore decided to carry out small scale bond tests at both low and elevated temperatures (Chapter 5). The tests gave a better insight in the bond behavior of the concrete-adhesive-CFRP joint in these temperature ranges. Additional finite element analyses were carried out to further increase the insight in the bond behavior (Chapter 6).

Full scale CFRP strengthened beams can, however, fail after initiation of different types of debonding, which can all be affected by temperature in a different way. Prior to this investigation, to the author's knowledge, no experimental research was carried out into the effect of elevated temperatures on full scale CFRP strengthened beams. In this research project four different beam configurations were investigated at three different temperatures, 20°C, 50°C and 70°C (Chapter 7). These experiments were also simulated by finite element analyses to further increase the insight in the debonding behavior at room and elevated temperatures (Chapter 8).

The findings of the experiments and analyses are summarized and discussed in this chapter. Based on the results, the following five effects of temperature on the behavior of a flexural CFRP strengthened (reinforced) concrete structure can be distinguished:

- a. The development of thermal stresses in the concrete-adhesive-CFRP joint due to the difference in the coefficient of thermal expansion between concrete and CFRP (Section 9.2).
- b. The reduced Young's modulus of the adhesive at elevated temperature (Section 9.3).
- c. The increased creep of the adhesive at elevated temperature (Section 9.4).
- d. The reduced bond strength with an increased scatter at elevated temperatures, especially when the type of bond failure changes (Section 9.5).
- e. The decreased tensile strength and fracture energy of concrete at elevated temperatures (Section 9.6).

In each of the following sections, one of these temperature effects is discussed. In reality, of course, these effects occur simultaneously. However, for the sake of clarity, they are discussed individually. The effects a. and e. occur gradually with increasing temperature, while the effects b., c. and d. suddenly become significant around the glass transition temperature of the adhesive.

In Section 2.4.3, the following debonding mechanisms were distinguished (Figure 9-1).

1. Debonding at flexural cracks
2. Debonding due to high shear stresses
3. Debonding at shear cracks
4. Debonding at the end anchorage
5. Plate-end shear failure
6. Concrete cover rip-off
7. Debonding due to the unevenness of the concrete surface

It turned out that a certain temperature effect could affect certain debonding mechanisms, while others were more or less unaffected. Based on the experimental and numerical results, it was decided to make a distinction in this chapter between the debonding mechanisms that are expected to initiate;

- in zone A, the end anchorage zone ('debonding at the end anchorage' (4)),
- at point B, exactly at the plate-end ('plate-end shear failure' (5) and 'concrete cover rip-off' (6))
- in zone C, outside the end anchorage zone in areas with high shear stresses between concrete and CFRP ('debonding due to high shear stresses' (2) and 'debonding at shear cracks' (3)).

Debonding at flexural cracks (1) and debonding due to the unevenness of the concrete surface (7) are not discussed in this chapter, as the first is expected only to lead to local debonding (Section 2.4.3.1), while the second can easily be prevented by removing the unevenness before applying the CFRP laminate (Section 2.4.3.6).

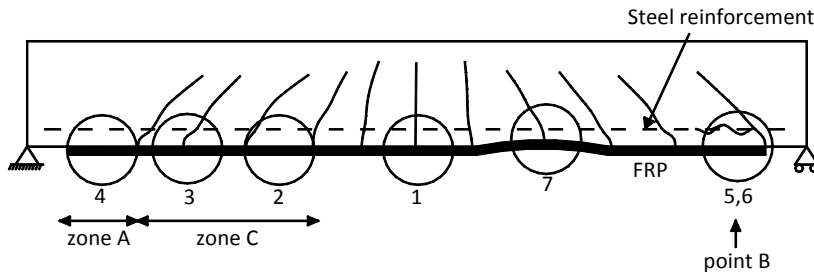


Figure 9-1: Debonding in the end anchorage zone (zone A), exactly at the plate-end (point B) and outside the end anchorage zone in areas with high shear stresses (zone C)

9.2 The development of thermal stresses

9.2.1 General

One of the effects of temperature is the development of thermal stresses due to the thermal mismatch between concrete and CFRP. A (reinforced) concrete structure expands with increasing temperature due to the positive coefficient of thermal expansion of concrete and steel ($\alpha_c \approx \alpha_s \approx 10 \cdot 10^{-6} / ^\circ\text{C}$) (Figure 9-2a). CFRP, however, has a significant lower, even negative, coefficient of thermal expansion ($\alpha_f \approx 0$ to $-1 \cdot 10^{-6} / ^\circ\text{C}$) (Section 4.4.3). The experiments showed that an externally bonded CFRP laminate, to a large extent, follows the expansion of the reinforced concrete (Figure 7-7), despite its significant lower coefficient of thermal expansion. The beam will also bend upwards with a temperature increase, due to the externally bonded CFRP, but this effect is very small. Both can be explained by the relatively small cross-section of the CFRP laminate, compared to that of the concrete structure to which it is bonded.

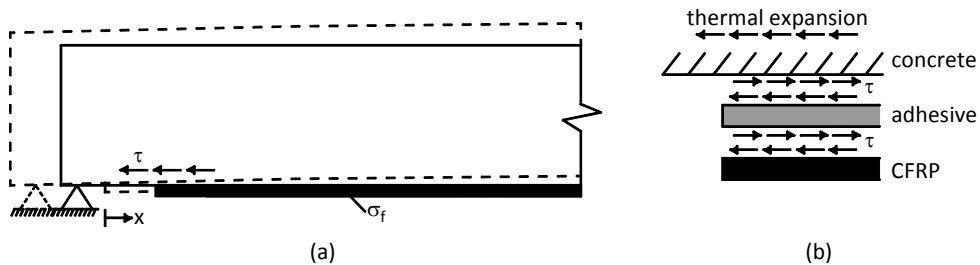


Figure 9-2: Thermal expansion of a CFRP strengthened structure (a) and the corresponding thermal shear stresses at the plate-end (b)

The imposed extension of the CFRP laminate due to a temperature increase causes tensile stresses in the CFRP laminate (Figure 9-3a). These tensile stresses are transferred to the concrete by means of shear stresses in the concrete adjacent to the concrete-adhesive interface (Figure 9-2b and Figure 9-3b).

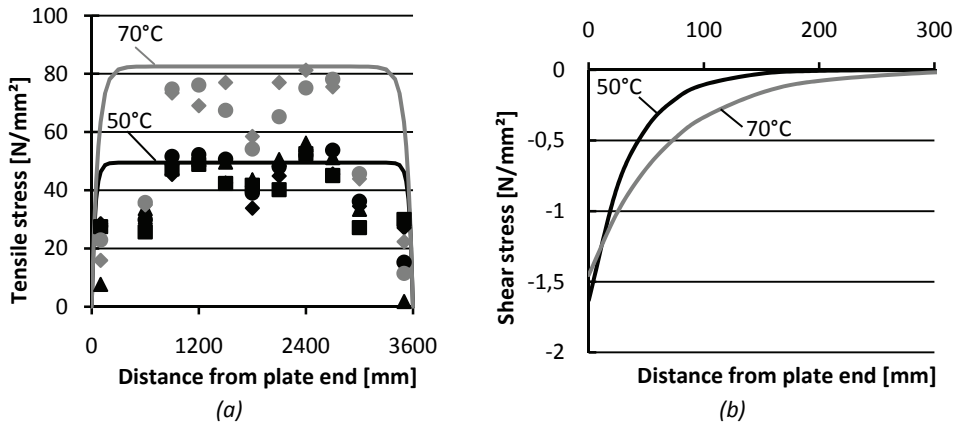


Figure 9-3: Experimental (dots) and analytical (lines) normal stress in an externally bonded CFRP laminate (a) and corresponding analytical shear stress in the concrete adjacent to the concrete-adhesive interface in the end anchorage zone (b) at 50°C and 70°C

It can be seen that thermal shear stresses are mainly concentrated in the anchorage zone close to the plate-end. It can therefore be expected that only the debonding mechanisms that are initiated in the end anchorage zone (zone A) (Section 9.2.2) and/or at the plate-end (point B) (Section 9.2.3) are possibly affected by the thermal mismatch between concrete and CFRP. The debonding mechanisms that are initiated outside the end anchorage zone (zone C) are not significantly affected by the thermal mismatch, as will be shown in Section 9.2.4.

9.2.2 Zone A: The end anchorage zone

Both loading and heating of a CFRP strengthened structure results in the development of tensile stresses in the CFRP laminate. This implies that the shear stresses due to a temperature increase act in the same way as the shear stresses due to loading of a beam. This could theoretically lead to a reduced failure load, as part of the anchorage capacity has to be used for anchoring of the thermal stresses.

The experimental results of the full scale beams showed however that the reduction of the failure load at 50°C is negligible for a beam that failed by debonding in the end anchorage zone (beam C), due to the positive effects of the reduced Young's modulus and creep behavior of the adhesive on the shear stress distribution in the end anchorage zone, as will be explained in Section 9.3 and Section 9.4.

At 70°C, beam C failed at a significant lower failure load. It is unlikely that this can be solely explained by the thermal mismatch between concrete and CFRP, but it is probably related to a combination of temperature effects, like the increased anchorage length (Section 9.3) and the reduced bond strength (Section 9.5) at elevated temperatures.

9.2.3 Point B: At the plate-end

Failure of a CFRP strengthened structure can also initiate at the plate-end (point B in Figure 9-1). Both 'concrete cover rip-off' and 'plate-end shear failure' are preceded by the initiation of a crack in the concrete in between the end of the CFRP laminate and the internal steel reinforcement, which can propagate further along the level of the internal steel reinforcement ('concrete cover rip-off') or as a shear crack ('plate-end shear failure') (Figure 9-4). Which of these two types of failure is governing mainly depends on the amount of shear reinforcement (Section 2.4.3.5).

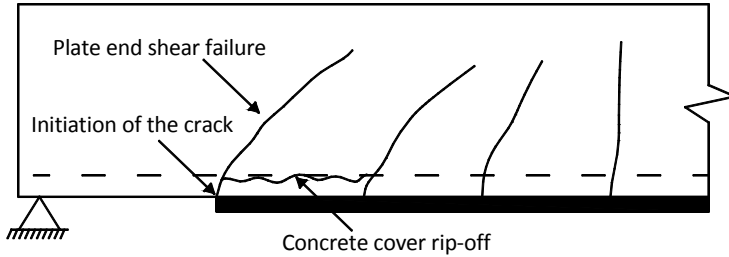


Figure 9-4: Plate-end shear failure and concrete cover rip-off

Failure is in this case not a result of bond failure of the concrete-adhesive-CFRP joint, but a result of cracking of the concrete at the plate-end. These mechanisms are therefore mainly related to the concrete properties and the stress concentrations in the concrete at the plate-end (Figure 9-5).

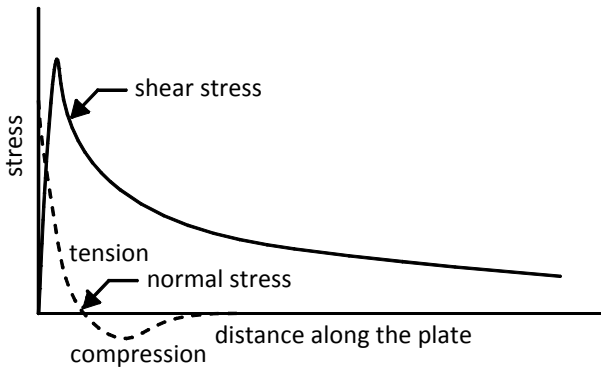


Figure 9-5: Shear stresses and normal stresses perpendicular to the bonded area in the concrete close to the FRP end (Roberts 1989)

Thermal shear stresses are also concentrated at the plate-end and act in the same way as the stresses due to loading, as has been explained in the previous section. They could therefore negatively affect the failure load of a beam that fails by one of these debonding mechanisms. As mentioned before, the reduced Young's modulus (Section 9.3) and the creep behavior (Section 9.4) of the adhesive at elevated temperature will cause a reduction of the stress concentrations at the plate-end and will therefore (partly) undo the negative effect of the thermal mismatch.

Both the full scale experiments (Section 7.5.4) and the finite element analyses (Section 8.4.4) showed that the failure load of a beam (beam D) that failed by 'concrete cover rip-off' decreased with about 5% at 50°C and 10% at 70°C (Table 8-8), both compared to room temperature. With additional analyses, in which the different effects of temperature were investigated individually, it was concluded that this reduction was mainly related to the reduction of the tensile strength and fracture energy of concrete at elevated temperature (Section 9.6), and not related to the additional thermal stresses. Hence, it can be concluded that the effect of thermal stresses on this mechanism is negligible within the tested temperature range.

9.2.4 Zone C: Outside the anchorage zone

The experiments and finite element analyses have shown that the debonding mechanisms that are initiated outside the anchorage zone, in areas with high shear stresses in the concrete adjacent to the concrete-adhesive interface ('debonding due to high shear stresses' and 'debonding at shear cracks') (Figure 9-6) are not significantly affected by the thermal stresses.

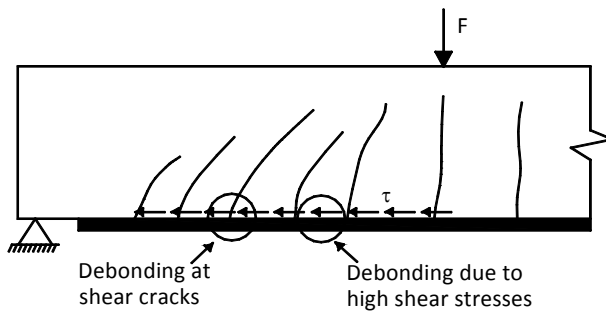


Figure 9-6: Thermal shear stresses in zone C after a temperature increase

Shear stresses are directly related to the difference in CFRP force (ΔN_{fd}) over a certain length (Δx) (Figure 9-7). The CFRP force due to a temperature change ($N_{f,\Delta T}$) is constant in zone C (Figure 7-8). The difference in the normal force over a short length Δx will therefore not change at low or elevated temperatures, as the thermal force ($N_{f,\Delta T}$) is the same at both sides of Δx in Figure 9-7. Shear stresses in zone C are, as a result, not affected by the additional thermal stresses in the CFRP laminate. The effect of the thermal mismatch between concrete and CFRP can therefore be neglected for these debonding mechanisms.

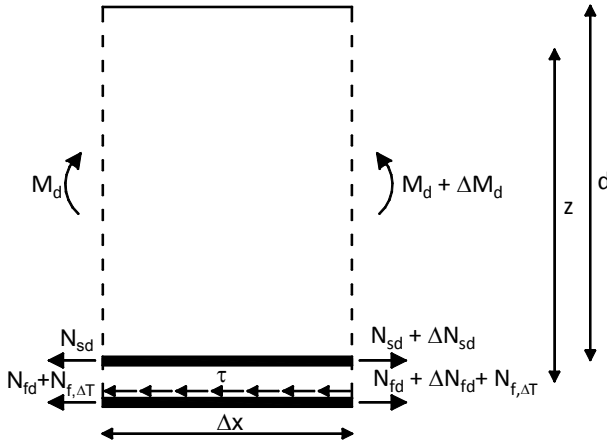


Figure 9-7: Shear stresses in the concrete at the interface with the FRP

9.3 The reduced Young's modulus of the adhesive at elevated temperatures

9.3.1 General

The second effect of temperature that was observed in the experiments is the reduction of the Young's modulus of the adhesive at elevated temperature, especially above the glass transition temperature of the adhesive (Figure 9-8). Note however that the glass transition temperature is increased after applying a temperature cycle, as can be seen in Figure 9-8.

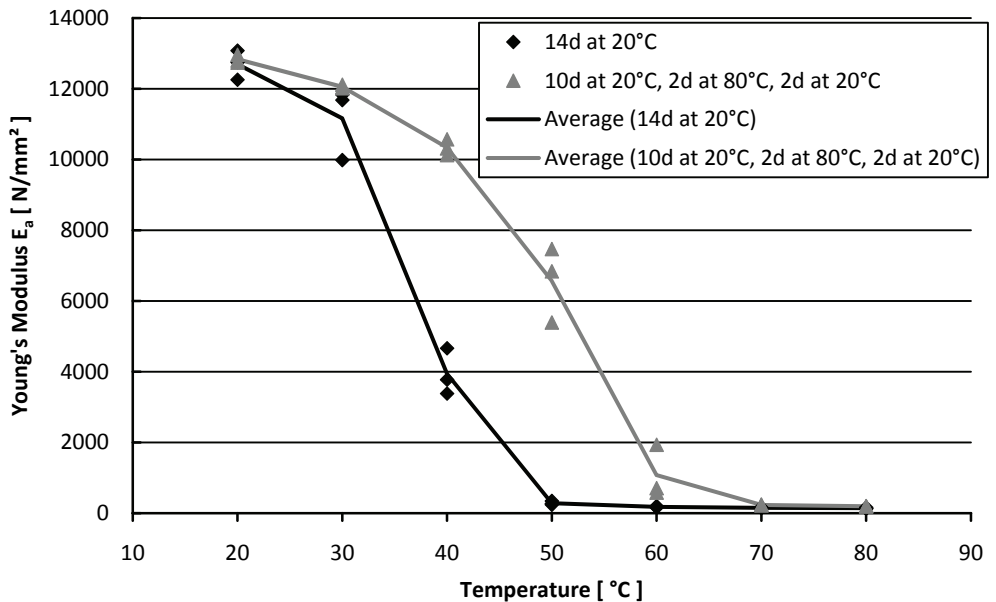


Figure 9-8: Influence of temperature on the Young's modulus of the applied adhesive

The results of the FE-analyses of the small scale bond tests showed that the reduced Young's modulus results in more linear distributed normal stresses in the CFRP laminate (Figure 9-9a) and lower peaks in shear stresses at the plate-end (Figure 9-9b).

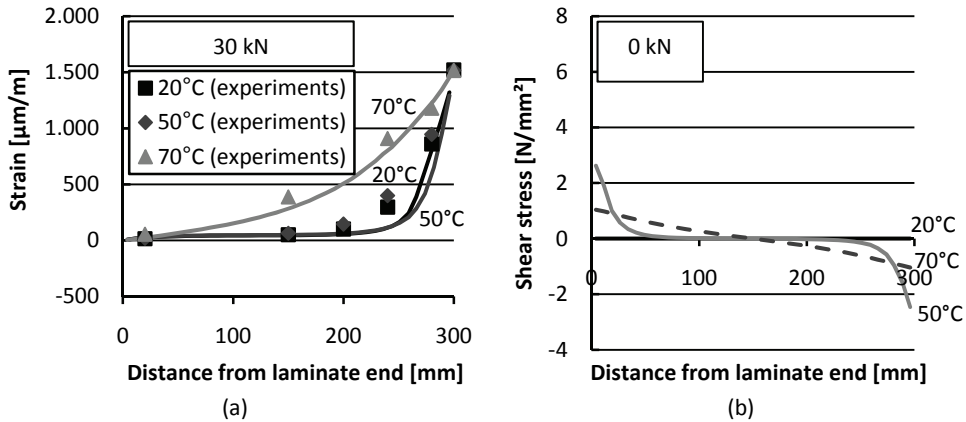


Figure 9-9: (a) The (mechanical) strain distribution in a CFRP laminate at 30 kN and the shear stresses in the concrete adjacent to the adhesive after the temperature change for 20°C, 50°C and 70°C

The reduced Young's modulus mainly affects the stress distributions at the plate-end and could therefore affect the debonding mechanisms that initiate in the end anchorage zone (zone A) (Section 9.3.2) and/or at the plate-end (point B) (Section 9.3.3). The experiments and finite element analyses also showed that the reduced Young's modulus of the adhesive did not have a significant effect on the stress distribution further away from the anchorage zone (zone C (Figure 9-1)) and does therefore not significantly affect the debonding mechanisms that are initiated in zone C (Section 9.3.4).

9.3.2 Zone A: The end anchorage zone

The reduced Young's modulus of the adhesive at elevated temperature reduces the shear stresses at the plate-end and could therefore have a positive influence on the failure load. The finite element analyses of the small scale bond tests showed however that the effect of the reduced Young's modulus of the adhesive on the anchorage capacity is negligible (Figure 6-12 and Figure 6-20b). The finite element analyses also showed that the anchorage length is increased by the reduced Young's modulus (Figure 9-9a) and could theoretically result in a situation that the available anchorage length is sufficient at room temperature, but becomes insufficient at elevated temperature.

The effect of the reduced Young's modulus of the adhesive on the anchorage length (ℓ_b) can also be determined analytically with the model of Yuan et al. (2004) (Appendix J). This model is, unlike most other analytical models for 'debonding at the end anchorage', able to take the (reduced) Young's modulus of the adhesive into account by applying a bi-linear bond-slip relation for the concrete-adhesive-CFRP interface in which the slip of the adhesive layer can be included. The full derivation is given in Appendix J.

The relation between the Young's modulus of the adhesive and the anchorage length of a CFRP laminate ($E_f = 165,000 \text{ N/mm}^2$) according to this model is plotted in Figure 9-10.

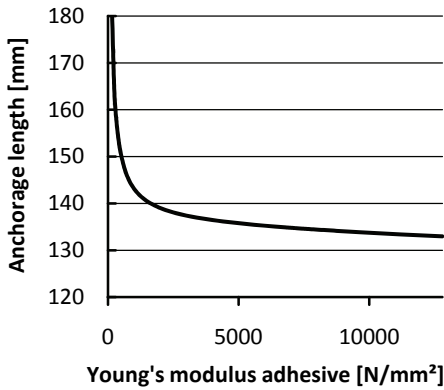


Figure 9-10: Effect of the Young's modulus of the adhesive on the anchorage length

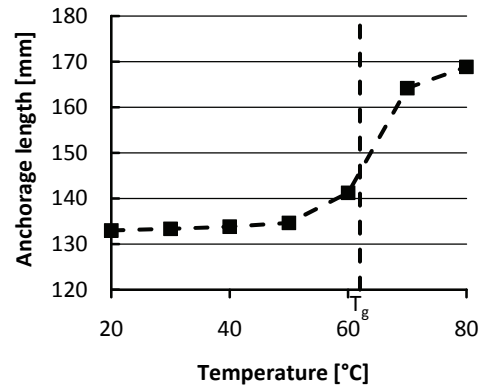


Figure 9-11: Effect of temperature on the anchorage length of SikaDur-30

It can be seen that for a very low Young's modulus of the adhesive a relatively large increase in anchorage length is found. When combined with the temperature-Young's modulus relation for SikaDur-30 (Figure 4-18), a temperature-anchorage length relation can be given for this specific adhesive (Figure 9-11). Up to the glass transition temperature, the anchorage length is not significantly affected, while above this temperature, it increases faster. It can however be seen that the increase in anchorage length is only 40 mm between 20°C and 80°C. For normal sized CFRP strengthened beams, the available anchorage length is generally significantly longer, which makes it unlikely that the increased anchorage length will affect the (design) failure load.

9.3.3 Point B: At the plate-end

The reduced Young's modulus of the adhesive will reduce the stress concentrations at the plate-end and could therefore have a positive effect on the failure load of beams that fail by 'concrete cover rip-off' or 'plate-end shear failure'. As has been explained in Section 9.2.3, the results from the experiments and the FE-analyses have however shown that the effect of temperature on the failure load is small (-5% at 50°C and -10% at 70°C) and is mainly related to the reduced tensile strength and fracture energy of concrete at elevated temperature (Section 9.6), while the effect of the additional thermal stresses and the reduced Young's modulus turned out to be negligible.

9.3.4 Zone C: Outside the anchorage zone

The experimental results have shown that the reduced Young's modulus of the adhesive is not affecting the stress distribution further away from the plate-end. This implies that the shear stress in the concrete adjacent to the concrete-adhesive interface is also not affected. Although not measured in the experiments, a reduced Young's modulus would probably affect local stress concentrations close to the crack tips. Based on the strain measurements in the full scale experiment, it is however expected that debonding in zone C is mainly related to the mean shear stress over a longer length, and only slightly to the (shear) stress concentrations near crack tips.

9.4 The increased creep of the adhesive at elevated temperatures

The third temperature effect that was distinguished in the experiments is the time-dependent creep behavior of the adhesive. The experimental results have shown that the thermal stresses in the end anchorage zone of a CFRP laminate partly disappear over time (Figure 7-7, Figure 9-12). Note that the points in Figure 9-12 where the stresses have been determined are connected by straight lines to show the tendency of the thermal stress distribution in the CFRP. In reality, the thermal strain distribution between two points will not be linear. Visual inspection during the tests did not show any cracking or debonding at the plate-end during heating of the beams. It is therefore expected that this behavior is related to the reduction of the Young's modulus and to short term creep of the applied epoxy adhesive.

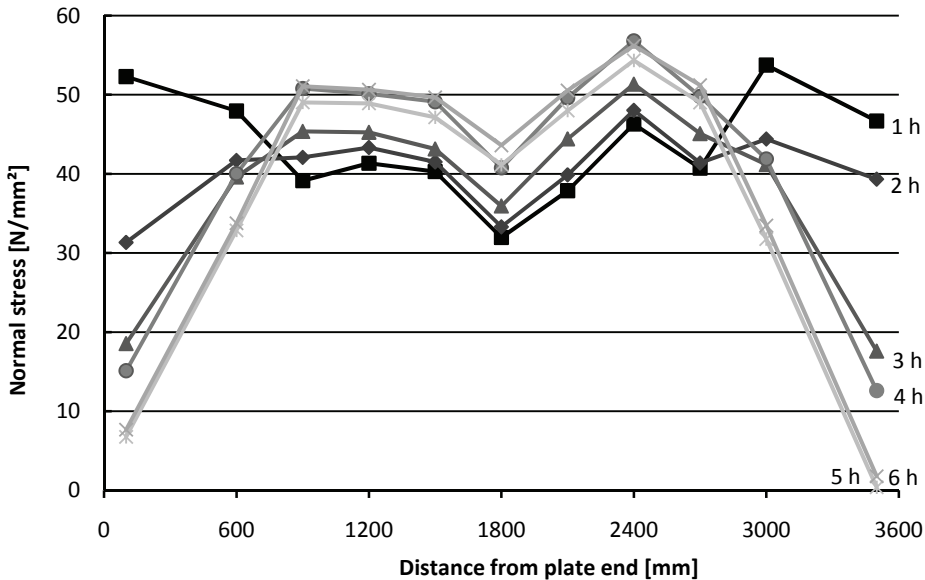


Figure 9-12: Reduction of thermal stresses over time in the full scale experiments at 50°C

Creep of the adhesive is relatively small at room temperature but becomes significantly higher at temperatures close to and above the glass transition temperature of the adhesive (T_g). The higher the temperature, the faster the thermal stresses disappeared (Figure 5-21). A reduction of the normal stresses in the anchorage zone of the CFRP laminate results in a reduction of the peak in shear stress in the concrete adjacent to the concrete-adhesive interface at the plate-end. The creep behavior of the adhesive will therefore reduce the effect of the thermal mismatch between CFRP and concrete.

Creep of the adhesive will not only affect the thermal stress distribution, but also the CFRP stress distribution due to (sustained) loads (e.g. dead weight). CFRP strengthening is, however, in most cases, applied for strengthening of existing structures, which implies that the level of sustained load carried by the CFRP is small. Moreover, at 50°C, it still takes about 5 hours till the stress distribution reaches its final distribution, as can be seen in Figure 9-12. The stress distribution due to short term loads is therefore not significantly affected by the creep behavior of the adhesive, while the stress distribution due to long term loading will be affected.

9.5 The reduced bond strength at elevated temperatures

9.5.1 General

The fourth effect of temperature observed in the experiments is the reduction of the bond strength with increasing temperature, especially around the glass transition temperature of the adhesive ($T_g = 62^\circ\text{C}$ (Sika 2009)) (Figure 9-13, Chapter 5.2).

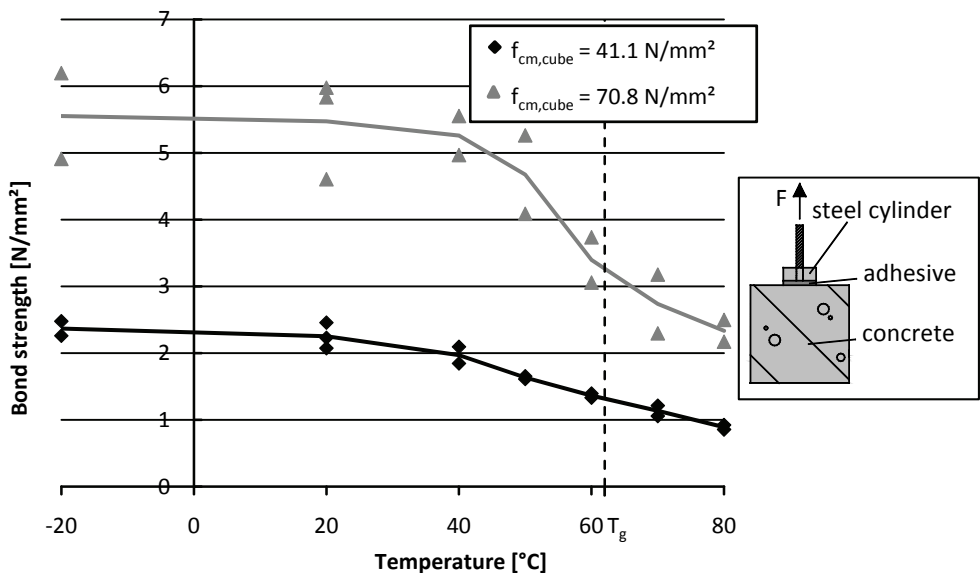


Figure 9-13: Reduction of the bond strength with increasing temperatures for two different concrete grades

At around this temperature, a change in the type of bond failure was observed in the small scale bond tests. At temperatures up to about the glass transition temperature of the adhesive, debonding is caused by bond failure in the concrete adjacent to the concrete-adhesive interface, leaving a small layer of concrete remaining attached to the adhesive after debonding (A in Figure 9-14). At higher temperatures, the type of failure changes to bond failure exactly in the concrete-adhesive interface, without leaving any concrete remaining attached to the CFRP (B in Figure 9-14).

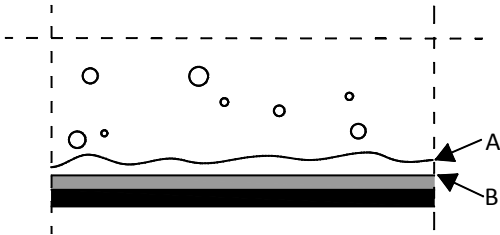


Figure 9-14: Bond failure in the concrete ($T < T_g$) (A) and in the concrete-adhesive interface ($T > T_g$) (B)

The change in type of bond failure is accompanied by a significant reduction in bond strength, which explains the reduced failure load of the small scale bond tests at temperatures above T_g (Section 5.3.2 and 5.4.2). Furthermore, a wider scatter in bond (shear) strength is observed above T_g , which makes it difficult to predict the reduction of the failure load at these temperatures.

The full scale beams (Chapter 7) that failed by debonding in the concrete adjacent to the concrete-adhesive interface (zone A and C) at room temperature did not show a significant change in the type of bond failure at 70°C, opposite to the small scale bond tests (Chapter 5). This is probably related to the applied temperature cycle during heating of the beams. A temperature cycle increases the glass transition temperature of the adhesive (Section 4.5.3).

9.5.2 Zone A: The end anchorage zone

In the full scale experiments, beam C was expected to have failed by debonding in the end anchorage zone (Section 7.5.3). The beam that was tested at 70°C showed a significantly lower failure load (91 kN) compared to the ones that were tested at 20°C and 50°C (± 130 kN). The change in type of bond failure was however not observed at 70°C, probably due to the temperature cycle, as mentioned before. There is no clear explanation for the large reduction of the failure load, without having a change in the type of bond failure. Probably a combination of thermal effects (thermal mismatch, increased anchorage length, reduced bond strength) and/or other effects, like a difference in the roughness of the concrete surface, has led to the reduced failure load at 70°C.

Based on the results of the small scale bond tests, it can be expected that the type of bond failure will change when further increasing the temperature of the full scale beams. It is also likely that further increasing the temperature will result in a sudden decrease the bond strength and, as a result, the anchorage capacity. The small scale bond tests even showed that heating up to 90°C resulted in bond failure, even before the actual loading was applied (Section 5.4.2).

9.5.3 Point B: At the plate-end

Failure in the debonding mechanisms ‘concrete cover rip-off’ and ‘plate-end shear failure’ is not caused by bond failure of the concrete-adhesive-CFRP joint, but by cracking of the concrete exactly at the plate-end. These debonding mechanisms themselves are therefore not affected directly by the reduction in bond strength. It is, however, likely that one of the bond related debonding mechanisms in zone A or C becomes governing over failure at point B at temperatures above T_g , given the significant reduction in bond strength at these temperatures. This was however not observed in the full scale experiments at 70°C (beam D), again probably due to the increased glass transition temperature due to the applied temperature cycle.

9.5.4 Zone C: Outside the anchorage zone

Debonding in zone C is, like in zone A, related to bond failure of the concrete-adhesive-CFRP interface, mainly due to high shear stresses. Both beam A and beam B were expected to have failed after the initiation of debonding in zone C. Only beam A showed a partial change in the type of bond failure at 70°C (Figure 9-15).

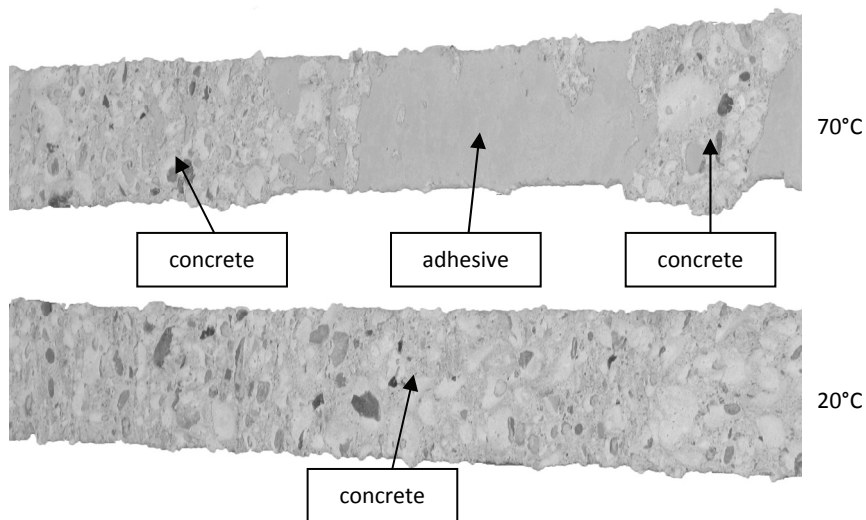


Figure 9-15: Failure surface after debonding of beam A at 20°C (bottom) and 70°C (top)

It was expected that the type of debonding had not completely changed to failure in between the concrete and the adhesive due to the temperature cycle during heating to 70°C, as explained before. Both beam A and beam B did also not show a significant change in failure load between 20°C and 70°C, again probably due to the same reason. It is however expected that further increasing temperature will soon lead to bond failure exactly in the concrete-adhesive interface and not in the concrete. It is likely that this will result in a lower failure load.

9.6 The reduced tensile strength and fracture energy of concrete at elevated temperatures

9.6.1 General

The tensile strength and the fracture energy of concrete are both reduced by a temperature increase. The reduction of the tensile strength, when increasing the temperature from 20°C to 70°C, is, according to Model Code 1990 (CEB 1993), between 0% and 25%, depending on the moisture content (Figure 4-2). The reduction of the fracture energy is, according to Model Code 1990, between 15% and 30%, also depending on the moisture content (Figure 4-3). It turned out that this reduction of the concrete properties is affecting the debonding mechanism ‘concrete cover rip-off’ (Section 9.6.2). The reduction of the concrete properties for the bond related debonding mechanisms in zone A and C is already described in Section 9.5, as the bond strength, up to the change in the type of failure, is related to the concrete strength.

9.6.2 Point B: At the plate-end

‘Concrete cover rip-off’ (Section 7.5.4), is initiated after cracking of the concrete exactly at the plate-end and is therefore directly related to the concrete properties in tension. Both the experiment and the finite element analyses showed that the failure load of a beam that failed after concrete cover rip-off (beam D) decreased with increasing temperature (5% at 50°C and 10 % at 70°C). The finite element analyses showed that the failure load of this beam was depending on the (applied) tensile strength and fracture energy of the concrete, as expected. Based on the analyses, it is expected that the reduction of the failure load of this beam in the experiment was mainly related to the reduction in tensile strength and fracture energy of concrete at elevated temperature. Nevertheless, the reduction in failure load was only small.

9.7 Summary

A temperature increase is affecting the behavior of a CFRP strengthened structure in different ways, as a temperature increase has different effects, like a change in material properties and the development of thermal stresses. The development of thermal stresses due to the thermal mismatch between concrete and CFRP mainly affects the debonding mechanisms that are expected to initiate in the end anchorage zone (zone A) and at the plate-end (point B), as thermal shear stresses in the concrete, adjacent to the concrete-adhesive interface mainly develop at the plate-end. The effect on the failure load is however small. The debonding mechanisms that are initiated outside the anchorage zone (zone C) are not affected by the thermal mismatch between concrete and CFRP.

A temperature increase also reduces the Young's modulus of the adhesive. This results in more equally distributed stresses in the end anchorage zone of the CFRP laminate and, as a result, in a reduction of the shear stress concentrations at the plate-end. The negative effect of the thermal mismatch between concrete and CFRP is therefore reduced by the reduced Young's modulus of the adhesive. It turned out that the reduced Young's modulus did not have a significant effect on the debonding mechanisms that initiated outside the anchorage zone.

The effect of the thermal mismatch between concrete and CFRP is also partly reversed by the creep behavior of the adhesive. Creep of the adhesive reduces the stresses in the end anchorage zone of the CFRP laminate and therefore reduces the shear stresses at the plate-end. It turned out that creep is significantly higher at temperatures close to and above the glass transition temperature of the adhesive.

Above the glass transition temperature of the adhesive, a different effect becomes governing, the change in the type of debonding. Debonding of the concrete-adhesive-CFRP joint changes from bond failure in the concrete, leaving a small layer of concrete remaining attached to the adhesive to bond failure exactly in the concrete-adhesive interface. This change in type of bond failure is accompanied by a significant reduction in bond strength. Moreover, the bond strength becomes wider scattered, which makes it difficult to make predictions of the failure load above the glass transition temperature of the adhesive.

A smaller effect of temperature is the change in the concrete properties, like the tensile strength and fracture energy. Although this change is relatively small in the temperature range up to the glass transition temperature of the adhesive, it is affecting the failure load of a beam that fails by 'concrete cover rip-off'. The reduction of the failure load is however small, as long as other debonding mechanisms do not become governing.

As explained, all the described effects of temperature are affecting the capacity of a CFRP strengthening of a concrete structure. Some of them reduce the capacity of a strengthened structure, while others have a positive effect. In general, it can be said that a temperature increase results in higher shear stresses at the plate-ends, due to the thermal mismatch, but the development of these stresses is partly reversed due to the creep and the reduced Young's modulus of the adhesive. The overall effect on the capacity therefore depends on which effect is the most governing effect. In the full scale experiments, there was no or only a small influence of temperature on the capacity of most CFRP strengthened beams, even above the glass transition temperature of the adhesive. The latter is probably due to the applied temperature cycle, which had increased the glass transition temperature, and the fact that the temperature at which the beam was tested (70°C) was only slightly higher than the glass transition temperature (62°C).

In general, it can be concluded that there is no significant influence of temperature on the capacity of a CFRP strengthened beam up to the glass transition temperature of the adhesive, when it is designed to fail by one of the debonding mechanisms where debonding initiates outside the end anchorage zone. The debonding mechanisms where failure is initiated after concrete cover rip-off or debonding close to the plate-end are more sensitive to temperature effects, although up to 50°C, the effect of temperature is still relatively small. However, close to the glass transition temperature, the capacity can suddenly drop. It is therefore recommended to design a CFRP strengthened structure such that the governing debonding mechanism is one of the debonding mechanisms where debonding initiates outside the anchorage zone, for example by applying a CFRP laminate with sufficient length.

10 Conclusions and recommendations

10.1 Conclusions

10.1.1 General

Up till now, only a limited amount of research has been carried out into the effect of temperature on CFRP strengthened concrete structures, despite the significant difference in the coefficient of thermal expansion between concrete and CFRP and the temperature dependent material properties of adhesives. Although it is generally assumed that the effectiveness of a CFRP strengthening application is not significantly affected at temperatures up to about 20°C below the glass transition temperature of the adhesive (fib 2001), no sound evidence has been available for this assumption. So far, only a limited number of test results at low and elevated temperature are available. Moreover, these test results are mainly based on small scale bond tests, while full scale CFRP strengthened structures can fail in a different way and can therefore also be affected by temperature in a different way.

10.1.2 Small scale bond tests

In this research project, the effect of temperature on CFRP strengthened structures was investigated with both small scale bond tests and full scale CFRP strengthened reinforced concrete beams. The bond behavior of the concrete-adhesive-CFRP joint was investigated with the small scale bond tests, both in the perpendicular (normal) and longitudinal (shear) direction of the bonded area (Section 5). The tests were carried out within the temperature range from -20°C till +80°C, which covers the outdoor circumstances of a large part of the world, including the circumstances of sun exposure. The tests were simulated by means of finite element analyses (Section 6), which further increased the knowledge of the bond behavior of the joint at low and elevated temperatures.

The results of the experiments and finite element analyses showed that the thermal mismatch between concrete and CFRP causes the development of thermal stresses in the CFRP and the adjacent concrete. Thermal shear stresses mainly develop near the plate-ends, where the thermal stresses are transferred from the CFRP to the concrete and vice versa. In the applied test setups, these shear stresses acted at elevated temperatures in the opposite direction as the shear stresses due to loading, which explains the observed (slowly) increasing failure load of the bond shear tests when increasing the temperature.

The experiments, however, also showed that thermal stresses partly disappear over time, due to creep of the adhesive. It turned out that creep is significantly higher at elevated temperatures, especially close to and above the glass transition temperature of the adhesive. Moreover, at around this temperature, the stiffness of the adhesive suddenly drops, which also results in a decrease of the shear stress concentrations at the plate-ends. Around the glass transition temperature, the type of bond failure changes from failure in the concrete, adjacent to the concrete-adhesive interface, leaving a small layer of concrete remaining attached to the adhesive and CFRP, to failure exactly in the concrete-adhesive interface, leaving no concrete remaining attached. This change in type of bond failure is accompanied by a significantly decreasing bond strength. Furthermore, the scatter in bond strength values also becomes much higher.

10.1.3 Full scale experiments

Unique full scale experiments were carried out on 4 meter long CFRP strengthened beams (Section 7). Full scale beams can fail in a different way compared to the small scale bond shear tests, because of additional influencing circumstances, like cracking of the beam, yielding of the internal steel reinforcement and the different loading configuration. All circumstances affect the debonding behavior. The beams were designed such that, at room temperature, most probably the four most commonly observed types of debonding would occur. The experiments showed that the debonding mechanisms that were initiated at or close to the plate-end ('debonding at the end anchorage zone' and 'concrete-cover rip-off') are affected more than the debonding mechanisms that were initiated outside the anchorage zone ('debonding due to high shear stresses' and 'debonding at shear cracks'). This is related to the fact that most thermal effects mainly affect the (shear) stress distribution in the anchorage zone and not (significantly) further away from the end anchorage zone.

Where in the small scale bond tests the thermal shear stresses at the plate-end acted opposite to the shear stresses due to mechanical loading, in the full scale experiments they acted in the same direction. Similar as in the small scale tests, it was found that these shear stress concentrations were partly reduced in time due to the reduced Young's modulus and the creep behavior of the adhesive at elevated temperature.

Most of the beams that were tested at 70°C did not show a change in the type of bond failure, as was found for the small scale bond tests. This was probably related to the temperature cycle that was applied during heating of the beams, which increases the glass transition temperature of the adhesive. This also explains why the failure load of most beams was not significantly affected at 70°C. Only the failure load of the beam that failed by debonding at the end anchorage zone showed a significant lower failure load at 70°C, probably due to a combination of various temperature effects in the anchorage zone. At 50°C, the effect of temperature on the failure load was relatively small for all beams.

The full scale experiments were also simulated by means of finite element analyses (Chapter 8). With the analyses, it was possible to simulate the different types of debonding that were observed in the experiments, both qualitatively and quantitatively. The analyses showed that the debonding behavior and the failure load of the full scale CFRP strengthened beams are not significantly affected by temperature, as long as the type of bond failure does not change. The small reduction of the failure load of the beam that failed by 'concrete cover rip-off' turned out to be mainly related to the reduction in the tensile strength and fracture energy of concrete at elevated temperature, and not to the additional thermal stresses at the plate-end.

10.2 Recommendations

10.2.1 General recommendations

Based on the results of the experiments and finite element analyses, it can be concluded that the effect of temperature is relatively small up to about the glass transition temperature of the adhesive (T_g). It is however recommended to avoid the structure being exposed to temperatures close to or above T_g as the capacity can suddenly drop with a small temperature increase, as has been observed with the small scale bond tests and the full scale beam that failed by 'debonding at the end anchorage zone'.

The current approach in *fib*-Bulletin 14 (*fib* 2001) to deal with the effect of temperature is to apply a lower boundary for the glass transition temperature of the applied adhesive (determined according to EN 12614 (CEN 2004a)). The glass transition temperature (T_g) should be higher than 45°C or the maximum shade air temperature plus 20°C, whichever is higher. For a CFRP strengthened structure that is strengthened with the epoxy adhesive that was used throughout this research project (SikaDur-30), this corresponds to a maximum shade air temperature of 42°C ($T_g = 62^\circ\text{C}$). However, based on the results of the experiments and the finite element analyses, it is recommended that the currently used value of 20°C for the difference between the maximum shade air temperature and T_g is decreased. Although only one adhesive is used in this investigation, it is likely that this difference can be decreased to approximately 10°C.

It is also recommended to design a CFRP strengthened concrete structure such that one of the debonding mechanisms where debonding initiates outside the end anchorage zone ('debonding due to high shear stresses' or 'debonding at shear cracks') is the governing debonding mechanism. The other debonding mechanisms where debonding/failure initiates close to the plate-end ('debonding in the end anchorage zone' or 'concrete cover rip-off') are more sensitive to temperature changes and should therefore be avoided, for example by applying a longer CFRP laminate.

In case the CFRP is exposed to higher temperatures, for example when being applied on a surface that is directly exposed to the sun, it is advised to apply an adhesive with a high glass transition temperature. Note that the glass transition temperature will also increase due to a temperature cycle or during life span, when subjected to natural temperature variations.

10.2.2 Recommendations for future research

Experimental research into the effect of temperature on full scale CFRP strengthened reinforced concrete structures is still rather limited and has only been investigated for one type of CFRP laminate and (epoxy) adhesive in this investigation. It is therefore recommended to investigate more full scale CFRP strengthened concrete structures at low and elevated temperatures to increase the amount of experimental data and to verify the findings of this research. Moreover, it is also recommended to investigate concrete structures that are strengthened with different types of FRPs (GFRP, AFRP, fabrics (wet lay-up)) and adhesives (polyester, vinylester, other epoxies), although similar results can be expected.

Another aspects that needs further research is a more detailed investigation into the time-dependent creep behavior of the adhesive at elevated temperatures, as it will affect the stress distributions in the anchorage zone of the CFRP laminate, and hence the stress concentrations at the plate-end. Although this effect is generally a positive effect for full scale beams, as it reduces the shear stress concentrations in the end anchorage zone, further research is recommended.

It is also recommended to investigate the effect of temperature on CFRP strengthened structures with adhesives with a relatively high T_g . Especially for temperatures above 100°C, additional phenomena do occur, like the evaporation of water from the concrete.

A last aspect that needs further research is the increase in the glass transition temperature of the adhesive due to temperature cycling. Although this effect did occur in the experiments, it was not investigated extensively in this research project.

References

ACI. *ACI 440.2R-02 Guide for the Design and Construction of Externally Bonded FRP Systems for Strengthening Concrete Structures*. Ed. ACI Committee 440. Farmington Hills, Michigan, American Concrete Institute, 2002.

Ambtliche Materialprüfanstalt für das Bauwesen. Prüfung des Epoxidharzklebers SikaDur 30 und des Primers Icosit 277. 1871/0054. 1994. Braunschweig, Germany, TU Braunschweig.

Bathe, K. *Finite element procedures*. Englewood Cliffs, New Jersey, Prentice-Hall Inc., 1996.

Baumert, M. E., Green, M. F., and Erki, M. A. "Low temperature behaviour of concrete beams strengthened with FRP sheets." *May 29, 1996. Proceedings of the 1996 CSECE annual conference*. Montreal: Canadian Society for Civil Engineering, 1996, 179-190.

Bažant, Z. P. *Fracture mechanics of concrete structures*. Abingdon, Oxon, USA, Taylor & Francis, 1992.

Bažant, Z. P. and M. F. Kaplan. *Concrete at high temperatures: Material properties and mathematical models*. Concrete design and constructions series. Essex, Longman Group Limited, 1996.

Bažant, Z. P. and Prat, P. C. "Effect of temperature and humidity on fracture energy of concrete." *ACI Materials Journal*, 85(4), 262-271, 1988.

Bisby, L. A., Williams, B., Kodur, V. K. R., Green, M. F., and Chowdhury, E. Fire performance of FRP systems for infrastructure: A state-of-the-art report. RR-179. 2005. Ottawa, Canada, National Research Council Canada.

Blaschko, M. "Strengthening with CFRP." *Müncher Massivbau Seminar*. München, Germany: TU München, 1997.

Blontrock, H. "*Analyse en modelleren van de brandweerstand van betonelementen uitwendig versterkt met opgelijmde composietlaminaten (in Dutch)*." Diss. Ghent University, 2003.

Busel, J. P. and White, D. "CFRP & GFRP composite applications for infrastructure rehabilitation and repairs." 2003. Saratoga Springs, NY, USA. <https://www.nysdot.gov/portal/page/portal/nasto/repository/programs/white.pdf>.

CEB. *CEB-FIP report on methods of assessment of the fire resistance of concrete structural members*. Wexham Springs, Slough, FIP and C&CA, 1978.

CEB. *CEB Bulletin d'information nr. 174: Model Code for Fire Design of Concrete Structures*. Lausanne, Switzerland, Comité Euro-International du Béton, 1987.

CEB. *CEB Bulletin d'information nr. 208: Fire design of concrete structures*. Lausanne, Switzerland, Comité Euro-International du Béton, 1991.

CEB. *CEB-FIP model code 1990: design code*. Lausanne, Switzerland, Comité Euro-International du Béton, 1993.

CEN. *EN 196-1: Methods of testing cement - Part 1: Determination of strength*. Brussels, Belgium, CEN, 1994.

CEN. *EN 1992-1-1: Eurocode 2. Design of concrete structures. Part 1-1: General rules and rules for buildings*. Brussels, Belgium, CEN, 1997a.

CEN. *EN-ISO 527 (1-5): Plastics - Determination of tensile properties*. Brussels, Belgium, CEN, 1997b.

CEN. *EN 1770: Products and systems for the protection and repair of concrete structures - Test methods - Determination of the coefficient of thermal expansion*. Brussels, Belgium, CEN, 1998.

CEN. *EN 13412: Products and systems for the protection and repair of concrete structures - Test methods - Determination of modulus of elasticity in compression*. Brussels, Belgium, CEN, 2002.

CEN. *EN 12614: Products and systems for the protection and repair of concrete structures - Test methods - Determination of glass transition temperatures of polymers*. Brussels, Belgium, CEN, 2004a.

CEN. *EN 1992-1-2: Eurocode 2. Design of concrete structures. Part 1-2: General rules - Structural fire design*. Brussels, Belgium, CEN, 2004b.

Concrete Society. TR 55: Design guidance for strengthening concrete structures using fibre composite materials. Technical Report No. 55. 2004. Surrey, The Concrete Society.

Cook, R. D., D. S. Malkus, and M. E. Plesha. *Concepts and applications of finite element analysis*. 3 ed. John Wiley & Sons Inc., 1989.

CUR. *CUR Aanbeveling 20. Bepaling van de hechtsterkte van mortels op beton (in Dutch)*. Gouda, the Netherlands, Stichting CUR, 1990.

CUR. *CUR Rapport 149. Brandwerendheid van betonconstructies. Deel 1: Uitgangspunten en gegevens voor een rekenkundige beoordeling (in Dutch)*. Gouda, the Netherlands, Stichting CUR, 1994.

CUR. *CUR Aanbeveling 91. Versterken van gewapend-betonconstructies met uitwendig gelijmde koolstofvezelwapening (in Dutch)*. 1st ed. Gouda, the Netherlands, Stichting CUR, 2002.

CUR. *CUR Aanbeveling 91. Versterken van gewapend-betonconstructies met uitwendig gelijmde koolstofvezelwapening (in Dutch)*. 2nd ed. Gouda, the Netherlands, Stichting CUR, 2007.

De Borst, R. and L. J. Sluys. *Computational methods in non-linear solid mechanics*. Delft, The Netherlands, Delft University of Technology, 2002.

De Lorenzis, L. and Nanni, A. "Bond between near surface mounted FRP rods and concrete in structural strengthening." *ACI Structural Journal*, 99(2), 123-133, 2002.

Deuring, M. Verstärken von stahlbeton mit gespannten faserverbundwerkstoffen (in German). Report Number 224. 1993. Dübendorf, Switzerland, EMPA.

Deuring, M. Brandversuche an nachtraglich verstärkten trägem aus beton (in German). Report number 148795. 1994. Dübendorf, Switzerland, EMPA.

Di Tommaso, A., Neubauer, U., Pantuso, A., and Rostásy, F. S. "Behavior of adhesively bonded concrete-CFRP joints at low and high temperatures." *Mechanics of Composite Materials*, 37(4), 327-338, 2001.

Dörr, K. "Ein beitrag zur berechnung von stahlbetonscheiben unter besonderer berücksichtigung des verbundverhaltens." Diss. University of Darmstadt, 1980.

El-Hacha, R., Green, M. F., and Wight, R. G. "Flexural behaviour of concrete beams strengthened with prestressed carbon fibre reinforced polymer sheets subjected to sustained loading and low temperature." *Canadian Journal of Civil Engineering*, 31, 239-252, 2004.

El-Hacha, R. and Rizkalla, S. H. "Near-surface-mounted fiber-reinforced polymer reinforcements for flexural strengthening of concrete structures." *ACI Structural Journal*, 101(5), 717-726, 2004.

El-Hacha, R., Wight, R. G., and Green, M. F. Prestressed fibre-reinforced polymer laminates for strengthening structures. *Progress in Structural Engineering and Materials* 3, 111-121. 2001.

Feenstra, P. H. "Computational aspects of biaxial stress in plain and reinforced concrete." Diss. Delft University of Technology, 1993.

Feldman, D. *Polymeric building materials*. London, Elsevier Applied Science, 1989.

fib. *fib Bulletin 14. Externally bonded FRP reinforcement for RC structures*. Lausanne, Fédération internationale du béton, 2001.

FIP. *FIP-CEB Recommendations for the design of reinforced and prestressed concrete structural members for fire resistance*. Wexham Springs, Slough, FIP and C&CA, 1975.

Fortius. FRP systemen. Gelijmde wapeningen (in Dutch). 2004.

Gamage, J. C. P. H., Al-Mahaidi, R., and Wong, M. B. "Bond characteristics of CFRP plated concrete members under elevated temperatures." *Composite Structures*, 75, 199-205, 2006.

Garden, H. N. and Hollaway, L. C. "An experimental study of the influence of plate end anchorage of carbon fibre composite plates used to strengthen reinforced concrete beams." *Composite Structures*, 42(2), 175-188, 1998.

Harries, K. A., Porter, M. L., and Busel, J. P. "FRP materials and concrete - research needs." *Concrete International*, 25(10), 69-74, 2003.

Hermes, M. The influence of temperature on reinforced concrete structures strengthened with externally bonded carbon fiber reinforced polymers. A-2006.08. 2006. Eindhoven, Eindhoven University of Technology.

Holzenkämpfer, P. *Ingenieursmodelle des verbunds geklebter bewehrung für betonbauteile (in German)*. Deutscher ausschuss für stahlbeton. Heft 473. Berlin, Westkreuz-Druckerei Ahrens KG, 1997.

Hughes Brothers. Aslan 500. Carbon Fiber Reinforced Polymer (CFRP) tape. 2002.

Hughes Brothers. "Aslan 100. Application photos." 2007. http://www.hughesbros.com/Aslan100/Aslan100_GFRP_rebar.html.

Italian National Research Council. *CNR-DT 200/2004 - Instructions for design, execution and control of strengthening interventions by means of Fibre-Reinforced composites (in Italian)*. 2004.

Jansze, W. *Strengthening of reinforced concrete members in bending by externally bonded steel plates : design for beam shear and plate anchorage*. Delft, Technische Universiteit Delft, 1997.

Jones, R., Swamy, R. N., and Charif, A. "Plate separation and anchorage of reinforced concrete beams strengthened by epoxy-bonded steel plates." *The Structural Engineer*, 66(5), 85-94, 1988.

Karbhari, V. M., Chin, J. W., Hunston, D., Benmokrane, B., Juska, T., Morgan, R., Lesko, J. J., Sorathia, U., and Reynaud, D. "Durability Gap Analysis for fiber-reinforced polymer composites in civil infrastructure." *Journal of Composites for Construction*, 7(3), 238-247, 2003.

Kim, D. H. *Composite structures for civil and architectural engineering*. London, E & FEN Spon, 1995.

Kim, W. and White, R. N. "Initiation of shear cracking in reinforced concrete beams with no web reinforcement." *ACI Structural Journal*, 88(3), 301-324, 1991.

Kodur, V. K. R., Bisby, L. A., and Green, M. F. "Experimental evaluation of the fire behaviour of insulated fibre-reinforced-polymer-strengthened reinforced concrete columns." *Fire Safety Journal*, 41, 547-557, 2006.

Kumahara, S., Masuda, Y., Tanano, H., and Shimizu, A. "Tensile strength of continuous fibre bar under high temperature." 1993. *Proceedings of the International Symposium on Fibre-Reinforced-Plastic Reinforcement for Concrete Structures (FRPRCS-1)*. Vancouver, USA: ACI, 1993, 731-742.

Leone, M., Aiello, M. A., and Matthys, S. "The influence of service temperature on bond between FRP reinforcement and concrete." June 5, 2006. *Fédération Internationale du Béton - Proceedings of the 2nd International Congress*. Naples: fib, 2006.

Lu, X. Z., Teng, J. G., Ye, L. P., and Jiang, J. J. "Bond-slip models for FRP sheets/plates bonded to concrete." *Engineering Structures*, 27(6), 920-937, 2005.

Maalej, M. and Bian, Y. "Interfacial shear stress concentration in FRP-strengthened beams." *Composite Structures*, 54(4), 417-426, 2001.

Malek, A. M., Saadatmanesh, H., and Ehsani, M. R. "Prediction of failure load of R/C beams strengthened with FRP plate due to stress concentration at the plate end." *ACI Structural Journal*, 95(2), 142-152, 1998.

Mapei. Mapei FRP system. 2001.

Matthys, S. "*Structural behaviour and design of concrete members strengthened with externally bonded FRP reinforcement*." Diss. Ghent University, 2000.

Meier, U. "Strengthening of structures using carbon fibre/epoxy composites." *Construction and Building Materials*, 9(6), 341-351, 1995.

Miwa, M., Takeno, A., Mori, Y., Yokoi, T., and Watanabe, A. "Effects of Young's modulus of epoxy resin on axial compressive strength of carbon fibre." *Journal of Materials Science*, 33, 3885-3890, 1998.

Morgan, P. *Carbon fibers and their composites*. Boca Raton, FL, USA, Taylor & Francis Group, 2005.

Nakaba, K., Kanakubo, T., Furuta, T., and Yoshizawa, H. "Bond behavior between fiber-reinforced polymer laminates and concrete." *ACI Structural Journal*, 98(3), 359-367, 2001.

NetComposites. "Guide to Composites." Nov. 22, 2006. 2006. NetComposites, <http://www.netcomposites.com/Education.asp>.

Neto, P., Alfaiate, J., Almeida, J. R., and Pires, E. B. "The influence of mode II fracture on concrete strengthened with CFRP." *Computers & Structures*, 82(17-19), 1495-1502, 2004.

Neubauer, U. and Rostásy, F. S. "Bond Failure of Concrete Fiber Reinforced Polymer Plates at Inclined Cracks – Experiments and Fracture Mechanics Model." 1999. *Proceedings of the Fourth International Symposium on Non-Metallic (FRP) Reinforcement for Concrete Structures (FRPRCS-4)*. Baltimore, USA: ACI, 1999, 369-382.

Niedermeier, R. and Zilch, K. "Zugkraftdeckung bei klebarmierten bauteilen." *Beton- und Stahlbetonbau*, 96(12), 759-770, 2001.

Nigro, E., Manfredi, G., Cosenza, E., and Zappoli, M. "Effects of high temperature on the performances of RC bridge decks strengthened with externally bonded FRP Reinforcement." June 5, 2006. *Fédération Internationale du Béton - Proceedings of the 2nd International Congress*. Naples: fib, 2006.

Niu, H. and Wu, Z. S. "Optimization of FRP-concrete interface in FRP bonding technique." 2004. *Proceedings of the First International Conference on Innovative Materials and Technologies for Construction and Restoration*. Lecce: 2004, 646-659.

Oehlers, D. J. "Reinforced concrete beams with plates glued to their soffits." *Journal of Structural Engineering*, 188(8), 2023-2038, 1992.

Pilakoutas, K. "Composites in Concrete Construction." *Failure analysis of industrial composite materials*. Ed. E. E. Gdoutos, K. Pilakoutas, and C. A. Rodopoulos. McGraw-Hill. 449-499, 2000.

Plecnik, J. M., Bresler, B., Cunningham, J. D., and Iding, R. "Temperature effects on epoxy adhesives." *Journal of Structural Division*, 106(1), 99-113, 1980.

Raof, M. and Zhang, S. "An insight into the structural behaviour of reinforced concrete beams with externally bonded plates." *Proceedings of the Institute of Civil Engineers: Structures and Buildings*, 122, 477-492, 1997.

Rehm, G. and L. Franke. *Kunstharzgebundene glasfaserstabe als bewehrung im betonbau*. Die Bautechnik. Heft 4. 1974.

Ritchie, P. A., Thomas, D. A., Lu, L. W., and Connelly, G. M. "External reinforcement of concrete beams using fiber reinforced plastics." *ACI Structural Journal*, 88(4), 490-500, 1991.

Roberts, T. M. "Approximate analysis of shear and normal stress concentrations in the adhesive layer of plated RC beams." *The Structural Engineer*, 67(12), 229-233, 1989.

Rostásy, F. S. Fibre composite elements and techniques as non-metallic reinforcement of concrete. Project 4142/BREU - CT 91 0515. 1992. Brite-Euram. Evaluation of potentials and production technologies of FRP, Technical Report Task 1.

Saafi, M. "Effect of fire on FRP reinforced concrete members." *Composite Structures*, 58, 11-20, 2002.

Savoia, M., Ferracuti, B., and Mazzotti, C. "Non linear bond-slip law for FRP-concrete interface." 2003. *Proceedings of FRPRCS6*. World Scientific Publishing Company, 2003, 163-172.

Schetters, L. P. T. Onderzoek naar op beton gelijmde koolstofvezelwapening. Research report. 2004. Eindhoven, Eindhoven University of Technology.

Schöck. Schöck combar: Kunststofwapening (in Dutch). 2004.

Sen, R., Mariscal, D., and Shahawy, M. "Investigation of S-2 glass/epoxy strands in concrete." *Proceedings of the International Symposium on Fibre-Reinforced-Plastics Reinforcement for Concrete Structures (FRPRCS-1)*. Vancouver, USA: ACI, 1993, 15-33.

Sika. Sika CarboDur systeem. Technologie voor structurele versterking conform CUR-Aanbeveling 91 (in Dutch). 2004.

Sika. "Sika® CarboDur® lamellen." 2005. http://www.sika.nl/tds_sikacarbodur_nl.pdf.

Sika. Sika CarboDur. Structural strengthening systems. 2006.

Sika. E-mail communication with SIKA. 2007.

Sika. "Sikadur® -30." 2009. http://www.sika.com.my/my-con-pds-sikadur_30.pdf.

Smith, S. T. and Teng, J. G. "Interfacial stresses in plated beams." *Engineering Structures*, 23(7), 857-871, 2001.

Smith, S. T. and Teng, J. G. "FRP-strengthened RC beams. I: review of debonding strength models." *Engineering Structures*, 24(4), 385-395, 2002.

Spagnolo, G. S. and Ambrosini, D. "ESPI: A Tutorial." 2001. http://www.techonline.com/community/ed_resource/feature_article/14420.

Štěpánek, P., Švaricková, I., and Adámek, J. "Strengthening of concrete beams using CFRP strips anchorage of externally glued strips." *International Symposium (NDT-CE 2003) Non-Destructive Testing in Civil Engineering 2003*. 2004.

Stormcable. "Room-Temperature Linear Coefficient of Thermal Expansion Values for Various Engineering Materials." 2009. http://www.stormcable.com/uploads/Thermal_expansion_data_table_tb06.pdf.

Tadeu, A. J. B. and Branco, F. J. F. G. "Shear tests of steel plates epoxy-bonded to concrete under temperature." *Journal of Materials in Civil Engineering*, 12(1), 74-80, 2000.

Täljsten, B. "Strengthening of beams by plate bonding." *Journal of Materials in Civil Engineering*, 9(4), 206-212, 1997.

Teng, J. G., et al. *FRP strengthened RC structures*. West Sussex, England, John Wiley & Sons, 2002.

Teng, J. G., Smith, S. T., Yao, J., and Chen, J. F. "Intermediate crack-induced debonding in beams and slabs." *Construction and Building Materials*, 17(6-7), 447-462, 2003.

Teng, J. G. and Yao, J. "Plate end debonding in FRP-plated RC beams - II: Strength model." *Engineering Structures*, 29(10), 2472-2486, 2007.

TNO DIANA B.V. *DIANA User's Manual*. Ed. F. C. De Witte and W. P. Kikstra. Delft, TNO DIANA B.V., 2005.

Triantafillou, T. C. and Plevris, N. "Strengthening of RC beams with epoxy-bonded fibre-composite materials." *Materials and Structures*, 25(4), 201-211, 1992.

Williams, B., Bisby, L. A., Kodur, V. K. R., Green, M. F., and Chowdhury, E. "Fire insulation schemes for FRP-strengthened concrete slabs." *Composites Part A: Applied Science and Manufacturing*, 37, 1151-1160, 2006.

Wu, Z. S., Iwashita, K., Yagashiro, S., Ishikawa, T., and Hamaguchi, Y. "Temperature effect on bonding and debonding behavior between FRP sheets and concrete (in Japanese)." *Journal of the Society of Material Science*, 54(5), 474-480, 2005.

Yuan, H., Teng, J. G., Seracino, R., Wu, Z. S., and Yao, J. "Full-range behavior of FRP-to-concrete bonded joints." *Engineering Structures*, 26, 553-565, 2004.

Zhang, S., Raoof, M., and Wood, L. A. "Prediction of peeling failure of reinforced concrete beams with externally bonded steel plates." *Proceedings of the Institute of Civil Engineers: Structures and Buildings*, 110, 257-268, 1995.

Zienkiewicz, O. C. and R. L. Taylor. *The finite element method, The basis*. 5th ed. 3 vols. 1. Oxford, Butterworth-Heinemann, 2000.

Zureick, A. H., Shih, B., and Muley, E. "Fiber-reinforced polymeric bridge decks." *Structrural Engineering Review*, 7(3), 257-266, 1995.

Appendices

Appendix A. Development of thermal stresses

Seen from the FRP laminate, the (shear) stiffness of concrete can be represented by springs with a linear elastic stiffness of k_{Gc} (Figure A-1).

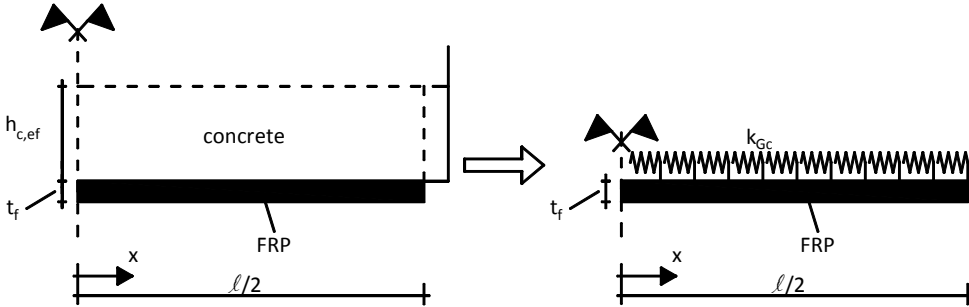


Figure A-1: Theoretical beam model (Di Tommaso et al. 2001)

The increase in normal force (N) in the CFRP over a small length dx has to be transferred via shear stresses to the concrete. Assuming a linear relation (k_{Gc}) between the shear stress ($\tau(x)$) and the elastic bond slip ($u(x)$) (Figure A-2), the following equation can be found;

$$\frac{dN}{b_f \cdot dx} = \tau(x) = k_{Gc} \cdot u(x) \quad (A.1)$$

where
 b_f is the width of the FRP

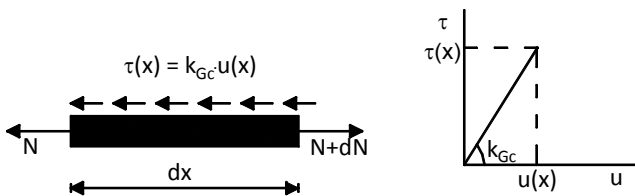


Figure A-2: Equilibrium of a small element and the idealized bond slip law (Di Tommaso et al. 2001)

Note that the model neglects the adhesive layer in between the concrete and CFRP. It also neglects the normal stresses perpendicular to the bonded area, due to the (small) distance between the FRP laminate and the concrete.

The strain in the FRP (ε_f) is divided into two parts, the strain due to the expansion of the concrete due to temperature variation ($\varepsilon_{\Delta T}$) and the strain in the CFRP itself, due to the (corresponding) CFRP force ($\varepsilon_{F,ext}$);

$$\varepsilon_f = \frac{du}{dx} = \varepsilon_{F,ext} + \varepsilon_{\Delta T} \quad (A.2)$$

where

$$\varepsilon_{\Delta T} = \alpha_c \cdot \Delta T$$

α_c is the coefficient of thermal expansion of concrete

ΔT is the variation in temperature

The CFRP force (N) can be expressed as;

$$N = E_f \cdot t_f \cdot b_f \cdot \left(\frac{du}{dx} - \varepsilon_{\Delta T} \right) \quad (A.3)$$

where

E_f is the Young's modulus of the CFRP

t_f is the thickness of CFRP

Differentiating equation (A.3) with respect to dx and rewriting equation (A.1) gives two expressions for dN/dx;

$$\frac{dN}{dx} = E_f \cdot t_f \cdot b_f \cdot \frac{d^2u(x)}{dx^2} \quad (A.4)$$

$$\frac{dN}{dx} = k_{Gc} \cdot u(x) \cdot b_f \quad (A.5)$$

Substituting equation (A.4) into equation (A.5) gives;

$$\frac{d^2u(x)}{dx^2} - \omega^2 \cdot u(x) = 0 \quad (A.6)$$

where

$$\omega^2 = \frac{k_{Gc}}{E_f \cdot t_f}$$

The general solution of equation (A.6) is;

$$u(x) = C \cosh(\omega x) + D \sinh(\omega x) \quad (\text{A.7})$$

C and D can be determined by using the boundary conditions, assuming that the displacement at midspan is zero and the CFRP force at the end of the laminate is zero;

$$x = 0 \Rightarrow u(0) = 0 \Rightarrow C = 0 \quad (\text{A.8})$$

$$x = \ell/2 \Rightarrow N(\ell/2) = 0 \Rightarrow \varepsilon_{F,ext} = 0 \Rightarrow \frac{du(\ell/2)}{dx} = \varepsilon_{\Delta T} \quad (\text{A.9})$$

D can be determined by substituting equation (A.9) in equation (A.7);

$$\begin{aligned} u(\ell/2) &= D \cdot \sinh(\omega \cdot \ell/2) \Rightarrow \frac{du(\ell/2)}{dx} = \omega \cdot D \cdot \cosh(\omega \cdot \ell/2) = \varepsilon_{\Delta T} \\ \Rightarrow D &= \frac{\varepsilon_{\Delta T}}{\omega \cdot \cosh(\omega \cdot \ell/2)} \end{aligned} \quad (\text{A.10})$$

$u(x)$, $\sigma_f(x)$ and $\tau(x)$ can then be expressed as;

$$u(x) = \frac{\varepsilon_{\Delta T}}{\omega \cdot \cosh(\omega \cdot \ell/2)} \sinh(\omega \cdot x) \quad (\text{A.11})$$

$$\sigma_f(x) = \frac{N(x)}{t_f \cdot b_f} = E_f \cdot \left[\frac{du}{dx} - \varepsilon_{\Delta T} \right] = E_f \cdot \left[\frac{\varepsilon_{\Delta T}}{\cosh(\omega \cdot \ell/2)} \cdot \cosh(\omega \cdot x) - \varepsilon_{\Delta T} \right] \quad (\text{A.12})$$

$$\tau(x) = \frac{dN(x)}{dx \cdot b_f} = -E_f \cdot t_f \cdot \omega \cdot \frac{\varepsilon_{\Delta T}}{\cosh(\omega \cdot \ell/2)} \sinh(\omega \cdot x) \quad (\text{A.13})$$

The normal stress in the FRP and the shear stress in the interface between the concrete and FRP can be calculated with equation (3.1) and (3.2) respectively. The only unknown is the stiffness k_{Gc} , which is incorporated in ω . To determine k_{Gc} , a linear elastic bond-slip behavior is assumed, which is related to the shear deformation of the concrete over an effective depth $h_{c,ef}$ (Figure A-3).

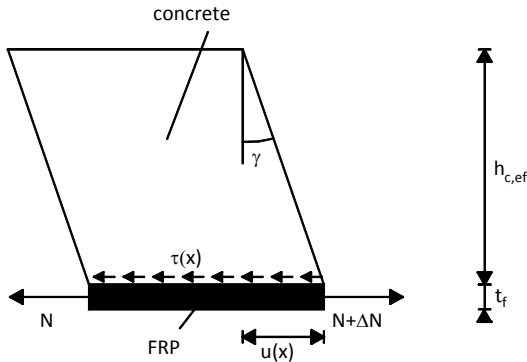


Figure A-3: Idealization of bond-slip behavior (Di Tommaso et al. 2001)

$h_{c,ef}$ depends on the aggregate size and can be taken 50 mm (about twice the dimension of the greatest aggregate) (Neubauer and Rostásy 1999). For small specimens, a smaller effective depth will have to be taken into account. Before cracking occurs, the behavior can be satisfactorily predicted by using Hooke's law;

$$\gamma = \frac{u(x)}{h_{c,ef}} = \frac{\tau(x)}{G_c} \quad (\text{A.14})$$

where

G_c is the shear modulus of concrete

$$= \frac{E_c}{2 \cdot (1 + \nu_c)}$$

With equation (A.13) and (A.14), the elastic slip ($u(x)$) can be calculated with;

$$u(x) = \frac{2 \cdot (1 + \nu_c) \cdot \tau(x) \cdot h_{c,ef}}{E_c} \quad (\text{A.15})$$

Finally, with equation (A.15) and $k_{Gc} = \tau(x)/u(x)$ (Figure A-2), the following expression for k_G can be given

$$k_{Gc} = \frac{E_c}{2 \cdot (1 + \nu_c) \cdot h_{c,ef}} \quad (\text{A.16})$$

Appendix B. Double-lap shear tests

B.1 Material properties

Table B-1: Test results of concrete cubic compressive tests (halfway during test program)

Cubic compressive strength	A (50 d) [N/mm ²]	B (63 d) [N/mm ²]
Test 1	41.2	70.8
Test 2	41.9	71.0
Test 3	40.4	70.7
Mean value	41.1	70.8

Table B-2: Test results of concrete tensile splitting tests (halfway during test program)

Tensile splitting strength	A (50 d) [N/mm ²]	B (63 d) [N/mm ²]
Test 1	3.20	3.47
Test 2	2.94	3.77
Test 3	-	4.12
Mean value	3.07	3.79

Table B-3: Test results of concrete Young's modulus tests (halfway during test program)

Young's modulus	A (50 d) [N/mm ²]	B (63 d) [N/mm ²]
Test 1	26,428	31,410
Test 2	25,969	31,143
Test 3	28,131	30,793
Mean value	26,800	31,000

B.2 Strain gauge properties

Table B-4: Properties of the applied strain gauges

Strain gauge type	TML PFL-6-11	TML PFL-10-11	TML PFL-30-11
Location	on CFRP	on CFRP	on concrete
Gauge factor	2.13 ± 1%	2.13 ± 1%	2.13 ± 1%
Coefficient of thermal expansion [$\cdot 10^{-6}$ /°C]	11.8	11.8	11.8
Temperature coefficient of gauge factor [/10°C]	+0.1 ± 0.05%	+0.1 ± 0.05%	+0.15 ± 0.05%
Tolerance [$\mu\text{m}/\text{m}$ /°C]	±0.85	±0.85	±0.85

B.3 Load-displacement curves

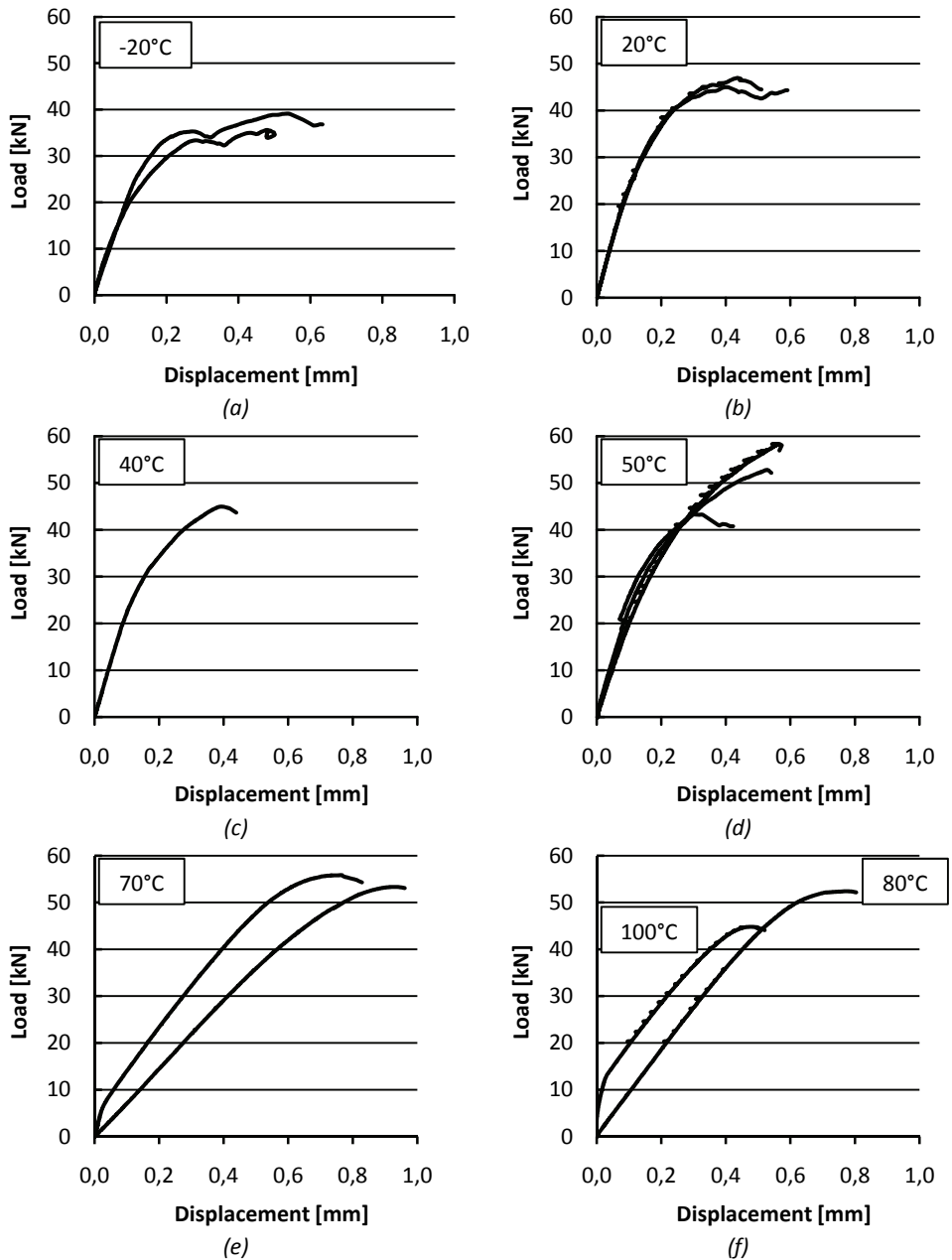
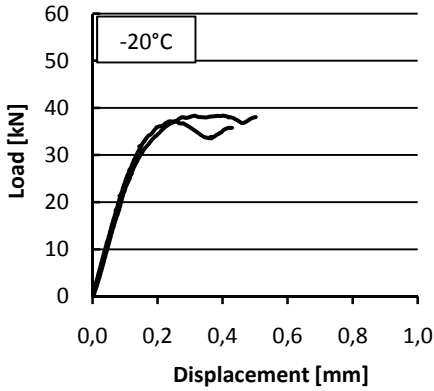
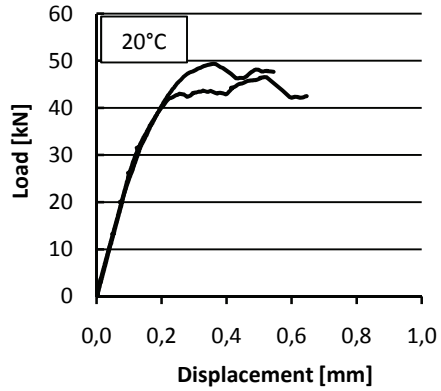


Figure B-1: Load-displacement curves of the double-lap shear tests ($f_{cm,cube} = 41.1 \text{ N/mm}^2$)

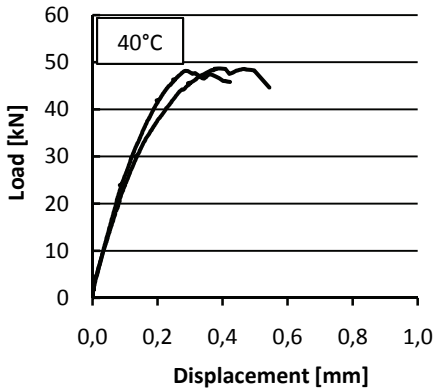
NB. The displacement corresponds to the mean value of the measurements of the two LVDTs.



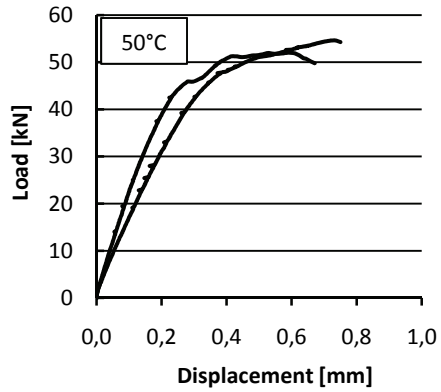
(a)



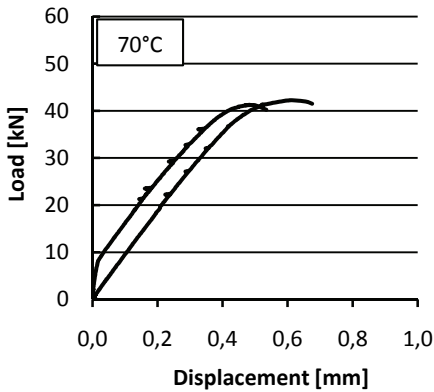
(b)



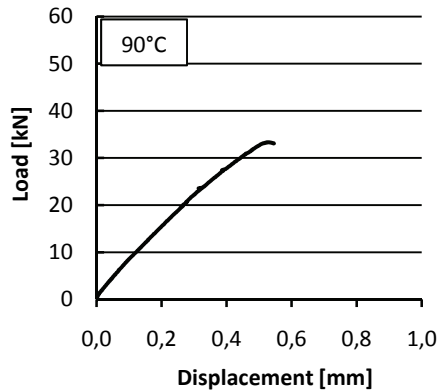
(c)



(d)



(e)



(f)

Figure B-2: Load-displacement curves of the double-lap shear tests ($f_{cm,cube} = 70.8 \text{ N/mm}^2$)

NB. The displacement corresponds to the mean value of the measurements of the two LVDTs.

B.4 Thermal strains

B.4.1 Thermal strains after heating to 50°C, cooling to 20°C and heating to 50°C

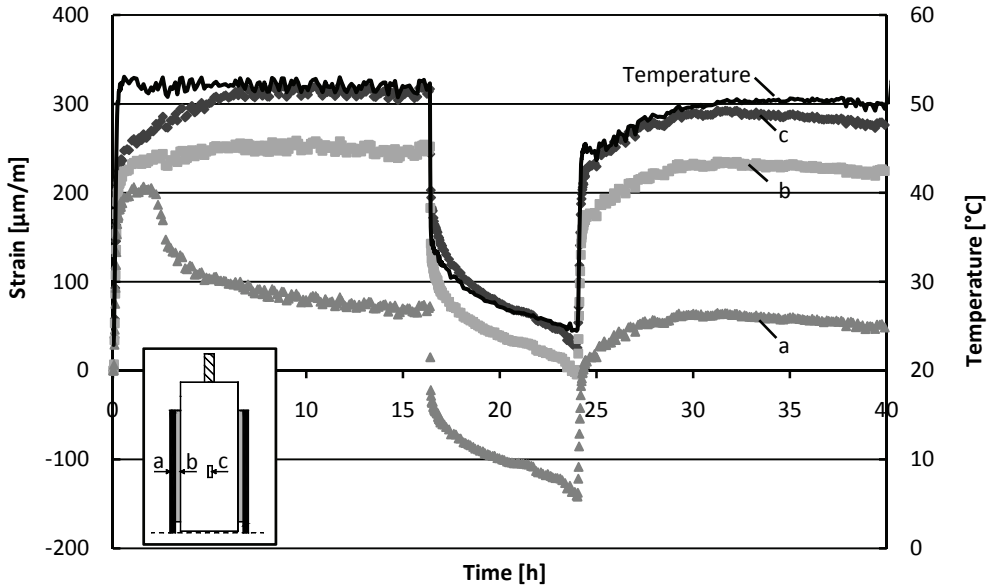


Figure B-3: Strain development in the CFRP (a), concrete-adhesive interface (b) and concrete (c) due to heating and cooling down of a double-lap shear test specimen ($f_{cm,cube} = 41.1 \text{ N/mm}^2$)

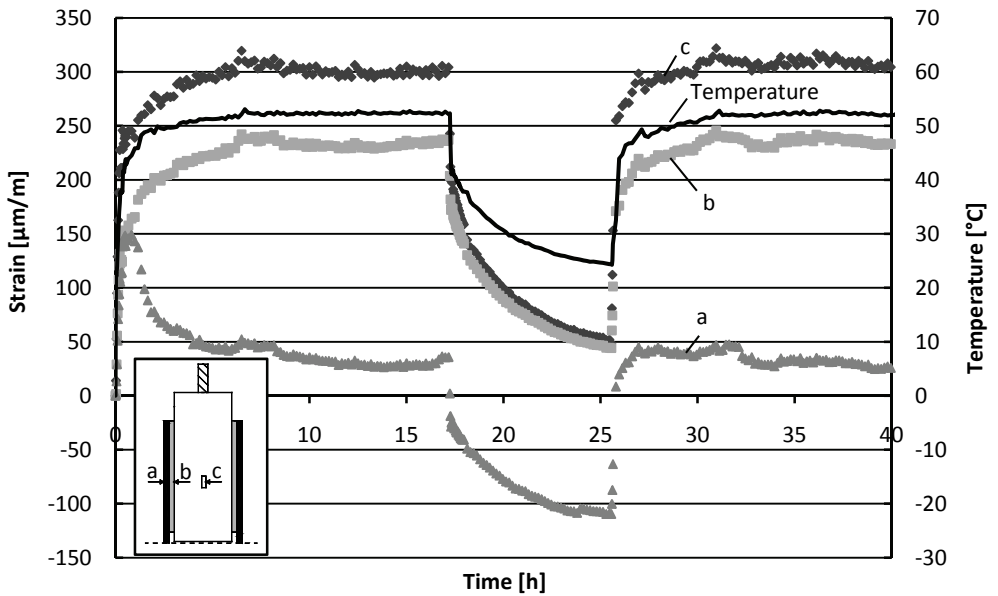


Figure B-4: Strain development in the CFRP (a), concrete-adhesive interface (b) and concrete (c) due to heating and cooling down of a double-lap shear test specimen ($f_{cm,cube} = 70.8 \text{ N/mm}^2$)

B.4.2 Thermal strains after heating to 40°C, 50°C and 70°C

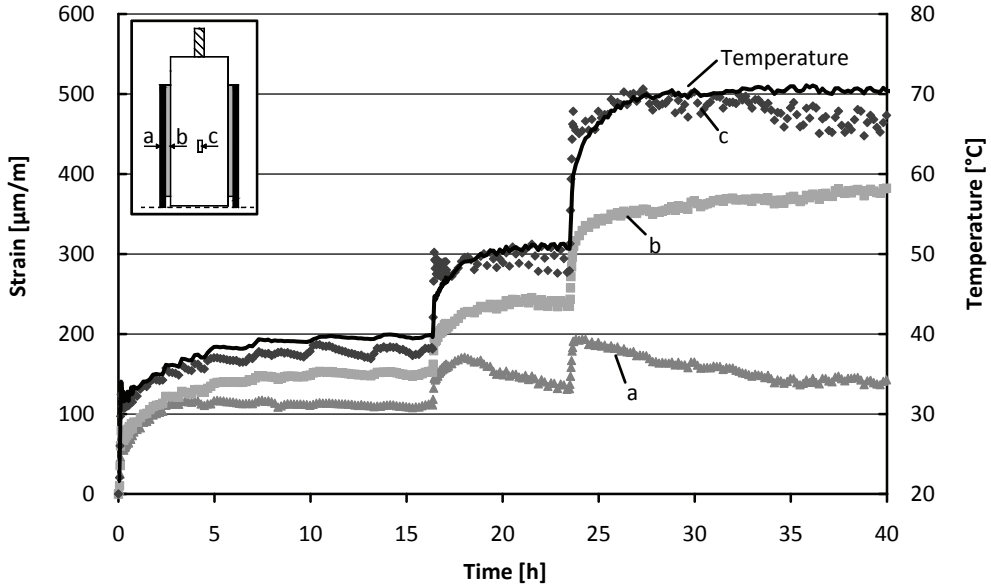


Figure B-5: Strain development in the CFRP (a), concrete-adhesive interface (b) and concrete (c) due to heating of a double-lap shear test specimen up to 40°C, 50°C and 70°C ($f_{cm,cube} = 41.1 \text{ N/mm}^2$)

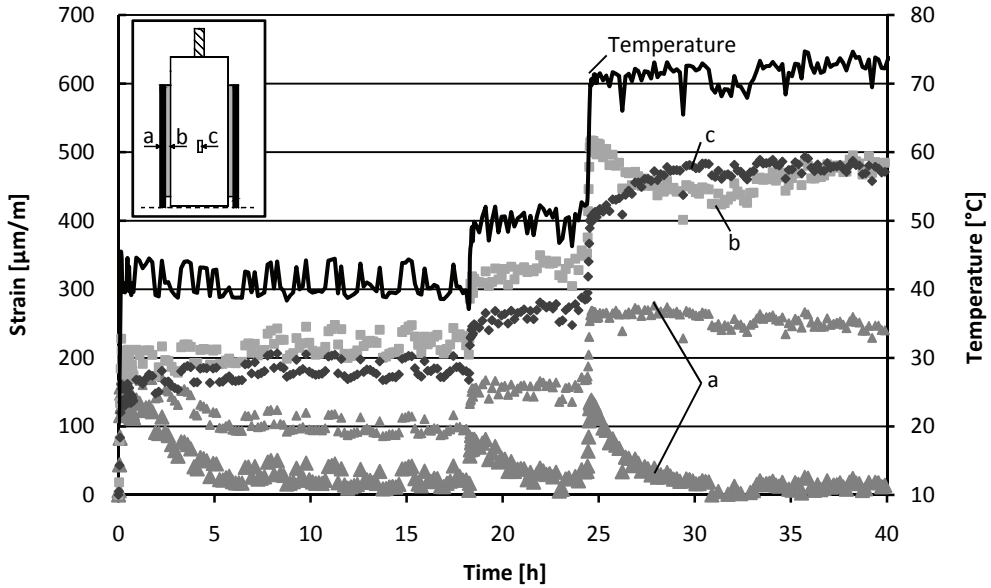
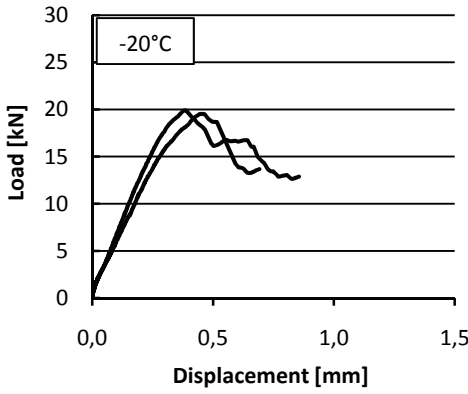


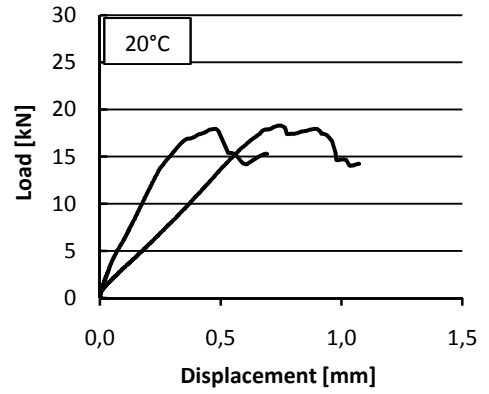
Figure B-6: Strain development in the CFRP (a), concrete-adhesive interface (b) and concrete (c) due to heating of a double-lap shear test specimen up to 40°C, 50°C and 70°C ($f_{cm,cube} = 70.8 \text{ N/mm}^2$)

Appendix C. Three-point bending tests

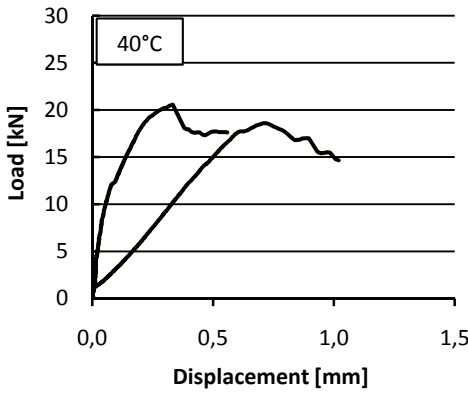
C.1 Load-displacement curves



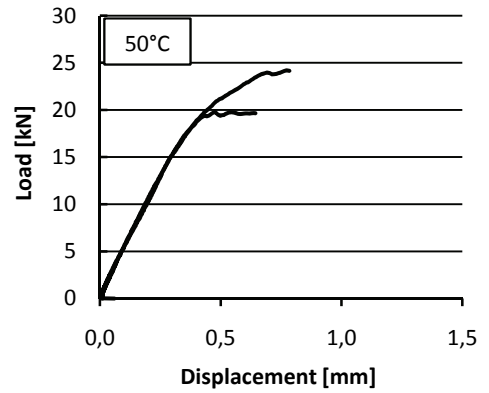
(a)



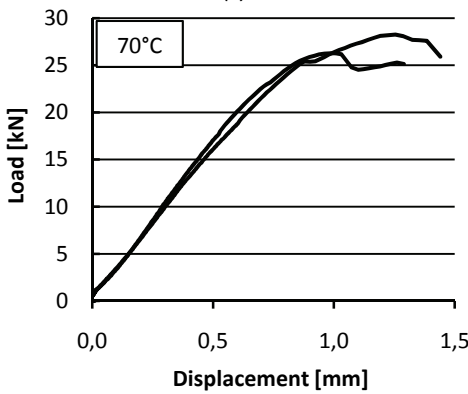
(b)



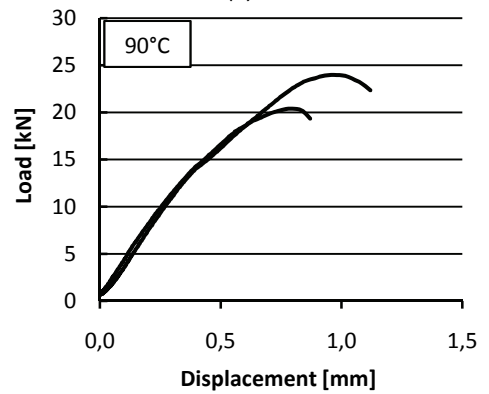
(c)



(d)

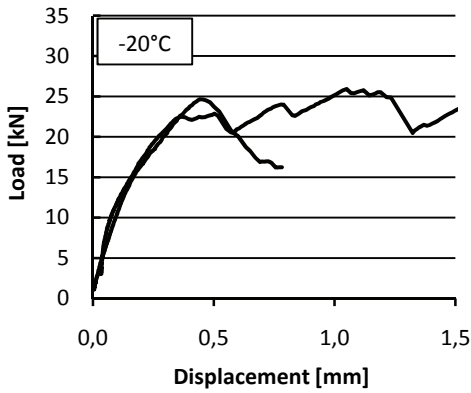


(e)

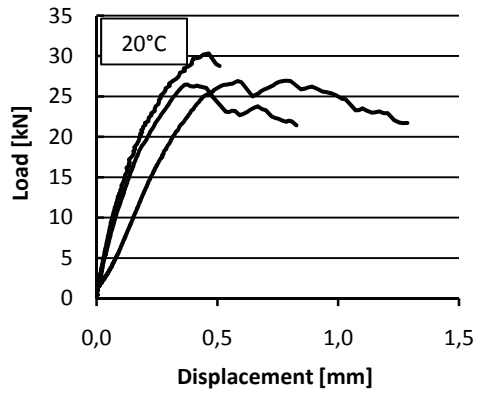


(f)

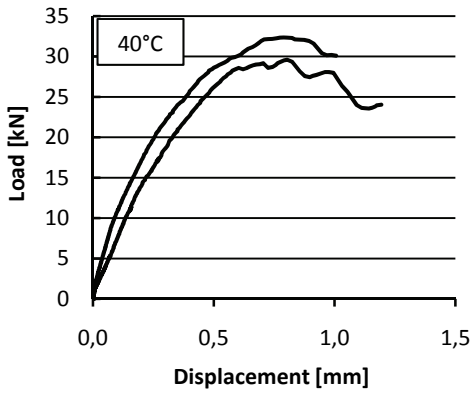
Figure C-1: Load-displacement curves of the three-point bending tests ($f_{cm,cube} = 41.1 \text{ N/mm}^2$)



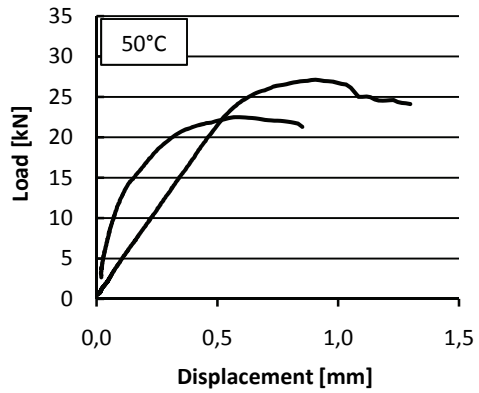
(a)



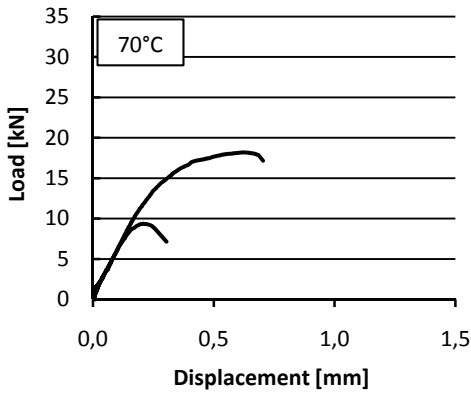
(b)



(c)



(d)



(e)

Figure C-2: Load-displacement curves of the three-point bending tests ($f_{cm,cube} = 70.8 \text{ N/mm}^2$)

NB. The displacement corresponds to the mean value of the measurements of the two LVDTs, when two LVDTs have been used.

C.2 Thermal strains

C.2.1 Thermal strains after heating to 50°C, cooling to 20°C and heating to 50°C

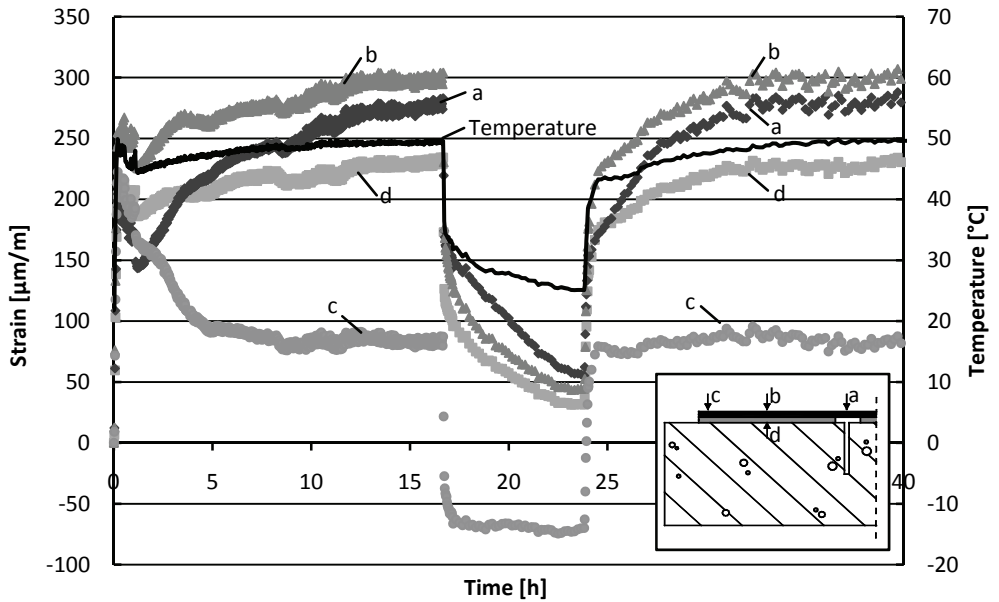


Figure C-3: Strain development in the CFRP (a), concrete-adhesive interface (b) and concrete (c) due to heating and cooling down of a three-point bending test specimen ($f_{cm,cube} = 41.1 \text{ N/mm}^2$)

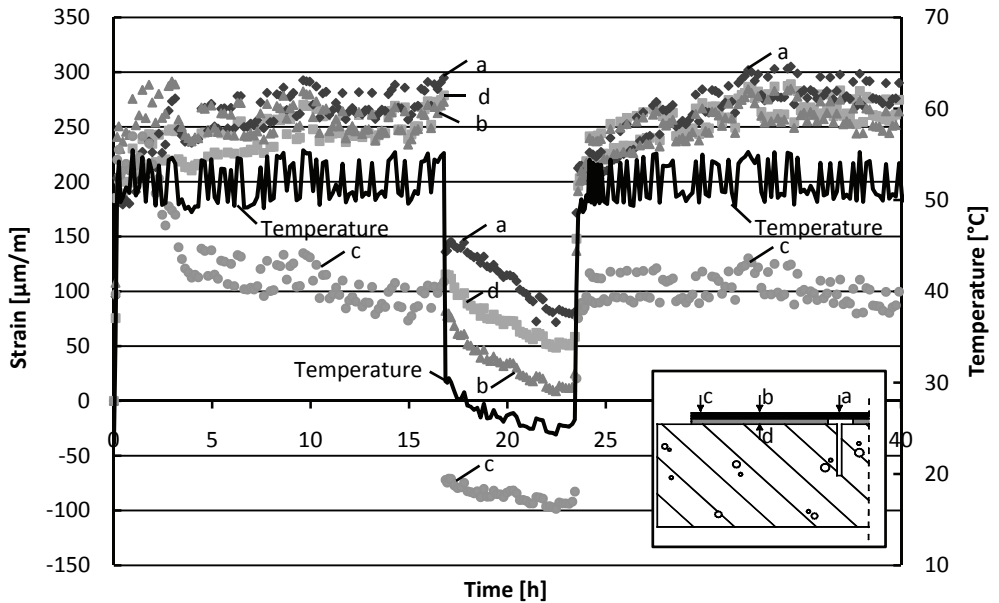


Figure C-4: Strain development in the CFRP (a), concrete-adhesive interface (b) and concrete (c) due to heating and cooling down of a three-point bending test specimen ($f_{cm,cube} = 70.8 \text{ N/mm}^2$)

C.2.2 Thermal strains after heating to 40°C, 50°C and 70°C

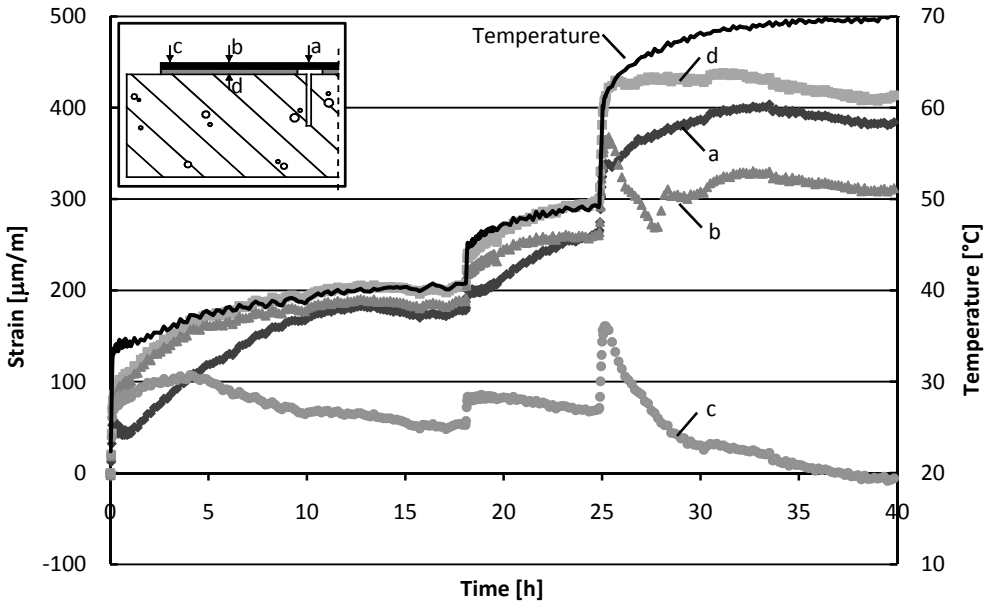


Figure C-5: Strain development in the CFRP (a), concrete-adhesive interface (b) and concrete (c) due to heating of a three-point bending test specimen up to 40°C, 50°C and 70°C ($f_{cm,cube} = 41.1 \text{ N/mm}^2$)

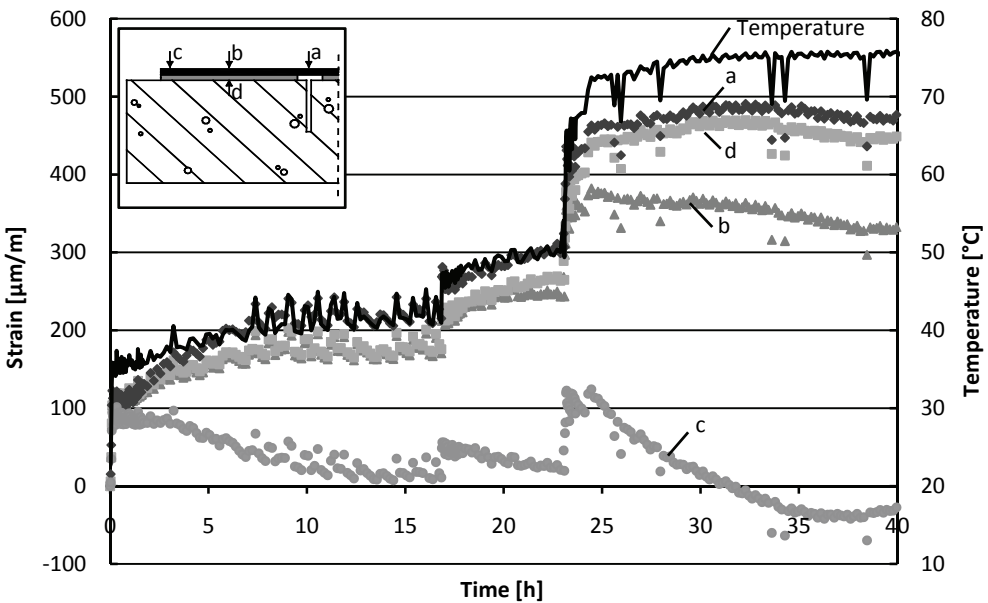


Figure C-6: Strain development in the CFRP (a), concrete-adhesive interface (b) and concrete (c) due to heating of a three-point bending test specimen up to 40°C, 50°C and 70°C ($f_{cm,cube} = 70.8 \text{ N/mm}^2$)

Appendix D. Loading angle tests

D.1 Material properties

Table D-1: Test results of concrete cubic compressive tests (halfway during test program)

Cubic compressive strength	A (11-12-2003) [N/mm ²]	B (12-12-2003) [N/mm ²]	C (18-12-2003) [N/mm ²]	D (6-1-2004) [N/mm ²]
Test 1	44,9	45,8	53,3	44,5
Test 2	43,9	45,2	51,5	41,0
Test 3	43,5	46,6	52,3	45,3
Mean value (46.5 N/mm ²)	44.1	45.9	52.4	43.6

Table D-2: Test results of concrete tensile splitting tests (halfway during test program)

Tensile splitting strength	A (11-12-2003) [N/mm ²]	B (12-12-2003) [N/mm ²]	C (18-12-2003) [N/mm ²]	D (6-1-2004) [N/mm ²]
Test 1	2.66	3.27	3.55	3.33
Test 2	3.03	2.90	3.20	3.14
Test 3	3.10	1.71	3.97	3.18
Mean value (3.1 N/mm ²)	2.93	2.63	3.57	3.22

Table D-3: Test results of concrete surface bond tests (halfway during test program)

Young's modulus	A (11-12-2003) [N/mm ²]	B (12-12-2003) [N/mm ²]	C (18-12-2003) [N/mm ²]	D (6-1-2004) [N/mm ²]
Test 1	4.20	3.80	3.33	3.07
Test 2	3.08	3.68	3.27	3.04
Mean value (3.4 N/mm ²)	3.64	3.74	3.30	3.06

Appendix E. Finite element analyses

E.1 Double-lap shear tests

E.1.1 Lower strength concrete specimens

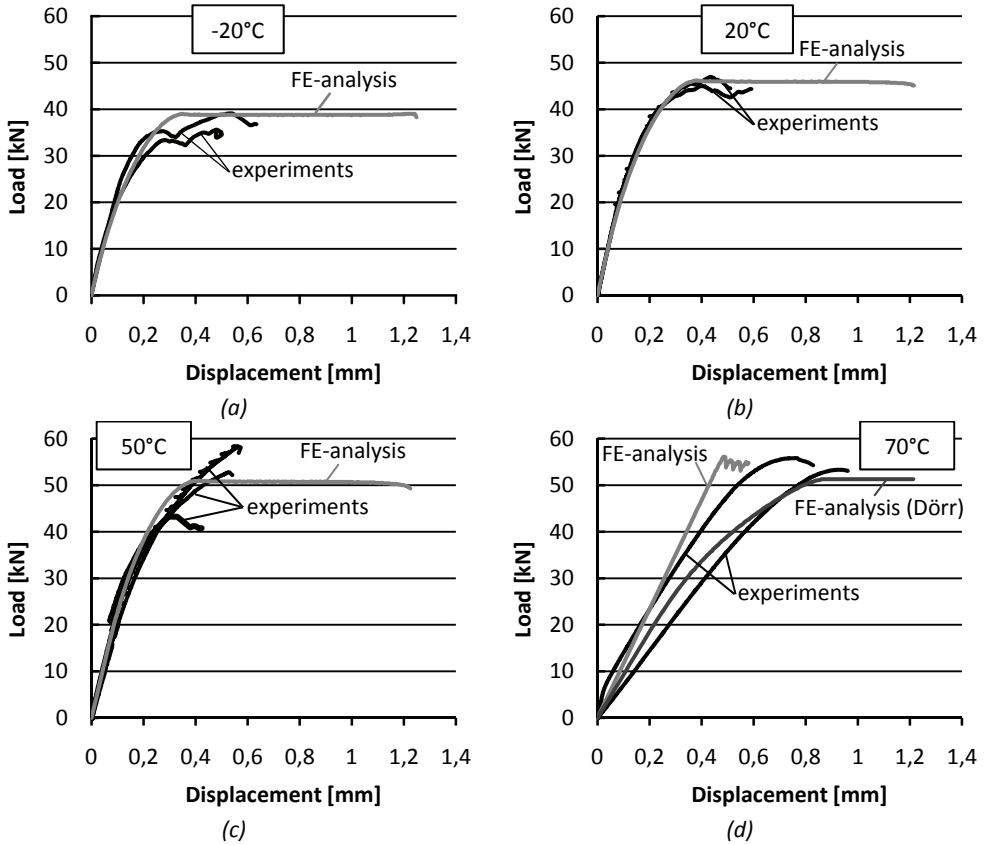


Figure E-1: Load-displacement curve of the double-lap shear tests from experiments and FE-analyses for -20°C (a), 20°C (b), 50°C (c) and 70°C (d) ($f_{cm,cube} = 41.1 \text{ N/mm}^2$)

E.1.2 Higher strength concrete specimens

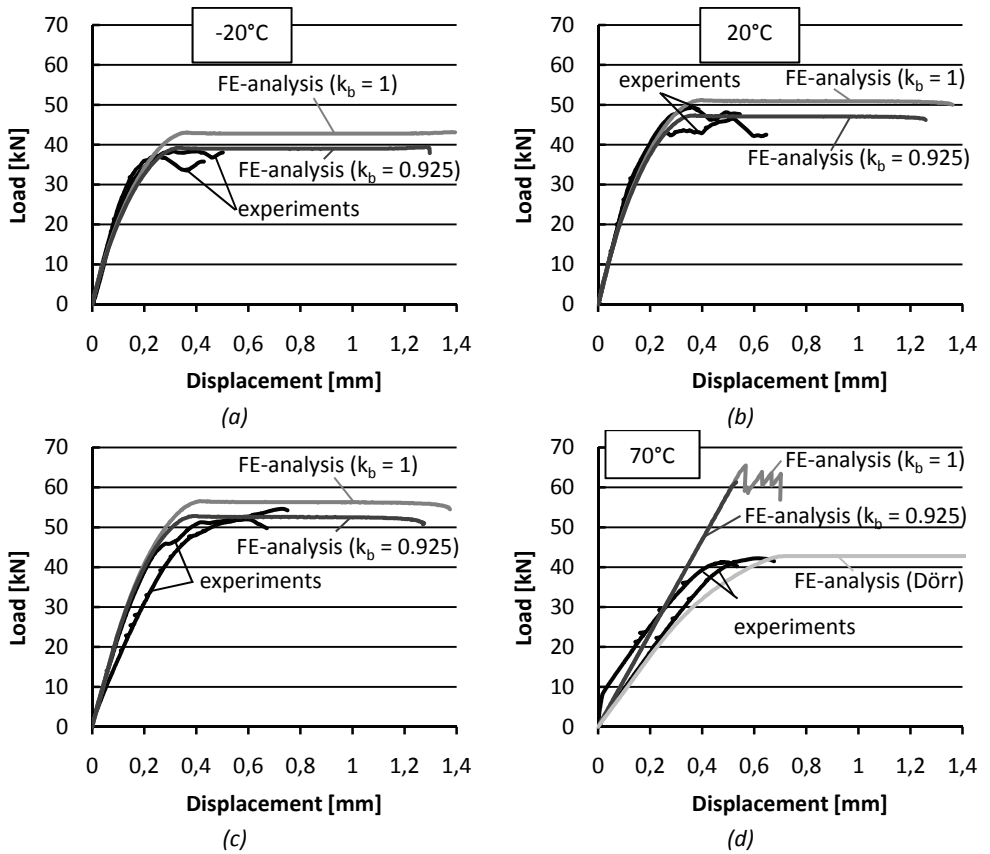


Figure E-2: Load-displacement curve of the double-lap shear tests from experiments and FE-analyses for -20°C (a), 20°C (b), 50°C (c), and 70°C (d) ($f_{cm,cube} = 70.8 \text{ N/mm}^2$)

E.2 Three-point bending tests

E.2.1 Lower strength concrete specimens

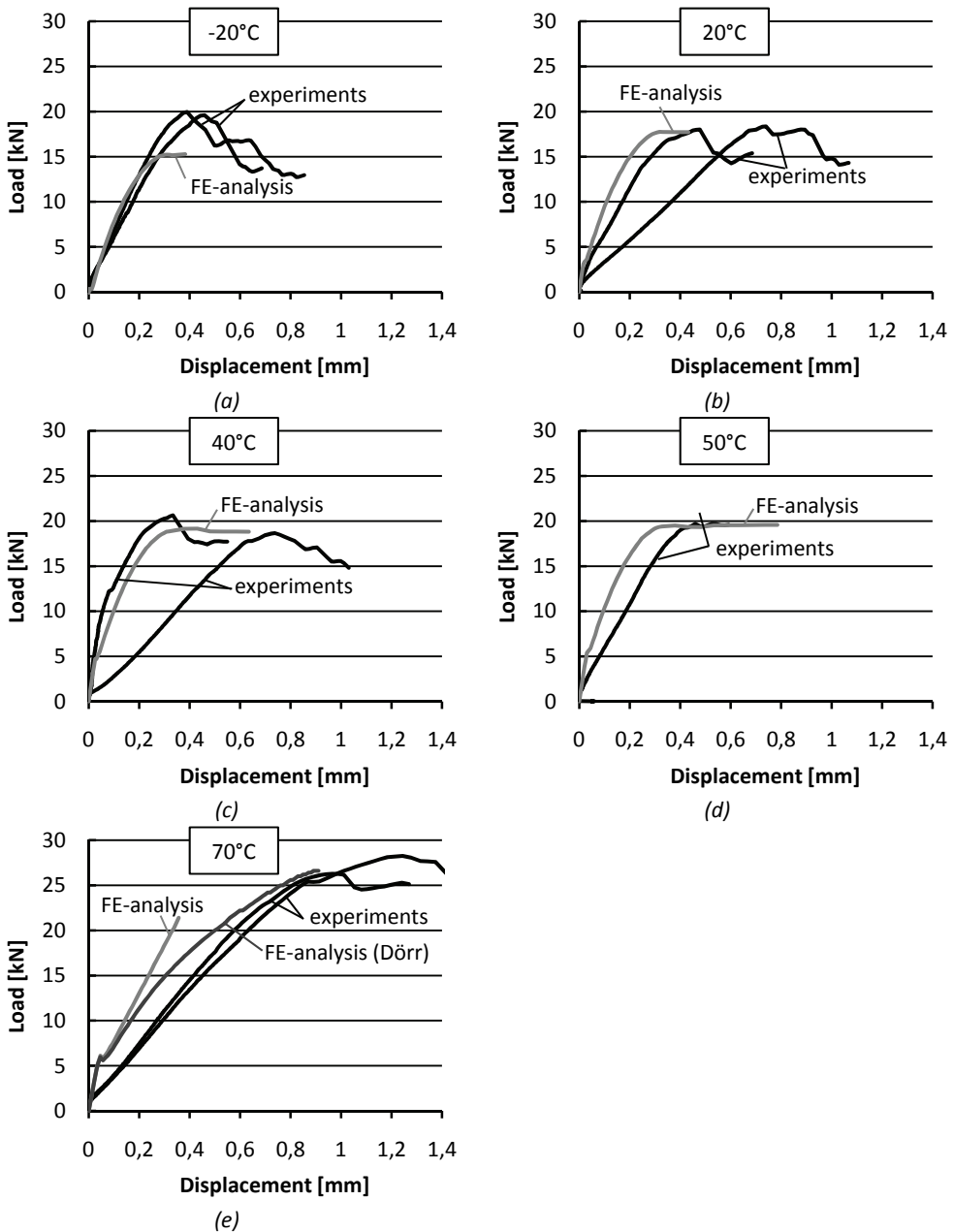


Figure E-3: Load-displacement curve of the three-point bending test from experiments and FE-analyses for -20°C (a), 20°C (b), 40°C (c), 50°C (d) and 70°C (e) ($f_{cm,cube} = 41.1 \text{ N/mm}^2$)

E.2.2 Higher strength concrete specimens

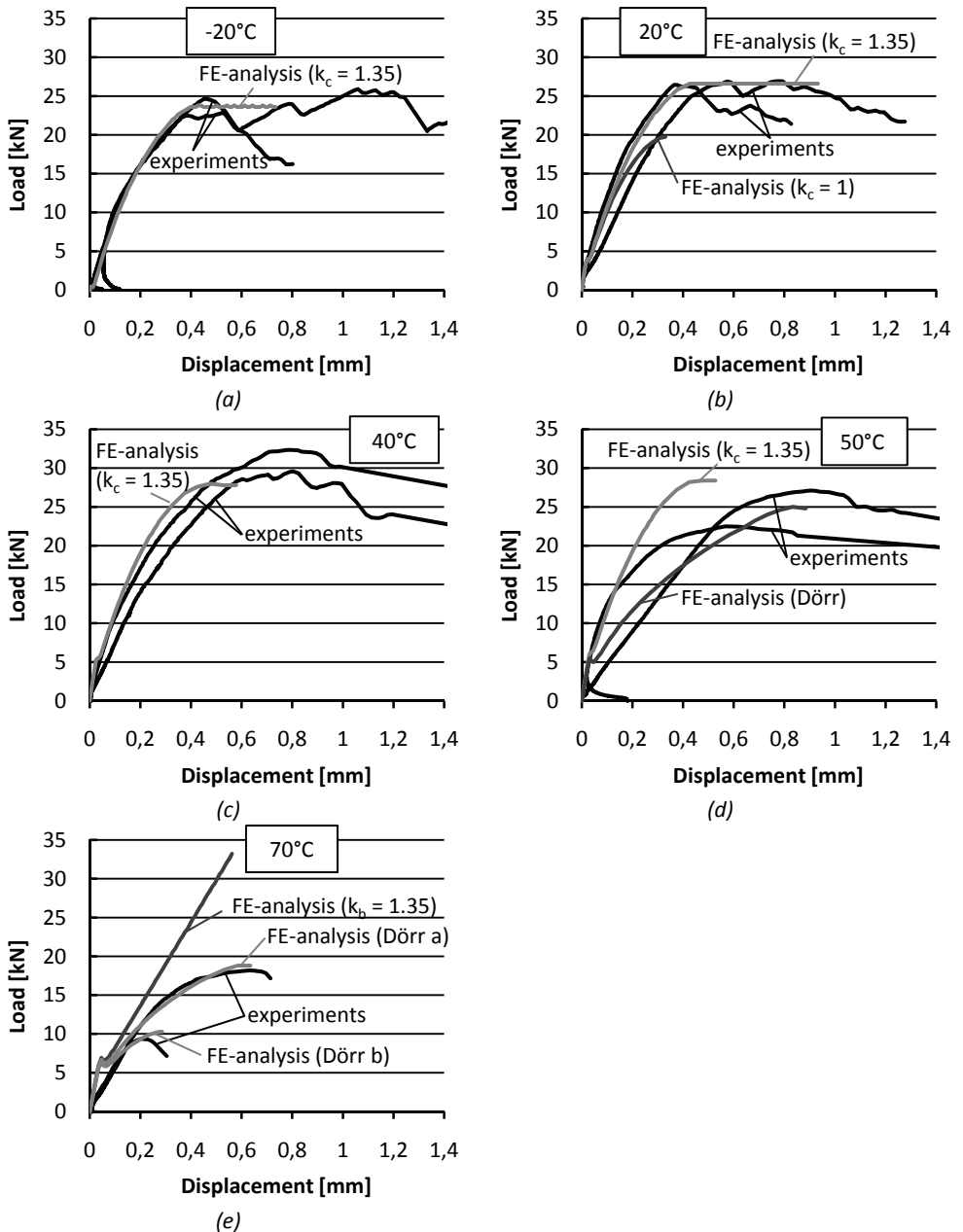


Figure E-4: Load-displacement curve of the three-point bending test from experiments and FE-analyses for -20°C (a), 20°C (b), 40°C (c), 50°C (d) and 70°C (e) ($f_{cm,cube} = 70.8 \text{ N/mm}^2$)

Appendix F. Material properties full scale experiments

F.1 Concrete material properties

Table F-1: Test results of concrete cubic compressive tests

Cubic compressive strength (28d)	C20/25a [N/mm ²]	C20/25b [N/mm ²]	C45/55a [N/mm ²]	C45/55b [N/mm ²]
Test 1	27.6	35.5	50.7	51.7
Test 2	28.1	36.7	51.0	52.3
Test 3	27.4	35.8	51.8	52.9
Mean value	27.7	36.0	51.2	52.3

Table F-2: Test results of concrete tensile splitting tests

Tensile splitting strength (28d)	C20/25a [N/mm ²]	C20/25b [N/mm ²]	C45/55a [N/mm ²]	C45/55b [N/mm ²]
Test 1	2.36	3.11	3.67	3.10
Test 2	2.35	3.17	3.51	4.22
Test 3	2.31	2.71	3.93	3.57
Mean value	2.34	3.00	3.70	3.63

Table F-3: Test results of concrete Young's modulus tests

Young's modulus (28d)	C20/25a [N/mm ²]	C20/25b [N/mm ²]	C45/55a [N/mm ²]	C45/55b [N/mm ²]
Test 1	20,875	19,486	24,906	25,858
Test 2	22,117	19,346	24,186	24,880
Test 3	21,762	-	24,583	24,811
Mean value	21,600	19,400	24,600	25,200

Table F-4: Test results of concrete surface bond tests at 20°C

Concrete bond strength (28d) 20°C	C20/25a [N/mm ²]	C20/25b [N/mm ²]	C45/55a [N/mm ²]	C45/55b [N/mm ²]
Test 1	2.60	3.36	5.09	4.63
Test 2	-	3.87	3.87	4.94
Mean value	2.60	2.78	4.48	4.79

Table F-5: Test results of concrete surface bond tests at 50°C

Concrete bond strength (28d) 50°C	C20/25a [N/mm ²]	C20/25b [N/mm ²]	C45/55a [N/mm ²]	C45/55b [N/mm ²]
Test 1	1.88	2.04	3.72	3.56
Test 2	1.78	2.29	4.02	3.97
Mean value	1.83	2.17	3.87	3.77

Table F-6: Test results of concrete surface bond tests at 70°C

Concrete bond strength (28d) 70°C	C20/25a [N/mm²]	C20/25b [N/mm²]	C45/55a [N/mm²]	C45/55b [N/mm²]
Test 1	-	1.27	2.44	2.70
Test 2	-	-	-	3.00
Mean value	n/a	1.27	2.44	2.85

Appendix G. Full scale experiments

G.1 Thermal strains CFRP

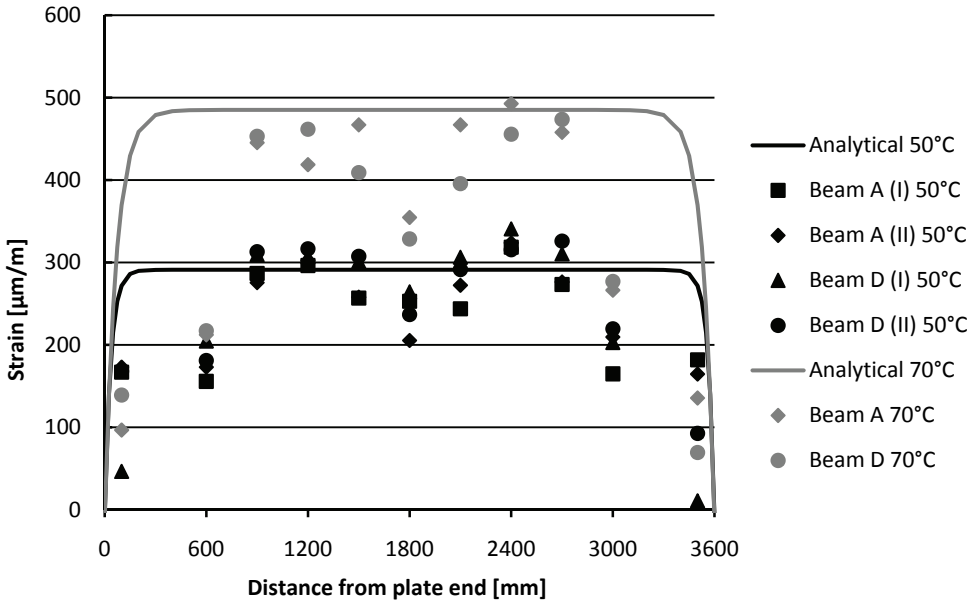


Figure G-1: Thermal strains in the CFRP at 50°C and 70°C for C20/25

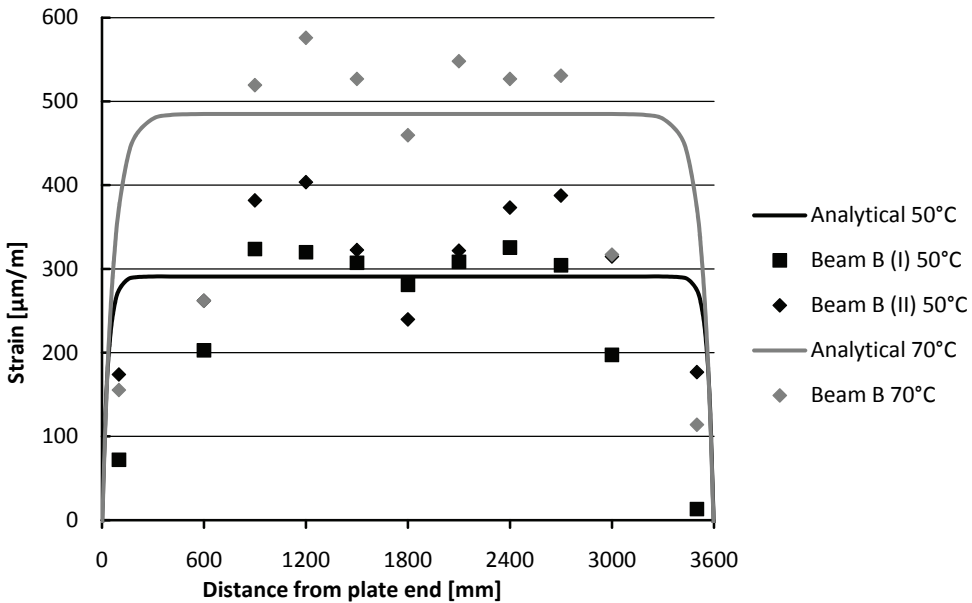


Figure G-2: Thermal strains in the CFRP at 50°C and 70°C for C45/55 and L=100 mm

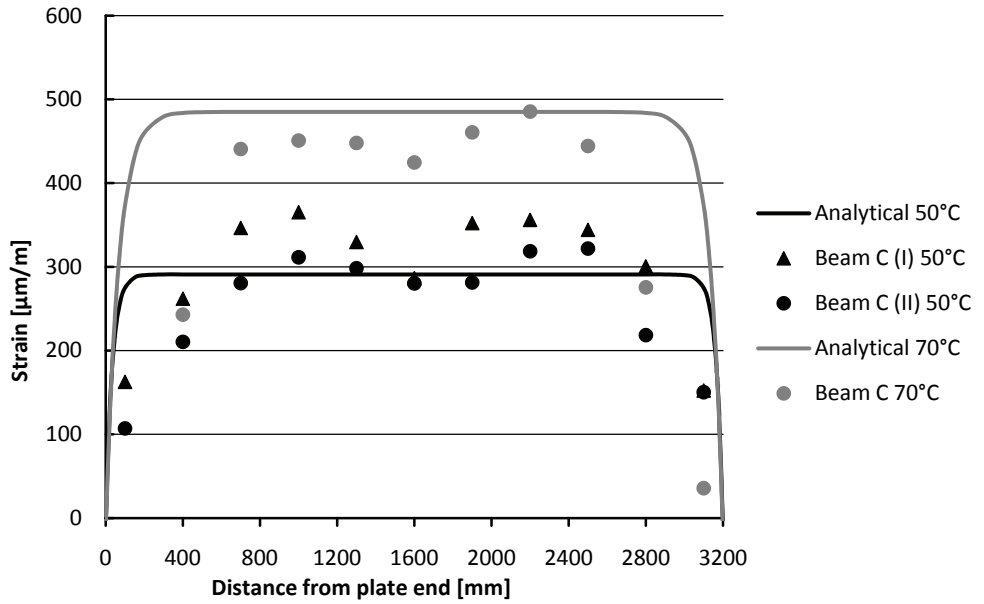


Figure G-3: Thermal strains in the CFRP at 50°C and 70°C for C45/55 and L=300 mm

G.2 Thermal shear stresses in the concrete-adhesive interface

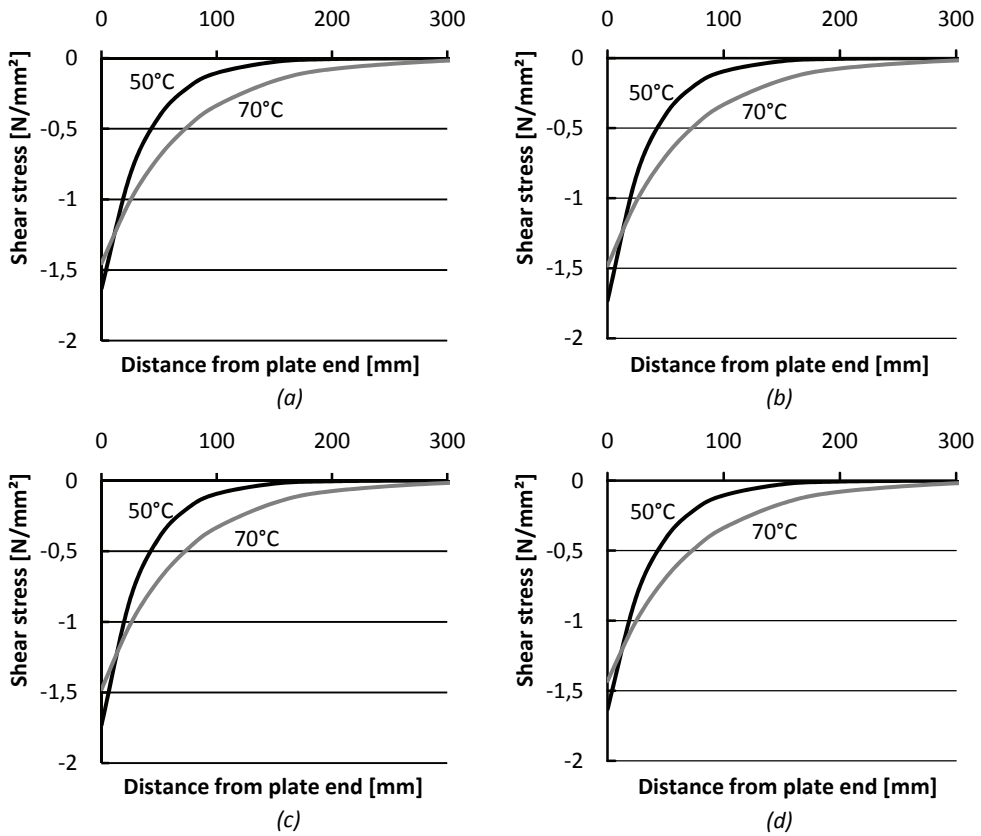


Figure G-4: Analytical thermal shear stresses in the concrete adjacent to the concrete-adhesive interface of beam A (a), B (b), C (c) and D (d) at 50°C and 70°C

Appendix H. Analytical calculations full scale beams

H.1 Introduction

The load-displacement curves have been determined with a cross-section analysis of the beam in Mathcad. For the stress-strain relation of concrete in compression, the parabola-rectangle diagram for concrete under compression was applied according to Eurocode 2 part 1-1 (CEN 1997a). Concrete compressive failure is assumed to occur at a strain of $\varepsilon_{cu2} = 3.5 \times 10^{-3}$. Cracking is assumed to occur at when the concrete reaches the flexural strength of concrete. The contribution of concrete in tension is neglected at yielding of the tensile steel reinforcement and at failure.

For the steel reinforcement, an ideal plastic stress-strain relation has been taken into account, with $f_{ym} = 560 \text{ N/mm}^2$, both in tension and compression. The maximum strain of the tensile reinforcement is taken equal to 32.5×10^{-3} . CFRP is assumed to be linear elastic up to failure ($f_{ftm} = 2800 \text{ N/mm}^2$) and the adhesive layer is neglected in the cross-section analyses. Debonding of the CFRP is not taken into account, and is calculated separately in Appendix I.

The displacement at midspan is approximated by assuming that the CFRP laminate is continuous over the entire length of the beam (Figure H-1). Cracking, yielding and/or crushing is also assumed to occur over the entire length of the beam, although in reality, this is not the case. Nevertheless, this approximation is reasonably accurate for the purpose of estimating the (analytical) load-displacement curves.

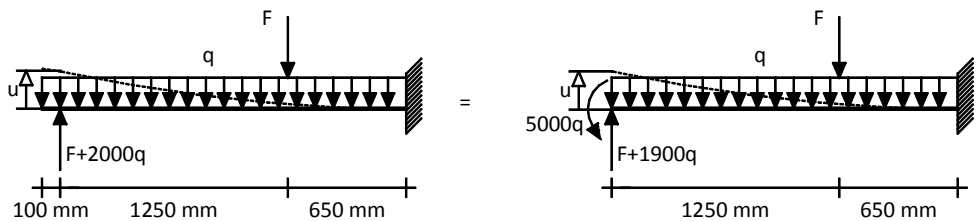


Figure H-1: Calculation of the displacement at midspan

The displacement at midspan is computed with the mechanical scheme of a half beam, as shown in Figure H-1. The external load (F) and the displacement (u) at midspan are approximated with;

$$F = \frac{M_{\text{total}} - M_q}{1250 \text{ mm}} \quad (\text{F.1})$$

$$u = -\frac{F \cdot 650^3}{3 \cdot EI^*} - \frac{F \cdot 650^2}{2 \cdot EI^*} \cdot 1250 - \frac{q \cdot 1900^4}{8 \cdot EI^*} + \frac{(F + 1900 \cdot q) \cdot 1900^3}{3 \cdot EI^*} - \frac{5000 \cdot q \cdot 1900^2}{2 \cdot EI^*}$$

$$u = \frac{1,9 \times 10^9 \cdot F + 2,7 \times 10^{12} \cdot q}{EI^*} \quad (\text{F.2})$$

where

- F Is the external load
- q Is the dead weight of the beam
- u Is the displacement
- M_{total} Is the total bending moment in the beam
- M_q Is the bending moment due to the dead weight
- $EI^* = \frac{M_{\text{total}}}{\kappa}$
- κ Is the curvature of the beam

H.2 Cracking of the concrete

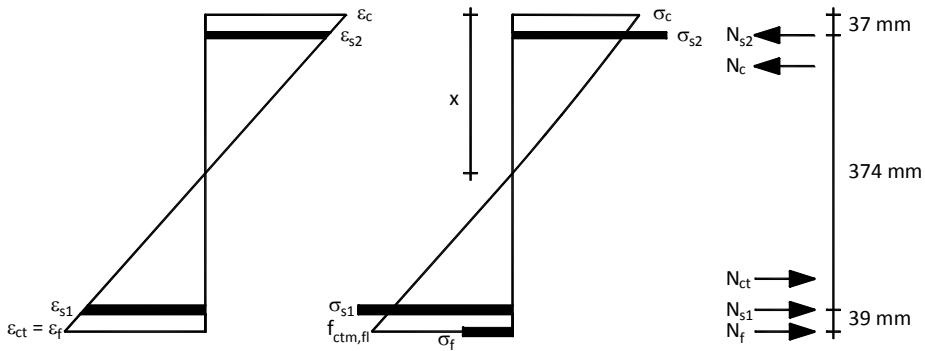


Figure H-2: Stresses and strains in the cross-section at cracking

Assumptions

$$\sigma_c = f_{ctm,fl} \approx 0.9 \cdot (1.6 - h) \cdot f_{ctm,sp} \quad \epsilon_{ct} = \frac{f_{ctm,fl}}{E_{cm}}$$

where

- $f_{ctm,fl}$ Is the mean flexural strength of concrete
- $f_{ctm,sp}$ Is the mean tensile splitting strength of concrete
- h Is the height of the beam
- ϵ_{ct} Is the tensile strain in the concrete
- E_{cm} Is the mean Young's modulus of concrete

Table H-1: Results of the cross-section analyses at cracking of the non-strengthened beam

	Beam A	Beam B	Beam C	Beam D
$f_{ctm,fl} =$	2.4 N/mm ²	3.8 N/mm ²	3.8 N/mm ²	3.1 N/mm ²
$\epsilon_{ct} =$	$1.1 \cdot 10^{-4}$	$1.49 \cdot 10^{-4}$	$1.56 \cdot 10^{-4}$	$1.60 \cdot 10^{-4}$
$M_{total} =$	19 kNm	32 kNm	33 kNm	27 kNm
$M_q =$	4 kNm	4 kNm	4 kNm	4 kNm
$M_F =$	15 kNm	28 kNm	29 kNm	23 kNm
$\kappa =$	$0.50 \cdot 10^{-3} \text{ m}^{-1}$	$0.60 \cdot 10^{-3} \text{ m}^{-1}$	$0.63 \cdot 10^{-3} \text{ m}^{-1}$	$0.67 \cdot 10^{-3} \text{ m}^{-1}$
$F_r =$	11.6 kN	22.3 kN	22.9 kN	18.1 kN
$EI^* =$	$37.0 \cdot 10^3 \text{ kNm}^2$	$52.9 \cdot 10^3 \text{ kNm}^2$	$51.8 \cdot 10^3 \text{ kNm}^2$	$39.8 \cdot 10^3 \text{ kNm}^2$
$u =$	-0.8 mm	-0.9 mm	-1.0 mm	-1.0 mm
$u_F =$	-0.6 mm	-0.8 mm	-0.9 mm	-0.9 mm

F_r Is the external load at cracking
 u_F Is the displacement due to the external load

Table H-2: Results of the cross-section analyses at cracking of the strengthened beam

	Beam A	Beam B	Beam C	Beam D
$M_{total} =$	19 kNm	33 kNm	34 kNm	28 kNm
$M_q =$	4 kNm	4 kNm	4 kNm	4 kNm
$M_F =$	15 kNm	29 kNm	29 kNm	24 kNm
$\kappa =$	$0.51 \cdot 10^{-3} \text{ m}^{-1}$	$0.61 \cdot 10^{-3} \text{ m}^{-1}$	$0.63 \cdot 10^{-3} \text{ m}^{-1}$	$0.68 \cdot 10^{-3} \text{ m}^{-1}$
$F_r =$	11.9 kN	22.9 kN	23.5 kN	19.3 kN
$EI^* =$	$37.4 \cdot 10^3 \text{ kNm}^2$	$53.9 \cdot 10^3 \text{ kNm}^2$	$52.8 \cdot 10^3 \text{ kNm}^2$	$41.5 \cdot 10^3 \text{ kNm}^2$
$u =$	-0.8 mm	-0.9 mm	-1.0 mm	-1.0 mm
$u_F =$	-0.6 mm	-0.8 mm	-0.9 mm	-0.9 mm

F_r Is the external load at cracking
 u_F Is the displacement due to the external load

H.3 Yielding of the tensile steel reinforcement

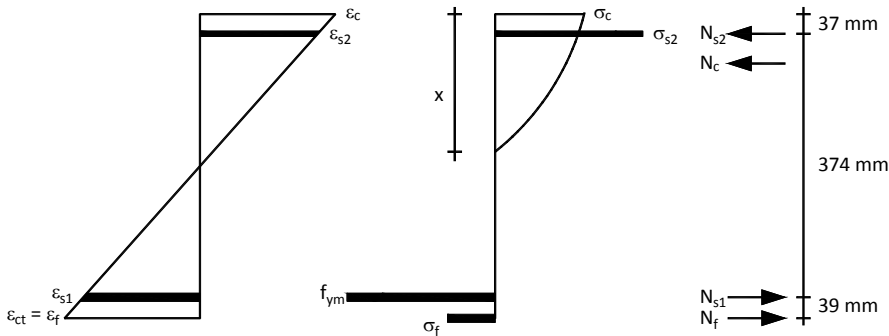


Figure H-3: Cross-section analyses of the strengthened beam at the yielding

Assumptions

$$\sigma_{s1} = f_{ym} = 560 \text{ N / mm}^2$$

where

σ_{s1} Is the stress in the tensile steel reinforcement

f_{ym} Is the Yield strength of steel

Table H-3: Results of the cross-section analyses at yielding of the non-strengthened beam

	Beam A	Beam B	Beam C	Beam D
$M_{total} =$	96 kNm	98 kNm	98 kNm	97 kNm
$M_q =$	4 kNm	4 kNm	4 kNm	4 kNm
$M_F =$	92 kNm	94 kNm	94 kN	93 kNm
$\kappa =$	$9.3 \cdot 10^{-3} \text{ m}^{-1}$	$8.5 \cdot 10^{-3} \text{ m}^{-1}$	$8.5 \cdot 10^{-3} \text{ m}^{-1}$	$8.9 \cdot 10^{-3} \text{ m}^{-1}$
$F_e =$	73.4 kN	75.5 kN	75.4 kN	74.3 kN
$EI^* =$	$10.3 \cdot 10^3 \text{ kNm}^2$	$11.6 \cdot 10^3 \text{ kNm}^2$	$11.6 \cdot 10^3 \text{ kNm}^2$	$10.9 \cdot 10^3 \text{ kNm}^2$
$u =$	-14 mm	-13 mm	-13 mm	-14 mm
$u_F =$	-14 mm	-13 mm	-13 mm	-13 mm

F_e Is the external load at yielding of the internal steel reinforcement

Table H-4: Results of the cross-section analyses at cracking of the non-strengthened beam

	Beam A	Beam B	Beam C	Beam D
$M_{total} =$	108 kNm	118 kNm	118 kNm	133 kNm
$M_q =$	4 kNm	4 kNm	4 kNm	4 kNm
$M_F =$	104 kNm	114 kNm	114 kN	129 kNm
$\kappa =$	$9.5 \cdot 10^{-3} \text{ m}^{-1}$	$8.7 \cdot 10^{-3} \text{ m}^{-1}$	$8.7 \cdot 10^{-3} \text{ m}^{-1}$	$9.4 \cdot 10^{-3} \text{ m}^{-1}$
$F_e =$	82.9 kN	91.3 kN	91.2 kN	103 kN
$EI^* =$	$11.3 \cdot 10^3 \text{ kNm}^2$	$13.6 \cdot 10^3 \text{ kNm}^2$	$13.6 \cdot 10^3 \text{ kNm}^2$	$14.2 \cdot 10^3 \text{ kNm}^2$
$u =$	-15 mm	-13 mm	-13 mm	-15 mm
$u_F =$	-14 mm	-13 mm	-13 mm	-14 mm

F_e Is the external load at yielding of the internal steel reinforcement

H.4 Failure of the beam

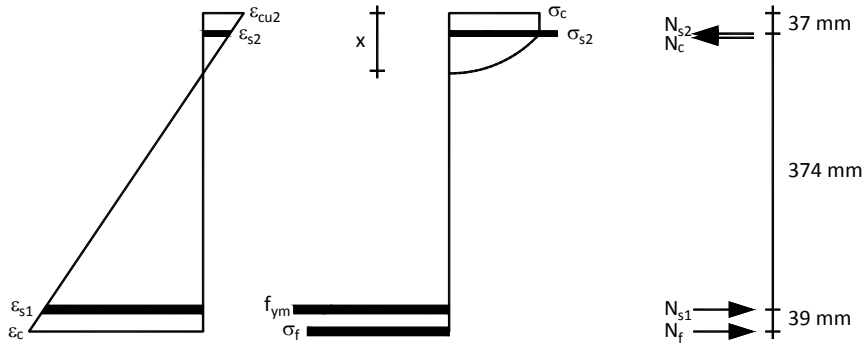


Figure H-4: Cross-section analyses of the strengthened beam at concrete compressive failure

Assumptions

Failure by concrete compressive failure, steel rupture or FRP rupture (assuming that compressive steel reinforcement is not yielding);

Concrete compressive failure $\epsilon_{cu2} = 3.5 \cdot 10^{-3}$

Steel failure $\epsilon_{s1} = 32.5 \cdot 10^{-3}$

Concrete compressive failure $\sigma_f = f_{ftm} = 2800 \text{ N/mm}^2$

where

ϵ_{cu2} Is the strain at compressive failure of concrete

ϵ_{s1} Is the strain at failure of steel

σ_f Is the stress in the FRP

f_{ftm} Is the mean FRP tensile strength

Table H-5: Results of the cross-section analyses at failure of the non-strengthened beam

	Beam A	Beam B	Beam C	Beam D
Failure mode	Concrete failure	Steel failure	Steel failure	Concrete failure
$M_{total} =$	100 kNm	102 kNm	102 kNm	101 kNm
$M_q =$	4 kNm	4 kNm	4 kNm	4 kNm
$M_F =$	96 kNm	98 kNm	98 kNm	97 kNm
$\kappa =$	$57.9 \cdot 10^{-3} \text{ m}^{-1}$	$85.0 \cdot 10^{-3} \text{ m}^{-1}$	$85.0 \cdot 10^{-3} \text{ m}^{-1}$	$72.0 \cdot 10^{-3} \text{ m}^{-1}$
$\sigma_{s2} =$	364 N/mm ²	129 N/mm ²	137 N/mm ²	280 N/mm ²
$\sigma_{s2} < 560 \text{ N/mm}^2$	Yes	Yes	Yes	Yes
$\epsilon_{s1} =$	$21 \cdot 10^{-3}$	$32.5 \cdot 10^{-3}$	$32.5 \cdot 10^{-3}$	$26.9 \cdot 10^{-3}$
$\epsilon_{s1} < 32.5 \cdot 10^{-3}$	Yes	Failure	Failure	Yes
$\epsilon_{cu2} =$	$3.5 \cdot 10^{-3}$	$3.1 \cdot 10^{-3}$	$3.2 \cdot 10^{-3}$	$3.5 \cdot 10^{-3}$
$\epsilon_{cu2} < 3.5 \cdot 10^{-3}$	Failure	Yes	Yes	Failure
$F_u =$	76.4 kN	78.5 kN	78.4 kN	77.4 kN
$EI^* =$	$1.72 \cdot 10^3 \text{ kNm}^2$	$1.20 \cdot 10^3 \text{ kNm}^2$	$1.20 \cdot 10^3 \text{ kNm}^2$	$1.39 \cdot 10^3 \text{ kNm}^2$
$u =$	-89 mm	-131 mm	-131 mm	-112 mm
$u_F =$	-86 mm	-126 mm	-126 mm	-107 mm
σ_{s1}	Is the stress in the compressive steel reinforcement			
ϵ_{s2}	Is the strain in the tensile steel reinforcement			
ϵ_{cu2}	Is the strain in the concrete at the top (compression)			
F_u	Is the failure load			

Table H-6: Results of the cross-section analyses at failure of the strengthened beam

	Beam A	Beam B	Beam C	Beam D
Failure mode	Concrete failure	FRP rupture	FRP rupture	Concrete failure
$M_{total} =$	151 kNm	212 kNm	212 kNm	224 kNm
$M_q =$	4 kNm	4 kNm	4 kNm	4 kNm
$M_F =$	147 kNm	208 kNm	208 kNm	220 kNm
$\kappa =$	$37.3 \cdot 10^{-3} \text{ m}^{-1}$	$45.0 \cdot 10^{-3} \text{ m}^{-1}$	$45.0 \cdot 10^{-3} \text{ m}^{-1}$	$31.4 \cdot 10^{-3} \text{ m}^{-1}$
$\epsilon_c =$	$3.50 \cdot 10^{-3}$	$3.25 \cdot 10^{-3}$	$3.30 \cdot 10^{-3}$	$3.50 \cdot 10^{-3}$
$\epsilon_c < 3.5 \cdot 10^{-3}$	Failure	Yes	Yes	Failure
$\sigma_{s1} =$	484 N/mm ²	390 N/mm ²	401 N/mm ²	518 N/mm ²
$\sigma_{s1} < 560 \text{ N/mm}^2$	Yes	Yes	Yes	Yes
$\epsilon_{s2} =$	$12 \cdot 10^{-3}$	$15 \cdot 10^{-3}$	$15 \cdot 10^{-3}$	$9.7 \cdot 10^{-3}$
$\epsilon_{s2} < 32.5 \cdot 10^{-3}$	Yes	Yes	Yes	Yes
$\sigma_f =$	2200 N/mm ²	2800 N/mm ²	2800 N/mm ²	1770 N/mm ²
$\sigma_f < 2800 \text{ N/mm}^2$	Yes	Failure	Failure	Yes
$F_u =$	118 kN	166 kN	166 kN	176 kN
$EI^* =$	$1.72 \cdot 10^3 \text{ kNm}^2$	$4.74 \cdot 10^3 \text{ kNm}^2$	$4.73 \cdot 10^3 \text{ kNm}^2$	$7.14 \cdot 10^3 \text{ kNm}^2$
$u =$	-58 mm	-69 mm	-69 mm	-48.5 mm
$u_F =$	-56 mm	-68 mm	-68 mm	-47.7 mm
σ_{s1}	Is the stress in the compressive steel reinforcement			
ϵ_{s2}	Is the strain in the tensile steel reinforcement			
ϵ_c	Is the strain in the concrete at the top (compression)			
F_u	Is the failure load			

Appendix I. Analytical calculation debonding mechanisms

I.1 Debonding due to high shear stresses

Matthys (2000) provides the following two equations for 'debonding due to high shear stresses';

$$\varepsilon_s < \varepsilon_{yd} : \frac{V_d}{b_f \cdot (0.95 \cdot d) \cdot \left(1 + \frac{A_s \cdot E_s}{A_f \cdot E_f}\right)} \leq \tau_{cbd} \quad (I.1)$$

$$\varepsilon_s \geq \varepsilon_{yd} : \frac{V_d}{b_f \cdot (0.95 \cdot d)} \leq \tau_{cbd} \quad (I.2)$$

Assuming that steel is yielding, using mean values and safety factors equal to 1, this results in;

$$V_m \leq b_f \cdot (0.95 \cdot d) \cdot \tau_{cbm} \quad (I.3)$$

where

τ_{cbm} is the mean bond strength in shear

$$\approx 1.8 \cdot f_{cbm}$$

f_{ctm} is the mean bond strength in tension

Table I-1: Applied values and results for the computation of debonding due to high shear stresses

	Beam A	Beam B	Beam C	Beam D
b_f	50 mm	80 mm	80 mm	150 mm
d	419 mm	419 mm	419 mm	419 mm
f_{cbm}	2.60 N/mm ²	4.79 N/mm ²	4.48 N/mm ²	2.78 N/mm ²
τ_{cbm}	4.68 N/mm ²	8.64 N/mm ²	8.06 N/mm ²	5.00 N/mm ²
$V_{m,max}$	93 kN	275 kN	257 kN	299 kN

1.2 Debonding at shear cracks

Matthys (2000) provides the following equation for 'debonding at shear cracks';

$$V_{Sd} \leq V_{Rpd} \quad (1.4)$$

where

V_{Sd} is the acting shear force

V_{Rpd} is the design shear capacity for debonding at shear cracks
 $= \tau_{Rpd} \cdot d \cdot b_c$

τ_{Rpd} is the design shear strength

$$\tau_{Rpd} = \tau_{Rpk} / \gamma_c$$

τ_{Rpk} is the characteristic shear strength

$$= 0.38 + 151 \cdot \rho_{eq}$$

$$\rho_{eq} = \frac{A_s + A_f \cdot \frac{E_f}{E_s}}{b_c \cdot d}$$

Using mean values and safety and material factors equal to 1.0, the following equation can be given;

$$V_{Sm} \leq V_{Rpm} \quad (1.5)$$

where

V_{Sm} is the acting shear force

$V_{Rpm} = \tau_{Rpm} \cdot d \cdot b_c$

$\tau_{Rpm} = 0.54 + 151 \cdot \rho_{eq}$

Table I-2: Applied values and results for the computation of debonding at shear cracks

	Beam A	Beam B	Beam C	Beam D
ρ_{eq}	0.0060	0.0063	0.0063	0.0071
τ_{Rpm}	1.44 N/mm ²	1.49 N/mm ²	1.49 kN	1.61 N/mm ²
$V_{Sm,max}$	121 kN	125 kN	125 kN	135 kN

1.3 Debonding at the end anchorage

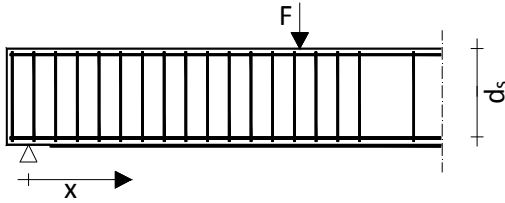


Figure I-1: Definition of x

In *fib*-Bulletin 14 (*fib* 2001), the approach according to Holzenkämpfer (1997), modified by Neubauer and Rostásy (1999), is given for 'debonding at the end anchorage'. The maximum anchorage force and corresponding length can be determined with;

$$N_{f_{a,max}} = \alpha \cdot c_1 \cdot k_c \cdot k_b \cdot b_f \cdot \sqrt{E_f \cdot t_f \cdot f_{ctm}} \quad (1.6)$$

$$l_{f_{a,max}} = \sqrt{\frac{E_f \cdot t_f}{c_2 \cdot f_{ctm}}} \quad (1.7)$$

where

$$\alpha = 0.9$$

$$c_1 = 0.64 \text{ mm}^{1/2}$$

$$c_2 = 2 \text{ mm}^{-1}$$

$$k_c = 1.0$$

$$k_b = 1.06 \sqrt{\frac{2 - \frac{b_f}{b_c}}{1 + \frac{b_f}{400 \text{ mm}}}} \geq 1$$

$$E_f = 165,000 \text{ N/mm}^2$$

$$t_f = 1.2 \text{ mm}$$

$$f_{ctm} \text{ is the tensile strength of concrete}$$

The location where the anchorage length can start has been determined based on the approach as given in Matthys (2000), and corresponds to the location where the internal steel starts yielding according to the shifted moment line (shifted over $z/2$).

$$N_{fad}(x) = \frac{A_s \cdot f_{ym}}{\left(1 + \frac{A_s \cdot E_s}{A_f \cdot E_f}\right)} \quad (1.8)$$

For an anchorage length smaller than $\ell_{fa,max}$, the anchorage force can be determined with;

$$N_{fa}(x) = N_{fa,max} \cdot \frac{\ell_b}{\ell_{b,max}} \cdot \left(2 - \frac{\ell_b}{\ell_{b,max}} \right) \quad (1.9)$$

The maximum force has been computed in an iterative procedure in Mathcad, as the maximum load depends on several parameters (anchorage length, moment distribution, location where steel starts yielding). The results are given in Table I-3. For beam C, the design value has also been computed (with $f_{ctd} = f_{ctm} / 2$).

Table I-3: Applied values and results for the computation of debonding at the end anchorage

	Beam A	Beam B	Beam C	Beam C (design value)	Beam D
b_f	50 mm	80 mm	80 mm	80 mm	150 mm
k_b	1.32	1.22	1.22	1.22	1.01
$f_{ctm,sp}$	2.34 N/mm ²	3.63 N/mm ²	3.70 N/mm ²	3.70 N/mm ²	3.00 N/mm ²
f_{ctm}	2.11 N/mm ²	3.27 N/mm ²	3.33 N/mm ²	1.67 N/mm ²	2.70 N/mm ²
$N_{fa,max}$	24.6 kN	45.4 kN	45.8 kN	32.4 kN	63.8 kN
$\ell_{fa,max}$	217 mm	174 mm	172 mm	244 mm	191 mm
$N_{fad}(x)$	25.0 kN	37.7 kN	37.7 kN	37.7 kN	62.6 kN
$N_{fad}(x) \leq N_{fa,max}$	No	Yes	Yes	No	Yes
F_{max}^*	192 kN	251 kN	168 kN	116 kN	217 kN
x^*	317 mm	203 mm	400 mm	545 mm	265 mm
$N_{fa}(x)^*$	24.6 kN	-	-	32.4 kN	-
ℓ_{fa}^*	217 mm	103 mm	100 mm	244 mm	165 mm
$N_{fa}(x) \leq N_{fa,max}$	Yes	Yes	Yes	Yes	Yes
$\ell_{fa} \geq \ell_{fa,max}$	Yes	Yes	Yes	Yes	Yes

* Determined in an iterative procedure in Mathcad

1.4 Concrete cover rip-off/plate-end shear failure

According to Jansze (1997), the following design equations can be used for 'concrete cover rip-off' / 'plate-end shear failure';

$$V_{sd} \leq V_{Rd} = \tau_{Rd} \cdot b_c \cdot d \quad (1.10)$$

where

τ_{Rd} the characteristic value of the nominal maximum shear stress at debonding

$$= 0.15 \cdot \sqrt[3]{3 \cdot \frac{d}{a_L}} \cdot \left(1 + \sqrt{\frac{200}{d}} \right) \cdot \sqrt[3]{100 \cdot \rho_s \cdot f_{ck}}$$

$$a_L = \sqrt[4]{\frac{(1 - \sqrt{\rho_s})^2}{\rho_s}} \cdot L^3 \cdot d$$

f_{ck} is the characteristic concrete compressive strength

L is the distance between the support and the end of the FRP reinforcement

The mean value can be found with;

$$V_{sm} \leq V_{Rm} = \tau_{Rm} \cdot b_c \cdot d \quad (1.11)$$

where

τ_{Rm} the mean value of the nominal maximum shear stress at debonding

$$= 0.18 \cdot \sqrt[3]{3 \cdot \frac{d}{a_L}} \cdot \left(1 + \sqrt{\frac{200}{d}} \right) \cdot \sqrt[3]{100 \cdot \rho_s \cdot f_{cm}}$$

$$a_L = \sqrt[4]{\frac{(1 - \sqrt{\rho_s})^2}{\rho_s}} \cdot L^3 \cdot d$$

f_{cm} is the mean concrete compressive strength

Table I-4: Applied values and results for the computation of concrete cover rip-off/plate-end peeling

	Beam A	Beam B	Beam C	Beam D
L	100 mm	100 mm	300 mm	100 mm
ρ_s	0.0054	0.0054	0.0054	0.0054
a_L	508 mm	508 mm	1158 mm	508 mm
$f_{cm,cube}$	27.7 N/mm ²	52.3 N/mm ²	51.2 N/mm ²	36.0 N/mm ²
f_{cm}	22.2 N/mm ²	41.84 N/mm ²	40.96 N/mm ²	28.8 N/mm ²
τ_{Rm}	0.94 N/mm ²	1.16 N/mm ²	0.87 N/mm ²	1.02 N/mm ²
$V_{sm,max}$	79 kN	98 kN	73 kN	86 kN
$a > L+d$	yes	yes	yes	yes
$a_L < a$	yes	yes	yes	yes

I.5 Overview

Table I-5: Maximum load according to the different models

	Beam A	Beam B	Beam C	Beam D
Debonding due to high shear stresses	93 kN	275 kN	257 kN	299 kN
Debonding at shear cracks	121 kN	125 kN	125 kN	135 kN
Debonding at the end anchorage	192 kN	251 kN	168 kN	217 kN
Concrete cover rip-off	79 kN	98 kN	73 kN	86 kN

Appendix J. Modified model of Yuan et al.

J.1 Young's modulus of the adhesive - anchorage length relation

To determine the relation between the Young's modulus of the adhesive and the anchorage length, it is needed to know the definition of the anchorage length. Most fracture mechanics based models define the anchorage length ($\ell_{b,max}$) as the bond length over which the shear stresses offers a total resistance of 97% of the applied load, assuming a joint with an infinite length (Holzenkämpfer 1997; Yuan et al. 2004) (Figure J-1).

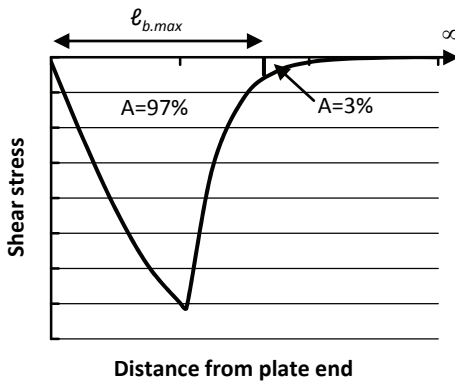


Figure J-1: Definition of the anchorage length for a bi-linear bond-slip model

For the bi-linear bond-slip relation according to Holzenkämpfer (1997), which is used in *fib*-Bulletin 14, the anchorage length can be computed with (Yuan et al. 2004);

$$\ell_{b,max} = a + \frac{1}{2 \cdot \omega} \ln \frac{\omega + \omega_2 \tan(\omega_2 a)}{\omega - \omega_2 \tan(\omega_2 a)} \quad (J.1)$$

where

$$a = \frac{1}{\omega_2} \arcsin \left[0.97 \cdot \sqrt{\frac{s_{f0} - s_{f1}}{s_{f0}}} \right]$$

$$\omega = \sqrt{\frac{k_G}{E_f \cdot t_f}}$$

$$\omega_2 = \sqrt{\frac{1}{E_f \cdot t_f} \cdot \frac{\tau_{max}}{s_{f0} - s_{f1}}}$$

s_{f0} is the slip at end of the bond-slip diagram

s_{f1} is the slip at τ_{max}

$$k_G = \frac{1}{\frac{1}{k_{Gc}} + \frac{1}{k_{Ga}}}$$

Note that this definition of the anchorage length is different compared to the one in *fib*-Bulletin 14. The definition in *fib*-Bulletin 14 was simplified for the use in the design guideline and is a design value. It neglects the properties of the adhesive layer, which makes it unsuitable for the analysis of the relation between the anchorage length and the Young's modulus of the adhesive.

To compute the anchorage length at elevated temperature, the bond-slip relation has to be determined at a certain temperature. The bond-slip relation can be composed of the individual contribution of respectively the concrete and the adhesive layer (Figure J-2a and b). For the purpose of the analysis, it is assumed that bond failure is governed by the concrete and that the adhesive acts as a linear elastic material, also above the glass transition temperature. In reality, this is not the case.

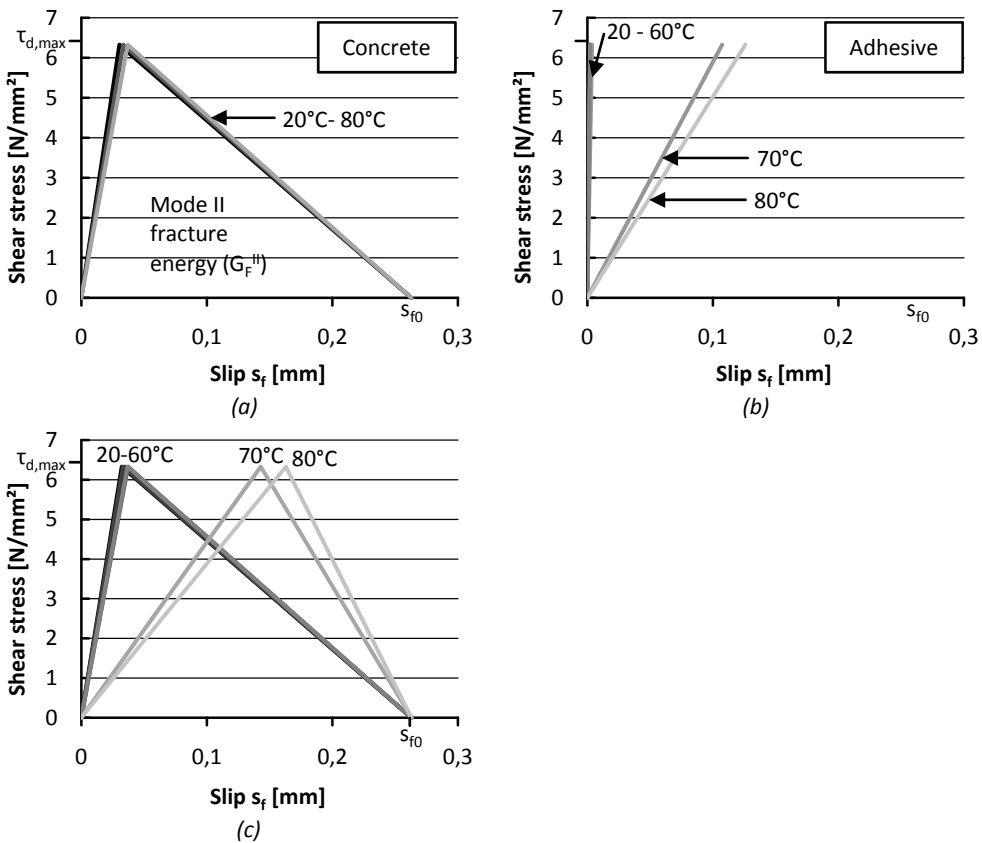


Figure J-2: Bond-slip behavior of the concrete (a), the adhesive (SikaDur-30) (b) and combined (c)

The mode II fracture energy and the shear strength of concrete are assumed to be constant with increasing temperature, similar as in the finite element analyses of the small scale bond tests (Chapter 6). The Young's modulus of concrete will slightly reduce with increasing temperature, due to the reduction of the Young's modulus at elevated temperature. This only slightly affects the slip at τ_{\max} (Figure J-2a). Taking the temperature-Young's modulus relation of SikaDur 30 (section 4.5.3) into account, it can be seen that the slip at τ_{\max} is negligible at temperatures up to 60°C, but becomes significantly higher the contribution of the concrete at 70°C and 80°C (Figure J-2b). Note again that the actual shear strength will be lower in reality, due to bond failure of the concrete-adhesive interface.

Figure J-2c shows the combined bond-slip relation. It can be seen that up to 60°C, the bond-slip relation is mainly governed by the concrete properties, while at 70°C and above, it is significantly affected by the adhesive properties. Note that the maximum slip (s_{f0}) does not increase, as the fracture energy is assumed to be constant. The slip at τ_{\max} (s_{f1}) and at the end of the bond-slip relation (s_{f0}) can be computed with (Holzenkämpfer 1997);

$$s_{f0} = 2 \cdot \frac{G_F^{\text{II}}}{\tau_{\max}} \quad (\text{J.2})$$

$$s_{f1}(T) = \frac{\tau_{\max}}{k_G} \quad (\text{J.3})$$

where

$$G_F^{\text{II}} = k_b^2 \cdot k_c^2 \cdot c_F \cdot f_{\text{ctm}}$$

$$\tau_{\max} = 1.8 \cdot k_b \cdot k_c \cdot f_{\text{ctm}}$$

$$k_b = 1.06 \sqrt{\frac{2 - \frac{b_f}{b_c}}{1 + \frac{b_f}{400 \text{ mm}}}} \geq 1$$

$$k_c = 1.0$$

$$c_F = 0.202 \text{ (value used in fib-Bulletin 14, according to Neubauer and Rostásy (1999))}$$

$$f_{\text{ctm}} \text{ is the tensile strength of concrete}$$

Curriculum Vitae

Personal data

Name: Ernst-Lucas Klamer
Date of birth: February 14th, 1979
Place of birth: Utrecht, The Netherlands
Address: Roskam 9
6641 XG Beuningen (Gld)
The Netherlands
E-mail: E.Klamer@gmail.com

Education

1991-1997: Dr. F.H. de Bruijne Lyceum, Utrecht,
Atheneum
1997-2003: Eindhoven University of Technology,
Faculty of Architecture, Building and Planning,
Department of Structural Design
Master thesis: Numerical simulation (FEM) of the debonding
mechanisms of concrete structures strengthened with externally bonded
CFRP (in Dutch)

PhD research

2003-2009 Eindhoven University of Technology,
Faculty of Architecture, Building and Planning
Department of Structural Design

Work

2008-now Corsmit Raadgevend Ingenieurs,
a company of Royal Haskoning
Structural Design

Influence of temperature on concrete beams strengthened in flexure with CFRP

This thesis provides the results of a PhD research project into the effect of temperature on concrete structures strengthened with externally bonded Carbon Fiber Reinforced Polymer (CFRP). Temperature can possibly affect the behavior of a CFRP strengthened structure, due to the significant difference in the coefficient of thermal expansion between concrete and CFRP and the change in the material properties of the adhesive at elevated temperatures, especially above the glass transition temperature.

Several small scale bond tests were carried out at different temperatures in the range from -20°C to $+80^{\circ}\text{C}$, in order to investigate the effect of temperature on the bond between concrete and CFRP. Additionally, twelve full scale experiments were carried out on 4 meter long CFRP strengthened beams at 20°C , 50°C and 70°C . With these experiments, the effect of temperature on different debonding mechanisms was investigated. Both types of experiments were numerically simulated by means of finite element analyses. Based on the results, it is concluded that, for the design of a CFRP strengthened structure, the effect of temperature can safely be neglected up to about 10°C below the glasstransition temperature of the adhesive.

